

# **Electrical Characterization of Long Conjugated Molecular Wires**

A THESIS

SUBMITTED TO THE FACULTY OF THE GRADUATE SCHOOL OF THE  
UNIVERSITY OF MINNESOTA

BY

*Seong Ho Choi*

IN PARTIAL FULFILLMENT OF THE REQUIREMENTS FOR  
THE DEGREE OF DOCTOR OF PHILOSOPHY

C. Daniel Frisbie, Adviser

April, 2010

© Seong Ho Choi 2010

## Acknowledgements

I thank my parents for their continuous support and attempts to understand and encourage me during what has been simultaneously the most enjoyable and most stressful part of my life. They made this document possible by encouraging and participating in experiences that ensured I would have the background and interest in trying to figure out how the world works.

The decision about whom to work for in graduate school is one of the events I have agonized the most about in my life. As promised, advisor-student relationship at graduate level is a complicated entity consisting of advisor, boss, counselor and friend that can change its active role without warning. Despite of this, I am confident to say that there is no other person besides Professor Dan Frisbie that I would rather have worked with during this process. I especially appreciate him for being given an unusual amount of invaluable support and willingness to direct the projects I was involved with to be accomplished and encouragement to equip me with the confidence against facing the difficulties in scientific researches. He was also an amazing mentor in the efficient management for large number of people, the teaching styles that complicate problems can be simplified with, and the creativity that I have always taken advantage of.

I also thank my collaborators: Dr. BongSoo Kim, Prof. X.-Y. Zhu, and Dr. Greg Haugstad for their major contributions on my researches. The knowledge and information they have transferred me allows subjects and even whole theme of this document to be powerful. I especially thank to Dr. Kim, who happens to be my old friend for his contagious enthusiasm toward science and meaningful conversation to have improved my understanding for this project.

Thank you to all of the past and current members of the Frisbie group. An innumerable amount of useful conversations have occurred thanks to the wonderful colleagues: Dr. JeongHo Cho, Dr. Jiyul Lee, Dr. Bryan Boudouris, Dr. Matt Panzer, Dr. Jihua Chen, Dr. Yu Xia, Dr. Xiuyu Cai, Dr. Jung Yong Kim, Dr. Liang Luo, Derek, Dave, Vivek, Yan, Moon Sung, Bryan, Mingting, Keun Hyung, Salil, Sipei, Wei. JeongHo and Moon Sung deserves extra thanks and I also thank to the past and current members of Korean association in Chemistry Department (Byungsu Kim, Junha Cheon, Juhee Cho,

SungJun Hong, Changhong Ko, Byungran So, Andrew Chung, Wonchul Yoo, Changyup Bak, JungSung Kang, Jabeom Han, Yongwook Kim, DongHyuk Kim) for providing positive distractions necessary to have made this work possible to get through when it felt like work. My time here would not have been nearly as fun without them.

## Abstract

The establishment of structure-property relationships is central to molecular science and this principle applies equally well to the developing field of molecular and organic/polymer electronics. My dissertation research centers on studying the structure-property relationship of charge transport in molecular wires. In particular it involves demonstrating a long-standing prediction of a mechanistic transition from tunneling to hopping as the lengths of molecular wires are varied. In analogous conceptual and technical frameworks, my research has continued to examine hopping conduction as a function of precisely controlled chain architectures. These experiments directly address variable rates of intrachain hopping conduction upon a change of structural entities, which will provide guidance in designing highly conductive molecular wires as well as understanding transport in bulk organic devices.

In this work, we provided direct evidence for a change in transport mechanism from tunneling to hopping in molecular junctions based on three conjugated systems; oligophenyleneimine (OPI) wires ranging in length from 1.5-7.3 nm, oligonaphthalene-fluoreneimine (ONI) wires from 2.3-10.1 nm, and oligotetrafulvalenepromellitimide-imine (OTPI) wires from 2.5-20.2 nm. Our experimental approach involved contacting molecular wires that were grown from one electrode using controlled aryl imine addition chemistry; a metal-coated atomic force microscope tip is used to make the second contact. We showed that near 4 or 5 nm in length the mechanism of transport in the wires changes abruptly, as evidenced by striking changes in length, temperature and electric field dependence of the current-voltage ( $I$ - $V$ ) characteristics. For longer wires, we have been able to analyze the bias dependence to establish at least three different regimes of transport, and we were also able to estimate the single wire conductivity and the hopping energy for each wires, which shows the great sensitivity of hopping transport to the precisely controlled wire architectures in solid-states for the first time. Overall, these experiments open significant opportunities to probe the physical organic chemistry of molecular conduction, e.g. the roles of specific functional groups and bonding architectures on hopping transport in molecular wires.

# Table of Contents

<b>Acknowledgements</b> -----	i
<b>Abstract</b> -----	iii
<b>Table of Contents</b> -----	iv
<b>List of Tables</b> -----	vi
<b>List of Figures</b> -----	vii
1. Molecular Wires-----	1
1.1. Thesis Overview-----	3
2. Molecular Junction -----	7
2.1. Charge Transport in Molecular Wires -----	8
2.1.1. Tunneling (direct Tunneling and Field demssion) -----	9
2.1.2 Hopping-----	14
2.2. Molecular Junction Fabrication Techniques -----	16
2.2.1 Scanning Tunneling Microscope Measurement -----	17
2.2.2. Break Junction Measurement -----	18
2.2.3. Mercury-Drop junctions -----	19
2.2.4. Cross-Wire Junctions -----	20
2.2.5. Nanopore Junctions-----	21
2.2.6. Conducting Probe Atomic Force Microscopy -----	22
2.3. Recent Results on Molecular Wires Connected to Metals-----	25
3. Molecular Self-Assembly and Molecular Wire growth -----	31
3.1. Self-Assembled Monolayers (SAMs) of Organothiols -----	32
3.1.1. Kinetics of Organothiol SAMs -----	32
3.1.2. Monlayer Sturcture of Organothiol SAMs-----	33
3.1.3. Monlayer Formation-----	34
3.2. Step-Wise Growth of Molecular Wires -----	35
3.3. Characterization of Molecular Wires -----	41
4. OligoPhenyleneImine (OPI) Wires-----	47
4.1. Abstract -----	47
4.2. Introduction -----	47

4.3. Experimental -----	49
4.4. Results and Discussion -----	60
5. OligoNaphthalenefluoreneImine (ONI) Wires -----	76
5.1. Abstract -----	76
5.2. Introduction -----	76
5.3. Experimental -----	79
5.4. Results and Discussion -----	84
5.5. Conclusion -----	117
6. Long Alternating Donor-Acceptor Molecular Wires-----	119
6.1. Abstract -----	119
6.2. Introduction -----	119
6.3. Experimental -----	121
6.4. Results and Discussion -----	126
6.5. Conclusion -----	150
7. Outlook: Probing the Physical Organic Chemistry of Hopping Conduction -----	151
7.1. Conjugated Oligoimine Wires-----	151
7.2. New Chemistry -----	155
<b>Bibliography</b> -----	158
<b>Appendices</b> -----	168
1. Curriculum Vitae-----	168
2. List of Publications-----	169
3. Copyright Permission Letters-----	170

## List of Tables

<b>Table 2.1</b> Charge transport mechanisms in a molecular junction-----	16
<b>Table 3.1</b> Various monolayers formed by self-assembly on several metals -----	32
<b>Table 4.1</b> Summary of experimental and calculated data for OPI wires -----	55
<b>Table 4.2</b> Surface coverage and RMS roughness of OPI wires -----	61
<b>Table 5.1</b> Redox properties and energy level alignments of ONI wires -----	90
<b>Table 5.2</b> Analyses of <i>I-V</i> characteristics for ONI wires -----	103
<b>Table 5.3</b> Torsion angles for the neutral (radical-cation) states of the ONI wires as determined at the M062X/6-31G** level of theory.-----	104
<b>Table 5.4</b> Torsion angles for the neutral (radical-cation) states of the OPI oligomer series as determined at the M062X/6-31G** level of theory.-----	105
<b>Table 5.5</b> Torsion angles for the neutral (radical-cation) states of the OPI and ONI oligomer series as determined at the B3LYP/6-31G** level of theory.-----	106
<b>Table 5.6</b> M062X/6-31G** data for the ONI wires. All energies in eV.-----	108
<b>Table 5.7</b> B3LYP/6-31G** data for the ONI wires. All energies in eV.-----	108
<b>Table 5.8</b> M062X/6-31G** data for the OPI wires. All energies in eV.-----	109
<b>Table 5.9</b> B3LYP/6-31G** data for the OPI wires. All energies in eV.-----	109
<b>Table 5.10</b> Estimated molecular height (d) above the gold surface (nm) as determined at the M062X/-31G** level of theory.-----	110
<b>Table 5.11</b> Estimated molecular height (d) above the gold surface (nm) as determined at the B3LYP/-31G** level of theory.-----	111
<b>Table 6.1</b> Redox properties and energy level alignments of OTPI wires. -----	134
<b>Table 6.2</b> Analyses of <i>I-V</i> characteristics for OTPI wires. -----	146



## List of Figures

<b>Figure 1.1</b> Schematic representation of a metal-molecule-metal junction -----	2
<b>Figure 2.1</b> Transmission of electron wave function through a potential barrier -----	7
<b>Figure 2.2</b> Simplified energy level diagram for a molecular electronic junction -----	10
<b>Figure 2.3</b> Fowler-Nordheim plot for the average of 100 $I$ - $V$ curves for a Au-anthracene thiol-Au junction measured by CP-AFM -----	13
<b>Figure 2.4</b> Schematic energy diagram for incoherent hopping -----	15
<b>Figure 2.5</b> A schematic of the mechanically controllable break junction -----	19
<b>Figure 2.6</b> Schematic illustration of mercury-drop junctions: <b>(a)</b> the mercury-mercury junction, <b>(b)</b> the mercury-silver junction. -----	20
<b>Figure 2.7</b> Schematic representation of the cross-wire tunnel junction. -----	21
<b>Figure 2.8</b> Schematic representation of the nanopore junction -----	22
<b>Figure 2.9 (a)</b> Measurement of molecular wire resistance using conducting probe atomic force microscopy (CP-AFM) <b>(b)</b> Transmission electron microscopy (TEM) image of a gold coated AFM tip -----	23
<b>Figure 2.10 (a)</b> Schematic of a nitrite substituted OPE (left), cartoon of an individual molecular junction and its corresponding SEM image (center up), and cartoon of an in-wire molecular junction and SEM image of a junction aligned between two large-area electrodes (center low). <b>(b)</b> Comparison of current versus temperature behavior in in-wire SAM junctions and isolated molecular junctions as a function of bias. -----	26
<b>Figure 2.11 (a)</b> Schematics of T-PTCDI in a STM break junction. <b>(b)</b> Arrhenius plot of conductance versus inverse temperature for T-PTCDI <b>(c)</b> A semilog plot of conductance versus inverse temperature for a T-PTCDI molecule in nonpolar solvent. -----	27
<b>Figure 2.12 (a)</b> Schematic representation of the stepwise growth of metal (M) coordinated molecular wires on a metal surface. <b>(b)</b> A semilog plot of current versus molecular length for the Fe(II) and Co(II)-based molecular wires. <b>(c)</b> A linear plot of current versus inverse molecular length for the Fe(II)-based molecular wires. -----	29
<b>Figure 2.13 (a)</b> STM image of a single polyfluorene chain end with its chemical structure superimposed. <b>(b)</b> Scheme of the chain pulling procedure <b>(c)</b> A semilog plot of conductance vs. distance between the tip and the metal substrate -----	30

<b>Figure 3.1</b> Alkanethiol hexagonal surface lattice on Au(111). -----	33
<b>Figure 3.2</b> Schematic description of <b>(a)</b> SAM formation process, <b>(b)</b> structure of rough gold, <b>(c)</b> preparation of the flat gold. -----	35
<b>Figure 3.3</b> <b>(a)</b> Molecular structure and synthetic route to OPI-p monolayers on gold substrates. <b>(b)</b> The corresponding RAIRS spectra. -----	37
<b>Figure 3.4</b> Molecular structure of ONI 10, the longest ONI wire that was prepared by stepwise additions of naphthalene-2,6-dicarboxaldehyde and fluorene-2,7-diamine. ---	37
<b>Figure 3.5</b> <b>(a)</b> Two-step sequence to bridge electrode surfaces. <b>(b)</b> Bridging by first forming a monolayer with the terpyridyl group and using cobalt ions to orchestrate wire formation. <b>(c)</b> Bridging gaps by first forming a thiol-terminated monolayer and then reacting with a diamine. -----	39
<b>Figure 3.6</b> <b>(a)</b> Schematic representation of the stepwise assembly of the metal centre molecular wires in situ metal surfaces. <b>(b)</b> AFM height image of micropatterned structure. <b>(c)</b> Cross-section analysis of map b at the indicated lines, and histogram analysis of b. <b>(d)</b> Height difference between the measured ODT lines and the molecular wires as a function of the number of coordination steps. -----	40
<b>Figure 3.7</b> Schematics of optical ellipsometry. -----	42
<b>Figure 3.8</b> Schematic picture of internal reflection in ATR. -----	44
<b>Figure 4.1</b> The current-voltage characteristics of <b>(a)</b> OPI 4, <b>(b)</b> OPI 6, and <b>(c)</b> OPI 10 at different temperatures -----	51
<b>Figure 4.2</b> Comparison of IR spectra of ATP and OPI 1-p -----	54
<b>Figure 4.3</b> Molecular structures (left) and RAIRS spectra (right) for the incorporation of a conjugation breaking unit (cyclohexyl group) -----	56
<b>Figure 4.4</b> Cyclic voltammograms of OPI wires-----	57
<b>Figure 4.5</b> UV/visible absorption spectra of <b>(a)</b> OPI wires and <b>(b)</b> CB-OPI wires -----	58
<b>Figure 4.6</b> UPS spectra of OPI wires <b>(a)</b> and CB-OPI wires <b>(b)</b> near the gold Fermi level ( $E_F$ ) -----	59
<b>Figure 4.7</b> <b>(a)</b> Molecular structure and synthetic route to OPI-p and OPI monolayers on gold substrates. <b>(b)</b> RAIRS spectra of OPI-p (left) and OPI monolayers (right) -----	63

<b>Figure 4.8 (a)</b> Measurement of molecular wire resistance using conducting probe atomic force microscopy (CP-AFM). <b>(b)</b> Semilog plot of $R$ versus $L$ for the gold/wire/gold junctions. <b>(c)</b> Arrhenius plot for OPI 4, OPI 6, and OPI 10. -----	64
<b>Figure 4.9</b> Proposed cartoon for OPI 10 -----	66
<b>Figure 4.10</b> Semilog plot of $R$ versus $L$ for gold/OPI/gold junctions and conjugation broken gold/CB-OPI/gold junctions. -----	68
<b>Figure 4.11 (a)</b> Semilog plot of the average current of 10 $I$ - $V$ traces for gold/wire/gold junctions. <b>(b)</b> Log-log plot of the average of 10 $I$ - $V$ traces for the gold/OPI 4/gold and gold/OPI 10/gold junctions. <b>(c)</b> Fowler-Nordheim plot for the OPI 4 data in (b). <b>(d)</b> Fowler-Nordheim plot for the OPI 10 data in (b). -----	71
<b>Figure 4.12</b> Comparison of IR spectra of OPI 10 (black) and OPI 10 which was exposed in ethyl alcohol (red), toluene (green), and acetonitrile (blue) for 96 hours. -----	75
<b>Figure 5.1</b> Schematic representation of hopping transport in a metal-molecule-metal junction (top) and structures of OPI and ONI wires (bottom).-----	78
<b>Scheme 5.1</b> Synthetic route for naphthalene-2,6-dicarboxaldehyde -----	80
<b>Figure 5.2 (a)</b> Molecular structure and synthetic route to ONIp and ONI monolayers on gold substrates. <b>(b)</b> RAIRS spectra of ONIp (left) and ONI monolayers (right). -----	86
<b>Figure 5.3</b> The measured thicknesses and estimated lengths for each ONI wires and conjugation broken (CB)-ONI wires. -----	87
<b>Figure 5.4</b> Cyclic voltammograms of selected ONI wires. -----	88
<b>Figure 5.5</b> UV/visible absorption spectra of ONI wires -----	91
<b>Figure 5.6</b> UPS spectra of ONI wires near the gold Fermi level ( $E_F$ ). -----	92
<b>Figure 5.7</b> Pictorial representation of the ground-state geometry (top) and HOMO and LUMO molecular orbital densities (bottom) for ONI 8 as determined at the M062X/6-31G** level of theory.-----	93
<b>Figure 5.8</b> Measurements of molecular wire resistance with conducting probe atomic force microscopy (CP-AFM). <b>(a)</b> A linear plot of $R$ versus $L$ for the gold/wire/gold junctions. <b>(b)</b> Semilog plot of $R$ versus $L$ for the gold/wire/gold junctions. -----	95
<b>Figure 5.9</b> A semilog plot of $R$ versus $L$ for gold/ONI/gold junctions and conjugation broken gold/CB-ONI/gold junctions. -----	97
<b>Figure 5.10</b> Arrhenius plot for <b>(a)</b> ONI 3 and ONI 4 <b>(b)</b> ONI 5, ONI 7, and ONI 10. -	106

<b>Figure 5.11</b> Pictorial representation of excess positive charge distributions for selected ONI wires as calculated using the M062X/6-31G** level of theory.-----	99
<b>Figure 5.12 (a)</b> Semilog plot of the average current of 20 $I-V$ traces for gold/wire/gold junctions. <b>(b)</b> Log-log plot of the average of 20 $I-V$ traces for the gold/ONI 3/gold and gold/ONI 8/gold junctions. <b>(c)</b> Fowler-Nordheim plot for the ONI 3 data in (b). <b>(d)</b> Fowler-Nordheim plot for the ONI 8 data in (b).-----	102
<b>Figure 5.13</b> Example torsion angles measured for the ONI wires. ONI4 is shown for reference. -----	105
<b>Figure 5.14</b> Change in bond length on ionization in the ONI series as determined at the M062X/6-31G** level of theory.-----	112
<b>Figure 5.15</b> Change in bond length on ionization in the OPI series as determined at the M062X/6-31G** level of theory.-----	113
<b>Figure 5.16</b> Change in bond length on ionization in the ONI series as determined at the B3LYP/6-31G** level of theory.-----	114
<b>Figure 5.17</b> Change in bond length on ionization in the OPI series as determined at the B3LYP/6-31G** level of theory.-----	115
<b>Figure 5.18</b> ONI3 (left) and ONI5 (right) normalized UPS spectra and one-electron density of states as determined at the M062X/6-31G** level of theory.-----	116
<b>Figure 5.19</b> OPI3 (left) and OPI5 (right) normalized UPS spectra and one-electron density of states as determined at the M062X/6-31G** level of theory.-----	117
<b>Scheme 6.1</b> Molecular Structure of OTPI 12, the longest wires among OTPI wires. --	121
<b>Scheme 6.2</b> Synthetic routes for <b>(a)</b> DF-TTF and <b>(b)</b> 4-ABI -----	123
<b>Figure 6.1 (a)</b> Molecular structure and synthetic route to OTPI p on gold substrates up to 5 <sup>th</sup> layers. <b>(b)</b> RAIRS spectra of OTPI-p monolayers up to 5 <sup>th</sup> layers. -----	128
<b>Figure 6.2 (a)</b> Molecular structure and synthetic route to OTPI-p and OTPI monolayers on gold substrates. <b>(b)</b> RAIRS spectra of OTPI-p (left) and OTPI monolayers (right). -----	129
<b>Figure 6.3 (a)</b> The measured thicknesses and estimated lengths for OTPI wires as a function of the number of repeat. <b>(b)</b> High resolution XPS spectra in the S 2p region (top), the N 1s region (middle), and the O 1s region (bottom) for the selected OTPI wires at different lengths. -----	130

<b>Figure 6.4</b> Cyclic voltammograms of selected OTPI wires. -----	133
<b>Figure 6.5</b> UV-vis absorption spectra of selected OTPI wires. -----	135
<b>Figure 6.6</b> Measurements of molecular wire resistance with conducting probe atomic force microscopy (CP-AFM). <b>(a)</b> Semilog plot of $R$ versus $L$ for the gold/wire/gold junctions. <b>(b)</b> A linear plot of $R$ versus $L$ for the gold/wire/gold junctions. -----	137
<b>Figure 6.7</b> Arrhenius plot for <b>(a)</b> OTPI 1, 2, 3 and 6 <b>(b)</b> OTPI 9 and 12. -----	140
<b>Figure 6.8</b> I-V curves in a range of temperature from 245 to 333 K for <b>(a)</b> OPTI 1, <b>(b)</b> OPTI 2, <b>(c)</b> OPTI 3, <b>(d)</b> OPTI 6, <b>(e)</b> OPTI 9, <b>(f)</b> OPTI 12. -----	141
<b>Figure 6.9</b> Semilog plot of the average current of 20 $I-E$ traces <b>(a)</b> for gold/short wires/gold junctions, <b>(b)</b> for gold/long wires (regime 1)/gold junctions, and <b>(c)</b> for gold/long wires (regime 2)/gold junctions.-----	143
<b>Figure 6.10</b> Fowler-Nordheim plots of the average of 20 $I-V$ traces <b>(a)</b> for the gold/OTPI 2/gold, and <b>(b)</b> for the gold/OTPI 12/gold. <b>(c)</b> Log-log plot for OTPI 2 and OTPI 12 in <b>(a)</b> and <b>(b)</b> , respectively. -----	145
<b>Figure 6.11</b> Temperature dependent $I-V$ characteristics for OTPI 12 on <b>(a)</b> a linear axes, <b>(b)</b> a log-log axes, and <b>(c)</b> Fowler-Nordheim axes. -----	149
<b>Figure 7.1</b> Oligoimine systems: Wire 1 is designed to release steric strain in the wire. Wire 2 is designed to planarize the dihedral angle with hydrogen bonds -----	152
<b>Figure 7.2</b> In wire 3, the fluorine substituents will lower the LUMO level perhaps allowing electron (as opposed to hole) conduction. Wire 4 is a thiophene-based architecture that may lead to a low oxidation potential with higher conductivity -----	154
<b>Figure 7.3</b> Schematic of electrochemical gating of long conjugated donor-acceptor wires. -----	155
<b>Figure 7.4</b> Metal containing systems: Wire 5 can be prepared by metal coordination chemistry and may be highly conductive by virtue of the multiple metal centers. Wire 6 contains a single redox center that might lead to charge correlation effects (Coulomb blockades) and interesting I-V behavior. -----	156
<b>Figure 7.5</b> Conjugated oligovinylene wires: Wire 7 can be prepared by step-wise Knoevenagel condensation. -----	157

# 1 Molecular Wires

Long,  $\pi$ -conjugated molecules are often described as “molecular wires”, a term that implies these molecules can transport charge efficiently over long distances<sup>1-5</sup>. Here “long” corresponds to perhaps ~5-100 nm, greater than typical tunneling lengths, but tiny in comparison to length scales in the everyday world. Interest in molecular wires has at least two principal motivations. Some workers have postulated that molecular conductors may be useful in future nanoelectronic devices where the inherent small size of molecules and their tunable electronic properties, sensitivity to specific analytes, and propensity for self-organization seem potentially advantageous<sup>4-8</sup>. On the other hand, fundamental studies of conduction in molecular wires offer opportunities to elucidate microscopic conduction mechanisms operative in films of conjugated polymers. This in turn may positively impact efforts to optimize these materials for applications in solar energy conversion<sup>9, 10</sup>, electroluminescent displays<sup>11-13</sup>, and printed electronics<sup>14, 15</sup>, for example.

The past decade has witnessed remarkable progress<sup>16-22</sup> in our ability to characterize electrical conduction in molecules using a simple testbed called a molecular junction. In a molecular junction, single molecules or an ensemble of molecules are connected between closely-spaced metal electrodes, Figure 1.1. In these nanostructures, the conductivity of the molecular wires is determined directly by recording the current-voltage (I-V) characteristics. There are now perhaps a half dozen different methods for forming reproducible molecular junctions that are summarized in this thesis and in several recent reviews<sup>18-22</sup>. The ability to contact molecules easily and reproducibly enables systematic measurements of conduction as a function of molecular architecture<sup>17, 23-25</sup>, molecular length<sup>25-27</sup>, applied voltage (electric field)<sup>28</sup>, temperature<sup>29-37</sup>, contact metallurgy<sup>27</sup>, and surface linker chemistry<sup>26, 32, 38-42</sup>. By combining organic synthesis with such systematic measurements, exciting opportunities are created for probing structure-transport relationships in molecular wires in a manner analogous to classical physical organic chemistry approaches for understanding reaction mechanisms<sup>43</sup>.

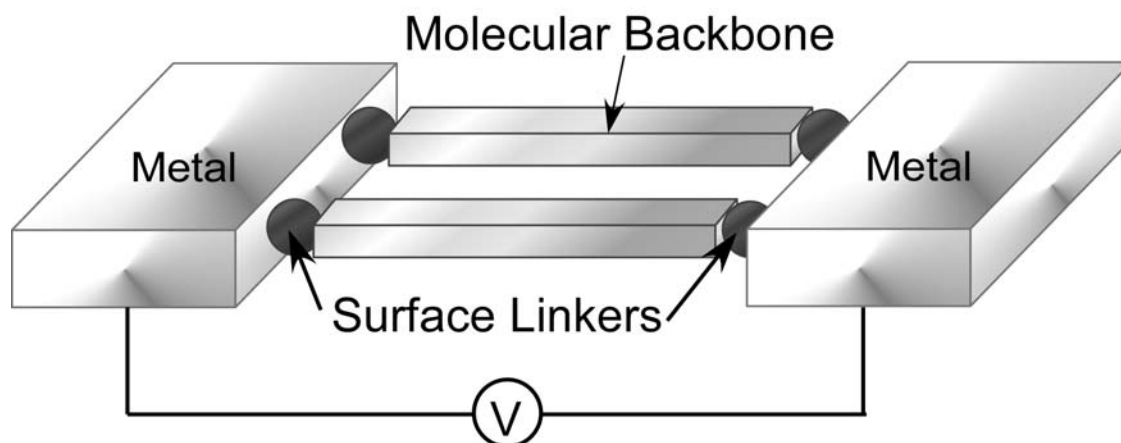


**Figure 1.1** Schematic representation of a metal-molecule-metal junction.

In this context, it is important to recognize that understanding of direct current (DC) conduction through molecules builds on several decades of prior work in the chemical community on electron-transfer (ET) processes within molecules dissolved in solution. Rate constants have been measured for intramolecular ET reactions on a wide range of systematically varied donor-bridge-acceptor (D-B-A) molecules<sup>2, 44-48</sup>. It is well established that ET rates depend on both the redox levels of the D and A components<sup>44, 49</sup>, the bonding architecture and length of the bridge<sup>50-54</sup>, as well as dynamic motions (vibrations) within the molecule<sup>48, 55</sup>. Furthermore, it has been demonstrated that different ET mechanisms (e.g., tunneling versus hopping) can be distinguished by varying the temperature<sup>48</sup>. A great body of literature on structure-property correlations for intramolecular ET reactions has accumulated<sup>2, 44-55</sup>, and predictions about steady-state DC conduction in molecular junctions can be made based on this prior work<sup>56, 57</sup>.

However, the presence of metallic contacts in molecular junctions also introduces significant electronic perturbations that make these solid state experiments fundamentally different from solution ET studies. Injection of charge into molecules from metals naturally depends on image forces and dipoles that can exist at metal-molecule interfaces, as well as on metal-molecule coupling and the energetic position of the Fermi level with respect to the molecular orbitals<sup>57-59</sup>. Additionally, the population of electrons that are

available for transport across a molecular junction is tuned by the applied bias, which is clearly different from the situation in isolated D-B-A molecules in which single electrons (or holes) are made available for transfer via an initial excitation step. Finally, steady-state DC conduction in molecules may lead to charge correlation phenomena (*e.g.*, Coulomb blockading<sup>60-62</sup>) that are not germane to typical solution ET experiments. However, solution ET studies allow the use of ultrafast spectroscopy to observe ET dynamics that cannot be accessed in molecular junctions. Thus, solution ET and solid state DC conduction experiments are best viewed as complementary approaches. Collectively, they produce a more complete picture of the problem of electron transport in molecular wires.

## **1.1 Thesis Overview**

The establishment of structure-property relationships is central to molecular science and this principle applies equally well to the developing field of molecular and organic/polymer electronics. My dissertation research centers on studying the structure-property relationship of charge transport in molecular wires. In particular it involves demonstrating a long-standing prediction of a mechanistic transition from tunneling to hopping as the lengths of molecular wires are varied. In analogous conceptual and technical frameworks, my research has continued to examine hopping conduction as a function of precisely controlled chain architectures. These experiments directly address variable rates of intrachain hopping conduction upon a change of structural entities, which will provide guidance in designing highly conductive molecular wires as well as understanding transport in bulk organic devices.

Specifically, the focus of this thesis is on DC electrical conduction in molecular junctions incorporating long conjugated molecular wires in which charges are injected into molecular orbitals and driven along the molecular backbone by an applied electric field, the so-called hopping transport regime. Elegant experiments involving single electron tunneling processes in molecular junctions<sup>60-62</sup>, for example, will not be covered as our emphasis here is on longer molecules in which multiple hopping events occur. Significant portions of the thesis will cover changes in transport mechanisms that are



driven by applied bias, temperature, or molecular length. We begin by reviewing basic charge transport mechanisms as comprehension of these is required to understand the broad spectrum of current-voltage behavior exhibited in molecular junctions. We conclude with an outlook on future hopping transport experiments in molecular wires.

Chapter 2 is devoted to explaining the theoretical background of molecular electronics and representative junction fabrication techniques that have been developed. Further, recent intriguing papers regarding hopping transport and long conjugated systems have been reviewed. Chapter 3 is intended to provide general information about self-assembled monolayers including molecular structure, preparation and characterization. In addition, step-wise growth of molecular wires, our method to prepare long conjugated systems will be described.

Chapter 4 through Chapter 6 presents my publications and details. Chapter 4 has been published as S. H. Choi, B.-S Kim, and C. D. Frisbie “Electrical Resistance of Long Conjugated Molecular Wires” *Science* **2008**, 320, 1482. In this work, we provided direct evidence for a change in transport mechanism from tunneling to hopping in molecular junctions based on conjugated oligophenyleneimine (OPI) wires ranging in length from 1.5-7.3 nm. Our experimental approach involved contacting OPI wires that were grown from one electrode using controlled aryl imine addition chemistry; a metal-coated atomic force microscope tip is used to make the second contact. We showed that near 4 nm in length the mechanism of transport in the wires changes abruptly, as evidenced by striking changes in length, temperature and electric field dependence of the current-voltage ( $I$ - $V$ ) characteristics. For longer wires, we have been able to analyze the bias dependence to establish at least three different regimes of transport, and we were also able to estimate the single wire conductivity and the hopping energy. Overall, these experiments open significant opportunities to probe the physical organic chemistry of molecular conduction, e.g. the roles of specific functional groups and bonding architectures on hopping transport in molecular wires.

Chapter 5 has been published as S. H. Choi, C. Risko, M. C. R. Delgado, B.-S Kim, J.-L. Bredas and C. D. Frisbie, “Transition from Tunneling to Hopping Transport in Long Conjugated Oligo-imine Wires Connected to Metals” *Journal of the American Chemical Society* **2010**, 132, 4358. The main advantage of aryl imine addition chemistry

is that the chemistry is adaptable to a wide variety of molecular building blocks. Thus it should be possible to study wire conduction as a function of precisely controlled chain architecture. We expect, for example, that we will be able to examine the dependence of wire conduction on energy levels tuned by additional functionalities of molecular building blocks and the strength of electronic couplings between them. In this work, we have taken the next steps in this direction by building wires from larger, more conjugated molecular building blocks. Specifically we have used alternating naphthalene and fluorene blocks to build wires up to 10 nm in length. We show that the addition chemistry works clearly and that in some respects these new oligo-naphthalene-fluorene-imine (ONI) wires are an even better system for transport studies than the original OPI wires. A change in transport mechanism from tunneling to hopping is also exhibited in molecular junctions based on ONI wires ranging in length from 2.5 to 10.3 nm, as supported by striking changes in the length, temperature, and electric field dependence of transport characteristics. Their dependencies, however, differ with OPI wires due to more efficient electronic coupling in the ONI structures. In particular, this effect is stronger in longer wires, which yield higher single-wire conductivity by factor of 2 and lower hopping energy by 30 meV compared to OPI wires. Overall, these experiments demonstrate the influence of molecular structure on hopping transport along the long wire backbone.

Chapter 6 has been prepared for submission to *Journal of the American Chemical Society* as S.-H. Choi and C. D. Frisbie, "Enhanced Hopping Conductivity in Alternating Donor-Acceptor Molecular Wires up to 20 nm in Length". This work describes another molecular system designed for controlling carrier density in molecular wires. OPI wires exhibited relatively low conductivity ( $\sim 1.0 \times 10^{-4}$  S/cm) partially due to the low carrier density. Utilizing donor-acceptor architectures within the molecular backbone may increase the amount of carriers present in wires. In the context of polymer electronics, the donor-acceptor systems cause partial intra-molecular charge transfer that enables manipulation of the electronic structure (HOMO/LUMO levels), leading to low band gap semiconducting polymers ( $< 2.0$  eV). In low band gap systems, the oxidation and reduction can be achieved at lower potentials, facilitating both electron and hole injections to the system. This approach also yields higher single chain conductivity by exhibiting doping effects on molecular wires.

Recent successes summarized in this thesis in building long molecular wires and measuring their DC conduction properties suggest that a wide variety of experiments can be undertaken to probe the influence of molecular structure on hopping transport. In Chapter 7, we consider several new wire designs aimed at understanding the roles of intramolecular steric interactions, electronic structures, and redox properties on hopping conduction. In particular, new chemistry based on Knoevenagel condensation and metal coordination will be introduced to open up a wide variety of possibility to build long conjugated molecular wires.

## 2 Molecular Junction

The ability to measure and control electrical current through molecules is a critical requirement toward the goal of building electronic devices using individual molecules<sup>63</sup>. This ability also offers us a unique opportunity to understand charge transport, an important phenomenon that occurs in many chemical and biological processes<sup>64, 65</sup>. Furthermore, it allows us to read the chemical information of molecules electronically,<sup>66</sup> which opens the door to chemical and biosensor applications based on the electrical detection of individual molecular binding events<sup>67</sup>. To realize this ability, one must first bring molecules into contact with a nanoscale spaced two external electrodes as its schematic depiction is shown in Figure 1.1, and can be defined as a molecular junction. In this nanoscopic junction, the contact must be robust, reproducible, and able to provide sufficient electronic coupling between molecule and the electrodes.

Recent advances<sup>68</sup> of organic electronics show the feasibility of the use of organic molecules in commercial electronics including organic light emitting devices (OLEDs) and organic field effect transistors (OFETs). These devices function on the basis of the macroscale properties of the molecules used in their fabrication. Bulk film structure plays a significant role in determining the electronic properties of these devices, as defects in the organic layer provide a means for charge to become trapped within the film.<sup>69</sup> In contrast, nanoscopic molecular junctions probe the electronic properties of either single molecules or finite arrays of molecules. The scale on which these junctions operate eliminates the effect of film defects and any other morphological complexities, and allows for a determination of the fundamental nature of charge transport through a molecular chain.

In fact, a wide variety of molecular systems has been studied in forms of a molecular junction. However, the measured electrical behaviors depend not only on the molecules itself, but also on the properties of the electrodes and the atomic-scale molecule-electrode contact geometry. It is thus important to note that molecular wires which involve long conjugated systems are a good candidate to study pure influence of molecular structures in charge transport because one can get rid of contact issues

incorporating with longer molecules in a junction. In this geometry, traveling charges may be free or less influential from image charges on metal leads.

## ***2.1 Charge Transport in Molecular Junction***

The charge transport mechanism of a wire can be revealed by how its electrical resistance varies with length and temperature. For example, the resistance of a conventional metallic wire is directly proportional to its length and increases with temperature generally following a polynomial.<sup>70</sup> This is a direct result of the diffusive (incoherent) carrier transport mechanism in the metal. However, this particular scaling need not hold for conduction through molecular wires connected to metal contacts. It is well understood that for sufficiently short molecules electrons can tunnel between the two contacts and in this case the junction resistance increases exponentially with molecular length and is only weakly temperature dependent.<sup>24-27, 29, 71-76</sup> The tunneling mechanism is often “non-resonant” in that the tunneling electron energies are not precisely matched with the molecular orbital energies; however, the frontier molecular orbitals still assist the tunneling process (i.e., they lower the junction resistance) by lowering the effective tunneling barrier.<sup>41</sup>

For longer wires at moderate temperatures, the rate of tunneling is strongly suppressed and instead charge can be injected into frontier orbitals of the wire molecules and transported by an incoherent hopping mechanism.<sup>75, 76</sup> In this case, the transport is thermally activated and the length dependence of resistance is predicted to be linear.<sup>75-79</sup> This is the regime of central interest for molecular wire studies. However, it is important to note that the charge transport mechanism in a junction depends on many factors including applied bias.<sup>28, 33</sup> Large biases may result in field emission, a tunneling mechanism that occurs when the tunneling barrier is strongly perturbed by the applied electric field.<sup>80-82</sup> In the following sections the predictions of simple tunneling, field emission, and hopping models are reviewed in more detail as a forerunner to discussion of recent results on DC electrical transport in molecular wires.

### 2.1.1 Tunneling (Direct Tunneling and Field Emission)

In coherent tunneling, electron waves traverse a potential barrier without any change in phase, and propagate again on the other side of the barrier. Figure 2.1 illustrates electron transmission through a rectangular barrier. A rectangular barrier is clearly an extremely crude approximation for a molecular junction, but the simplicity of this model and its qualitative predictions have made it widely used for initial analysis of molecular conduction in the tunneling regime.<sup>72</sup>

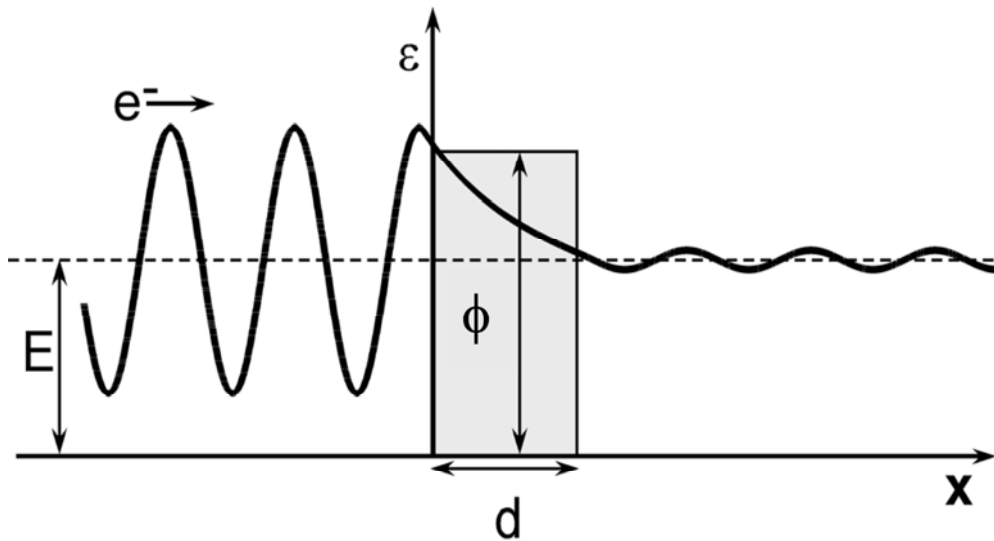


**Figure 2.1** Transmission of electron wave function through a potential barrier. The probability density to the right of the barrier is decreased due to the attenuation of the wave through the barrier. A classical particle would have zero probability of penetrating the barrier; however, the quantum behavior of the electron permits transmission.

In a common approximation for molecular junctions, the tunneling barrier has a height equal to the offset between the Fermi level and the closest molecular energy level (see Fig. 2.2), and a width equal to the length of the molecule. For systems where the Fermi level is far ( $> 1$  eV) from a molecular level (nonresonant tunneling), this approximation is perhaps reasonable. As the average barrier height decreases, the precise structure of electronic states in the junction becomes increasingly important, and the description of the junction as a single barrier clearly breaks down.<sup>83, 84</sup>

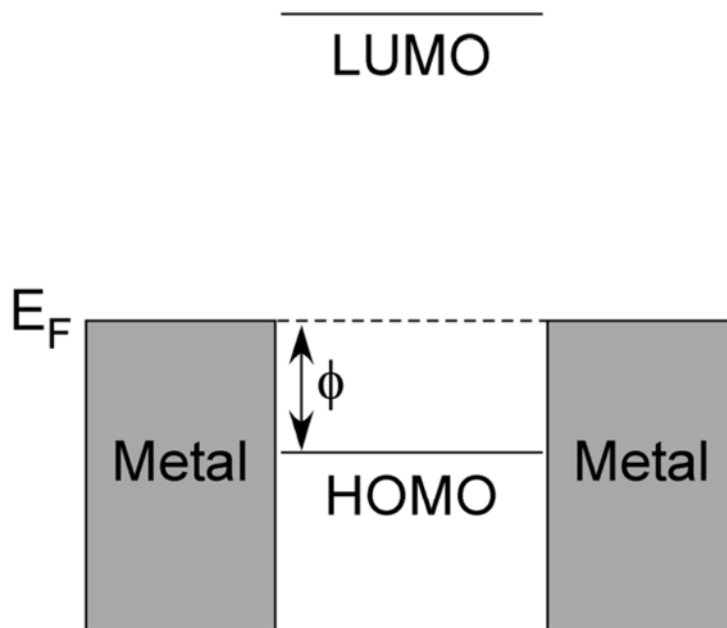


**Figure 2.2** Simplified energy level diagram for a molecular electronic junction. For most junctions studied to this point, the junction Fermi level lies closer to the molecular HOMO, defining the barrier height,  $\phi$ , as the energy offset between the HOMO and the Fermi level. In reality, the barrier height is not constant across the molecule, but varies with the energy of each site in the molecular wire.

According to the WKB (Wentzel-Kramers-Brillouin) approximation<sup>71</sup>, the amount of wave attenuation shown in Fig. 2.2 is affected by the height ( $\phi$ ) and length ( $L$ ) of the barrier. In the 1960's, Simmons derived an equation for current passing through an arbitrary tunneling barrier using the WKB approximation, and it is reduced to the following expression in the very low bias range<sup>72</sup>:

$$J = \frac{e^2 V}{4\pi^2 \hbar^2 d} (2m\phi)^{1/2} \exp\left[\frac{-2d}{\hbar} (2m\phi)^{1/2}\right] \quad (2.1)$$

where  $J$  is the current density,  $\phi$  is the mean barrier height,  $e$  is the elementary charge,  $d$  is the barrier length, and  $V$  is the applied bias.

Equation 2.1 can be rewritten in terms of resistance ( $R$ ) and simplified to a formulation useful for experiments, where resistance exhibits exponential dependence on the barrier length:<sup>24-27, 85</sup>

$$R = R_0 \exp(\beta d) \quad (2.2)$$

Here  $R_0$  is the effective contact resistance, and  $\beta = 2(2m\phi)^{1/2}/\hbar$  is a structure-dependent attenuation factor. (The factor  $\beta$  also appears in the theory of variable range hopping in disordered media, where it is interpreted as the inverse of the charge localization length<sup>86, 87</sup>.) According to Eq. 2.2, the fit parameters  $R_0$  and  $\beta$  are extracted from a semilog plot of resistance versus molecular length;  $\beta$  is the slope of the best-fit line to the data points and  $R_0$  is the y-intercept.<sup>27</sup>

Length dependent measurements are thus extremely useful to determine the efficiency of electron tunneling through molecular bonds. More efficient tunneling is characterized by lower  $\beta$  values. Conjugated molecules with delocalized  $\pi$  electrons often exhibit  $\beta$  values in the range of 2.0 - 5.0 nm<sup>-1</sup>, while saturated chains have  $\beta$  between 7.0 and 10.0 nm<sup>-1</sup>.<sup>25</sup> The contact resistance  $R_0$  reflects the type of metal and the surface linker chemistry used to bind the molecules in the junction<sup>27, 85, 88</sup>. The importance of contact resistance in a molecular junction can be assessed directly by length dependent measurements. Junction measurements on molecules of only one length leave open substantial questions regarding what fraction of the measured resistance (at a given bias) is due to contact effects versus the transport along the molecular backbone. The important role of length dependent transport measurements will be emphasized again in chapter 4 to 6 of this thesis.

Equation 2.2 works well for coherent non-resonant tunneling in the low bias regime, and this equation has also been derived from a combination of the Landauer formula and the Green's function formulation,<sup>27</sup> which provides a clear connection between the transmission probability and the conductance.<sup>58, 73, 75, 89-91</sup> The importance of the Green's function formulation stems in part from the ability to factorize the total transmission probability into the molecule-metal and the molecular backbone components<sup>91</sup>. This formalism also takes into account the mixing of molecular orbitals with the metal electron states at the contacts. The coupling of molecular levels to metal leads to broadening of the molecular states, an important effect that modifies the overall junction



transmission. In junctions where tunneling is the dominant charge transport mechanism, current is predicted to have very weak dependence on temperature (Table 2.1).<sup>75, 76</sup>

Equation 2.1 describes current through a rectangular barrier in the low bias limit, and can be simplified to

$$I \propto V \exp\left(-\frac{2d\sqrt{2m_e\phi}}{\hbar}\right) \quad (2.3)$$

which is a useful form, as will be demonstrated below. At the opposite limit, when the applied bias exceeds the barrier height, the barrier shape switches from rectangular to triangular, and the current-voltage dependence is described as follows:

$$\ln\left(\frac{I}{V^2}\right) \propto -\frac{4d\sqrt{2m_e\phi^3}}{3\hbar qV} \left(\frac{1}{V}\right) \quad (2.4)$$

Tunneling through a triangular barrier is termed “*field emission*” or Fowler-Nordheim tunneling.<sup>92</sup> In field emission, a plot of  $\ln(I/V^2)$  against  $1/V$  is expected to yield a line with a negative slope, the absolute value of which will depend on the barrier height based on Eq. 2.4.

A transition from direct tunneling to field emission is evident in a variety of molecular junctions.<sup>81, 82</sup> To examine experimentally the transition from direct tunneling to field emission requires recasting Eq. 2.3 in terms of the variables  $\ln(I/V^2)$  and  $1/V$  so it can be directly compared to Eq. 2.4. The resulting equation is as follows:

$$\ln\left(\frac{I}{V^2}\right) \propto \ln\left(\frac{1}{V}\right) - \frac{2d\sqrt{2m_e\phi}}{\hbar} \quad (2.5)$$

From Eq. 2.5, a plot of  $\ln(I/V^2)$  against  $1/V$  exhibits a logarithmic growth in the low-bias regime. Therefore, a transition from logarithmic growth to linear decay in a plot of  $\ln(I/V^2)$  against  $1/V$  is a signature of a transition from direct tunneling to field emission.

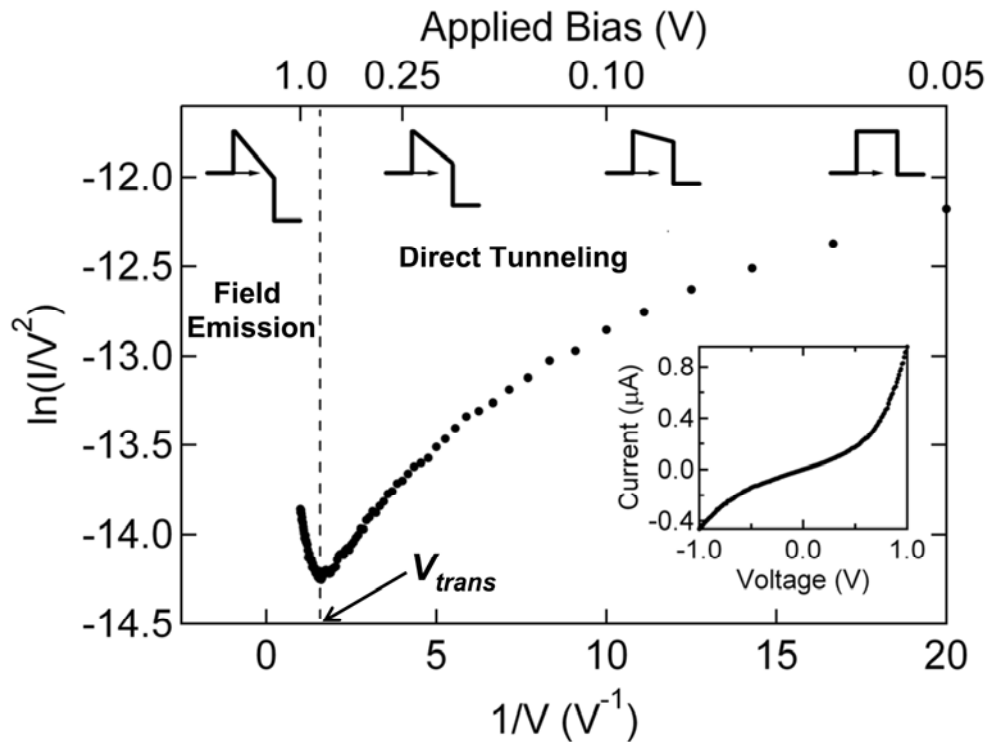


**Figure 2.3** Solid circles represent the average of 100  $I$ - $V$  curves for a Au-anthracenethiol-Au junction. The dashed line corresponds to the voltage at which the tunneling barrier transitions from trapezoidal to triangular ( $V_{trans}$ ). Also shown are representations of the barrier shape at various values of applied bias. The inset shows current-voltage data on standard axes. [Adapted from<sup>81</sup> with permission; Copyright 2006 by the American Physical Society]

Figure 2.3 shows a Fowler-Nordheim plot for a Au-anthracenethiol-Au tunnel junction<sup>81</sup>. The inset displays the same data plotted on standard current-voltage axes. The dashed line in Fig. 2.3 denotes the voltage required for transition from direct tunneling to field emission for anthracenethiol, which is referred as the transition voltage ( $V_{trans}$ ). The shape of the curve in the two bias regions matches the shape predicted by Eqs. 2.4 and 2.5 (linear decrease at high bias and logarithmic growth at low bias). Furthermore, the specific value of  $V_{trans}$  provides a means of experimentally estimating the height of the original rectangular barrier of a given molecule. Note that  $V_{trans}$  remains an estimate, and not an exact measure of the barrier height because the original tunneling equation as outlined in Eq. 2.2 does not explicitly account for voltage drops at the contacts or the

image potential of the tunneling electron. Nevertheless, the point of Fig. 2.3 is that proper analysis of I-V characteristics can reveal the onset of field emission in molecular junctions. This will be important in the analysis of molecular wire transport in chapter 4-6.

### 2.1.2 Hopping

For conjugated wire molecules greater than a few nanometers in length the coherent tunneling model discussed above breaks down, particularly near room temperature. Instead of direct metal-to-metal tunneling, the charge conduction process may be viewed as a series of discrete steps involving first injection of charge into the molecular orbitals, field-induced drift of the charge carrier down the length of the molecule, and finally extraction of the charge into the receiving contact. In this incoherent limit, the charge has a relatively long residence time on the molecule and consequently there is substantial vibronic coupling between molecular motions and the charge, *i.e.* polarons are formed. One can roughly estimate the charge residence time with knowledge of the molecule-metal coupling energy. If this coupling is on the order of 0.1 eV<sup>93</sup>, the Uncertainty Principle suggests the residence time will be > 40 fs. This time is comparable to the time scales of typical vibrations (10 fs – 1 ps)<sup>1</sup>, meaning vibronic coupling and polaron formation will likely occur. A better way to estimate the carrier residence time is to use actual current density data for molecular junctions, as will be shown later.

The polaronic charge carrier moves along the molecular backbone by hopping between localized states (orbitals), Fig. 2.4. This hopping process is thermally activated around room temperature. Indeed many researchers working on molecular wires implicitly define hopping conduction as thermally activated, although in the solid state physics literature hopping is generically defined as transport between localized states regardless of whether the hop involves thermal activation or tunneling.<sup>77-79, 94</sup> In the hopping regime around room temperature, one expects that the junction resistance might follow classical Arrhenius behavior,<sup>46, 78</sup>

$$R = R_o \exp\left(\frac{E_a}{kT}\right) \quad (2.6)$$

where  $E_a$  is an activation energy, and  $k$  is Boltzmann constant. This Arrhenius-type thermal activation is readily explicable in the Marcus picture of electron transfer.<sup>46, 51, 95</sup> Thermal motion of nuclei within the molecular wire (e.g., a bond rotation) results in a favorable geometry that facilitates electronic coupling and migration of charge. In this picture, the activation energy ( $E_a$ ) corresponds to the energy required to reach the transition state. The precise temperature dependence of transport will likely depend on the specific molecular wires under study (e.g. the density of states distribution) and certainly this currently remains an open question.<sup>86, 87, 96</sup>

Hopping transport is not predicted to exhibit exponential length dependence characteristic of coherent tunneling, but instead scales linearly with the length in the low bias regime (Table 2.1). The weaker length dependence facilitates the transport of charge over greater distances, and thus it is the hopping regime that might be considered most “wire-like”. Linear length dependence is also a signature of ohmic conduction where the charge transport is field driven. However, hopping conduction at higher applied biases can deviate from ohmic behavior in principle, e.g., it is interesting to consider the role of space charge limited conduction which is commonly observed in semiconductors, and for which current normally scales as the applied bias squared.<sup>97, 98</sup>

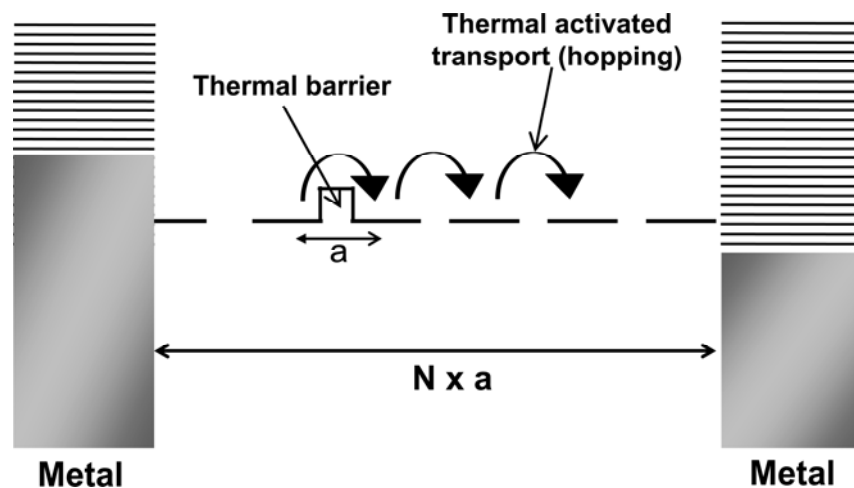


**Figure 2.4** Schematic energy diagram for incoherent hopping through  $N$  sites separated by distance  $a$  on a molecular wire.

**Table 2.1** Charge transport mechanisms in a molecular junction.

Conduction Mechanism	Characteristic Behavior	Temperature Dependence	Length Dependence	Bias Dependence
Nonresonant tunneling	$R \propto \exp\left(\frac{2d}{\hbar} \sqrt{2m\phi}\right)^a$	Weak	$\ln R \propto d$	$J \propto V$
Field Emission	$J \propto V^2 \exp\left(-\frac{4d\sqrt{2m\phi^3}}{3q\hbar V}\right)$	Weak	$J \propto \exp(-d)$ At a given bias	$\ln\left(\frac{J}{V^2}\right) \propto \frac{1}{V}$
Hopping	$R \propto d \exp\left(\frac{\phi}{kT}\right)^a$	$\ln R \propto \frac{1}{T}$	$R \propto d$	$J \propto V$

(<sup>a</sup>The characteristic behavior described here is for the low-bias regime.  $J$  is the current density.) [Reproduced with permission from<sup>29</sup>; Copyright 2003 by the American Physical Society]

## 2.2 Molecular Junction Fabrication Techniques

A variety of strategies have been devised for forming nanoscale molecular junctions, in which molecules are delicately engaged between two metal contacts.<sup>18-22</sup> Each method has inherent advantages and disadvantages, generally relating to issues of yield, reproducibility, ease of formation, and the number of molecules incorporated. In principle, these techniques can be divided into two broad categories: single-molecule and molecular ensemble measurements. As with many analytical techniques, there are pros and cons for each type of measurement. Ensemble measurements usually provide simple, rapid analyses of the system, while single-molecule techniques tend to yield more information on the local structure, identity, and electronic characteristics of the system, but are usually more difficult to fabricate and to analyze. However, both types of measurements have a good agreement in the understanding of the charge transport properties of molecules and for the demonstration of many device functions. For example, conjugated molecules are shown to be more conductive than saturated molecules of the same length,<sup>17, 25</sup> and the intriguing switching behavior of a given molecule has been exhibited in both type of junction.<sup>99</sup> Single-molecule measurements

include scanning tunneling microscopy (STM) and break junction, and latter one includes mercury drop junction, nanopore junction, crossed wire junction, and conducting probe atomic force microscopy (CP-AFM). In this section, the principle of each method is briefly explained, along with some experimental results.

### **2.2.1 Scanning Tunneling Microscope Measurement (STM)**

A feedback tunneling current loop in STM produces a nanoscale junction,<sup>41, 100, 101</sup> which involves the use of an atomically sharp metallic tip which is made of W or a Pt/Ir alloy. The STM tip approaches the monolayer until it acquires a set tunneling current, and concurrently forms a vacuum gap between the molecular film and tip. Electrons can tunnel across the vacuum barrier because of overlapping electron wave functions from tip and monolayer. The atomic sharpness of the tip allows this technique to characterize a very small number of molecules. In addition to the normal current-voltage response, STM has played a unique role in the field of molecular electronics because it allows one to image individual molecules adsorbed on a conductive substrate with submolecular resolution. As a result, one can measure local difference of electrical properties. For example, Nakasa *et al.*<sup>102</sup> have examined localized differences in conductance due to such conditions as a mixed monolayer assembly of conductive and insulating molecules. In such experiments, there is an obvious contrast difference between the two types of molecules. Also, Tao<sup>103</sup> studied Fe-porphyrin coadsorbed in the ordered array of porphyrin molecules in an electrochemical cell. The work shows that the current through the redox active Fe-porphyrin is much higher than through the redox inactive porphyrin when the electrode potential is tuned near the redox potential of Fe-porphyrin.

Problems associated with the STM technique are that the junction is not under any sort of feedback control when I-V measurements are made, and that the length of the tunneling barrier is ambiguous. Because the STM relies on a current feedback mechanism for placement of the tip relative to the substrate, it is not possible to simultaneously maintain position and monitor the electrical characteristics of the junction. This results in the possibility of tip drift, both laterally and vertically, during the course of measurement. Vertical tip drift changes the length of the tunneling barrier, upon which current is exponentially dependent. If the substrate is relatively rough, then lateral drift results in

sampling of local hills and valleys on the substrate, and thus indirectly changes the barrier length. The initial tip/substrate distance is determined by an increase in the amount of current over the vacuum current, and it is critically important to choose the correct distance, or the measured electrical characteristics may correspond to an undesired junction type. For example, if the tip is placed too far from the substrate, a vacuum gap of some distance exists between the tip and monolayer. While it is quite difficult to differentiate the tunneling current through the vacuum gap from through the monolayer, electrons will begin their journey inside the monolayer if the tip is placed too close to the substrate.

### 2.2.2 Break Junction Measurement

Mechanically-Controlled Break Junctions<sup>104, 105</sup> were devised by Reed and Tour in an attempt to contact a very small number of molecules. The technique begins with gluing a notched gold wire to a beam, and the wire is then split by an electrically-controlled piezo crystal that stresses the beam. The gap between two Au contacts can be adjusted by piezoelectrically stressing a “bending beam”. Then, a molecule can bridge the gap to form the atomically sharp wire contact after a solution containing the molecules is introduced to the gap. Figure 2.5 illustrates a schematic of the mechanically controlled break (MCB) junction. The advantage of break junctions is that they are less susceptible to temperature drift and vibrations because a large reduction factor between the piezo elongation and the electrode separation results in two electrodes which are inherently stable with respect to each other. Furthermore, they allow the experimentalist to conduct variable temperature measurements of the junction as several methods do. This allows one to assign a transport mechanism because the current-voltage characteristic is independent of temperature for a tunneling process, whereas the hopping and thermionic emission mechanism show a temperature dependency. However, a MCB junction is difficult to characterize monolayer structure and they often fail due to electrical shortening.<sup>106</sup>

Tao *et al.* developed a STM-break junction method<sup>41, 107</sup> that quickly creates thousands of molecular junctions by repeatedly moving a STM tip into and out of contact with the substrate electrode in the presence of sample molecules. The molecules in the

study have two terminal groups that can bind to the tip and the substrate electrode, respectively. A STM tip is pushed into contact with molecules adsorbed on an electrode, and the tip is then pulled away from the substrate. Molecules break contact with one of the two electrodes individually, which is shown as a series of stepwise decreases in the current. The process is repeated until a large number of molecular junctions are created and measured. However, the conductance histogram in statistical analyses shows that the distribution is often too broad thus to result in the inaccuracy of the measurements.

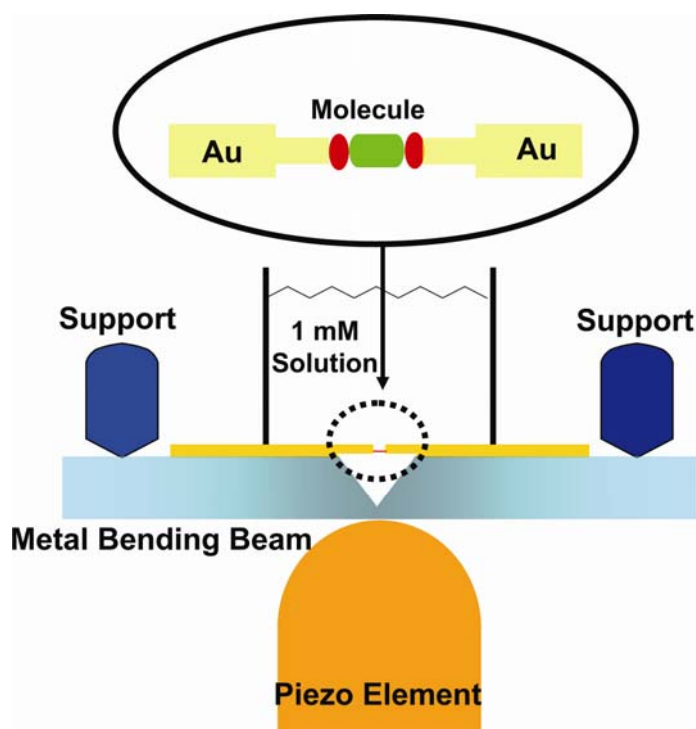


**Figure 2.5** A schematic of the mechanically controllable break junction (Reproduced with permission from reference <sup>104</sup>. Copyright 1997 AAAS)

### 2.2.3 Mercury-Drop Junctions

Majda group<sup>108, 109</sup> and Whitesides group<sup>110</sup> reported that molecular junctions can be made between two mercury drops or between Hg and a solid metal (Ag, Au, Cu). Former junction is fabricated by positioning two micrometrically driven hanging mercury drops (see Fig. 2.6a). The latter one is formed by contacting the monolayer with a hanging mercury drop from a syringe (see Fig. 2.4b). A SAM is then made on the Hg drop when it is immersed in the solution of interest. The noticeable feature of this



junction comes from its large contact area (1.0 mm in diameter), which contains  $10^{11} - 10^{13}$  molecules. Since the junction includes several different SAM domains, leading to defects at the SAM/Hg interface, the effects of many unwanted defects are averaged into the data. A positive aspect of HMDE is that the high surface tension of Hg drops decreases the probability for a metal to infiltrate into monolayer, producing a conformal contact. Also, the roughness caused by molecular deformation can be minimized in this junction because of the flowing nature of liquid Hg.

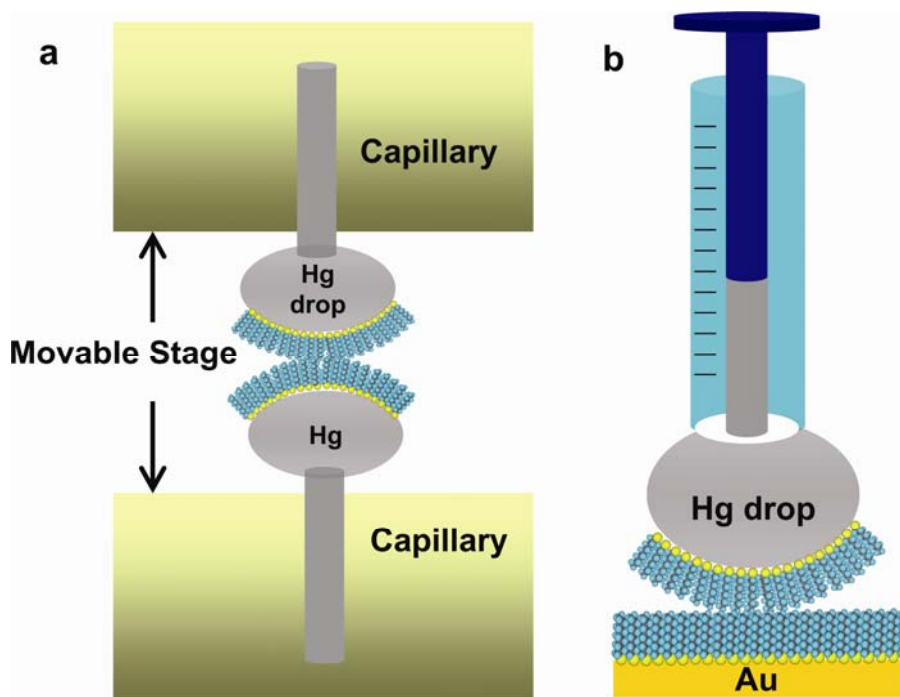


**Figure 2.6** Schematic illustration of mercury-drop junctions: (a) the mercury-mercury junction, (b) the mercury-silver junction. (Reproduced with permission from reference <sup>108</sup> and <sup>110</sup>, respectively. Copyright 1999 and 2001 American Chemical Society)

## 2.2.4 Crossed Wire Junctions

The current-voltage ( $I$ - $V$ ) characteristics of self-assembled monolayers (SAMs) can be measured by a cross-wire tunnel junction. A schematic of this device structure is shown in Fig. 2.7. The crossed-wire tunnel junction consists of two  $10 \mu\text{m}$  Au wires, one containing a SAM of the molecule of interest. The wires are mounted to a custom built test stage in such a manner that the wires are in a crossed geometry with one wire perpendicular to the applied magnetic field ( $\mathbf{B}$ ). The junction separation is controlled by

deflecting this wire with the Lorentz force generated from a small dc current ( $<5$  mA). The deflection current is slowly increased so that the wires can make a junction at the contact point. This approach allows formation of molecular junctions with a high degree of control and the choice of the metal used. Using this method, Kushmerick *et al.*<sup>111</sup> observed that  $\pi$ -conjugated systems facilitate charge transport. Moreover, they found that the smaller bond-length alternation in a  $\pi$ -conjugated molecular wire leads to greater conductivity because of the resulting smaller HOMO-LUMO gap.

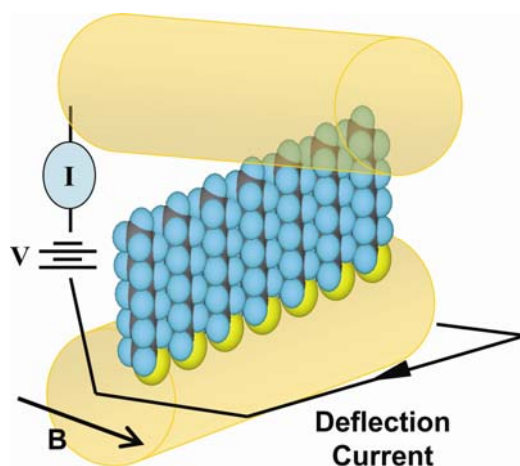


**Figure 2.7** Schematic representation of the cross-wire tunnel junction. (Reproduced with permission from reference <sup>111</sup>. Copyright 2002 American Chemical Society)

## 2.2.5 Nanopore Junctions

Nanopore junction fabrication was developed by the Reed group.<sup>112</sup> It was designed to create a nanoscale cavity consisting of a metal top contact, a self-assembled monolayer of molecular wires, and a metal bottom contact (see Fig. 2.8). Both metal contacts are fixed at the same position, which gives the stability to the junction. As a result, it is possible to perform electrical measurement repeatedly and consistently through a small number of molecules over a long time period. Also, the stability of a junction makes it possible to perform temperature varying experiments similar to those done with a MCB junction. In order to form a junction, a 50nm layer of  $\text{Si}_3\text{N}_4$  is first deposited on a polished silicon wafer by low-pressure chemical vapor deposition (LPCVD). The silicon wafer is then etched anisotropically using 35% KOH solution to

create a suspended silicon nitride membrane. A single bowl-shaped nanopore ( $\sim 30$  nm in diameter) is made through the membrane by electron beam lithography and reactive-ion etching. Gold is thermally evaporated on the nanopore, followed by forming a SAM on top of the gold in solution. The second electrode is then introduced to the other side of monolayer by thermal evaporation. A Ti layer, well-defined interface was introduced between SAM and gold leads to avoid the problem of electrical short circuits shorts.<sup>112</sup> However, a nanopore junction often exhibits an asymmetric behavior due to the different metal contacts. This technique have good control over the small device area and intrinsic contact stability, like break junctions and produce a large number of devices with acceptable yield (80 %), so that statistical results can be extracted. Another attractive feature of this method is that we can study molecular junctions at various temperatures. Variable temperature conductance measurements with 1,4-phenylene diisocyanide-metal (Au or Pd) junctions have revealed the dominant charge transport mechanism changes from hopping conduction to thermionic emission depending on the temperature and applied bias.<sup>113</sup>

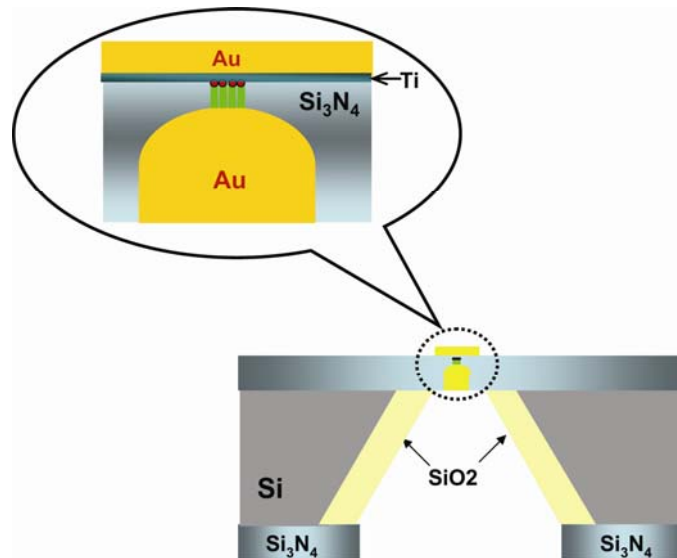


**Figure 2.8** Schematics of a nanopore junction fabrication. Blow-up shows molecular structure sandwiched with Au electrodes. (Reproduced with permission from reference <sup>112</sup>. Copyright 1999 AAAS)

## 2.2.6 Conducting Probe Atomic Force Microscopy

Over the last ten years, we and others have demonstrated that conducting probe atomic force microscopy (CP-AFM) is a particularly convenient and reproducible

approach.<sup>24-27, 81, 85, 88, 114-117</sup> In CP-AFM, a metal-coated AFM tip is brought into contact with a self-assembled monolayer (SAM) of molecular wires under controlled load (see Fig. 2.9a).<sup>118, 119</sup> The metal-coated tips are prepared by vapor deposition of a 5 nm chromium adhesion layer followed by a 100 nm metal layer. The probe position is adjusted through an optical feedback system using a laser that reflects off the back surface of the AFM tip and in this way the load on the junction can be precisely controlled; the load is typically several nN and the tip-SAM contact areas are on the order of  $10 \text{ nm}^2$  for a tip with a 50 nm radius of curvature.  $I$ - $V$  characteristics of the molecular wire monolayer are measured by sweeping the tip voltage.

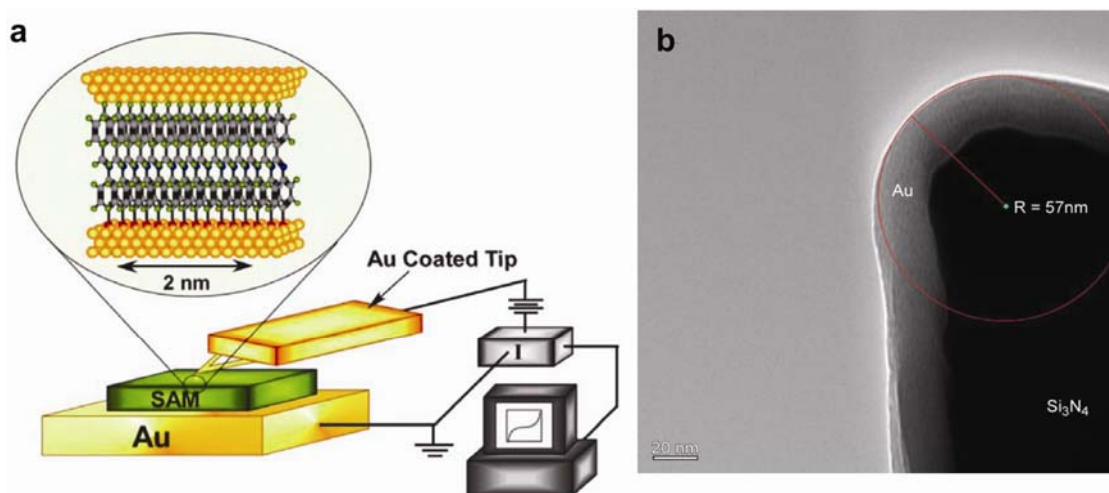


**Figure 2.9 (a)** Measurement of molecular wire resistance using conducting probe atomic force microscopy (CP-AFM). A gold coated tip is brought into contact with a monolayer on a gold substrate. **(b)** Transmission electron microscopy (TEM) image of a gold coated AFM tip.

One can view the force microscope operated in this manner as essentially a molecular probe station analogous to device probe stations used in semiconductor electronics. This CP-AFM or molecular probe station approach has several attractive features. First, it is inherently a soft contact, non-destructive method. By virtue of the flexible cantilever attached to the probe tip, the top contact is spring loaded and the force is easily adjusted so that permanent (plastic) deformation of the SAM layer is avoided.

Second, the CP-AFM method is simple and fast. No micro- or nanofabrication processes are necessary, meaning that junctions can be made and tested in the time span of a few hours or less. Third, the dimensions of the junctions are inherently small because of the small radius of curvature of the AFM tip (see Fig. 2.9b). This reduces the probability of electrical shorts and means that conduction can be probed through of a small number of molecules ( $\sim 100$ )<sup>27</sup>. Fourth, CP-AFM offers significant experimental flexibility in that the tip and substrate can be coated with different metals, which allows the role of metal contacts on junction  $I$ - $V$  behavior to be assessed<sup>27</sup>. Finally, the technique is also compatible with variable temperature measurements, which is important for verifying transport mechanisms<sup>33</sup>. These collective attributes make the CP-AFM testbed a very powerful and versatile method for molecular wire experiments.

Our group has published two papers regarding the contact resistance dependence on metal work function<sup>4,31</sup>. For alkanethiol or dithiol SAMs, it was apparent that junction contact resistance decreases with increasing metal work function. Third, the delicate control of load in CP-AFM renders opportunities to examine conduction as a function of molecular deformation. Also, the current-contact area behavior can be established. Our group<sup>33</sup> and Cui *et al.*<sup>35</sup> have already investigated the resistance-load dependence. Finally, when compared to STM, CP-AFM allows the probe tip to be controllably positioned in direct contact with the monolayer. STM uses the current through both the molecules and the vacuum gap present between the molecules and the STM tip to control tip-positioning. Since the conductivity of the molecules is generally unknown, the position of the probe with respect to the molecules can be dubious. Moreover, the vacuum gap may affect junction transport, so that we cannot estimate the intrinsic molecular conductivity. However, CP-AFM can provide higher reliability than STM. The efficacy of this method is brought about because we examine the surface in stationary contact mode, and use an independent feedback signal, allowing the tip to touch the molecules at a desired position. Cui *et al.*<sup>36</sup> demonstrated that CP-AFM can be reliably utilized to measure the resistance of a single octanedithiol molecule (900 M $\Omega$ ), and they pointed out that the intrinsic molecular conductance measurements required chemically bonded contacts.

## 2.3 Recent Results on Molecular Wires Connected to Metals

In light of the foregoing discussion on transport mechanisms, it is clear that the predominance of any mechanism- direct tunneling, field emission or hopping- will depend on numerous factors including the electronic structure of the molecular wires and their length, the applied bias, and temperature. The interplay of these factors has yet to be sorted out experimentally and theoretically. However, there have been a few reports on observations of mechanistic transitions in molecular wires connected to metals. Thermal effects on DC conduction through nitrite-substituted oligo-phenylene-ethynylene (OPE) molecules have been reported in pioneering work by Selzer, *et. al*, Fig. 2.10.<sup>30, 36, 37</sup> Red curves in Fig. 2.10b shows Arrhenius plots of current versus temperature for a single molecule OPE junction in which there is a characteristic transition from temperature-independent behavior at low temperatures, where conduction is dominated by tunneling, to temperature-dependent hopping behavior at high temperatures. The activation energy in the hopping regime corresponds very well with theoretical calculations of barriers for rotations of the rings in the nitrite-substituted OPE.<sup>30</sup> Thus, Selzer and colleagues argued that above the transition temperature of  $\sim 100$  K, the onset of torsional fluctuation of the phenyl rings leads to vibronic coupling that suppresses tunneling and facilitates a hopping process. They also suggested that local heating of the molecules, resulting from IV power dissipation in the junction, may play a role in the thermally activated hopping.<sup>37</sup>

Further, they have investigated the effect of local environment by comparing the temperature dependent conduction in two test beds with the same OPE molecule – one based on an isolated OPE and the other on a self-assembled monolayer (SAM) between two gold nanowire segments (“in-wire” junctions, Fig. 2.10a).<sup>36</sup> Figure 2.10b shows total current of the isolated molecule junction (red curves) compared to normalized current-per-molecule for an in-wire junction (black curves) as a function of temperature (10-300 K). While currents in the in-wire junction display temperature independence over entire temperature range, thermal activated behavior is exhibited only above 100 K in the single molecule junction. The failure to observe a transition to hopping in the in-wire junction was attributed to a higher barrier for the rotation of the phenylene rings, due to a restricted volume for torsional modes in a close packed SAM matrix. The issue of

intermolecular interactions in molecular junction measurements remains an important question.

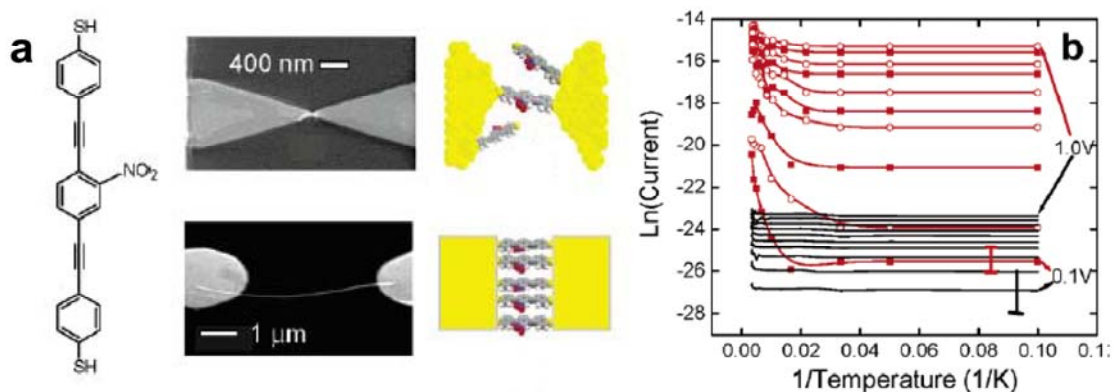


**Figure 2.10 (a)** Schematic of a nitrite substituted OPE (left), cartoon of an individual molecular junction and its corresponding SEM image (center up), and cartoon of an in-wire molecular junction and SEM image of a junction aligned between two large-area electrodes (center low). **(b)** Comparison of current versus temperature behavior in in-wire SAM junctions and isolated molecular junctions as a function of bias. The bias increment between curves is 0.1 V, and the bias of the lowest curve is 0.1 V. [Adapted from <sup>36</sup> with permission; Copyright 2006 by the American Chemical Society]

Tao and colleagues<sup>32</sup> have observed thermally activated hopping in redox active perylene tetracarboxylic dimides (PTCDI) molecules connected between an STM tip and a gold substrate, Fig. 2.11. In these experiments charge was electrochemically induced on the PTCDI molecules and conduction through the charged molecules was thermally activated, consistent with a hopping mechanism (Fig. 2.11b). However, when the same molecules were probed without inducing charge, the temperature dependence of conduction was much weaker, indicative of a tunneling mechanism (Fig. 2.11c).

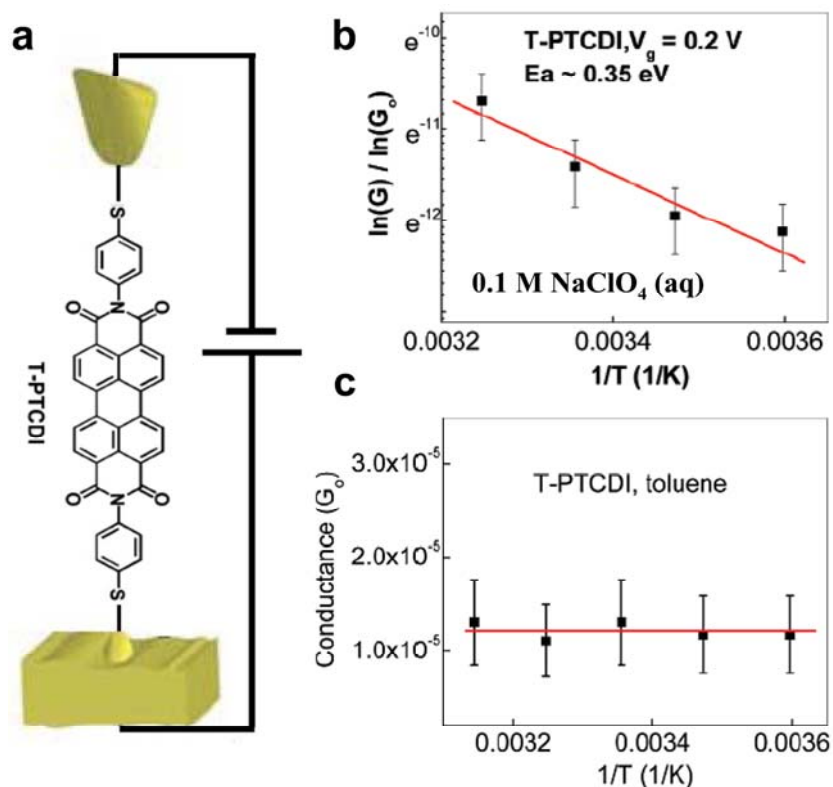


**Figure 2.11** (a) Schematics of T-PTCDI in a STM break junction. Solvent (not shown) surrounds the molecule. (b) Arrhenius plot of conductance versus inverse temperature for T-PTCDI that has been electrochemically reduced in electrolytes. (c) A semilog plot of conductance versus inverse temperature for a T-PTCDI molecule in nonpolar solvent. [Adapted from <sup>32</sup> with permission; Copyright 2007 by the American Chemical Society]

Very recently, Rampi and colleagues have reported the preparation and characterization of extremely long molecular wires, up to 40 nm in length. These wires were synthesized using metal ion coordination chemistry (Fig. 2.12a).<sup>120</sup> Although the authors have not yet reported the temperature dependence of conduction, a multistep charge hopping process between the metal centers in the backbone is implicated by the linear length dependence they observed for the conduction (Figs. 2.12b and c).

Even longer conjugated molecular wires with lengths greater than 100 nm were recently prepared by in-situ polymerization of dibromoterfluorene monomers on an Au (111) surface.<sup>121</sup> The conductance of a single polyfluorene chain was measured as a function of distance between an STM tip attached to one end of the molecule and the Au



surface (Figs. 2.13a and b). However, the conductance at small bias voltages was only measurable over an adjustable distance of 0-4 nm because the current levels for longer lengths of this wire molecule were below the apparatus detection limit. Over the short range of lengths that was measured there was an exponential attenuation of current with length, indicative of tunneling (Fig. 2.13c).

In the following chapters, we describe the preparation and characterization of a different conjugated molecular wire system that clearly exhibits a mechanistic transition from tunneling to hopping as a function of wire length.<sup>33</sup> The synthetic flexibility of these wires opens considerable opportunities for systematic investigation of molecular wire conduction as a function of controlled molecular architecture.

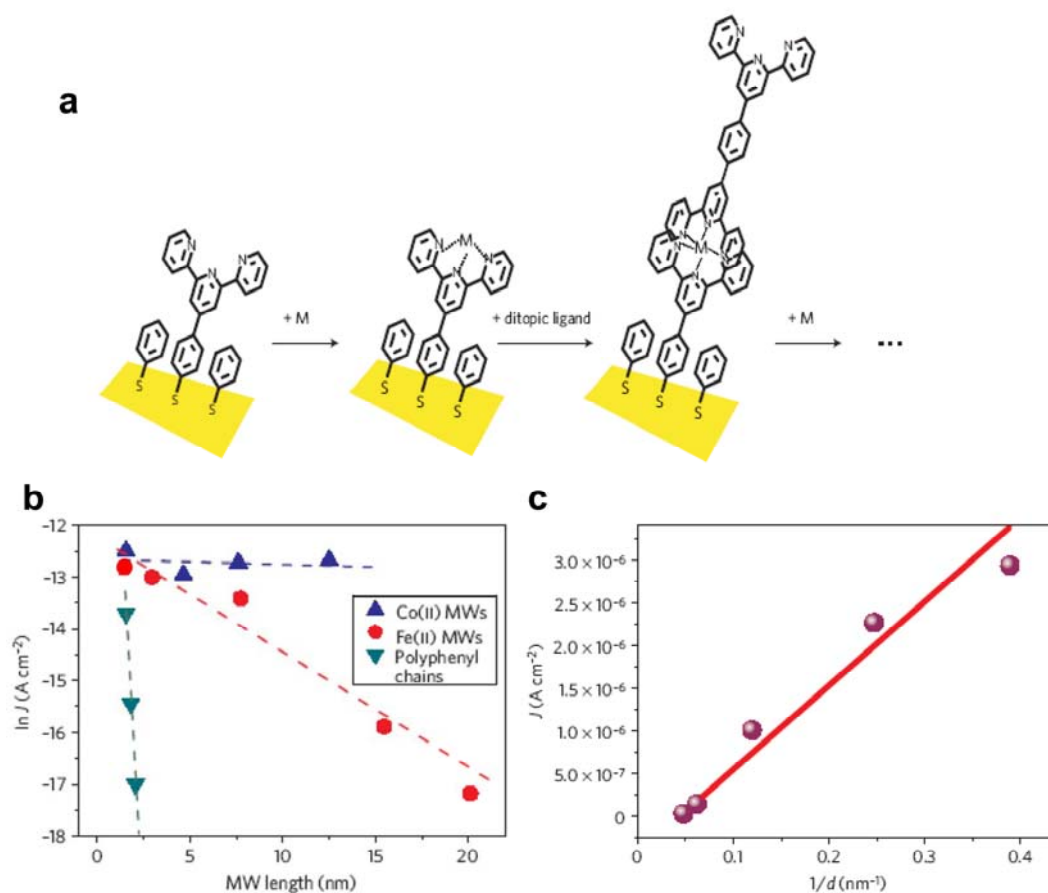


**Figure 2.12** (a) Schematic representation of the stepwise growth of metal (M) coordinated molecular wires on a metal surface. (b) A semilog plot of current versus molecular length for the Fe(II) and Co(II)-based molecular wires. Filled down triangles: Data reported from previously published work for junctions incorporating polyphenyl-based molecular wires.<sup>110</sup> (c) A linear plot of current versus inverse molecular length for the Fe(II)-based molecular wires. [Adapted from <sup>120</sup> with permission; Copyright 2009 by the Nature Publishing Group]

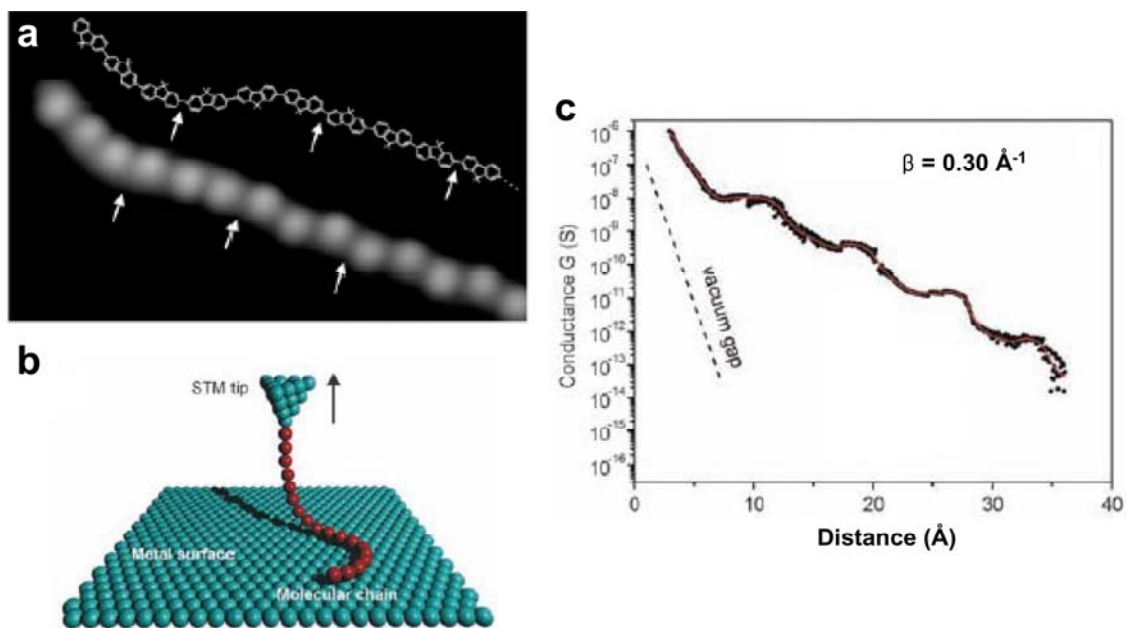


**Figure 2.13** (a) STM image (5.9 by 3.6 nm) of a single polyfluorene chain end with its chemical structure superimposed (using a different scaling). (b) Scheme of the chain pulling procedure: After contacting a molecular chain to the STM tip, the chain can be lifted from the surface in a ropelike manner upon tip retraction because of its flexibility and weak interaction with the substrate. (c) A semilog plot of conductance versus distance between the tip attached to the chain and the metal substrate, which exhibits an exponential decay with a  $\beta$  value of  $3.0 \text{ nm}^{-1}$ . The characteristic oscillations with a period of about  $10 \text{ \AA}$  reflect mechanical deformation of the molecular wire, as it slides over the metal surface during the pulling process. [Adapted from <sup>121</sup> with permission; Copyright 2009 by the AAAS]

### 3 Molecular Self-Assembly and Molecular Wires Growth

The basic principle in self-assembly is originated from the biological processes such as the cellular membrane formation, protein folding and aggregation, and pairing of base pairs in DNA. Multiple weak and reversible interactions including intra/inter hydrogen bonding, ionic bonding, and van der Waals interactions enable molecules to assemble into stable aggregates. These interactions are thermodynamically controlled at equilibrium to create a well-defined structure.

The pioneering approaches of Langmuir and Blodgett involve the modified non-biological systems, in which a self-assembled monolayer (SAM) of amphiphiles is formed by applying external pressure.<sup>122-124</sup> While the monolayer structure obtained in this manner is relatively robust and stable, the rough nature of metal surface significantly affects the contact geometry in floating films because the interfaces is formed by physically contacting a Langmuir Blodgett (LB) film with metal electrodes. This gives rise to a large difference in a molecular junction measurement for a given molecular system. For reproducible and quantitative analyses, another alternative includes terminal functionalized molecules which have a specific affinity to a metal substrate. This strategy has applied well for a variety of well-assembled chains or rodlike molecular films that are chemically anchored to substrates.<sup>125</sup> Table 3.1 shows various examples in which molecules with specific affinities are chemisorbed on different substrates.

In the context of molecular electronics, understanding charge transport through organic molecules is of critical importance for real nanodevices. Organothiols have the potential of being used in charge transport systems due to their ability to make strong bonds to the coinage metals. Thus, the self-assembly of organothiols is a significant tool to unravel charge transport mechanisms at the molecular scale. However, it has been difficult to systematically examine the hopping regime in conjugated molecular wires connected to metallic contacts because of the relatively large range of molecular lengths required (spanning many nanometers) and the complexities of adsorbing long molecules to metal surfaces while controlling orientation. There is a synthetic challenge of rigid and long conjugated molecules mostly due to their poor solubility. The long molecules

generally do not proceed to form a densely packed self-assembled monolayer (SAM).<sup>126</sup> In last section of this chapter, I will briefly review a versatile technique for the controlled fabrication of  $\pi$ -conjugated phenylene imine (azomethine) oligomers bound to a substrate recently reported by the current author.

**Table 3.1** Various monolayers formed by self-assembly on several metals (adapted from reference <sup>125</sup>)

Metal substrate	Molecule	Binding
Au	RSH, ArSH (thiols)	RS-Au
Au	RSSR (disulfides)	RS-Au
Ag	RSH, ArSH	RS-Ag
Cu	RSH, ArSH	RS-Cu
Pt	RSH, ArSH	RS-Pt
Pt	RNC	RNC-Pt

### 3.1 Self-Assembled Monolayers (SAMs) of Organothiols

#### 3.1.1 Kinetics of Organothiol SAMs

The kinetics of forming organothiol SAMs can be understood in two steps. In an optical ellipsometry study, Bain *et al.* observed that the thickness of a C<sub>18</sub> monolayer formed from 1 mM ethanol rapidly achieved 80-90% of the maximum value, while it takes several hours to reach 100%.<sup>127</sup> In the first step, the strong chemical absorption of sulfur onto gold (45kcal/mol for S-Au) rapidly drives the surface reaction. Then, the molecules align themselves slowly, decreasing structural defects in the film. This step is a thermodynamically-controlled process that maximizes the enthalpic benefit gained from intramolecular interactions to overcome the entropy condition that leads to film disorder. Recently, several scanning-probe-microscopy experiments suggested a more complicated growth mechanism in alkanthiol SAMs. Yamada and Uosaki performed STM measurements that monitored alkanethiol growth on Au (111) from a heptane solution ( $\sim\mu\text{M}$ ).<sup>128, 129</sup> They insisted that three basic steps exist. Initially, disordered island-like aggregates grow on Au. In the second step, they observed a striped pattern appear that is

composed of thiol molecules lying down on the surface. In the third step, thiol molecules undergo a transition into a standing-up phase, that shows a hexagonal pattern consisting of ( $\sqrt{3} \times \sqrt{3}$  R  $30^\circ$ ) epitaxial arrangement (see Fig. 3.1). Later, Xu and coworkers revealed that the transition from the lying down phase to the standing up phase was faster for a  $C_{22}$  than a  $C_{18}$  thiol film.<sup>130</sup> They conclude that van der Waals interactions contribute to the overall enthalpy, and SAM crystallinity increases according to chain length.

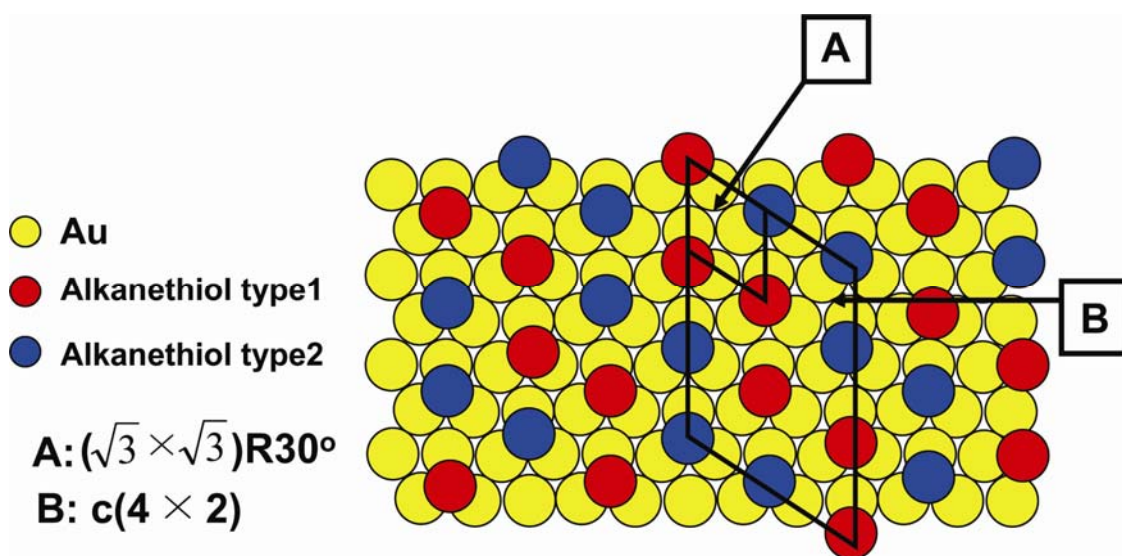


**Figure 3.1** Alkanethiol hexagonal surface lattice on Au(111).  $c$  represents a lattice height.

### 3.1.2 Monolayer Structure of Organothiol SAMs

Electron diffraction, helium diffraction and atomic force microscopy (AFM) experiments revealed that alkanthiol molecules on a gold (111) surface are packed with the hexagonal lattice symmetry ( $\sqrt{3} \times \sqrt{3}$  R  $30^\circ$ ).<sup>131</sup> Later, more in-depth studies using scanning tunneling microscopy (STM) studies showed that a few variants of a  $c(4 \times 2)$  superlattice places atop, indicating a height difference of some fraction of alkanthiols (see Fig. 3.1).<sup>132, 133</sup> Also, the alkanthiol molecules exist in a predominantly all-trans configuration within the lattice, tilted away from the gold substrate normal at about  $30^\circ$ .<sup>134</sup> This tilted nature enables the monolayer to maximize the van der Waals interactions between the chains, resulting in a well-defined structure. In the case of

aromatic thiols, the molecular cross section is bigger than in an alkanethiol, so that all sulfur binding sites can not be occupied due to the steric hinderance. As a result, aromatic thiols SAMs are expected to have a poorly ordered structure. Sabatini *et al.* found a tilt angle of  $80^\circ$  for benzenethiol on gold, indicating that the aromatic ring, without other functional groups, tends to lay flat on the surface.<sup>135</sup> However, longer aromatic thiol chains have a well-ordered and reproducible structure. Ishida *et al.* observed a  $\sqrt{3} \times \sqrt{3} R 30^\circ$  structure for p-terphenylmethanethiol on Au (111) from STM studies.<sup>136</sup> Kim *et al.* have been able to image a SAM of 4-amino thio phenol on Au (111) and found a  $(\sqrt{3} \times \sqrt{3} R 30^\circ)$  superstructure, which is generally found geometry for alkanthiols on gold.<sup>137</sup>

### 3.1.3 Monolayer Formation

SAM preparation begins with immersing a gold substrate into a desired dilute ( $\sim 1.0\text{mM}$ ) alkanethiol solution of an organic solvent such as absolute ethanol.<sup>138</sup> After allowing molecules to incubate for about 24 hours, the SAM becomes densely packed, as molecules on the surface reorganize and fill up remaining voids. A strong covalent bond between sulfur and gold provides the driving force for the formation of a well-ordered self-assembled monolayer (SAM) film. Figure 3.2a shows a schematic of the SAM formation process.

In general, a layer of gold is formed via thermal evaporation on Si substrate. Then, 5nm thick of a Cr adhesion layer is deposited followed by up to 100 nm thick of gold deposition (see Fig. 3.2b). Our group often fabricate atomically flat gold using the template stripping method<sup>139, 140</sup> to allows for a more reproducible molecular junction to be made. We can take advantage of the atomic surface flatness of silicon wafer, which decreases the height difference of monolayer over the substrate. Flat gold is made by transferring 300~500nm of a gold coating layer to a small piece of Si wafer (1cm x 1cm) that is glued by an epoxy (EPO-TEK 377) after thermal curing ( $130^\circ\text{C}$ , 1h 30min). Figure 3.2c illustrates the flat gold preparation.

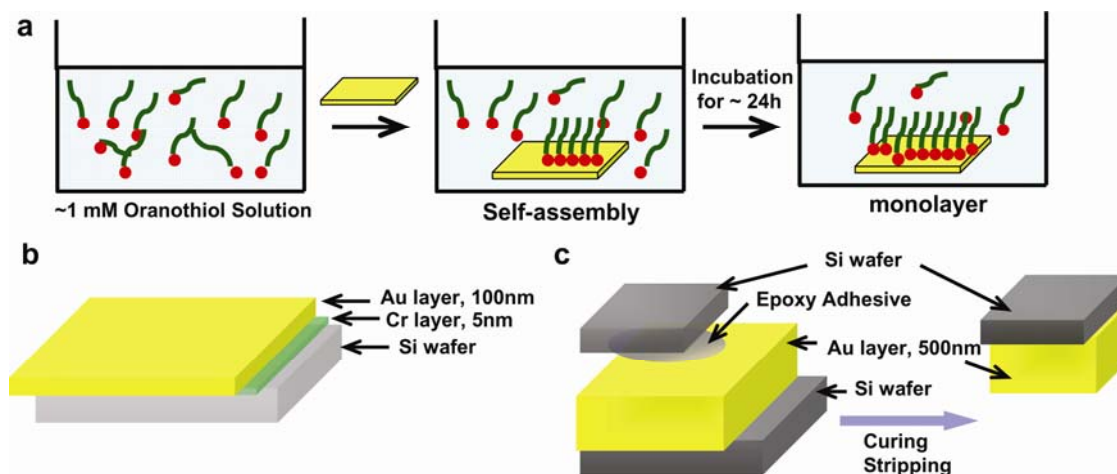


**Figure 3.2** Schematic description of (a) SAM formation process, (b) structure of rough gold, (c) preparation of the flat gold.

### 3.2 Step-wise Growth of Molecular Wires

A versatile technique for the controlled fabrication of  $\pi$ -conjugated phenylene imine (azomethine) oligomers bound to a substrate was recently reported by the current authors who followed a procedure originally described by Rosink, et al (Fig. 3.3a)<sup>141</sup>. The growth procedure begins by adsorption of a monolayer of 4-aminothiophenol on gold. Benzenedicarboxaldehyde is then added in solution, allowing formation of a second layer by reaction of one aldehyde group with the amine bound to the surface. The resulting imine extends conjugation over both of the individual layers. By reaction with phenylenediamine, a third layer can be formed that further extends the degree of conjugation. Thus, by a sequence of alternating addition of dialdehyde and diamine, the length of the oligomer is continually extended. In this stepwise fashion, long conjugated oligophenyleneimine (OPI) molecules are readily built, controlling the orientation. The surface density of the wire molecules remains essentially constant with increasing length as long as the reaction nearly completes at each step. Each OPI p wire terminated with  $-\text{NH}_2$  or  $-\text{CHO}$  groups can be end-capped with benzaldehyde or aniline, respectively<sup>33</sup>. The end-capping provides a consistent terminal group throughout the OPI series that facilitates reproducible electrical characterization.



The growth of OPI wires is conveniently monitored using reflection-absorption Fourier transform infrared spectroscopy (RAIRS). RAIRS data, shown in Fig. 3.3b, reveal the alternate appearance and disappearance of carbonyl stretches ( $1710\text{ cm}^{-1}$ ) and symmetric amine stretches ( $3350\text{ cm}^{-1}$ ) in the OPI-p wires, which verifies the imination mechanism and indicates near quantitative reaction of all exposed reactive endgroups. The intensity of imine stretching ( $1620\text{ cm}^{-1}$ ) and the benzene ring vibrational mode ( $1500\text{ cm}^{-1}$ ) increase with the number of repeat units, as expected. Complete end-capping to form finished OPI wires is confirmed by the disappearance of the terminal group vibrational modes (not shown)<sup>33</sup>.

The main advantage of this stepwise imine chemistry lies in its compatibility with a variety of molecular building blocks. Wires may be built with precisely controlled chain architecture, and at the end of this thesis we suggest some different building blocks designed to examine the role of steric interactions and redox properties on wire transport. Recently, we have taken the next step to prove the versatility of the method by building wires from larger, more conjugated building blocks. Specifically, alternate addition of naphthalene and fluorene blocks has been employed to build oligonaphthalene-fluorene-imine (ONI) wires up to 10 nm in length (Fig. 3.4, and Chapter 5). Preliminary results confirm that the addition chemistry also works cleanly for growth of these ONI wires and this work will be reported elsewhere.

OPI wires ranging in length from 1.5 to 7.3 nm have been reported and their transport properties were characterized in detail as a function of molecular length, temperature, and applied bias<sup>33</sup>. In the next chapter, we cover the experimental details of the characterization of OPI wires, including the conducting probe atomic force microscopy (CP-AFM) approach employed for electrically contacting them. We describe the I-V behavior in detail, focusing in particular on transitions in the conduction mechanism from tunneling to hopping to field emission.

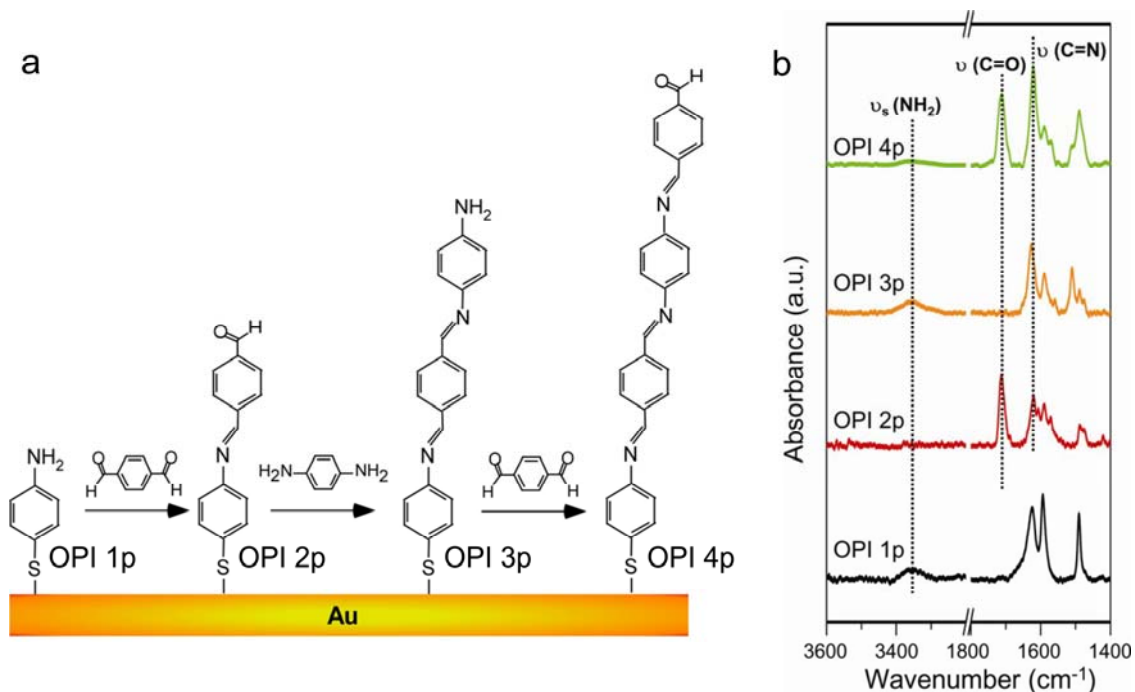


**Figure 3.3 (a)** Molecular structure and synthetic route to OPI-p monolayers on gold substrates. (shown up to fourth layers) **(b)** The corresponding RAIERS spectra. Vertical dashed lines indicate positions of symmetric amine stretches ( $\text{NH}_2$ ,  $3350 \text{ cm}^{-1}$ ), carbonyl stretches ( $\text{C}=\text{O}$ ,  $1710 \text{ cm}^{-1}$ ), and imine stretches ( $\text{C}=\text{N}$ ,  $1620 \text{ cm}^{-1}$ ). Peaks for  $\text{NH}_2$  and  $\text{C}=\text{O}$  appear in the uncapped OPI p wires with odd and even numbers of repeat units, respectively. Subsequent capping of OPI p molecules with either aniline or benzaldehyde produce the finished OPI wires that were subsequently measured. [Modified from <sup>33</sup> with permission; Copyright 2008 by the AAAS]

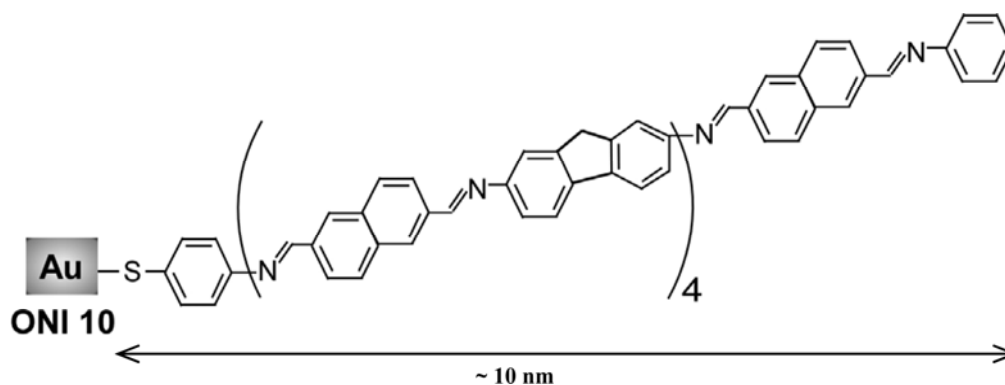


**Figure 3.4** Molecular structure of ONI 10, the longest ONI wire that was prepared by stepwise additions of naphthalene-2,6-dicarboxaldehyde and fluorene-2,7-diamine.

Others also have reported a step-wise approach within nanoscale sockets<sup>142</sup> and on a gold substrate<sup>120</sup>. Nuckolls group<sup>142</sup> have shown a method to integrate aryimine addition and metal coordination chemistry with the formation of nanoscale electrical “sockets” to allow the *in-situ* construction of molecular wires. As shown in Fig. 3.5, first they assemble a bifunctional molecules into a monolayer on the electrode surface, such that only one end of the molecule reacts with the electrode; then, they use a second molecule to bridge the gap between the termini of the films. In a recent research letter, Rampi group<sup>120</sup> studied very long (up to 40 nm) and highly conductive molecular wires that are assembled *in-situ* on metal surfaces via a sequential stepwise coordination of metal ions by terpyridine-based ligands (Fig. 3.6a). The increase of molecular length was quantified with AFM measurement on micropatterned Au surface. In particular, they have microcontact-printed the gold substrates with octadecanethiol (ODT) lines, and functionalized ODT-free areas with metal centre molecular wires with different lengths. Figure 3.6 b and c shows the AFM height of image and the relative cross-section with a histogram analysis that provides an average value of the height differences between lines. The linear correlation between the measured height differences and the number of coordination steps of Fig. 3.6d proves that molecular wires as long as 26 nm still assemble in highly ordered structures. The slope indicates a height increase of ~1 nm per coordination step.

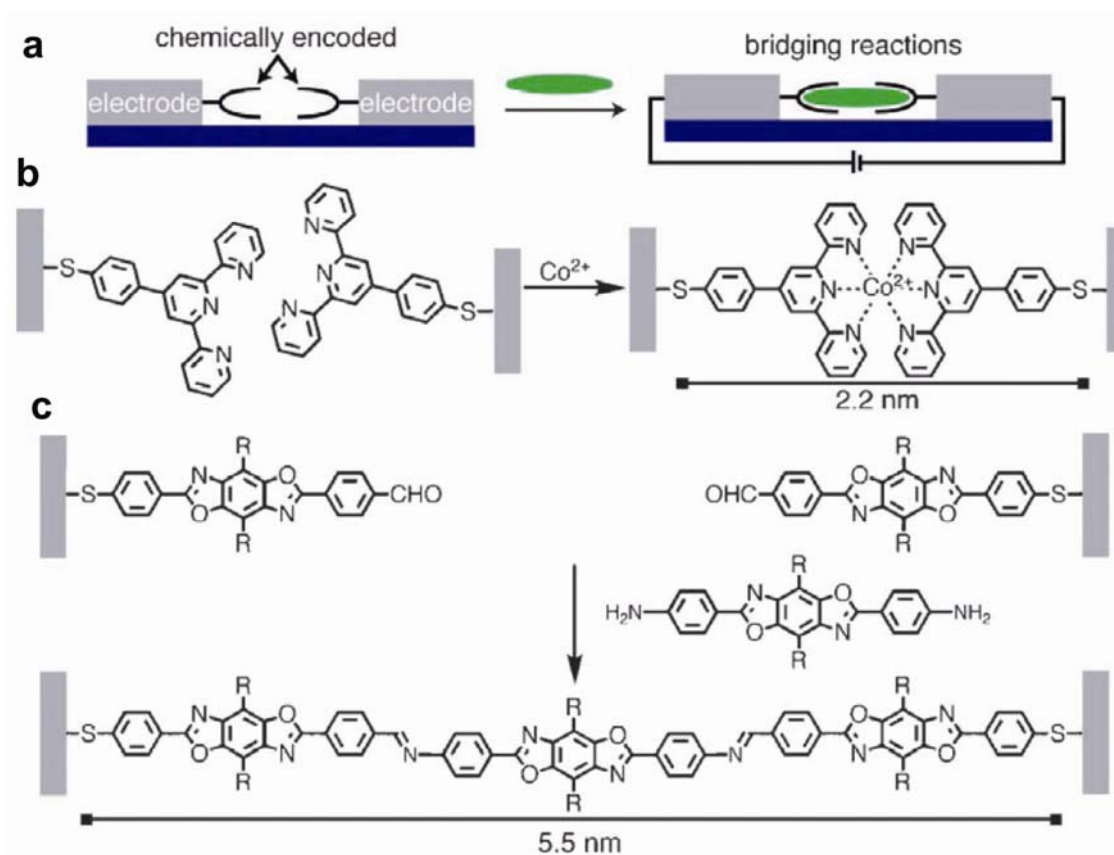


**Figure 3.5** (a) Two-step sequence to bridge electrode surfaces. (b) Bridging by first forming a monolayer with the terpyridyl group and using cobalt ions to orchestrate wire formation. (c) Bridging gaps by first forming a thiol-terminated monolayer and then reacting with a diamine. The R group is a 4-dodecyloxy-substituted phenyl group added to improve solubility. [Modified from <sup>142</sup> with permission; Copyright 2007 by Wiley-VCH]

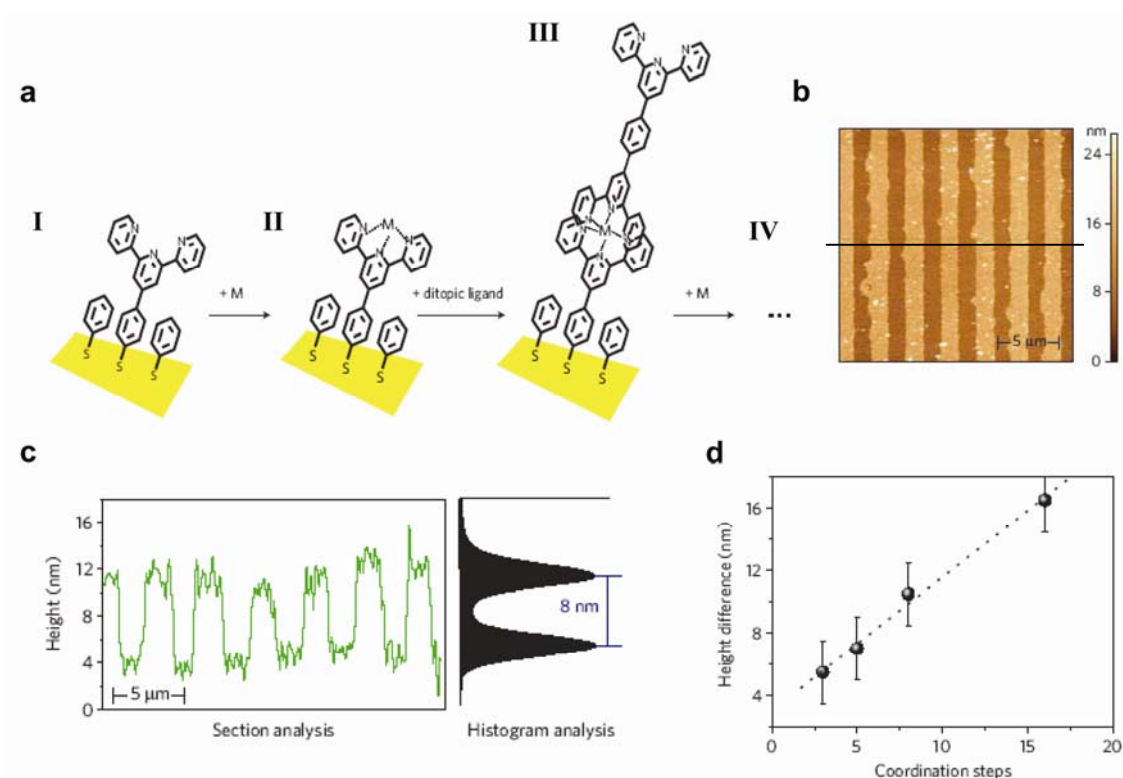


**Figure 3.6 (a)** Schematic representation of the stepwise assembly of the metal centre molecular wires in situ metal surfaces. I. Assembly on the gold surface II. Coordination of the metal to the ligand. III. Coordination of the terpyridine ligand. IV. The process II and III are repeated iteratively to increase the length of wires. **(b)** AFM height image of micropatterned structure. **(c)** Cross-section analysis of map b at the indicated lines, and histogram analysis of b providing an average value of the height difference between molecular wires. **(d)** Height difference between the measured ODT lines and the molecular wires as a function of the number of coordination steps. Error bars are estimated from the width of the height distribution in the histogram analysis. [Modified from <sup>120</sup> with permission; Copyright 2009 by Nature publishing group]

### **3.3 Characterization of Molecular Wires**

Self-assembled monolayers and molecular wires have been characterized by a wide variety of techniques. In this section, several representative techniques to characterize self-assembled monolayers are described.

**Optical Ellipsometry.** Ellipsometry is a technique which allows one to measure the complex dielectric function of a given material accurately. It observes the change in polarization of light reflected from the surface of a sample to be studied. A typical setup of an ellipsometry experiment is sketched in Fig. 3.7. The incident light is linearly polarized with finite field components  $E_p$  and  $E_s$  in the directions parallel and perpendicular to the plane of incidence of the light respectively. The light becomes elliptically polarized due to the optical properties and thicknesses of the various layers. Detecting the change in polarization allows for the optical properties and thickness to be measured. The experimental data is expressed in terms of  $\tan\psi$  and  $\Delta$  (relative phase shift), which are related to the Fresnel-reflection-coefficient  $R_p$  and  $R_s$  for p- and s-polarized light respectively. The Fresnel-reflection coefficient are complex functions of the angle of incidence  $\Phi_o$ , the wavelength  $\lambda$ , the optical constants of the substrate( $N_s$ ), substrate( $n_o$ ) and layers( $n_j, k_j$ ), and of the layer thicknesses( $d_j$ ), respectively.

Thickness of film can be obtained through the following procedures. First, the polarized angle of bare gold can be measured at a fixed incident angle ( $75^\circ$ ) and over a range of wavelengths (250nm ~ 900nm). Instrument software can extrapolate the optical constants ( $n$  and  $k$ ) under the assumption of infinite gold thickness. Then, the same angle measurement is performed on a SAM on gold. The fitted data at a given initial value ( $n=1.5, k=0.0$ ) provides the thickness of film. Because this method is convenient and accurate, it is used broadly in SAM characterization.

**Contact Angle Measurement.** This technique is a simple but sensitive probe for surface analysis related to surface energy and tension. Contact angle measurements can be used to estimate the degree of order and the polarity of the monolayer surface functional groups.

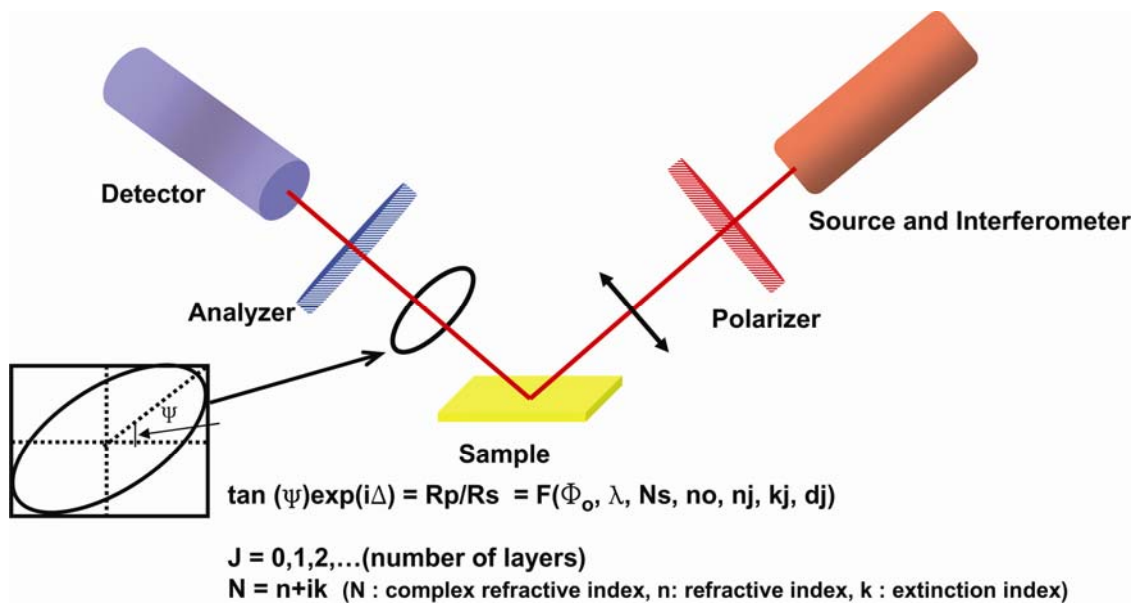


**Figure 3.7** Schematics of optical ellipsometry.

In addition, the surface free energy of the monolayers can be determined by measuring contact angles as a function of surface tension of a series of liquids. The contact angle is defined by the shape of a liquid droplet resting on a solid surface. When drawing a tangent line to the droplet at the solid surface interface, the contact angle is the angle between the tangent line and the solid surface. The shape of this interface is governed by the interactions of the monolayer, the liquid, and the surrounding medium. When a liquid drop is on a solid surface in equilibrium, the relationship between the surface free energies from Young's equation is given by:<sup>143</sup>

$$\gamma_{lv} \cos\theta = \gamma_{sv} - \gamma_{sl} \quad (3.1)$$

where  $\gamma_{lv}$ ,  $\gamma_{sv}$ , and  $\gamma_{sl}$  represent the surface tensions of the liquid-vapor, solid-vapor and solid-liquid interfaces, respectively, and  $\theta$  is the contact angle. For a liquid which wets the surface, the solid-liquid surface tension is very small, and thus  $\cos\theta$  approaches 1, and  $\theta$  goes to zero. On the contrary, if the liquid does not wet the monolayer, then  $\gamma_{sl}$  becomes large relative to the other terms. In this case,  $\cos\theta$  can be zero, or even negative, corresponding to contact angles of  $90^\circ$  or greater. Although any suitable pure liquid can be used for contact angle measurements, the water contact angle,  $\theta_{H_2O}$ , is most commonly used for alkanethiols SAMs. For a close-packed long-chain n-alkanethiol monolayer

terminated with  $-\text{CH}_3$ ,  $\theta_{\text{H}_2\text{O}}$  is reported to be  $112^\circ$ . In contrast, a similar monolayer terminated with  $-\text{OH}$  or  $-\text{COOH}$  showed  $\theta_{\text{H}_2\text{O}}$  is  $0^\circ$ .<sup>144</sup>

Another useful quantity is the hysteresis of the contact angle, defined as the difference between advancing contact angle and receding contact angle ( $\theta_{\text{ADV}} - \theta_{\text{REC}}$ ). The advancing angle ( $\theta_{\text{ADV}}$ ) is the largest possible angle and the receding ( $\theta_{\text{REC}}$ ) is the smallest possible contact angle. Qualities of SAMs such as surface roughness and uniformity can be estimated by the hysteresis.<sup>143</sup>

**Fourier Transform Infrared Spectroscopy.** FT-IR is a very powerful method for the investigation of the composition of a surface, analyzing film crystallinity, molecular orientation and surface coverage.<sup>134, 145-148</sup> In general, if molecules undergo a change of dipole moment, infrared radiation can be absorbed, responding actively in molecular vibrational modes such as bending, stretching and wagging. Here, I will focus on surface-sensitive techniques for the IR spectroscopic characterization of ultrathin adsorbate films on flat solid substrates, including infrared reflection-absorption spectroscopy (IRRAS) and attenuated total internal reflection FT-IR (ATR).

IRRAS is a well established technique for studying substances adsorbed on metal surfaces. As the name suggests, the infrared light is reflected off a surface rather than transmitted through the sample. It takes advantage of the great difference in the absorption of polarized light at high angles of incidence. This technique is normally used for the characterization of thin films on highly reflecting metal substrates, but can also be applied to non-metals with the aid of spectral simulation. Arnold *et al.* found that p-terphenylthiols form SAM on gold with a tilt angle of  $24^\circ$  via this IR technique.<sup>149</sup>

In ATR, a semiconducting or insulating crystal serves as a wave guide for IR beams (see Fig. 3.8). The IR penetrates a fraction of a wavelength beyond the reflecting surface into the rarer medium. This evanescent wave can protrude only a few microns ( $0.5\text{-}5\mu\text{m}$ ) beyond the crystal surface and into the sample. Therefore, good contact between the SAM and crystal is necessary. The wave is attenuated by molecular absorption in the IR region. The wave then enters the detector from the opposite end of the crystal. Another requirement for internal reflection is that the reflective index of the crystal be much higher than the sample. Thus, Zinc Selenide, Silicon and Germanium are most commonly used as ATR crystals. Recently, the Zhu group probed the



conformational and structural changes at a molecule/metal interface using ATR,<sup>150</sup> where molecules are self-assembled atop gold coated ( $\sim 30\text{\AA}$ ) silicon (111) crystal.

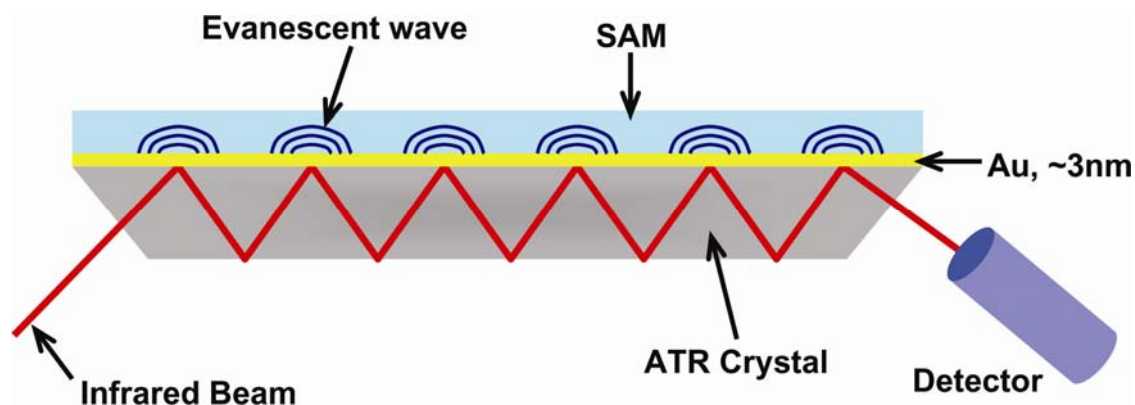


**Figure 3.8** Schematic picture of internal reflection in ATR. (adapted from reference<sup>150</sup>)

**Cyclic Voltammetry.** In cyclic voltammetry, the current is measured as a function of electrode potential. In order to measure current and potential simultaneously, three electrodes are required. The reference electrode is typically a Ag/AgCl. A platinum wire or gauze is used as a counter electrode, and a monolayer-coated metal surface is incorporated as a working electrode. This working electrode may be a portion of a bare or monolayer-coated gold electrode. To obtain a cyclic voltammogram, the current flow between the working electrode and counter electrode is recorded as a sawtooth potential is applied to the working electrode. At the same time, the magnitude of the resulting potential is measured between the working and reference electrodes.

While ellipsometry and IR spectroscopy provide average molecular properties of adsorbed molecules, cyclic voltammetry provides means to probe the nature and extent of structural defects and coverage, as well as to determine the dynamics of electron transfer reactions occurring in the monolayer. Porter *et al.*<sup>138</sup> examined the SAMs of alkanethiols by cyclic voltammetry using  $\text{Fe}(\text{CN})_6^{3-}$  and  $\text{Fe}(\text{H}_2\text{O})_6^{3+}$  as an electroactive species, and found that the shape of the current behavior may suggest an assembly of pinholes in the monolayer. Sikes *et al.*<sup>151</sup> measured rapid electron tunneling transfer through oligophenylenevinylene bridges between a gold electrode and a tethered redox species, Ferrocene. They revealed that electronic coupling for oligophenylenevinylene bridges up

to 28 Å long does not limit the rate constants, suggesting that oligophenylenevinylene bridges could be useful wires for molecular electronic applications.

**X-ray Photoelectron Spectroscopy.** X-ray Photoelectron Spectroscopy (XPS) provides a way to examine the chemical composition in the monolayer. X-ray photoelectron spectroscopy involves irradiation of a sample under vacuum by x-rays of known energy, which causes the ejection of photoelectrons from the atoms near the surface. The emitted electrons have a kinetic energy  $E_k$ , given by:

$$E_k = h\nu - E_b - \Phi \quad (3.2)$$

where  $h\nu$ ,  $E_b$ , and  $\Phi$  represent the photon energy, the binding energy, and the work function, respectively. The dispersion of kinetic energy of the ejected electrons provides a spectrum of binding energies. The locations of peaks in this spectrum indicate both the presence of specific elements and their respective oxidation states.

In addition, the intensity of a photoelectron peak varies linearly with the surface concentration of the corresponding element. Within the shallow region, the signal from atoms buried within the monolayer will be attenuated according to their depth. By varying the take-off angle, the effective escape depth for photoelectrons from low-lying species can be increased or decreased. Thus, spectra taken at a series of different take-off angles can be used to construct a crude depth profile of a monolayer. Nuzzo and Allara<sup>152</sup> were the first to use XPS to characterize self-assembled monolayers of thiols on gold. Bain *et al.*<sup>144</sup> studied the formation of terminally functionalized alkanethiol monolayers by observing the presence of heteroatoms in the monolayer with XPS.

Many researchers have also used this technique to determine the film-thickness. There are two main approaches to obtaining thickness. In one technique, attenuation of photoelectron peaks from metal substrate is used. The intensity of x-ray photoelectrons from the metal is defined by:

$$I = I_0 \exp\left(-\frac{d}{\lambda \sin \theta}\right) \quad (3.3)$$

where  $I$  = the intensity of the metal photoelectrons attenuated by a monolayer,  $I_0$  = the intensity from a clean metal substrate,  $d$  = the thickness of the monolayer,  $\lambda$  = the attenuation length, and  $\theta$  = the angle between the surface parallel and the analyzer axis (take-off angle). Measurement of the thickness of the monolayer ( $d$ ) is accomplished

experimentally by measuring intensities of x-ray photoelectrons with a known attenuation length ( $\lambda$ ) at a fixed photoelectron kinetic energy.<sup>153</sup> The second method involves using the relative x-ray photoelectron intensities. For instance, in the case of organothiol monolayer on gold, the sample thickness can be calculated using the relative intensities of the Au 4f and the C 1s peaks and by using decanethiol on Au as a reference system. (Assuming the same attenuation length of the gold ( $\lambda_{Au}$ ) and carbon ( $\lambda_C$ ) photoelectrons for the alkane or aromatic films.) The calculation is based on:<sup>154</sup>

$$\frac{\frac{I_C}{I_{Au}}(sample)}{\frac{I_C}{I_{Au}}(reference)} = \frac{\left\{1 - \exp\left(-\frac{d_{sample}}{\lambda_C}\right)\right\} \exp\left(-\frac{d_{reference}}{\lambda_{Au}}\right)}{\exp\left(-\frac{d_{sample}}{\lambda_{Au}}\right) \left\{1 - \exp\left(-\frac{d_{reference}}{\lambda_C}\right)\right\}} \quad (3.4)$$

where  $I_C$  = the intensity of C 1s photoelectons and  $I_{Au}$  = the intensity of Au 4f photoelectrons.

## 4 OligoPhenyleneImine (OPI) Wires

### 4.1 Abstract

An important property of a wire is its electrical resistance per unit length. We have measured the resistance and current-voltage characteristics of conjugated molecular wires ranging in length from 1 to 7 nm, connected between metal electrodes. We observe for the first time the theoretically predicted change in DC transport from tunneling to hopping as a function of systematically controlled wire length. We also demonstrate that site-specific disruption of conjugation in the wires greatly increases resistance in the hopping regime but has only a small effect in the tunneling regime. These nanoscale transport measurements elucidate the role of molecular length and bond architecture on molecular conductivity and open opportunities for greater understanding of electrical transport in conjugated polymer films.

### 4.2 Introduction

Transport of charge through long,  $\pi$ -conjugated molecules is of broad importance to many fields of chemistry, physics, and biology.<sup>1-3</sup> The term “molecular wire” is often used to describe conjugated molecules that serve as efficient conduits for charge over long distances,<sup>4,5</sup> e.g. the  $\beta$ -carotene molecule that can transfer electrons over tens of Angstroms.<sup>6</sup> In the context of molecular electronics, where the ultimate goal is the fabrication of circuitry based on the prescribed electronic function of individual molecules<sup>155, 156</sup>,<sup>4,7</sup> it is desirable to have a quantitative definition of what constitutes a molecular wire.

A fundamental property of a wire is the scaling of its resistance (or conductance) with length. The length dependence of resistance is a direct consequence of the charge transport mechanism. In the macroscopic world, the resistance of a metallic wire increases linearly with length as a result of the diffusive nature of carrier transport in the metal. However, this particular scaling need not hold for conduction in molecules over nanometer length scales, as has been pointed out theoretically<sup>8-10</sup> and observed

experimentally.<sup>2,3,11,12</sup> For short molecules (< 3 nm) connected between metallic contacts, it is well-accepted that resistance scales exponentially with length according to Eq. 4.1.

$$R = R_0 \exp(\beta L) \quad (4.1)$$

where  $R$  is the junction resistance,  $R_0$  is an effective contact resistance,  $L$  is molecular length, and  $\beta$  is the exponential pre-factor that depends on the nature of bonding in the molecular backbone. The exponential length dependence in Eq. 1 results directly from the transport mechanism in metal-molecule-metal junctions based on short molecules, namely direct (non-resonant) tunneling.

For longer molecules connected between metal electrodes, the scaling of resistance with length can be anticipated by comparison to fundamental studies of electron transfer in solution. Both theory and experiment on soluble donor-bridge-acceptor (D-B-A) systems<sup>157-161</sup> indicate that for long molecular bridges the charge transport mechanism changes from direct tunneling to hopping as evidenced by a change in the length dependence of the electron transfer rate constant. Specifically, for short bridges the length dependence is exponential, corresponding to the tunneling regime, and for long bridges the scaling is linear as expected for hopping transport; in the experiments reported by Wasielewski, *et al.*<sup>158</sup>, the transition occurs when the conjugated bridge becomes longer than ~2.5 nm. Importantly, the weaker length dependence associated with the hopping regime facilitates the transport of charge over greater distances, and it is this regime that might be considered most “wire-like”, although tunneling through saturated peptide bonds, for example, has also been shown to provide enhanced transport over relatively large distances in redox proteins.<sup>162, 163</sup>

In the context of molecular electronics, it has been difficult to systematically examine the hopping regime in conjugated molecular wires connected to metallic contacts because of the relatively large range of molecular lengths required (spanning many nm) and the complexities of adsorbing long molecules to metal surfaces in an oriented fashion. Electrical transport measurements on molecules up to 18 nm in length have been reported<sup>164</sup>, and charge hopping in molecular junctions has been observed,<sup>165-167</sup> but the systematic length dependence of conduction has not been a principal focus. To date, a clear observation of the predicted transition from tunneling to hopping conduction in a molecular wire contacted by metal electrodes has not been reported. It remains an

important goal for molecular electronics to establish the nature of transport in long conjugated molecules, and the results of such experiments have important implications not only for molecular electronics, but also for the microscopic picture of electrical transport in conjugated polymer films.

In this report, we provide direct evidence for a change in transport mechanism from tunneling to hopping in molecular junctions based on conjugated oligophenyleneimine (OPI) wires ranging in length from 1.5–7.3 nm. Our experimental approach involves contacting OPI wires that are grown from one electrode using controlled aryl imine addition chemistry; a metal-coated atomic force microscope tip is used to make the second contact. We show that near 4 nm in length the mechanism of transport in the wires changes abruptly, as evidenced by striking changes in the length, temperature, and electric field dependence of the current-voltage ( $I$ - $V$ ) characteristics. For longer wires, we have been able to analyze the bias dependence to establish at least three different regimes of transport, and we are also able to estimate the single wire conductivity. Overall, these experiments open significant opportunities to probe the physical organic chemistry of molecular conduction, *e.g.*, the roles of specific functional groups and bonding architectures on hopping transport in molecular wires.

### **4.3 Experimental**

#### **CP-AFM Junction formation and measurement**

Molecular junctions were formed by bringing a gold-coated tip into contact with a monolayer, as illustrated in Fig. 2.9. These experiments were performed with a multimode AFM from Veeco Instruments. Gold-coated tips and flat gold substrates were prepared as reported previously.<sup>40, 41</sup> We have examined  $I$ - $V$  characteristics of OPI wires up to  $\pm 1.0$  V for OPI 1–2 and  $\pm 1.5$  V for OPI 3–10 and CB-OPI wires. The resistance was determined from the linear current-voltage relationship within the range of  $\pm 0.3$  V. Three gold-coated AFM tips having a radius of  $\sim 50$  nm were used for the measurements, each of which gave the same resistance value for tunneling through an octanethiol SAM (an effective calibration standard). The three tips were used separately to examine three sets of wires: OPI 1–4 (tip 1), OPI 4–7 (tip 2), and OPI 7–10 (tip 3). Note that OPI 4 and OPI 7 were each measured with two different tips to confirm that the same resistances

were obtained. For measurement on CB-OPI wires, we used another two gold-coated AFM tips for two sets of wires: CB-OPI 3 and CB-OPI 4 (tip 4), and CB-OPI 8 and CB-OPI 10 (tip 5); these tips were also calibrated with an octanethiol SAM. We confirmed that tips 4 and 5, respectively, gave the same resistance values for OPI 3 and OPI 4, and OPI 8 and OPI 10, measured by tips 1 and 3. The number of molecules in each junction was estimated from the size of the tip radius and the wire surface coverage to be  $\sim 100$ .<sup>42</sup>

### **Variable temperature measurements**

Variable temperature measurements of the OPI wire resistances were performed with an environmentally controlled Molecular Imaging PicoScan/PicoSPM. The most important feature of this instrument is that the tip and temperature controlled substrate stage were held in an isolated chamber where the humidity is regulated. Keeping the humidity of chamber low ( $< 5\%$  RH) increases the accuracy of measurement by preventing water condensation on sample below room temperature. We have checked that the tunneling current of the octanethiol SAM remains constant within an error range<sup>40</sup> from  $-30\text{ }^{\circ}\text{C}$  (243 K) of a setpoint temperature to room temperature in  $< 5\%$  RH of chamber humidity. Two different sample stages, a normal heating stage and a peltier stage were used to vary temperature above and below room temperature, respectively. Silver paste was painted at the edge of each sample to make thermal contact between the sample and stage. The measured temperatures on samples were consistent with the setpoint temperatures. The resistances were determined from linear current-voltage relationships within the range of  $\pm 0.2\text{ V}$ , and are the average values of resistances obtained at six different locations on the samples. The current-voltage curves of OPI 6 and OPI 10 at different temperatures are shown in Fig. 4.1. Two gold-coated AFM tips having a radius of  $\sim 50\text{ nm}$  were used for the measurements, each of which gave the same resistance value for tunneling through an octanethiol SAM and OPI 4. The two tips were used separately to examine the resistances of OPI 4, OPI 6, and OPI 10 in two temperature ranges:  $246\text{--}293\text{ K}$  (tip 1), and  $303\text{--}333\text{ K}$  (tip 2). Note that all measurements were performed while keeping the humidity of chamber below  $5\%$  RH.

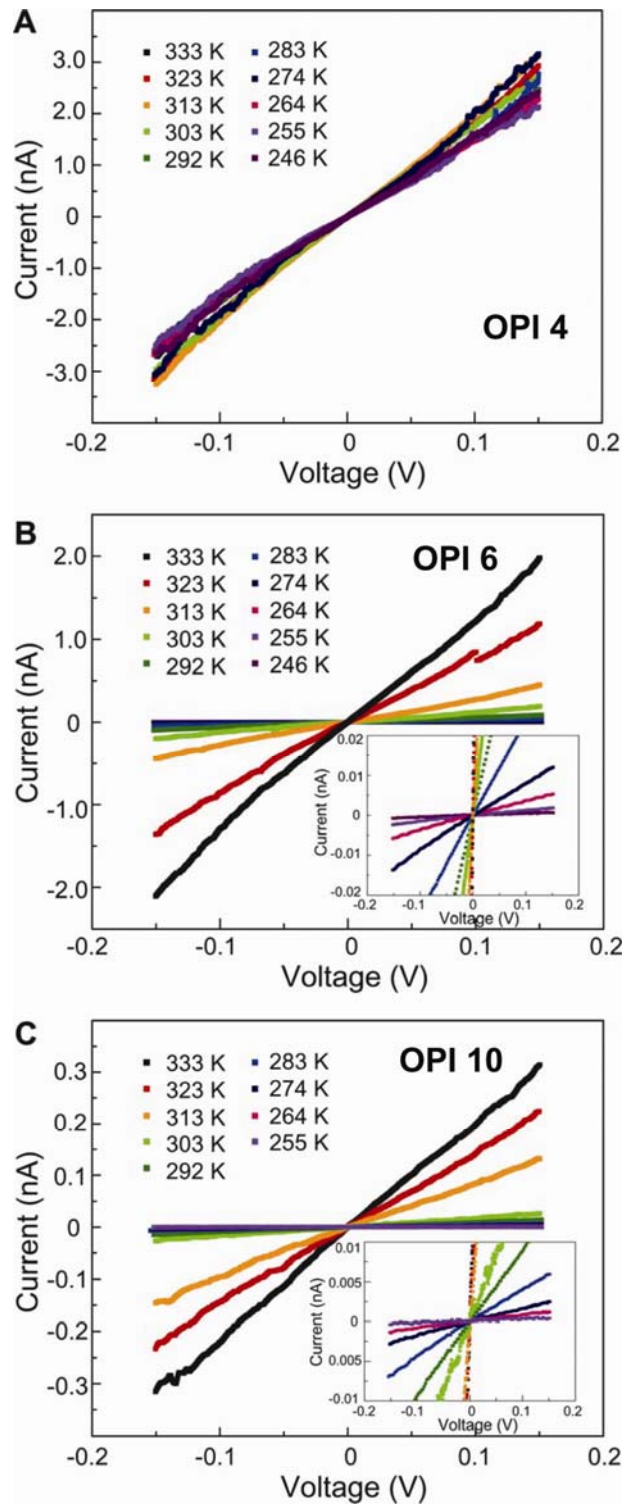


**Figure 4.1** The current-voltage characteristics of (A) OPI 4, (B) OPI 6, and (C) OPI 10 at different temperatures. Insets show the  $I$ - $V$  curves with a magnified current axis.



### Monolayer Characterization

OPI-p, OPI and CB-OPI wires were characterized by ellipsometry, X-ray photoelectron spectroscopy (XPS), reflection-absorption Fourier transform infrared spectroscopy (RAIRS), and cyclic voltammetry. Ellipsometric measurements were made using a Sopra ES4G spectroscopic ellipsometer equipped with a xenon light source. Measurements of the polarization angles  $\psi$  and  $\Delta$  were taken as a function of wavelength ( $\lambda$ ) between 500 and 900 nm at an incident angle of  $75^\circ$  from the surface normal. The indices of refraction ( $n$ ) and extinction coefficient ( $k$ ) of gold-coated substrates were determined by measurement of the polarization angles prior to monolayer deposition. After molecular films were formed, the polarization measurements were repeated on each sample in the same orientation as when gold substrates were measured. Using the new  $\psi$  and  $\Delta$  values and fixed values for  $n$  and  $k$  (1.5 and 0, respectively), the instrument software calculated film thicknesses. The calculation is based on a parallel layer model of substrate/film/ambient assuming that films are homogeneous and isotropic and substrates have an infinite thickness. Thicknesses in Table 4.1 represent an average over 5 different samples for each SAM.

XPS spectra were taken on a Perkin-Elmer Phi 5400 spectrometer with a Mg  $K\alpha$  X-ray source (1253.6 eV) using a hemispherical analyzer in an ultrahigh vacuum ( $< 10^{-9}$  Torr) system. The X-ray anode was operated at 200 W, and the analyzer was set at a pass energy of 89.45 eV for survey scans and 17.9 eV for high-resolution scans. The binding energy scales were referenced to the  $Au_{4f7/2}$  peak (84.0 eV). The monolayer thickness was calculated using the relative intensities of the  $Au_{4f}$  and  $C_{1s}$  peak and by using hexadecanethiol SAM on Au as a reference ( $d = 1.86$  nm). Assuming the same attenuation length of gold ( $\lambda_{Au} = 3.46$  nm) and carbon ( $\lambda_C = 3.02$  nm) photoelectrons for monolayers, the calculation based on Eq. (4.2) yielded the thickness<sup>168-170</sup>.

$$\frac{\frac{I_C}{I_{Au}}(sample)}{\frac{I_C}{I_{Au}}(reference)} = \frac{\left\{1 - \exp\left(-\frac{d_{sample}}{\lambda_C}\right)\right\} \exp\left(-\frac{d_{reference}}{\lambda_{Au}}\right)}{\exp\left(-\frac{d_{sample}}{\lambda_{Au}}\right) \left\{1 - \exp\left(-\frac{d_{reference}}{\lambda_C}\right)\right\}} \quad (4.2)$$

where  $I_C$  = the intensity of  $C_{1s}$  peaks,  $I_{Au}$  = the intensity of  $Au_{4f}$  peaks, and  $d$  is the thickness. The estimated length and film thickness measured by ellipsometry and XPS for all OPI-p, OPI, and CB-OPI wires are shown in Table 4.1.

RAIRS was taken with a Nicolet Series II Magna-IR System 750 FTIR with a Harrick Seagull accessory for grazing angle specular reflectance measurements. The infrared beam was incident at an  $84^\circ$  angle with respect to the surface normal. A total of 2000 scans were collected at  $1.0\text{ cm}^{-1}$  resolution. RAIRS was used not only for monitoring step-wise imination as shown in Fig. 4.7, but also for revealing the orientation of 4-amionthiophenol (ATP) on gold. Figure 4.2 displays the comparison of RAIRS of ATP and bound ATP on Au (OPI 1-p). Two blue circles indicate IR absorption for aromatic amine stretching ( $3450\text{ cm}^{-1}$ ) and the aromatic C-H out-of-plane wagging mode ( $820\text{ cm}^{-1}$ ). Both peaks are clearly absent in the RAIRS of OPI 1-p, which because of the surface selection rule<sup>171</sup>, indicates that ATP has an upright orientation with respect to the gold substrates. Moreover, the imination of aldehyde-terminated OPI-p wires (OPI 2-p, OPI 6-p) with 1,4-diaminocyclohexane and the following imination with benzene-1,4-dicarboxaldehyde on the terminal amine of the cyclohexyl subunit were monitored using RAIRS. Figure 4.3 compares IR spectra before and after imination with a cyclohexyl unit, and shows that step wise iminations were successfully completed. The conjugation broken wires have the following IR absorption peaks; symmetric amine stretching ( $NH_2$ ,  $3350\text{ cm}^{-1}$ ), carbonyl stretching ( $C=O$ ,  $1710\text{ cm}^{-1}$ ), imine stretching ( $C=N$ -(aromatic),  $1620\text{ cm}^{-1}$ ), and imine stretching ( $C=N$ -(aliphatic),  $1640\text{ cm}^{-1}$ ).

Cyclic voltammetry (CV) experiments were undertaken to determine the redox states of OPI wires and to measure surface coverage. In these experiments, a three-neck electrochemical cell was used. A clean O-ring (1.0 cm diameter) in a cylindrical cavity surrounding a hole in the bottom of the cell was placed between the cell and a SAM-coated Au substrate, which acted as the working electrode. The cell was filled with 0.2 M tetrabutylammonium hexafluorophosphate ( $Bu_4NPF_6$ ) in purified acetonitrile which was deoxygenated by three cycles of freeze-pump-thaw treatments. A Pt gauze was used as the counter electrode and the cell was referenced to a Ag wire. Prior to examining the monolayer oxidation potentials, the system was calibrated to the ferrocene oxidation potential. For each monolayer, the scan was recorded at a sweep rate of  $300\text{ mV/s}$  and the

CV curves were reproducible and stable to electrochemical cycling within the range of  $-0.2 - +1.2$  V vs. Ag wire. A reversible oxidation wave was evident for OPI 1–OPI 10 at  $\sim +0.8$  V vs. Ag wire ( $\sim +0.4$  V vs.  $\text{Fc}^+/\text{Fc}$ ). In addition, the surface coverage ( $\Gamma$ ) was determined according to the following Eq. (4.3):

$$\Gamma = \frac{Q}{nFA} \quad (4.3)$$

where  $Q$  is the charge injected into the SAM,  $n$  is the number of electrons involved in the electron-transfer process,  $F$  is the Faraday constant, and  $A$  is the surface area of the monolayer examined, that is, the area inside of the O-ring.  $Q$  was obtained by integrating the area under the forward cyclic voltammogram using the oxidation wave for each of the monolayers. Cyclic voltammograms of OPI wires are displayed in Fig. 4.4. Oxidation potentials and the estimated surface coverages for all OPI wires are compiled in Table 4.1 and 4.2, respectively.

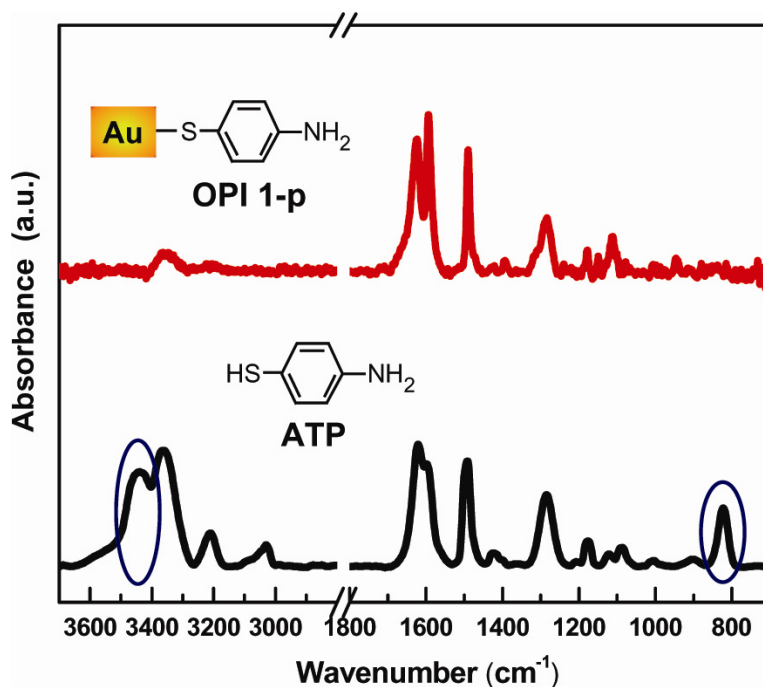


**Figure 4.2** Comparison of IR spectra of ATP and OPI 1-p. Two blue circles indicate IR absorption for asymmetric amine stretching ( $3450\text{ cm}^{-1}$ ) and aromatic C-H out-of-plane wagging mode ( $820\text{ cm}^{-1}$ ). Disappearance of both IR peaks in the OPI 1-p spectrum indicates that ATP has an upright orientation with respect to the gold substrate according to surface selection rules.<sup>46</sup>

**Table 4.1** Summary of experimental and calculated data for OPI wires.

Monolayer	Estimated Molecular Length* (nm)	Film Thickness (By Ellipsometry/XPS†) (nm)	$E_g$ (eV)	Oxidation Potential (V)‡	n in I, I'		$V_{trans}$ (V)	$V_{II'}$ (V)	$\phi_{FE}$ (eV)
					$I \propto V^n$	$I \propto V^n$			
OPI 1	1.5	1.4 / 1.4	3.7	0.22	1.1	-	0.95 [6.3]	-	-
OPI 2	2.1	1.8 / 1.6	3.1	0.22	1.1	-	0.85 [4.0]	-	-
OPI 3	2.8	2.5 / 1.9	2.6	0.14	1.1	-	0.75 [2.7]	-	-
CB-OPI 3	2.7	2.5 / 1.9	3.7	-	1.2	-	0.85 [3.1]	-	-
OPI 4	3.4	3.0 / 2.1	2.6	0.06	1.3	-	0.75 [2.2]	-	-
CB-OPI 4	3.4	3.2 / 2.3	3.1	-	1.2	-	0.80 [2.3]	-	-
OPI 5	4.1	3.6 / 2.5	2.6	0.05	0.8	2.2	1.20 [2.9]	0.45 [1.1]	0.3-0.6
OPI 6	4.7	4.1 / 2.7	2.6	0.05	1.2	2.6	1.00 [2.1]	0.5 [1.0]	0.3-0.5
OPI 7	5.4	4.4 / 2.9	2.6	0.03	1.2	2.7	1.00 [1.9]	0.45 [0.8]	0.2-0.5
OPI 8	6.0	4.6 / 3.2	2.6	0.01	0.9	2.3	0.90 [1.5]	0.40 [0.7]	0.3-0.6
CB-OPI 8	6.0	4.6 / 3.4	2.6	-	1.1	2.5	0.80 [1.3]	0.35 [0.6]	0.3-0.5
OPI 9	6.7	4.9 / 3.6	2.6	0.00	1.0	2.0	1.00 [1.5]	0.35 [0.5]	0.3-0.5
OPI 10	7.3	5.3 / 4.0	2.6	0.00	0.9	2.6	0.95 [1.3]	0.40 [0.6]	0.3-0.5
CB-OPI 10	7.3	5.2 / 4.3	2.6	-	1.1	2.5	0.90 [1.2]	0.35 [0.5]	0.3-0.5

\*Molecular length was estimated with the Cambridge Scientific Chem3D software. Molecular length is the terminal H to S distance plus the Au-S bond length. It was assumed that Au-S bond length is 2.36 Å<sup>39</sup>.

†XPS data are underestimated because the intensity of photoelectrons from N-atoms is not considered in the calculation of film thickness.

‡The oxidation potentials were determined from lower edge of the oxidation peak of OPI wires referenced by ferrocenium/ferrocene (Fc<sup>+</sup>/Fc).

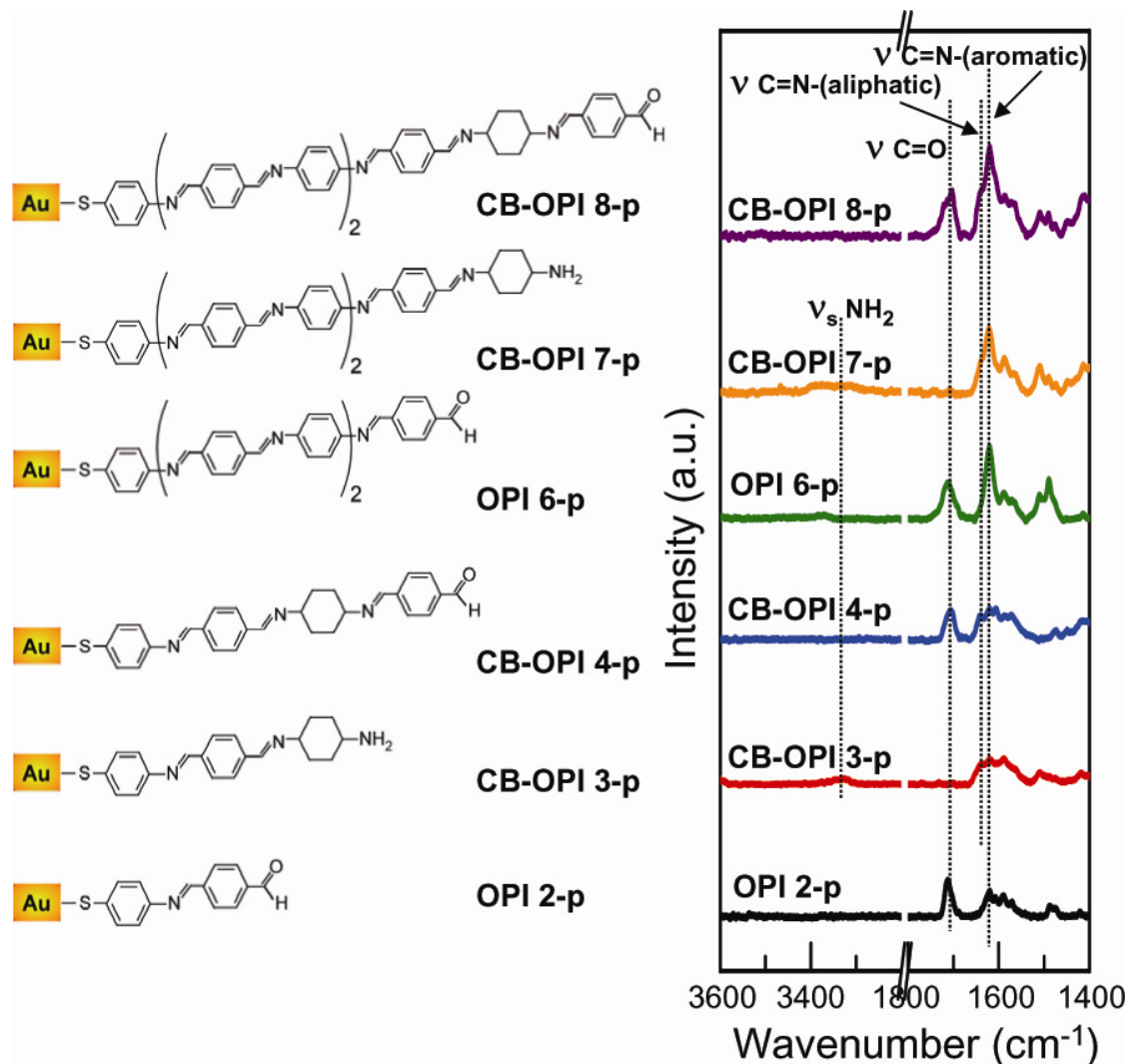


**Figure 4.3** Molecular structures (left) and RAIRS spectra (right) for the incorporation of a conjugation breaking unit (cyclohexyl group). Vertical dashed lines indicate positions of representative IR peaks. Sequential iminations with a cyclohexyl unit are proven by the presence of IR peaks of end-functional groups in the corresponding molecules. IR absorption for aliphatic imine stretching ( $1640\text{ cm}^{-1}$ ) next to cyclohexyl also appeared with incorporation of a cyclohexyl unit.

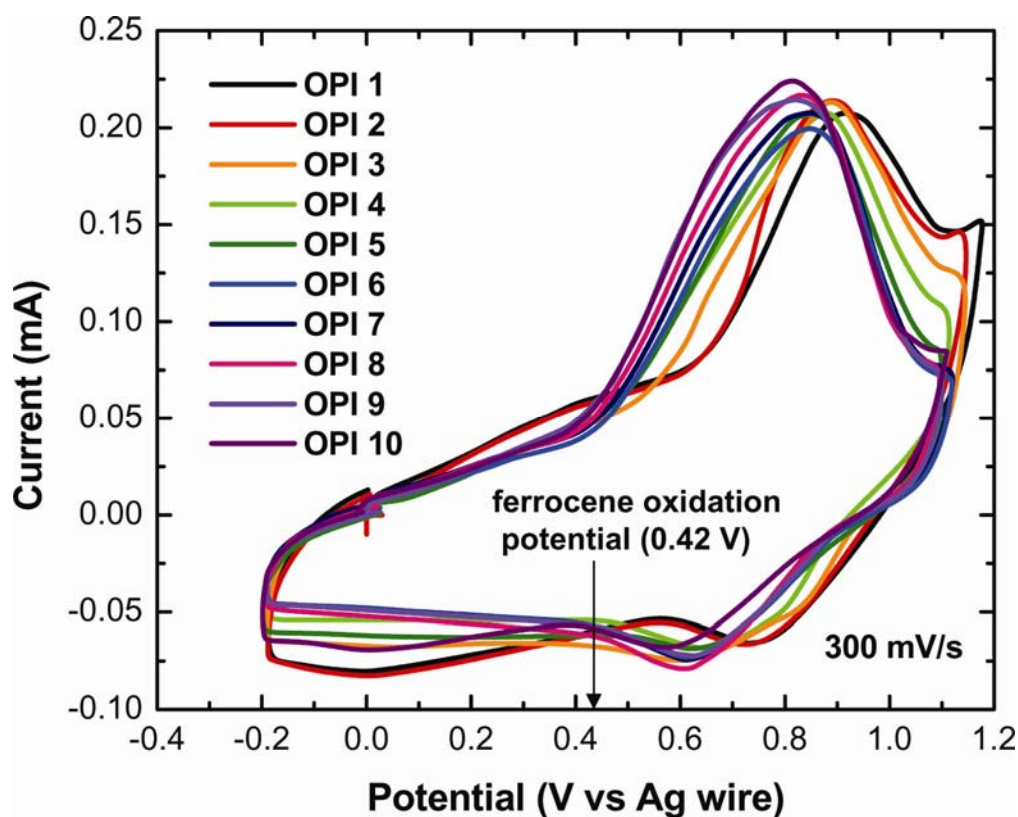


**Figure 4.4** Cyclic voltammograms of OPI wires. The reference and counter electrodes were Ag wire and Pt gauze, respectively. The scan rate was 300 mV/s.

### Electronic structure

The electronic structures of the wires were determined by UV/visible spectroscopy and UV photoelectron spectroscopy (UPS) experiments. UV/visible absorption spectra were taken of the molecular films on semi-transparent thin gold films using Beckman Coulter DU720 UV/visible spectrometer. 20 nm thick gold films were thermally deposited on a polystyrene UV cell. Molecular films were formed on the gold film in the same way described in the main text. Figure 4.5 shows the UV/visible absorption spectra for all OPI and CB-OPI wires, and their optical gaps obtained from the absorption edge are given in Table 4.1. As discussed in the main text, the absorption edge of OPI wires is red-shifted up to OPI 3 and remains constant for longer OPI wires because of the nonplanar conformation in the wire structure (see Fig. 4.5A). In addition,

the absorption features for CB-OPI wires in Fig. 4.5B reveal that the conjugation is broken over the cyclohexyl unit because the absorption edge of CB-OPI 3 and CB-OPI 4 is blue-shifted compared to OPI 3 and 4 wires, respectively. Absorption maxima of CB-OPI 8 and CB-OPI 10 are different from OPI 8 and OPI 10.

UPS spectra were also taken with He I ( $h\nu = 21.2$  eV) radiation incident at  $45^\circ$  from the sample normal to examine the electronic structure of OPI wires. Photoemitted electrons were collected at normal emission with a pass energy of 4.45 eV. All spectra were acquired at an applied bias of -7 V on the sample and the energy scale was referenced to the Fermi level of gold ( $E_F$ ). The intensities of the raw spectra were normalized at  $E_F$ . Figure 4.6 shows UPS spectra of OPI wires, CB-OPI wire and bare Au. We found similar  $E_F$ - $E_{HOMO}$  offsets for all OPI and CB-OPI wires ( $\sim 0.7$  eV).

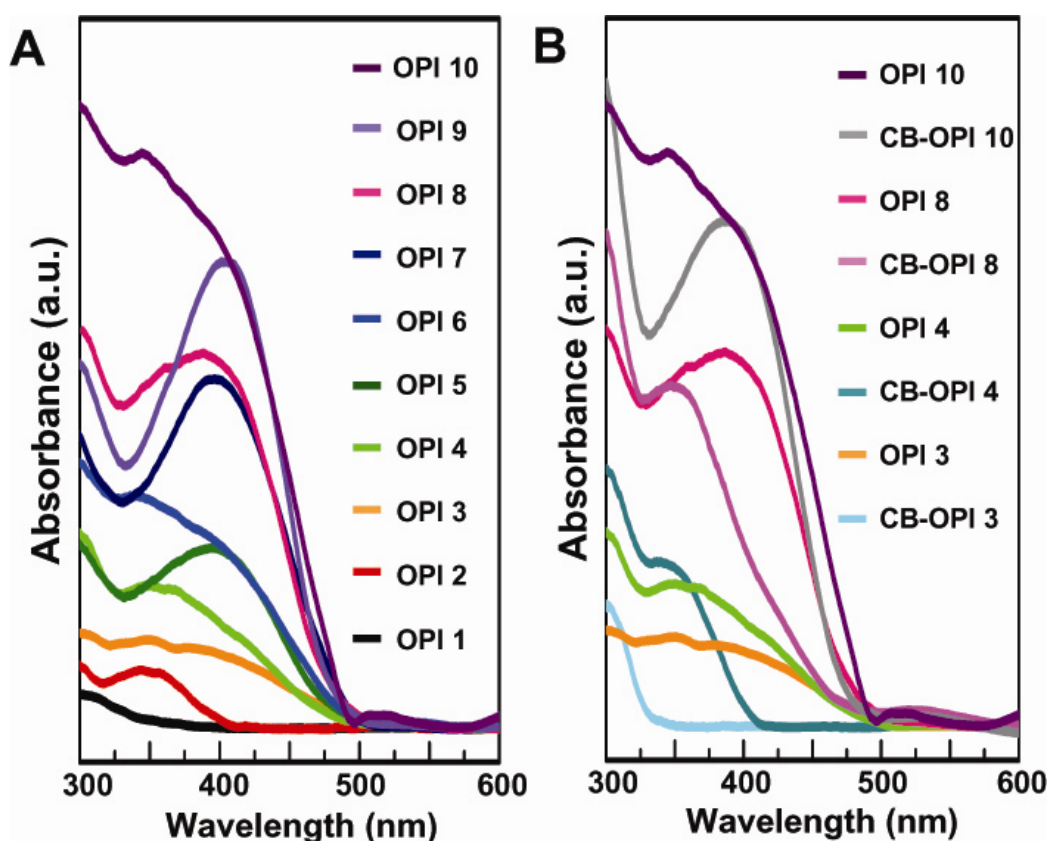


**Figure 4.5** UV/visible absorption spectra of (A) OPI wires and (B) CB-OPI wires.

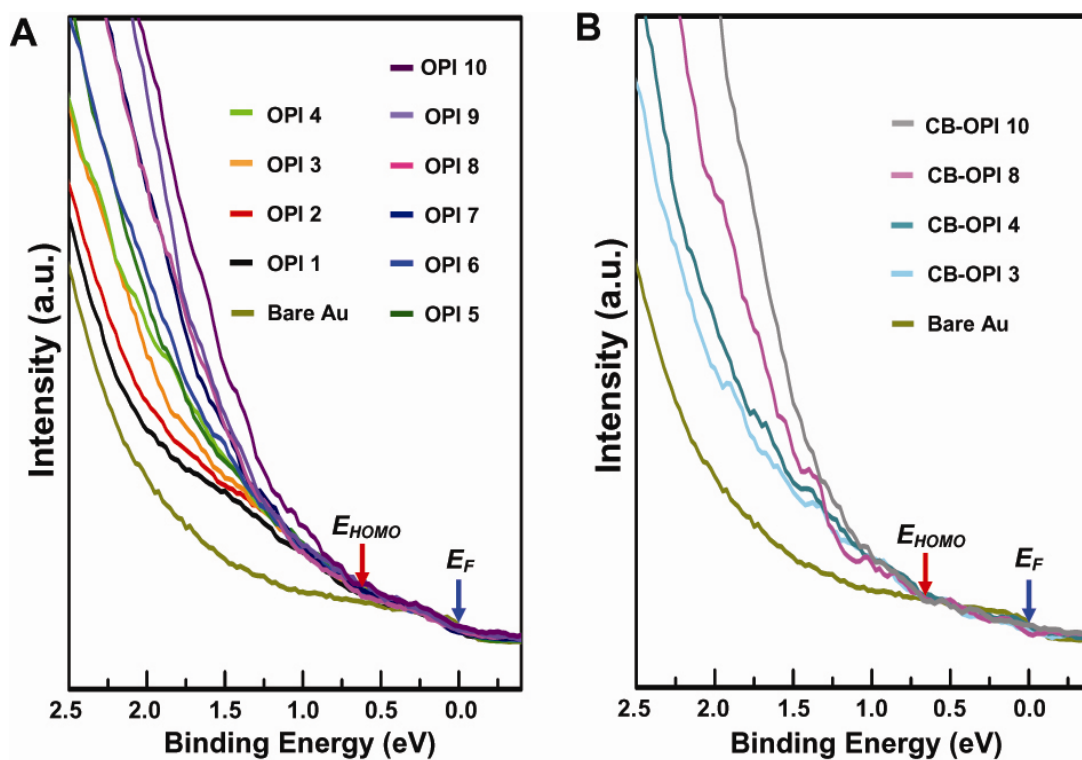


**Figure 4.6** UPS spectra of OPI wires (**A**) and CB-OPI wires (**B**) near the gold Fermi level ( $E_F$ ). The red arrows indicate the onset position of all UPS spectra, where  $E_{HOMO}$  lies.



**Table 4.2 Surface coverage and RMS roughness of OPI wires**

Monolayer	Surface Coverage ( $\Gamma$ )* ( $\times 10^{-10}$ mol/cm <sup>2</sup> )	RMS Surface $\dagger$ Roughness ( $\text{\AA}/\mu\text{m}^2$ )
OPI 1	2.5	2.8
OPI 2	3.0	3.2
OPI 3	3.8	3.8
OPI 4	4.4	4.6
OPI 5	4.4	3.1
OPI 6	5.3	4.0
OPI 7	5.2	5.4
OPI 8	5.5	6.5
OPI 9	5.7	4.5
OPI 10	5.6	4.3

\* measured by CV.

$\dagger$  measured by AFM and include the RMS surface roughness value ( $2.8 \text{\AA}/\mu\text{m}^2$ ) of flat, template-stripped Au substrate.<sup>41</sup>

#### **4.4 Results and Discussion**

OPI wires on gold substrates were prepared by a slight modification of a previously reported method.<sup>19</sup> Figure 4.7A shows the molecular structure of OPI wire precursors (OPI-p) and OPI wires, and synthetic routes. The growth of OPI wires begins with OPI 1-p, prepared by immersing gold substrates into 1 mM 4-aminobenzenethiol in absolute ethanol for 24 h. OPI-p wires were then grown via step-wise imination with alternate addition of benzene-1,4-dicarboxaldehyde and benzene-1,4-diamine, as shown in Fig. 4.7A. Each OPI-p wire terminated with  $-\text{NH}_2$  or  $-\text{CHO}$  groups was end-capped with benzaldehyde or aniline, respectively. The end-capping provided a consistent terminal group throughout the OPI series that facilitated reproducible electrical characterization. After each growth, both OPI-p and OPI monolayers were thoroughly rinsed with absolute ethanol, and then dried in a stream of  $\text{N}_2$ .

Both OPI-p and OPI monolayers were characterized extensively by ellipsometry, X-ray photoelectron spectroscopy (XPS), reflection-absorption Fourier transform infrared spectroscopy (RAIRS), and cyclic voltammetry (CV). Key results are summarized in Table 4.1 as well as Table 4.2. Monolayer thickness from ellipsometry and XPS measurements increases gradually as expected upon the repeated imination. From the difference between estimated wire length and the measured monolayer thickness, we conclude that the OPI wires are tilted with an angle increasing from 20–45 ° with respect to the surface normal as wire length increases. RAIRS data, shown in Fig. 4.7B (left), reveal the alternate appearance and disappearance of carbonyl stretches (1710 cm<sup>-1</sup>) and symmetric amine stretches (3350 cm<sup>-1</sup>) in OPI-p molecules verifying the imination mechanism and indicating near quantitative reaction of all exposed reactive endgroups. The intensity of imine stretching (1620 cm<sup>-1</sup>) and the benzene ring vibrational mode (1500 cm<sup>-1</sup>) increases with the number of repeat units, as expected. Complete end-capping was confirmed by the disappearance of the terminal group vibrational modes in Fig. 4.7B (right). Cyclic voltammograms (CV) of OPI wires are displayed in Fig. 4.4 and oxidation potentials and the estimated surface coverages for each OPI wire are compiled in Table 4.1 and 4.2, respectively. CV sweeps of the OPI wires show nearly identical surface coverage ( $2.5\text{--}5.5 \times 10^{-10}$  mol/cm<sup>2</sup>) over the entire set of wires. Evidently, packing density is not greatly affected by molecular length. Collectively, the surface characterization data indicate that high quality monolayers of OPI wires were prepared.

The transport characteristics of OPI wires were investigated using conducting probe atomic force microscopy (CP-AFM) (Fig. 4.8A), a technique that has been used to measure conduction in a variety of molecular systems.<sup>20-22</sup> Figure 4.8B displays a semilog plot of resistance ( $R$ ) versus molecular length ( $L$ ) for OPI wires. Each data point represents the average of 10  $I$ - $V$  traces. A clear transition of the length dependence of resistance is observed near 4 nm (OPI 5), indicating that the conduction mechanism is different in short (OPI 1–4) and long OPI wires (OPI 6–10). In short wires, the linear fit in Fig. 4.8B indicates that the data are well described by Eq. 4.1 for non-resonant tunneling. The  $\beta$  value is found to be 3 nm<sup>-1</sup>, which is within the range of  $\beta$  values of typical conjugated molecules.<sup>23, 24</sup>

For long OPI wires, there is a much flatter resistance versus molecular length relationship ( $\beta \sim 0.9 \text{ nm}^{-1}$ ). The extremely small  $\beta$  suggests that the principal transport mechanism is hopping as has been concluded in solution electron transfer studies of D-B-A systems.<sup>2, 11, 25</sup> In fact, a plot of  $R$  versus  $L$  (see inset) for long wires is linear, which is consistent with hopping and indicates that Eq. 4.1 does not apply for long wires. The change in transport mechanism apparent in the length dependent measurements is verified by the temperature dependence. Figure 4.8C shows that resistance for OPI 4 is independent of temperature from 246 to 333 K, as expected for tunneling.

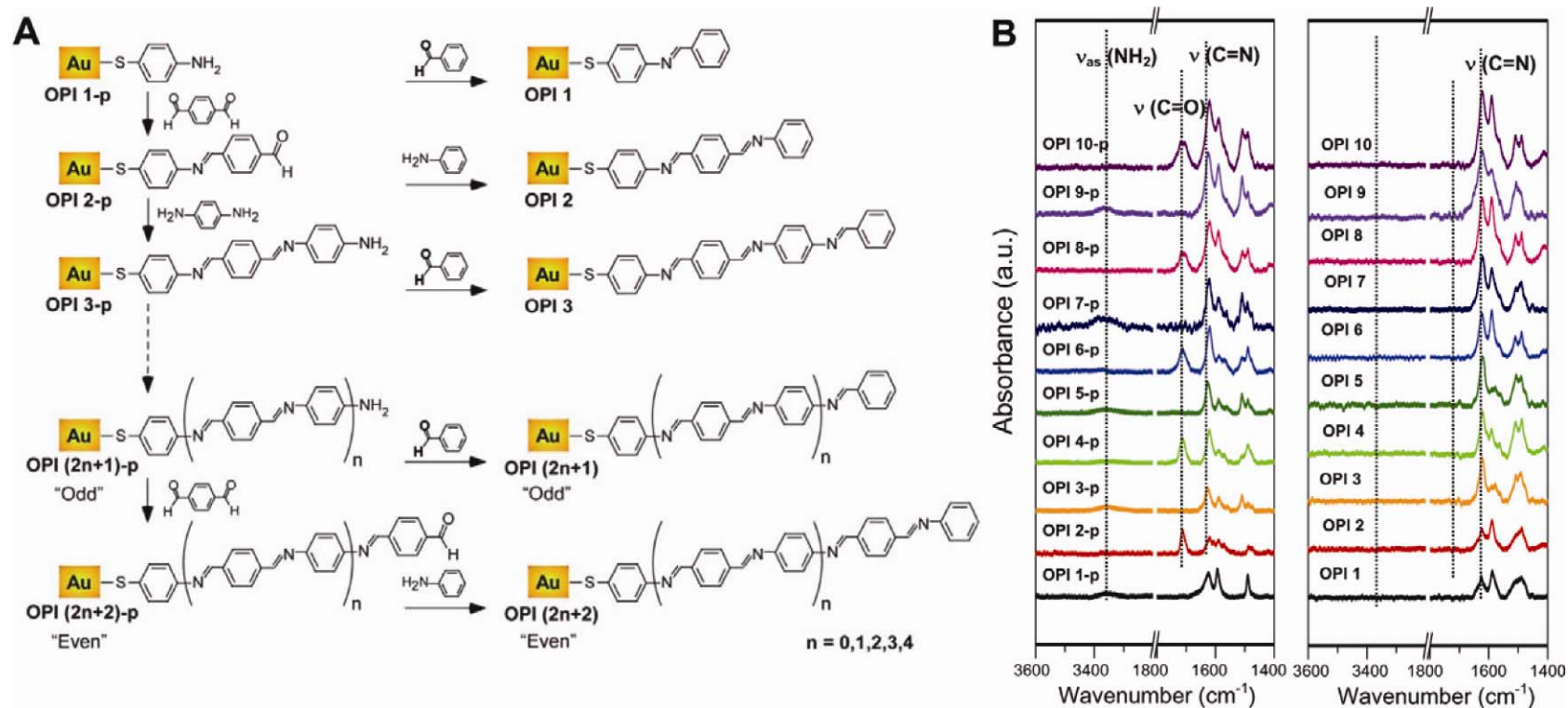


**Figure 4.7** (A) Molecular structure and synthetic route to OPI-p and OPI monolayers on gold substrates. (B) RAIRS spectra of OPI-p (left) and OPI monolayers (right). Vertical dashed lines indicate positions of symmetric amine stretches ( $\text{NH}_2$ ,  $3350 \text{ cm}^{-1}$ ), carbonyl stretches ( $\text{C}=\text{O}$ ,  $1710 \text{ cm}^{-1}$ ), and imine stretches ( $\text{C}=\text{N}$ ,  $1620 \text{ cm}^{-1}$ ). Peaks for  $\text{NH}_2$  and  $\text{C}=\text{O}$  appear in the uncapped OPI-p wires with odd and even numbers of repeat units, respectively.

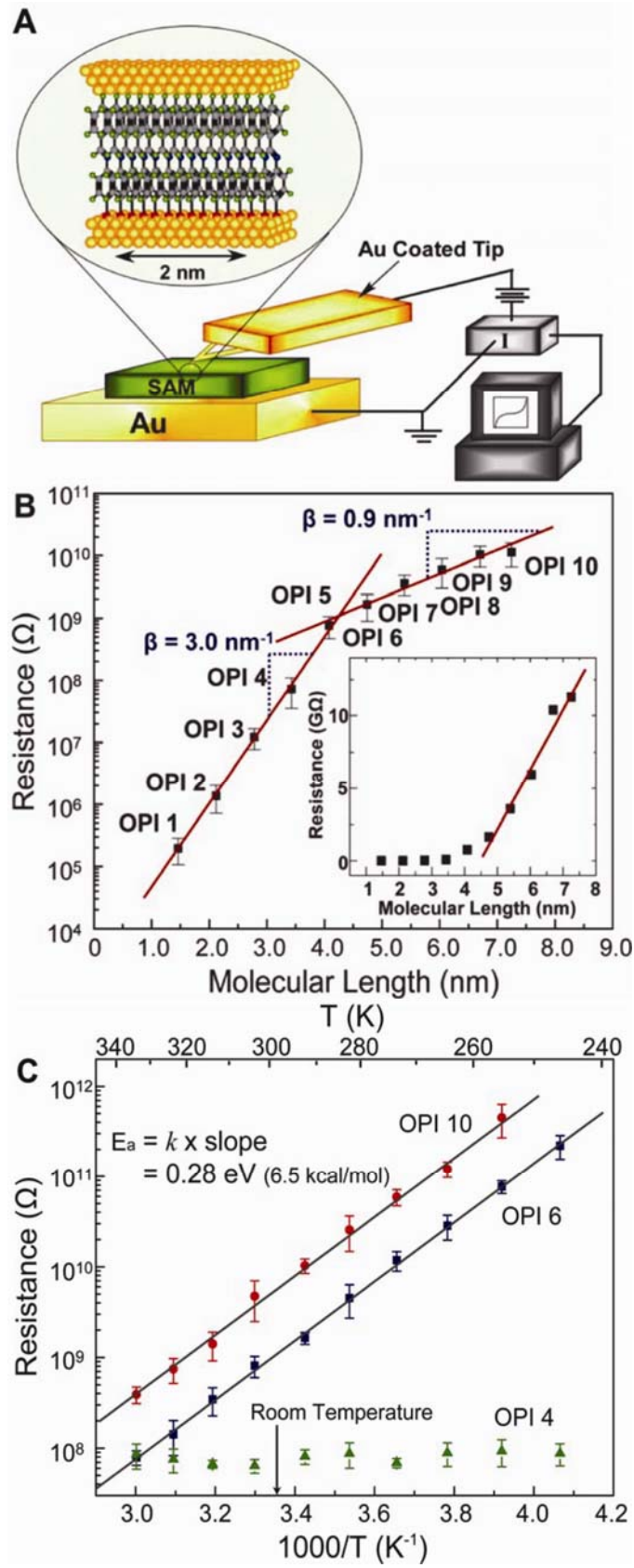


**Figure 4.8 (A)** Measurement of molecular wire resistance using conducting probe atomic force microscopy (CP-AFM). A gold coated tip is brought into contact with an OPI monolayer on a gold substrate. I-V traces are obtained over  $\pm 1.5$  V for OPI 3–10 and  $\pm 1.0$  V for OPI 1–2 at a load of 2 nN on the tip contact. **(B)** Semilog plot of R versus L for the gold/wire/gold junctions. Each data point is the average differential resistance obtained from 10 I-V traces in the range -0.3 to +0.3 V. Error bars represent one standard deviation. Straight lines are linear fits to the data according to Eq. 1. Inset: A linear plot of R versus L, demonstrating linear scaling of resistance with length for the long OPI wires. **(C)** Arrhenius plot for OPI 4, OPI 6, and OPI 10. Each data point is the average differential resistance obtained at six different locations of samples in the range -0.2 to +0.2 V. Error bars represent one standard deviation. Straight lines are linear fits to the data.

On the other hand, both OPI 6 and OPI 10 display strongly thermally activated transport, characteristic of hopping. The activation energies determined from the slopes of the data are identical at 0.28 eV (6.5 kcal/mol) for both OPI 6 and 10. Contact effects are not responsible for the activated transport, as straightforward calculation shows that the injection efficiency is  $> 99\%$ .<sup>26</sup> Collectively, the data in Fig. 4.8 indicate the conduction mechanism transitions from tunneling to hopping near 4 nm.

A key question concerns the nature of the hopping sites in the long wires and the origin of the 0.28 eV activation energy. An important point in this regard is that the ultraviolet (UV)-visible absorption data on OPI wire SAMs show that the conjugation does not extend over the entire wire. The optical gap ( $E_g$ ) reduces with molecular length up to OPI 3, and then remains constant at 2.6 eV for longer OPI wires.<sup>33</sup> This result indicates that the  $\pi$ -conjugation extends over three repeating units via the imine linkage and that longer wires contain weakly linked conjugated subunits. From prior work it is known that electronic delocalization is limited in aromatic oligoimines because of the non-zero dihedral angle between the benzene ring and the imine bonds, *i.e.*, the wire molecules are not flat and the  $\pi$ -conjugation is broken. Indeed, the activation energy for twisting of the phenyl rings has been measured to be 0.3 eV, in remarkable agreement with the activation energy measured in the junction transport experiments.

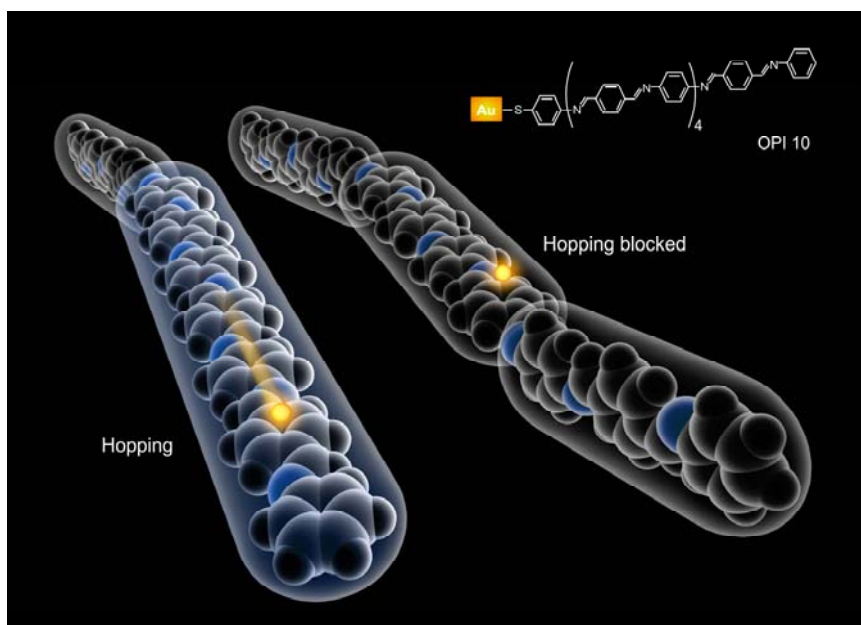


**Figure 4.9** Proposed cartoon for OPI 10. A charge (yellow ball) is localized at the conjugation subunit where three repeats are strongly coupled (right). Once molecular motions couples transiently the conjugation subunits, a charge can be driven down the wire (left).

A cartoon illustrating the proposed charge hopping process in OPI wires is shown in Fig. 4.9. The picture emerges that charge (likely holes) injected from the positive contact into the long OPI wires is localized to a subunit consisting of approximately three repeat units. Field-induced drift of the charge down the backbone requires that the dihedral angle between conjugated sub-units decrease to near  $0^\circ$ , a process that transiently extends the conjugation along the molecule and allows the charge to hop. This nuclear motion is thermally activated and concerted, involving rotation of the phenyl rings coupled with alteration of the C=N bond length. This physical model of conduction gated by torsional motion of conjugated subunits is very much consistent with prior

studies of electron transfer in D-B-A compounds, and it underscores the hugely important role of nuclear motion in charge conduction in molecular wires.

One can further check the consistency of this model by calculating the average residence time for charge on OPI wire and comparing that time to timescale associated with the torsional fluctuation. At + 0.2 V bias, the current through OPI 6 is  $2 \times 10^{-10}$  A. For this calculation, we take the number of molecules in the junction to be  $\sim 100$  so that the current per molecule is  $2 \times 10^{-12}$  A, which is approximately  $10^7$  electrons/second per molecule. This means average charge residence times are on the order of 0.1 microsecond, far slower than the period of the torsional mode ( $\sim 50$  fs), as expected.

To examine the sensitivity of conduction to the wire architecture, we designed conjugation-broken OPI wires (CB-OPIs) in which an aliphatic cyclohexyl group was inserted into the molecular backbone. To incorporate the cyclohexyl moiety, we performed the imination with 1,4-diaminocyclohexane at elevated temperature (40 °C) in pure ethanol for 24 h. The structure of CB-OPI wires and their low voltage resistances are shown in Fig. 4.10. For CB-OPI 3 and CB-OPI 4, the resistance is increased compared to OPI 3 and OPI 4, as expected, because the aliphatic cyclohexyl links raise the average tunneling barrier. However, for the longer CB-OPI 8 and CB-OPI 10 molecules, the resistance change from the corresponding OPI 8 and OPI 10 wires is considerably greater, nearly two orders of magnitude. Evidently, conduction in the long wires is much more sensitive to the presence of the cyclohexyl group than in the short wires, which also supports a difference in the charge transport mechanism. For hopping transport in the long wires, a large change in resistance is expected upon interrupting the conjugation. Ratner, *et al.*<sup>33, 34</sup> have calculated the site-to-site hopping probabilities for molecular wires and indeed a disruption in conjugation has a dramatic impact on electron transfer rates. On the other hand, tunneling is relatively insensitive to small perturbations in the conjugation of molecular bridges, as the tunneling rate reflects the *average* potential barrier of the bridge, not the barrier of the discrete cyclohexyl group alone. Thus, the conjugation blocking experiments confirm that conduction depends upon the bond architecture and they also support the conclusion that tunneling occurs in the short wires and hopping transport prevails in the long wires.



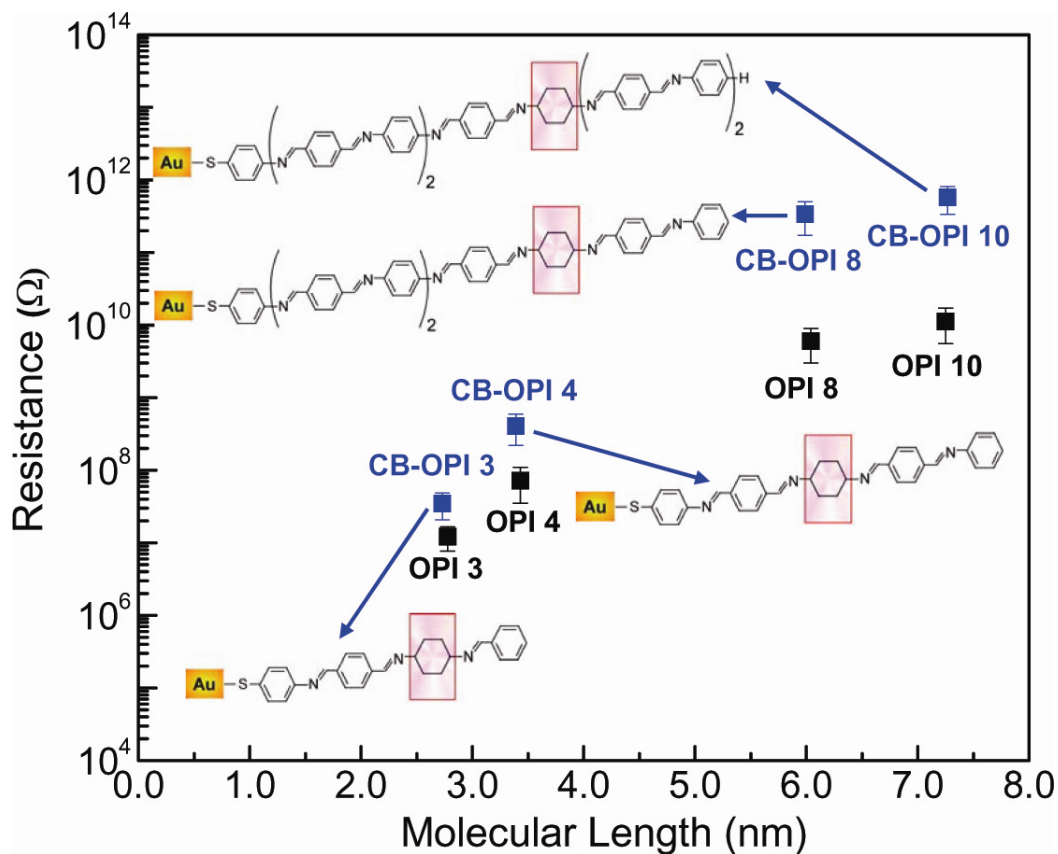


**Figure 4.10** Semilog plot of  $R$  versus  $L$  for gold/OPI/gold junctions and conjugation broken gold/CB-OPI/gold junctions. Each data point is the average differential resistance from 10  $I$ - $V$  traces in the interval  $-0.3$  V to  $0.3$  V. Error bars represent one standard deviation. The blue squares are the resistances of conjugation-broken OPI (CB-OPI) wires. Pink boxes indicate the position where conjugation is broken.

We have also carefully examined the voltage and electric field dependence of the  $I$ - $V$  characteristics, Fig. 4.11. The semilog plot of  $I$  versus  $V$  for OPI wires in Fig. 4.11A demonstrates that current decreases as wire length increases, in keeping with the resistance results shown in Fig. 4.8B. For the short wires (OPI 1–4), increasing molecular length yields large decreases in the current at all potentials. However, for the long wires (OPI 6–10), the log  $I$ - $V$  curves show smaller decreases in current with increasing length.

A plot of  $\log I$  versus electric field ( $E$ ) (see inset) reveals that the traces for the long wires collapse nearly on top of one another. This indicates that for the long wires transport is *field driven*, as expected for a hopping mechanism in which the electric field pushes the carriers along the molecules. On the other hand, for the short wires, the  $I$ - $E$  curves do not collapse on top of one another because tunneling is a *voltage driven* process.

A log-log plot of the  $I$ - $V$  characteristics facilitates more detailed analysis. Figure 4.11B displays  $\log I$  -  $\log V$  characteristics for OPI 4 and OPI 10, representative of the short and long wires. For OPI 4, there are two different transport regimes, labeled I and II; the transition occurs at 0.75 V. For OPI 10, the dependence is more complex with three identifiable transport regimes (I', II', III') and transitions at 0.40 V and 0.95 V.

The data for OPI 4 in Fig. 4.11B demonstrate that in regime I the current scales linearly with voltage. Linear  $I$ - $V$  behavior is expected for tunneling in the low bias regime. To a first approximation, the metal-wire-metal junction can be modeled as a simple trapezoidal tunneling barrier. In this case, the tunneling current at low bias is given by Eq. 4.4.

$$I \propto V \exp\left(-\frac{2d\sqrt{2m_e\phi}}{\hbar}\right) \quad (4.4)$$

where  $d$  is the barrier width (wire length),  $m_e$  is the electron effective mass, and  $\phi$  is the effective barrier height. At higher bias the electric field changes the shape of the tunneling barrier from trapezoidal to triangular.<sup>35</sup> In this case, the  $I$ - $V$  behavior can be described by the Fowler-Nordheim relationship:

$$\ln\left(\frac{I}{V^2}\right) \propto \frac{-4d\sqrt{2m_e\phi^3}}{3\hbar q} \left(\frac{1}{V}\right) \quad (4.5)$$

where  $q$  is the elementary charge.

The Fowler-Nordheim plot in Fig. 4.11C reveals a striking change in conduction behavior. For low voltages (Regime I) the current scales logarithmically with  $1/V$  as expected from Eq. 4.4, indicative of direct tunneling. Above the transition voltage  $V_{trans} = 0.75$  V (Regime II), the current scales linearly with  $1/V$  with a negative slope characteristic of field emission (Eq. 4.5). The transition point,  $V_{trans}$  is an estimate of the low voltage barrier height, and corresponds to the voltage where the slope of the OPI 4

data changes in Fig. 4.11B. The  $V_{trans}$  values for the other short OPI wires are listed in Table 1. The decrease of  $V_{trans}$  with length in short wires indicates that the estimated barrier height decreases as expected from the trend in oxidation potentials of OPI wires determined by cyclic voltammetry (see Table 4.1 and 4.2). Collectively, the data in Figs. 4.8-4.11 allow the conclusion that the transport mechanism in the short wires at low bias is direct (non-resonant) tunneling and transitions to field emission at higher bias.

We have carried out a similar analysis of the  $I$ - $V$  behavior for long wires, OPI 6-10. The Fowler-Nordheim plot for OPI 10 in Fig. 4D reveals three distinct regimes corresponding with regimes I', II', and III' in Fig. 4B. In the low bias regime I', the current scales linearly with voltage, which is consistent with ohmic hopping conduction. Linear scaling with  $V$  was taken as support for non-resonant tunneling in short wires in the discussion above (Eq. 4.1), but it is already clear that the low bias mechanisms are different for the long and short wires, and direct tunneling is not consistent with the dependence of resistance on length or temperature evident in Fig. 4.11B. Ohmic (field-driven) conduction is also linear in  $V$ , and requires that carriers be present in the wires. We propose that carriers are introduced in the long wires from the gold contacts, and that these carriers facilitate ohmic hopping conduction at low biases up to  $V_{II'}$ , the transition voltage from regime I' to II'.

The negative slope in the high voltage regime III' of Fig. 4.11D suggests that field emission may also occur in OPI 10 (similar results were obtained for OPI 6-9). From the slope in regime III' we calculated the emission barrier height ( $\phi_{FE}$ ) to be in the range of 0.3-0.5 eV assuming carrier effective mass ratios in the range 0.1-1.0, which are typical for molecular junctions.<sup>23</sup> This barrier height is in reasonable agreement with the 0.7 eV  $E_F$ - $E_{HOMO}$  offset. We also considered other possible transport mechanisms in the metal/wire/metal junction, such as Schottky emission at the contact, Poole-Frenkel emission in the wires, and space charge limited transport in the presence of traps.<sup>36,27</sup> However, we did not obtain reasonable values for extracted physical parameters with these other mechanisms (will discuss later). The estimated emission barrier heights for the other long OPI wires are also listed in Table 4.1. Regime II' is a transitional regime between ohmic conduction and field emission for OPI 10, and it may correspond to space charge limited conduction (SCLC), based on the slope of 2.6 in the  $\log I$  versus  $\log V$  plot

(Fig. 4.11B) and the slope of -3.5 in the  $\log I$  versus  $\log L$  plot at 0.7 V (inset in Fig. 4.11B).<sup>37,38</sup> Further work is necessary to conclusively establish the transport mechanism in this regime.

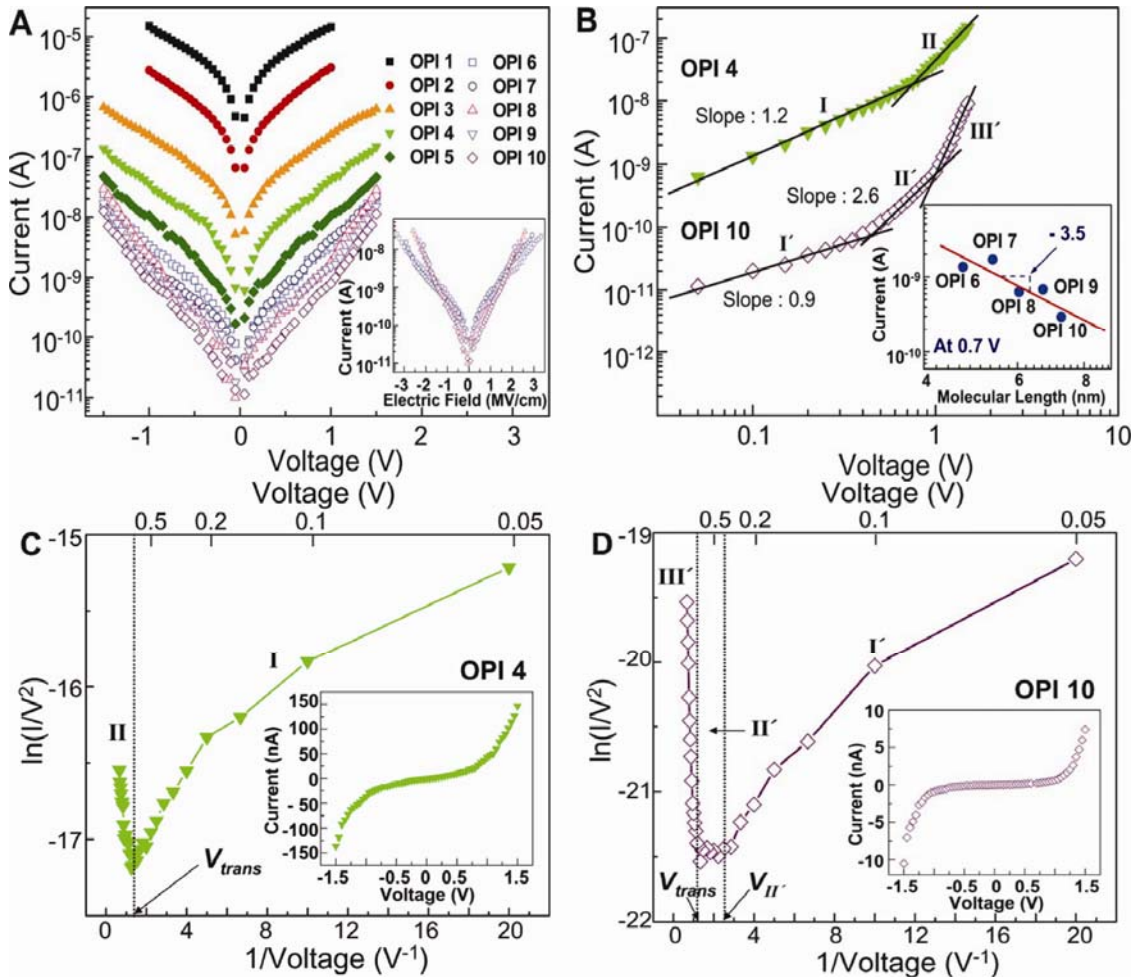


**Figure 4.11** (A) Semilog plot of the average current of 10  $I$ - $V$  traces for gold/wire/gold junctions. The inset is a semilog plot of  $I$  versus electric field ( $E$ ) for long OPI wires. (B) Log-log plot of the average of 10  $I$ - $V$  traces for the gold/OPI 4/gold and gold/OPI 10/gold junctions. Fits are shown in the different transport regimes. Inset: A log-log plot of  $I$  versus  $L$  obtained at 0.7 V for all long OPI wires, displaying the linear fit with a slope of -3.5 (0.7 V is the bias at which all long OPI wires are within regime II'). (C) Fowler-Nordheim plot for the OPI 4 data in (B). Two distinct regimes (I and II) are clearly observable with an inflection point at  $V_{trans}$ , indicating the switch from tunneling to field

emission. The inset displays the sigmoidal current-voltage curve on a linear scale. **(D)** Fowler-Nordheim plot for the OPI 10 data in (B). Three distinct regimes (I', II', and III') are evident. The inset shows the sigmoidal current-voltage curve.

### **Local Environment**

Although the transition in the transport mechanism is clearly apparent, a question still remains: is the increasing molecular length purely responsible for this transition? Selzer *et al.*<sup>47</sup> have carried out temperature dependent studies using two different platforms (single molecule vs. a monolayer), and have shown that the packing density or local environment of molecules alone can change the transport mechanism from tunneling to hopping. However, we have strong evidences that the local monolayer environment of OPI wires remains nearly identical even with changes in the length of wires or thickness of the SAMs. First, cyclic voltametry (CV) sweeps of the OPI wires show almost identical surface coverage over the entire set of wires. (see Table 4.1 and Fig. 4. 4) Furthermore, the RMS surface roughness taken from AFM images of long OPI wires are still on the order of the atomic level (~several Angstroms, see Table 4.2). Evidently, packing density and film disorder are not changed greatly by growing molecular wires. In addition, IR experiments indicate dense packing of OPI molecules. Figure 4.12 shows IR spectra of OPI 10 after exposure to different solvents including toluene, ethyl alcohol, and acetonitrile for 96 hours before the spectra were taken. Identical peak positions and relative intensities of the IR fingerprint absorptions support the conclusion that OPI wires are dense enough to prevent solvent molecules from penetrating the SAM, otherwise, the different polarities of the solvent molecules would affect the corresponding IR spectra. We also note that the measured activation energy for transport (0.28 eV) is the same for OPI 6 and OPI 10. This is very strong evidence that the transport mechanism is the same and not influenced by environment. Thus, the mechanistic transition shown in Fig. 4.8B is due to the lengthening of wires and not to an environmental effect.

### Further discussion on high field conduction mechanism for long OPI wires. (Regime III')

In order to analyze the  $I$ - $V$  behavior in regime III' of Fig 4.11B and 4D, we considered four mechanisms for basic high field conduction processes in insulators<sup>172-175</sup>: (i) field emission, (ii) space charge limited current (SCLC) in the trap filling limit, (iii) Poole-Frenkel conduction, and (iv) Schottky emission. We have concluded in the main text that field emission is an appropriate explanation for  $I$ - $V$  behavior in regime III'. In this section, we will discuss why the other mechanisms, ii-iv, cannot be operative.

In the case of space charge limited transport, current density  $J$  obeys Eq. 4.6.

$$J = \frac{8}{9} \varepsilon \varepsilon_o \mu \frac{V^2}{L^3} \Theta \quad (4.6)$$

where  $\varepsilon$  is the dielectric constant,  $\varepsilon_o$  is the permittivity,  $\mu$  is the charge mobility,  $L$  is the molecular length of wire, and  $\Theta$  is the ratio of free to trapped charge with assumption that  $\mu$  is independent of electric field. When enough carriers are injected to fill all the traps, there is an abrupt increase of current at  $V_{TFL}$ , given by.

$$V_{TFL} = \frac{qN_t L^2}{2\varepsilon \varepsilon_o} \quad (4.7)$$

where  $N_t$  is the number of traps. We extracted  $N_t$  for the OPI wires from Eq. 4.7 by assuming that  $V_{TFL}$  was equal to  $V_{trans}$ ; we also assumed that  $\varepsilon$  is 3.5 for OPI wires.<sup>52</sup> The extracted value for  $N_t$  is  $7.0$ – $17.3 \times 10^{17}/\text{cm}^3$  for all long OPI wires. However, this trap concentration corresponds to less than 1 trap per junction ( $\sim 25\text{nm}^2$ ) on average. This suggests that trap-filling in the SCLC regime cannot be the reason for the change in  $I$ - $V$  behavior between regime II' and III'.

In the case of Poole-Frenkel conduction,<sup>48</sup> current density  $J$  is given by Eq. 4.8.

$$J \propto E \exp \left[ \frac{-q(\phi - \sqrt{qE/\pi\varepsilon\varepsilon_o})}{kT} \right] \quad (4.8)$$

where  $\phi$  is the barrier height for carrier emission, and  $T$  is temperature. Poole-Frenkel conduction originates from field-dependent thermionic emission of carriers within the bulk (in this case, the wires). We made a plot of  $\ln(J/E)$  against  $E^{1/2}$  and extracted the dielectric constant from its slope.  $\varepsilon$  is found to be 13.8–54.8, which is much larger than

the dielectric constant of phenyleneimine molecule, 3.5.<sup>52</sup> Note that dielectric constants in nanoscopic junctions should remain constant or be even lower than in bulk as reported previously.<sup>53-55</sup> The extremely large value of the extracted dielectric constant suggests that Pool-Frenkel conduction is inappropriate to explain the high field  $I$ - $V$  behavior.

Finally, Schottky emission<sup>50,51</sup> is thermionic emission from a metal electrode into the bulk (the wires in this case). Current density is given by Eq. 4.9.

$$J = A^* T^2 \exp \left[ \frac{-q(\phi - \sqrt{qE/4\pi\epsilon\epsilon_0})}{kT} \right] \quad (4.9)$$

where  $A^*$  is the effective Richardson constant. The dielectric constant was extracted from the slope of a semilog plot of current density versus square root of electric field ( $\ln J$  versus  $E^{1/2}$ ) and found to be 3.8–6.4 which is reasonable. However, if barrier heights are considered to be equal to the  $E_F$ - $E_{\text{HOMO}}$  offset, 0.7 eV (see Fig. 4.5), the extracted effective Richardson constant is 4.6–104  $\times 10^{10}$  A/cm<sup>2</sup>K<sup>2</sup>, which is much greater than the typical Richardson constant, 120 A/cm<sup>2</sup>K<sup>2</sup>. Therefore, this mechanism is not responsible for the  $I$ - $V$  behavior in the regime III', which is also consistent with our prior conclusion that transport is not contact limited.

In summary, we have measured DC electrical conduction in a set of conjugated molecular wires having systematically controlled lengths between 1.5 and 7.3 nm. At low bias voltages, we observed the predicted transition from tunneling to hopping transport for molecular lengths  $> 4$  nm. We also demonstrated that hopping conduction is very sensitive to the bond architecture of the wires, opening opportunities to manipulate wire resistance precisely and to explore further the connection between chemical bonding and electrical transport. At high biases, field emission obtains in both short and long wires. Overall, length dependent molecular conduction experiments provide significant opportunities to improve fundamental understanding of electrical transport in conjugated molecules, supporting both the development of molecular electronics and the physical description of transport in conjugated polymer films.

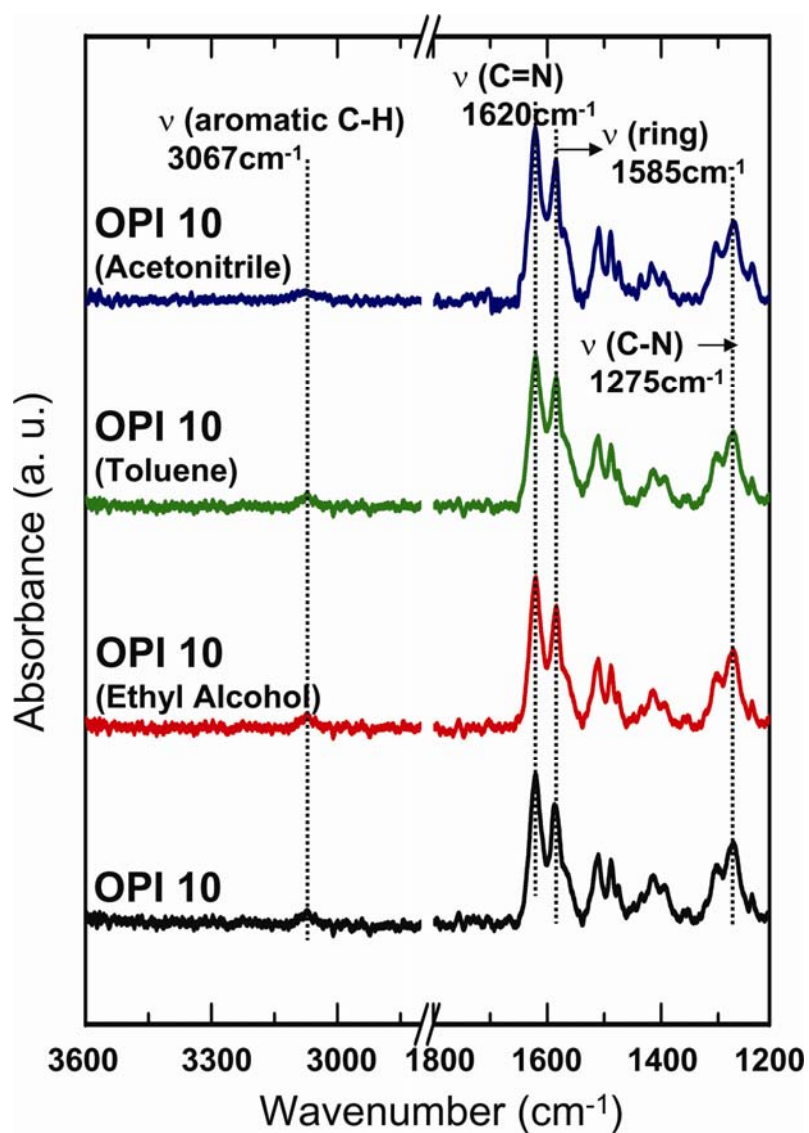


**Figure 4.12** Comparison of IR spectra of OPI 10 (black) and OPI 10 which was exposed in ethyl alcohol (red), toluene (green), and acetonitrile (blue) for 96 hours. Vertical dashed lines indicate positions of aromatic C-H stretches ( $3067\text{ cm}^{-1}$ ), imine stretches (C=N,  $1620\text{ cm}^{-1}$ ), ring stretches ( $1585\text{ cm}^{-1}$ ), and aromatic C-N stretches ( $1275\text{ cm}^{-1}$ ).



## 5 OligoNaphthaleneFluorenelmine (ONI) Wires

### 5.1 Abstract

We report the electrical transport characteristics of conjugated oligonaphthalenefluoreneimine (ONI) wires having systematically varied lengths up to 10 nm. Using aryl imine addition chemistry, ONI wires were built from gold substrates by extending the conjugation length through imine linkages between highly conjugated building blocks of alternating naphthalenes and fluorenes. The resistance and current-voltage characteristics of ONI wires were measured as a function of molecular length, temperature, and electric field using conducting probe atomic force microscopy (CP-AFM). We have observed a transition in direct current (DC) transport from tunneling to hopping near 4 nm as previously established for oligophenyleneimine (OPI) wires. Furthermore, we have found that long ONI wires are less resistive than OPI wires. The single-wire conductivity of ONI wires is  $\sim 1.8 \pm 0.1 \times 10^{-4}$  S/cm, a factor of  $\sim 2$  greater than that of OPI wires, and consistent with the lower transport activation energy ( $\sim 0.58$  eV versus 0.65 eV or 13 versus 15 kcal/mol). Quantum chemical calculations reveal that charge is preferentially localized on the fluorene sub-units and that the molecules are substantially twisted. Overall, this work confirms that imine addition chemistry can be used to build molecular wires long enough to probe the hopping transport regime. The versatility of this chemistry, in combination with CP-AFM, opens up substantial opportunities to probe the physical organic chemistry of hopping conduction in long conjugated molecules.

### 5.2 Introduction

Understanding electrical conduction in molecules is a long-standing goal in chemistry that is motivated by the importance of inter- and intramolecular electron transfer in biological processes (*e.g.*, photosynthesis and enzyme catalysis)<sup>176, 177</sup> and also by emerging applications of conjugated molecular films in electronic devices<sup>18</sup> such as transistors,<sup>61, 178, 179</sup> diodes,<sup>6, 180, 181</sup> and sensors.<sup>99, 182</sup> The most direct way to probe

conduction in molecules is to connect them between electrodes so that their current-voltage ( $I$ - $V$ ) characteristics can be recorded directly, a strategy that is clearly challenging because of the nanoscopic dimensions of molecules and the need for reliable chemistry to orient and fix the molecules in place. Nevertheless, several reliable techniques for making metal, semiconductor, or conducting polymer contacts to molecules have been developed over the last decade.<sup>17, 21, 22, 29, 183-187</sup> The development of these methods has created unprecedented opportunities for detailed, systematic examination of structure-transport relationships in molecules, *e.g.*, the role of bond architecture,<sup>23, 25, 188</sup> molecular length,<sup>25-27, 33</sup> and contact chemistry<sup>38-41, 189-191</sup> in molecular conduction.

To date, the majority of measurements on molecular junctions have been made in the direct tunneling regime. That is, the molecules spanning the inter-electrode gap are short enough that electrons tunnel directly from one contact to the other. The efficiency (length dependence) of this tunneling process depends on the architecture of the molecular backbone, and there are many intriguing effects that remain to be resolved concerning the role of the contacts, the electronic structures of the molecules, and the influence of intermolecular interactions. However, it is also interesting to consider the role of molecular structure in the *hopping regime*, that is, in situations where molecules are long enough that direct electrode-to-electrode tunneling is not possible and instead charge must be injected onto the molecular backbone and driven along the molecule by the applied electric field (see Figure 5.1). Hopping conduction is a principal charge conduction mechanism in thin films of conjugated organic molecules employed in devices.<sup>192</sup> Consequently, a richer understanding of the microscopic hopping conduction process along individual conjugated “molecular wires” may ultimately aid efforts to make better polymer semiconductors for applications in organic solar cells,<sup>9, 10</sup> thin film transistors,<sup>14, 15</sup> and light emitting diodes.<sup>11, 12</sup> Transport in the hopping regime at nanoscopic length scales is almost entirely unexplored because of the difficulties associated with contacting sufficiently long conjugated molecules.

Recently, we<sup>33</sup> and others<sup>120, 121</sup> have shown that it is possible to build long conjugated molecular wires attached to metal electrodes and to probe direct current (DC) transport as a function of length. In our work, we employed aryl imine addition chemistry to build oligophenyleneimine (OPI) wires up to 7 nm in length. In principle, an attractive

feature of the aryl imine chemistry is that it is adaptable to other types of molecular building blocks, affording opportunities to examine wire conduction as a function of precisely controlled chain architecture.

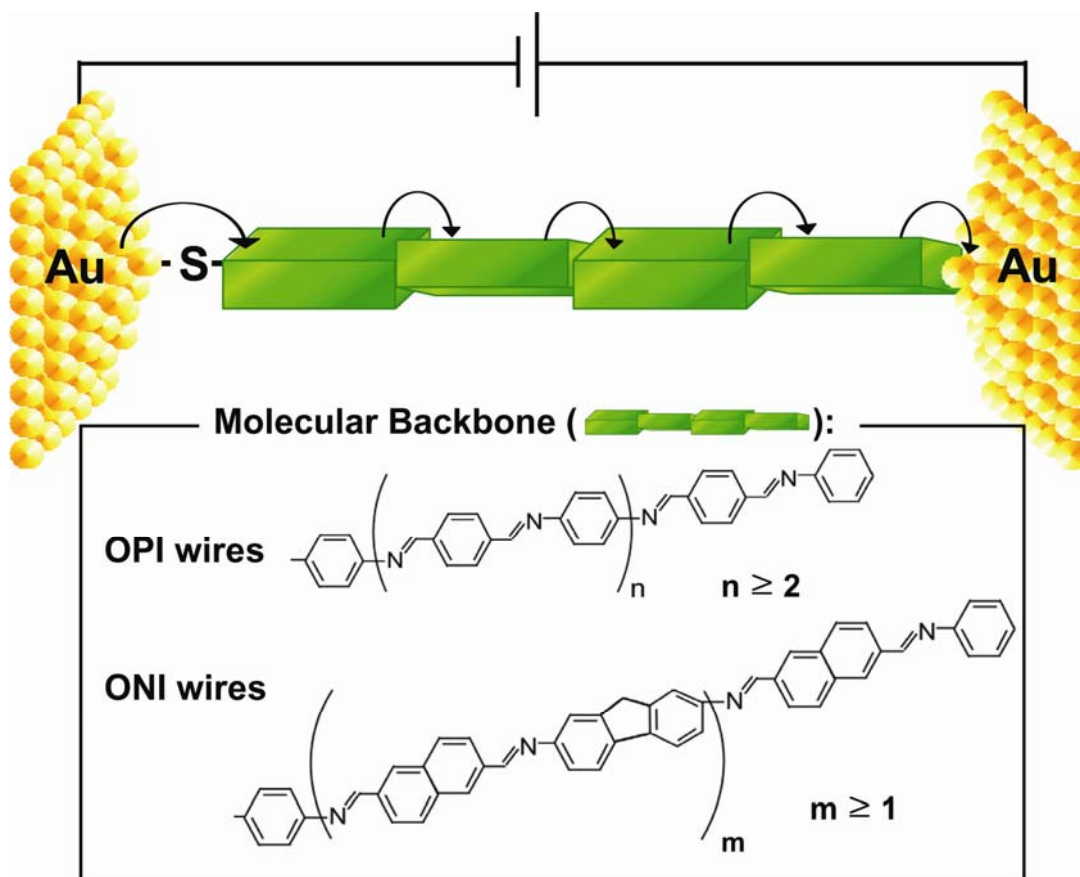


**Figure 5.1** Schematic representation of hopping transport in a metal-molecule-metal junction (top) and structures of OPI and ONI wires (bottom). Green rectangular boxes represent conjugated sub-units (local hopping sites) for charge carriers (electrons or holes). Curved arrows represent charge hopping over thermal barriers between local sites. In long wires, where tunneling is suppressed, hopping transport can be the principal transport mechanism (OPI,  $n \geq 2$  and ONI,  $m \geq 1$ ). The charge conduction process can be viewed as a series of discrete steps involving first injection of charge into the molecular orbitals, field-induced hopping of the charge carrier down the length of the molecule, and finally extraction of the charge into the receiving contact.

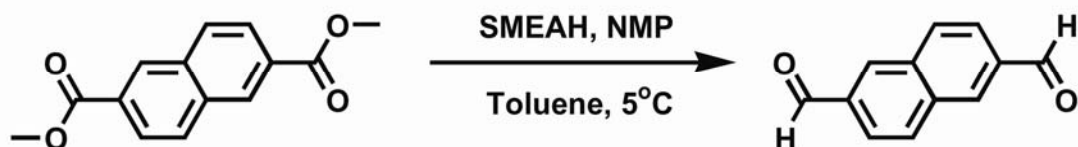
Here we have taken the next steps in this direction by demonstrating that the imine addition chemistry can be employed to assemble wires from larger conjugated molecular building blocks based on naphthalene dialdehydes and fluorene diamines. The resulting oligonaphthalene-fluoreneimine (ONI) wires are longer than the OPI wires (the structure is shown in Figure 5.1); we have achieved wires up to 10 nm in length, though our data suggest that longer wires could be grown. Using conducting probe atomic force microscopy (CP-AFM) to measure the  $I$ - $V$  characteristics of the wires, we observed a clear change in the transport mechanism from tunneling to hopping as a function of ONI wire length, consistent with prior studies of electron transfer in solution,<sup>2, 75, 77, 193</sup> and our previous report on OPI wires.<sup>33</sup> The change in mechanism is manifested by self-consistent changes in the length, temperature, and electric field dependence of the  $I$ - $V$  characteristics. To our knowledge the ONI wires described here are the longest wires to date to be examined systematically in terms of length, temperature, and field dependence of conduction. In addition, we show that in some respects the ONI wires are a better system for transport studies than the original OPI wires. Specifically, the ONI wires grow perpendicular to the gold substrate, which lessens the uncertainties regarding intermolecular hopping in the conduction path. We also describe detailed quantum chemical calculations of the structure and charge distributions in the ONI wires in an effort to understand the key geometrical aspects of the wire architecture and the nature of the polaronic charge carriers. Overall, the current work demonstrates that the imine synthesis chemistry is a general approach to building long wires with different molecular sub-units. This versatile chemistry, in combination with a simple and reproducible measurement method (CP-AFM), opens new opportunities to carefully examine the relationship between wire conductivity and molecular architecture in the hopping regime.

### **5.3 Experimental**

**Materials** Gold nuggets (99.999% pure) were purchased from Mowrey, Inc. (St. Paul, MN). Evaporation boats and chromium evaporation rods were purchased from R. D. Matthis (Long Beach, CA). Silicon (100) wafers were purchased from WaferNet (San Jose, CA). Contact mode AFM tips (DNP or NP silicon nitride probes) were purchased

from Veeco Instruments (Camarillo, CA). Absolute ethanol was purchased from Fisher Scientific.

**Synthesis of Molecular Building Blocks** Fluorene-2,7-diamine (FDA) was purchased from Aldrich and naphthalene-2,6-dicarboxaldehyde (NDC) was synthesized as in the literature<sup>194</sup> (Scheme 5.1). Compound was a light yellow solid, yielding 72%.



**SMEAH: Sodium bis(2-methoxyethoxy) aluminium hydride 65% in toluene**

**Scheme 5.1** Synthetic route for naphthalene-2,6-dicarboxaldehyde.

**Growth and Characterization of Molecular Wires** The Au substrates were 1000 Å thick films on silicon (with a 50 Å Cr adhesion layer) prepared in a Balzers thermal evaporator at a rate of 1.0 Å/s at a base pressure of  $\leq 2 \times 10^{-6}$  Torr. The metal films were immersed for 18-24 h in 10 ml of 1 mM solutions of 4-aminothiophenol (ATP) in argon purged absolute ethanol. After removing the sample from the solutions and immersing with absolute ethanol for a half hour to get rid of physisorbed molecules, the sample was immersed in 10 mM of NDC solution in absolute ethanol for 24 hours at 40 °C to ensure the complete formation of imine bonds. The sample was then immersed in absolute ethanol for 1 hour, and the same procedure was followed in 10 mM of FDA solution in absolute ethanol. Wire molecular lengths were controlled with the number of the alternating additions of NDC and FDA on Au substrates. Odd and even ONI wires were end-capped with benzaldehyde and aniline, respectively. All ONI wires were rinsed with absolute ethanol and dried under a stream of N<sub>2</sub> before all measurements.

ONI wires were characterized by ellipsometry, X-ray photoelectron spectroscopy (XPS), reflection-absorption Fourier transform infrared spectroscopy (RAIRS), and cyclic voltammetry. Ellipsometry measurements were carried out on a VASE spectroscopic ellipsometer (J. A. Woollam Co., Inc.). Measurements of the polarization angles ( $\Psi$  and  $\Delta$ ) were taken as a function of wavelength ( $\lambda$ ) between 600 and 1000 nm at

an incident angle of 65°. The indices of refraction ( $n(\lambda)$ ) and extinction coefficients ( $k(\lambda)$ ) of the Au-coated substrates were determined by measurement of the polarization angles prior to monolayer deposition and wire growth. The instrument software converted these values to  $n(\lambda)$  and  $k(\lambda)$  of Au films and saved them as a material file. After monolayer formation and wire growth on Au substrates, the polarization angles were measured again and the film thicknesses were determined by a built-in algorithm. The  $n(\lambda)$  and  $k(\lambda)$  of the SAMs were assumed to be 1.45 and 0, respectively, over the 600–1000 nm wavelength range.

XPS spectra were taken on a Perkin-Elmer Phi 5400 spectrometer with a Mg K $\alpha$  X-ray source (1253.6 eV) using a hemispherical analyzer in an ultrahigh vacuum ( $< 10^{-9}$  Torr) system. The X-ray anode was operated at 200 W, and the analyzer was set at a pass energy of 89.45 eV for survey scans and 17.9 eV for high-resolution scans. The binding energy scales were referenced to the Au<sub>4f7/2</sub> peak (84.0 eV). The monolayer thickness was calculated using the relative intensities of the Au<sub>4f</sub> and C<sub>1s</sub> peak and by using a hexadecanethiol SAM on Au as a reference ( $d = 1.86$  nm). As we will discuss later, similar surface coverages ( $\sim 4 \times 10^{-10}$  mol/cm<sup>2</sup>)<sup>195</sup> of both SAMs allow us to use a hexadecanethiol SAM as a reference in the estimation of ONI monolayer thickness. Assuming the same attenuation length of gold ( $\lambda_{Au} = 3.46$  nm) and carbon ( $\lambda_C = 3.02$  nm) photoelectrons for the reference and wire monolayers, calculation based on Equation 5.1 yielded the thickness.<sup>169, 196, 197</sup>

$$\frac{\frac{I_C}{I_{Au}}(sample)}{\frac{I_C}{I_{Au}}(reference)} = \frac{\left\{1 - \exp\left(-\frac{d_{sample}}{\lambda_C}\right)\right\} \exp\left(-\frac{d_{reference}}{\lambda_{Au}}\right)}{\exp\left(-\frac{d_{sample}}{\lambda_{Au}}\right) \left\{1 - \exp\left(-\frac{d_{reference}}{\lambda_C}\right)\right\}} \quad (5.1)$$

where  $I_C$  = the intensity of C<sub>1s</sub> peaks,  $I_{Au}$  = the intensity of Au<sub>4f</sub> peaks, and  $d$  is the thickness. The estimated length and film thickness measured by ellipsometry and XPS for all ONI wires are shown in Figure 5.3.

RAIRS was taken with a Nicolet Series II Magna-IR System 750 FTIR with a Harrick Seagull accessory for grazing angle specular reflectance measurements. The infrared beam was incident at 84° with respect to the surface normal. A total of 2000 scans were collected at 1.0 cm<sup>-1</sup> resolution. RAIRS was used for monitoring step-wise

mination, as shown in Figure 5.2b. Cyclic voltammetry (CV) experiments were undertaken to determine the redox states of ONI wires and to measure surface coverage. In these experiments, a three-neck electrochemical cell was used. A clean O-ring (1.0 cm diameter) surrounding a hole in the bottom of the cell was placed between the cell and a monolayer-coated Au substrate, which acted as the working electrode. The cell was filled with 0.2 M tetrabutylammonium hexafluorophosphate ( $\text{Bu}_4\text{NPF}_6$ ) in purified acetonitrile which was deoxygenated by three cycles of freeze-pump-thaw treatments. A Pt wire was used as the counter electrode and the cell was referenced to Ag wire. Prior to examining the monolayer oxidation potentials, the system was calibrated to the ferrocene oxidation potential. For each monolayer, the scan was recorded at a sweep rate of 300 mV/s and the CV curves were reproducible and stable to electrochemical cycling within the range of -1.0 – +1.5 V vs. Ag wire. In addition, the surface coverage ( $\Gamma$ ) was determined according to Equation 5.2:<sup>33</sup>

$$\Gamma = \frac{Q}{nFA} \quad (5.2)$$

where  $Q$  is the charge injected into the SAM,  $n$  is the number of electrons involved in the electron-transfer process ( $n$  is taken to be 1),  $F$  is the Faraday constant, and  $A$  is the surface area of the monolayer examined, that is, the area inside of the O-ring.  $Q$  was obtained by integrating the area under the forward sweep of the cyclic voltammogram using the first oxidation wave for each wire.

**Determination of Molecular Energy Levels** The electronic structures of ONI wires were determined by UV/visible spectroscopy and UV photoelectron spectroscopy (UPS) experiments. UV/visible absorption spectra were taken of the molecular films on semi-transparent thin Au films using a Beckman Coulter DU720 UV/visible spectrometer. 20 nm thick Au films were thermally deposited on a polystyrene UV cell. Molecular films were formed on the Au film in the same way described above. Figure 5.5 shows the UV/visible absorption spectra for all ONI wires, and their optical gaps obtained from the absorption edge are given in Table 5.1.

UPS spectra were taken with He I ( $h\nu = 21.2$  eV) radiation incident at  $45^\circ$  from the sample normal to examine the electronic structure of ONI wires. Photoemitted electrons were collected at normal emission with a pass energy of 4.45 eV. All spectra

were acquired at an applied bias of -7 V on the sample and the energy scale was referenced to the Fermi level of Au ( $E_F$ ). The intensities of the raw spectra were normalized at  $E_F$ .

**Electrical Measurements.** Molecular junctions were formed by bringing an Au-coated tip into contact with a wire SAM. These experiments were performed with a multimode AFM from Veeco Instruments in a glove box ( $O_2 < 8$  ppm). 2 nN load force was used to make a soft contact. Au-coated tips were prepared as reported previously.<sup>119</sup> The room temperature  $I$ - $V$  characteristics were examined up to  $\pm 1.5$  V for the entire set of ONI wires. The resistance was determined from the linear  $I$ - $V$  relationship within the range of  $\pm 0.1$  V. Three Au-coated AFM tips having a radius of  $\sim 50$  nm were used for the measurements, each of which gave the same resistance value for tunneling through an octanethiol SAM (an effective calibration standard). The three tips were used separately to examine three sets of wires: ONI 1–3 (tip 1), ONI 3–7 (tip 2), and ONI 7–10 (tip 3). Note that ONI 3 and 7 were each measured with two different tips to confirm that the same resistances were obtained. The number of molecules in each junction was estimated from the size of the tip radius and the wire surface coverage to be  $\sim 100$ .<sup>85</sup>

Variable temperature measurements of the ONI wire resistances were performed with an environmentally controlled Molecular Imaging PicoScan/PicoSPM. We have checked that the tunneling current of the octanethiol SAM remains constant within  $\pm 10\%$ <sup>27</sup> from a setpoint temperature of  $-30$  °C (243 K) to room temperature at  $< 5\%$  relative humidity. Two different sample stages, a normal heating stage and a peltier cooling stage, were used to vary temperature above and below room temperature, respectively. Silver paste was painted at the edge of each sample to make thermal contact between the sample and stage. The measured temperatures on the samples were consistent with the setpoint temperatures. The resistances shown in Figure 5.10 were determined from linear  $I$ - $V$  relationships within the range of  $\pm 0.1$  V, and are the average values of resistances obtained at six different locations on the samples. Two Au-coated AFM tips having a radius of  $\sim 50$  nm were used for the measurements, each of which gave the same resistance value for tunneling through an octanethiol SAM and ONI 3. The two tips were used separately to examine the resistances of ONI 3, 4, 5, 7, and 10 in two



temperature ranges: 245–293 K (tip 1), and 303–333 K (tip 2). Note that all measurements were performed while keeping the relative humidity of chamber below 5%.

**Computational Methods.** Analysis of the ground neutral and radical-cation states of the ONI oligomer structures were carried out using density functional theory (DFT); for comparison, the OPI oligomer structures were also examined. The B3LYP<sup>198-200</sup> and M062X<sup>201</sup> functionals were used in conjunction with the 6-31G\*\* basis set. Time-dependent DFT (TD-DFT) was used to determine the vertical energies, oscillator strengths, and electronic configurations of the first excited states. The geometric and electronic structure parameters determined with the two functionals (*e.g.*, oligomer backbone twist, bond-length alternation changes on oxidation, adiabatic/vertical ionization potentials, molecular orbital densities and eigenvalues, and vertical transition energy to the first excited state) showed similar trends. Data derived with the M062X functional are reported herein, with all M062X and B3LYP data provided in the Supporting Information. Electronic density of states (DOS) for the oligomers were determined by convoluting the one-electron occupied molecular orbital eigenvalues with Gaussian functions characterized by a full width at half-maximum (fwhm) of 0.5 eV.<sup>202-204</sup> All calculations were performed with Gaussian 09 (Revision A.02),<sup>205</sup> and molecular orbital density plots were generated with ArgusLab 4.0.1.<sup>206</sup>

## 5.4 Results and Discussion

**Growth and Characterization of Molecular Wires.** ONI wires were prepared from an Au substrate using the aryl imine chemistry with alternate addition of 2,6-naphthalenedicarboxaldehyde and 2,7-fluorenediamine, as shown in Figure 5.2a. Each ONIp wire terminated with –NH<sub>2</sub> or –CHO groups was end-capped with benzaldehyde or aniline, respectively. The end-capping provided a consistent terminal group throughout the ONI series that facilitated reproducible electrical characterization.

The growth of wires was monitored using reflection-absorption Fourier transform infrared spectroscopy (RAIRS). The RAIRS data, shown in Figure 2b (left), reveal the alternate appearance and disappearance of carbonyl stretches (1697 cm<sup>-1</sup>) and symmetric

amine stretches ( $3360\text{ cm}^{-1}$ ) in ONIp molecules, which verified the imination mechanism and indicated near quantitative reaction of all exposed reactive endgroups. The intensity of imine stretching ( $1620\text{ cm}^{-1}$ ) and the benzene ring vibrational mode ( $1470\text{ cm}^{-1}$ ) increased with the number of repeat units, as expected. Complete end-capping was confirmed by the disappearance of the terminal group vibrational modes in Figure 5.2b (right).

In addition, ONI monolayers were extensively characterized by ellipsometry, X-ray photoelectron spectroscopy (XPS), and cyclic voltammetry (CV). Key results are shown in Figures 5.3 and 5.4, and compiled in Table 5.1. Importantly, monolayer thicknesses from ellipsometry and XPS measurements have a very nice correlation with the estimated length (Figure 5.3), which indicates that the wires grow with an upright (essentially untilted) orientation with respect to the Au substrate. The molecular lengths determined from the M062X/6-31G\*\* geometry optimization agree well with the empirically-determined data (Table 5.10).

The ONI wires are redox-active, as demonstrated by the cyclic voltammograms (CV) of selected wires in Figure 5.4. The potentials of the oxidation states and the estimated surface coverages for each ONI wire are tabulated in Table 5.1. All oxidation peaks were reversible within the range of  $-0.9$ – $0.7\text{ V}$  versus ferrocenium/ferrocene ( $\text{Fc}^+/\text{Fc}$ ), and no reduction was detected within the solvent electrochemical window for all ONI wires. The oxidation peak shifts to lower potential as wire length increases, which is largely expected based on the increased conjugation length. These results are confirmed by the adiabatic ionization potential energies determined at the M062X/6-31G\*\* level of theory (see Table 5.1). Integration of the CV sweeps of the ONI wires reveals nearly identical surface coverage ( $3.1 \times 10^{-10}$  to  $5.1 \times 10^{-10}\text{ mol/cm}^2$ ) over the entire set of wires. These surface coverage data indicate that the number of molecular wires contacted by the electrodes in junction experiments varies by a factor of 2 or so, and thus differences in the magnitude of measured current cannot be explained by surface coverage arguments in the analysis of CP-AFM data. Collectively, the surface characterization data indicate that quality monolayers of ONI wires were prepared.

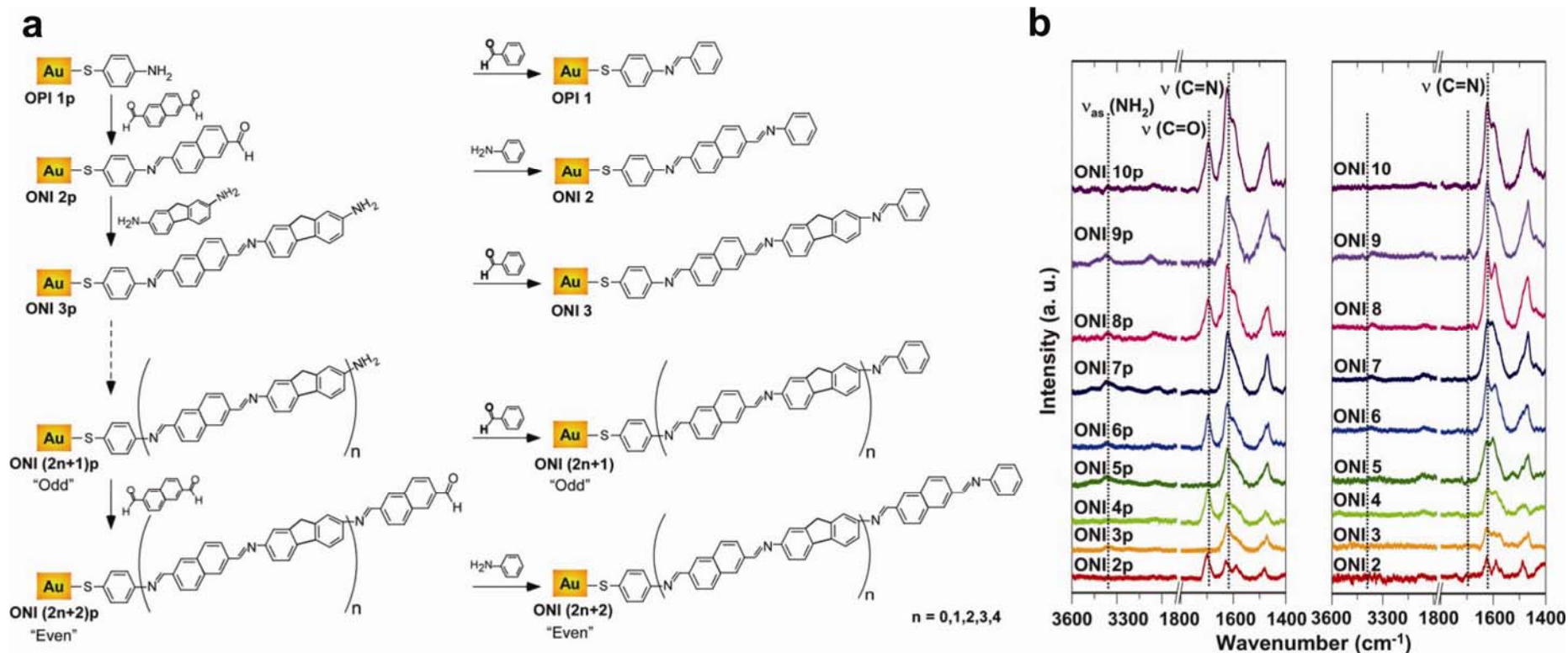


**Figure 5.2 (a)** Molecular structure and synthetic route to ONIp and ONI monolayers on Au substrates. **(b)** RAIRS spectra of ONIp (left) and ONI monolayers (right). Vertical dashed lines indicate positions of the symmetric amine stretch ( $\text{NH}_2$ ,  $3360\text{ cm}^{-1}$ ), carbonyl stretch ( $\text{C}=\text{O}$ ,  $1697\text{ cm}^{-1}$ ), and imine stretch ( $\text{C}=\text{N}$ ,  $1620\text{ cm}^{-1}$ ). Peaks for  $\text{NH}_2$  and  $\text{C}=\text{O}$  appear in the uncapped ONIp wires with odd and even numbers of repeat units, respectively.

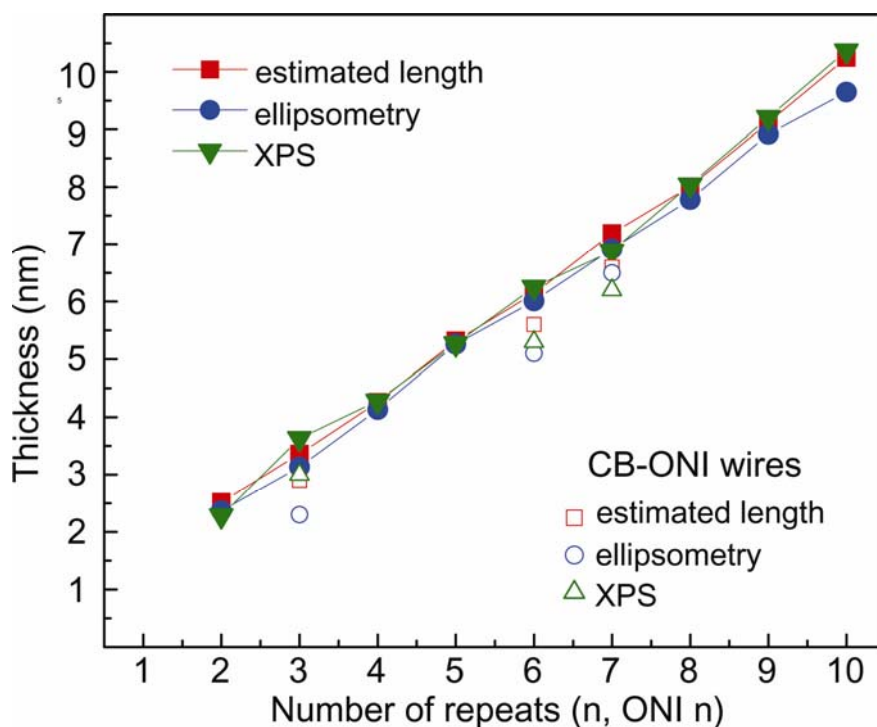


**Figure 5.3** Measured thicknesses and estimated lengths for ONI wires and conjugation broken (CB)-ONI wires. The structure of CB-ONI wires are given in Figure 5.9. Blue circles and green inverse triangles indicate the measured thickness, respectively, by ellipsometry and XPS. The estimated lengths are represented in red squares and were obtained with the Cambridge Scientific Chem3D software. Molecular length is the terminal H to S distance plus the Au-S bond length. The Au-S bond length was taken to be 2.36 Å.<sup>126</sup>

**Energy Level Alignment.** The electronic structures of ONI wires were examined with ultraviolet-visible (UV-vis) absorption spectroscopy and ultraviolet photoelectron spectroscopy (UPS). Oligo or poly(arylazomethine) molecules generally exhibit a twisted conformation mostly due to the steric interaction between hydrogen atoms on adjacent aromatic rings. Previously, we reported based on UV-vis absorption data that electronic delocalization extends only over three repeating units of OPI wires, presumably because of their nonplanar conformation.<sup>33</sup> For ONI wires, the optical band gap ( $E_g$ ) is significantly reduced with molecular length up to ONI 3, which indicates that electronic

coupling between adjacent fluorene and naphthalene building blocks is very strong (Table 5.1).

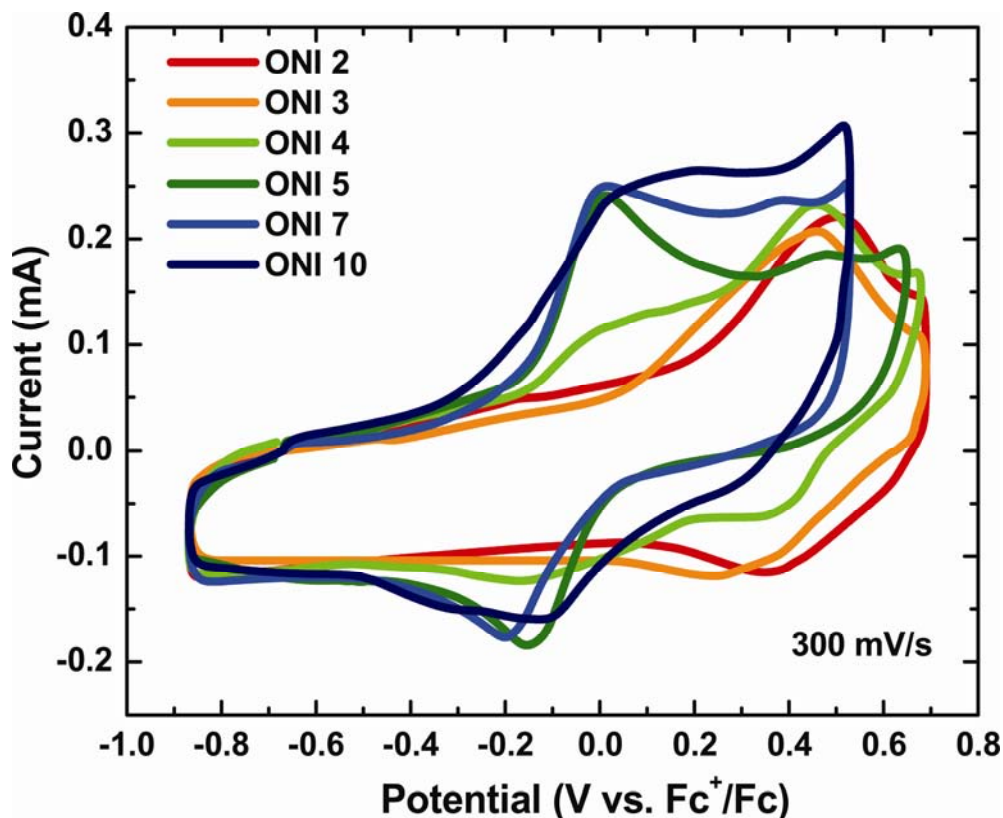


**Figure 5.4** Cyclic voltammograms of selected ONI wires obtained in 0.2 M Bu<sub>4</sub>NPF<sub>6</sub>/CH<sub>3</sub>CN. The reference and counter electrodes were Ag wire and Pt wire, respectively. The scan rate was 300 mV/s.

The optical gaps for wires longer than ONI 3 are more gradually reduced up to ONI 7, and remain constant at 2.4 eV for ONI 8-10 (Table 5.1 and Figure 5.5); similar trends are shown with the TD-DFT calculations, with the electronic configuration of the first excited state being predominantly a HOMO→LUMO transition. Collectively, these results indicate that there is significant  $\pi$ -orbital coupling along the ONI chains, but that shorter segments may be more strongly coupled, as could be expected. We note that the optical band gaps in ONI wires are relatively smaller by 0.1 ~ 0.2 eV compared to those in the analogous OPI wires;<sup>33</sup> the vertical transition energies from the TD-DFT calculations of both the ONI and OPI wires reveal a similar result (Table 5.6). This bathochromic shift has been observed in various oligoimine systems when phenylene

rings are replaced by naphthalenes or fluorenes.<sup>207-209</sup> The electronic coupling in ONI wires is enhanced by the contribution of highly conjugated building blocks, which is consistent with lower oxidation potentials in the CV measurements.

The energy offsets ( $E_F - E_{HOMO}$ ) between the Au Fermi level ( $E_F$ ) and the highest occupied molecular orbital (HOMO) ( $E_{HOMO}$ ) were determined over the entire set of ONI wires (Table 5.1 and Figure 5.6). As the wires become longer,  $E_F - E_{HOMO}$  is reduced from 0.5 to 0.3 eV, which is also consistent with the observed trend in oxidation potentials. The barrier heights at the interface of ONI wires are smaller compared to an interfacial barrier energy of 0.7 eV in OPI wires.<sup>33</sup> While the smaller barrier may result in higher ONI wire conductivity, as discussed below, it is important to recognize that barriers in the metal-molecule-metal junctions may be even lower than the barrier determined for the single metal-wire interface.<sup>178, 179, 210</sup> That is, additional metal-molecule charge transfer can occur when making the second contact, and naturally this is not accounted for in UPS measurements of molecule-metal interfaces.

**Table 5.1** Redox properties and energy level alignments of ONI wires. The oxidation potentials were determined from lower edge of the oxidation peak of ONI wires referenced to ferrocenium/ferrocene ( $\text{Fc}^+/\text{Fc}$ ). The energy offsets ( $E_F - E_{HOMO}$ ) and optical gaps ( $E_g$ ) are determined from onset of UPS and UV-vis spectra, respectively. Adiabatic ionization potential (AIP, eV) and first vertical transition ( $E_{\text{vert}}$ , eV) energies for the ONI wires as determined at the M062X/6-31G\*\* level of theory are also provided.

Monolayer	Oxidation potentials (V)	AIP (eV)	Surface coverage ( $\times 10^{-10}$ mol/cm <sup>2</sup> )	$E_g$ (eV)	$E_{\text{vert}}$ (eV)	$E_F - E_{HOMO}$ (eV)
ONI 2	0.22	7.23	3.1	3.0	3.74	0.5
ONI 3	0.06	6.78	3.6	2.6	3.50	0.5
CB-ONI 3	-	-	-	3.2	-	0.7
ONI 4	-0.13	6.77	3.8	2.6	3.43	0.5
ONI 5	-0.15	6.74	4.2	2.5	3.38	0.4
ONI 6	-0.15	6.74	4.6	2.5	3.36	0.4
CB-ONI 6	-	-	-	2.6	-	0.5
ONI 7	-0.17	6.70	4.9	2.4	3.34	0.4
CB-ONI 7	-	-	-	2.6	-	0.5
ONI 8	-0.20	6.70	5.1	2.4	3.33	0.3
ONI 9	-0.22	6.67	5.0	2.4	3.32	0.3
ONI 10	-0.25	6.67	4.8	2.4	3.31	0.3

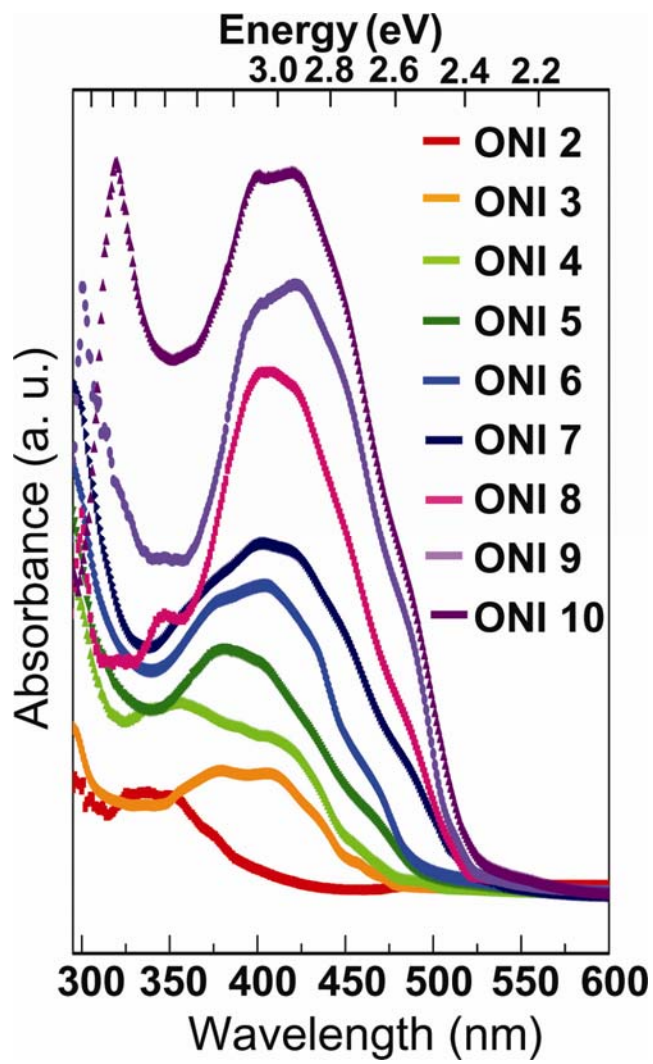


**Figure 5.5** UV/visible absorption spectra of ONI wires



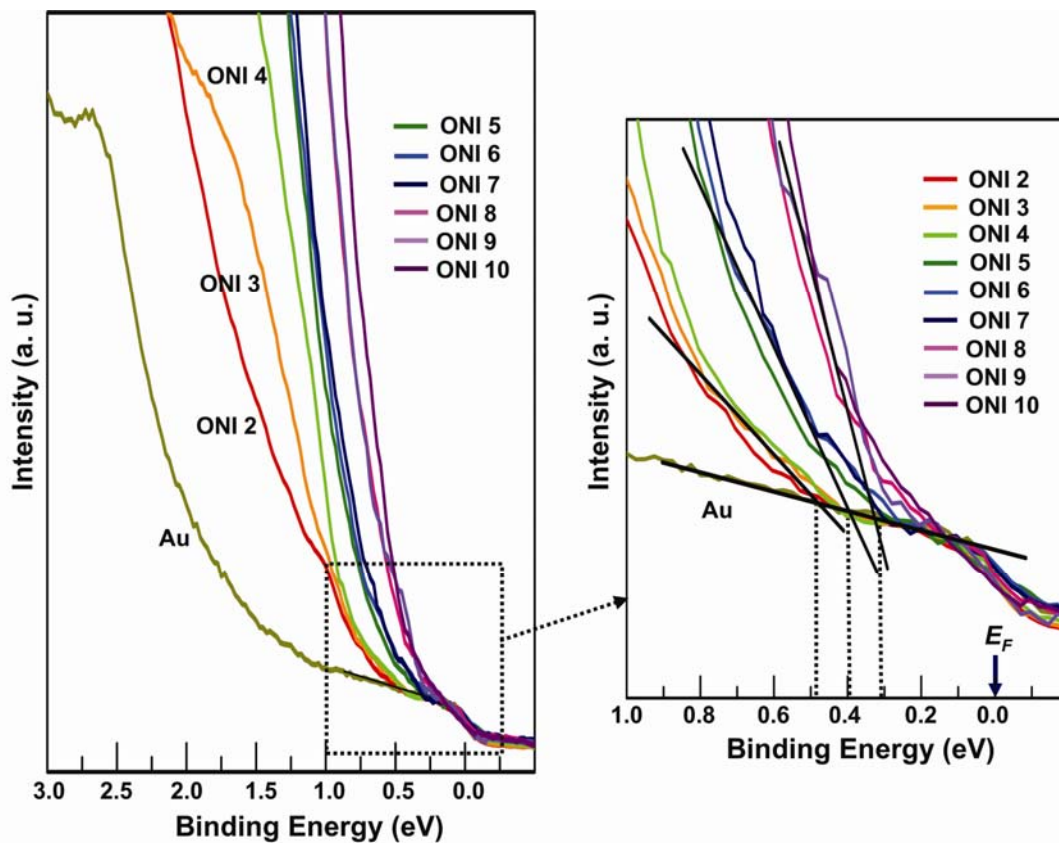


**Figure 5.6** UPS spectra of ONI wires (left) and the magnified UPS spectra of a dotted rectangular regime (right) near the gold Fermi level ( $E_F$ ). The dotted lines indicate the onset position of UPS spectra, where  $E_{\text{HOMO}}$  lies (0.5 eV for ONI 2-4, 0.4 eV for ONI 5-7, 0.3 eV for ONI 8-10).  $E_{\text{HOMO}}$  for each ONI wire was determined from where the intensity of photoemission rises abruptly with respect to the photoemission of bare Au (see black lines).

**Conformation of the Wires.** Quantum chemical calculations on isolated ground-state configurations of the ONI wires reveal their highly twisted structure, Figure 5.7. Torsion angles about the C-N bonds in the wires are typically 38-40° (see Table 5.3), which indicate that, in spite of substantial steric interactions,  $\pi$ -electronic coupling between the naphthalene and fluorene building blocks remains significant.<sup>211</sup> Of course, the calculations only take into account a static, isolated picture of the oligomeric structures and do not account for the dynamic processes within the junction. The

conformations of the wires in the junction will most certainly be affected by intermolecular interactions and the pressure applied by the CP-AFM tip (~100 MPa).

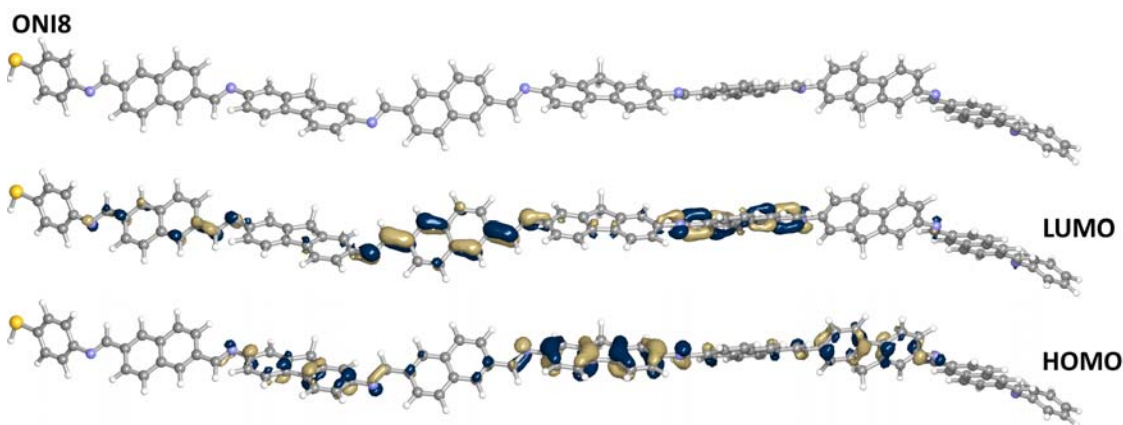


**Figure 5.7** Pictorial representation of the ground-state geometry (top) and HOMO and LUMO molecular orbital densities (bottom) for ONI 8 as determined at the M062X/6-31G\*\* level of theory.

**Length Dependent Resistances.** We investigated the transport characteristics of ONI wires using CP-AFM as shown in the inset to Figure 5.8a; CP-AFM has been used previously to measure conduction in a variety of molecular systems including OPI wires.<sup>26, 27, 33, 114, 117, 119</sup> A current-voltage ( $I$ - $V$ ) sweep generally yielded a sigmoidally shaped curve as will be shown later, but over a small voltage range ( $\pm 0.1$  V) the  $I$ - $V$  response was linear. The resistances shown in Figure 5.8 are low voltage resistances determined over this small range, and averaged for 20  $I$ - $V$  traces. In the linear plot of resistance ( $R$ ) versus molecular length ( $L$ ) (Figure 5.8a), a clear transition in the length dependence of resistances is exhibited near 4 nm (ONI 4), implying a change of transport mechanism. For long wires (ONI 4 – ONI 10), the linear relationship of the resistance as a function of length suggests that hopping transport prevails in this regime.<sup>43,45</sup> This linear dependence is indicated by the dashed line in the semi-log plot of  $R$  versus  $L$  (Figure 5.8b). Figure 5.8b reveals that the resistances for long wires have much weaker length dependence than those for short molecules, as expected for hopping transport. From the slope of  $R$  versus  $L$  in Figure 5.8a and the estimated number of wires in the junction ( $\sim 100$ ),<sup>85</sup> we calculated a single-wire conductivity of  $(1.8 \pm 0.1) \times 10^{-4}$  S/cm.

It is important to note that this value may be influenced by intermolecular interactions. Recently, Landau, Kronik, and Nitzan used a computational approach to investigate the role of intermolecular interactions on molecular conduction.<sup>70</sup> They had two main findings. First they determined that the conductance per molecule in an adlayer can differ substantially from the conductance of a single, isolated molecule. However, the single molecule conductance can be either greater or less than the conductance per molecule in an adlayer depending on the details of the metal-molecule coupling (broadening of energy states) and the Fermi level alignment in the junction. Second, they found that conductances of parallel molecular wires can be summed (so-called linear scaling) provided that the junction incorporates at least a few tens of molecules. Our calculation of single-wire conductivity thus has to be interpreted in this context, namely that the measurement involved many molecules (~100), and measurements on isolated ONI wires may yield different estimates of the wire conductivity. Nevertheless, within the uncertainty of our measurement, the conductivity of ONI wires is higher than that of OPI wires  $((1.0 \pm 0.1) \times 10^{-4} \text{ S/cm})$ ,<sup>23</sup> indicating that ONI wires are perhaps more efficient hopping conductors than OPI wires.

For short molecules (ONI 2, ONI 3), the semi-log plot of  $R$  versus  $L$  in Figure 5.8b clearly displays that the resistances increase exponentially with length, as expected for a non-resonant tunneling process. In this case,  $R$  is well described by

$$R = R_0 \exp(\beta L) \quad (5.3)$$

where  $R$  is the junction resistance,  $R_0$  is the effective contact resistance,  $L$  is molecular length, and  $\beta$  is the tunneling attenuation factor that depends on the nature of bonding in the molecular backbone.<sup>24, 26, 27, 85, 116</sup> The  $\beta$  value obtained from a linear fit is  $2.5 \text{ nm}^{-1}$ , smaller than the value obtained for short OPI molecules,  $3.0 \text{ nm}^{-1}$ ,<sup>33</sup> and indicates that tunneling through ONI molecules is more efficient than OPI molecules. This is consistent with the lower energy offset ( $E_F - E_{HOMO}$ ) of short ONI molecules relative to short OPI molecules, which should reduce the effective tunneling barrier height.

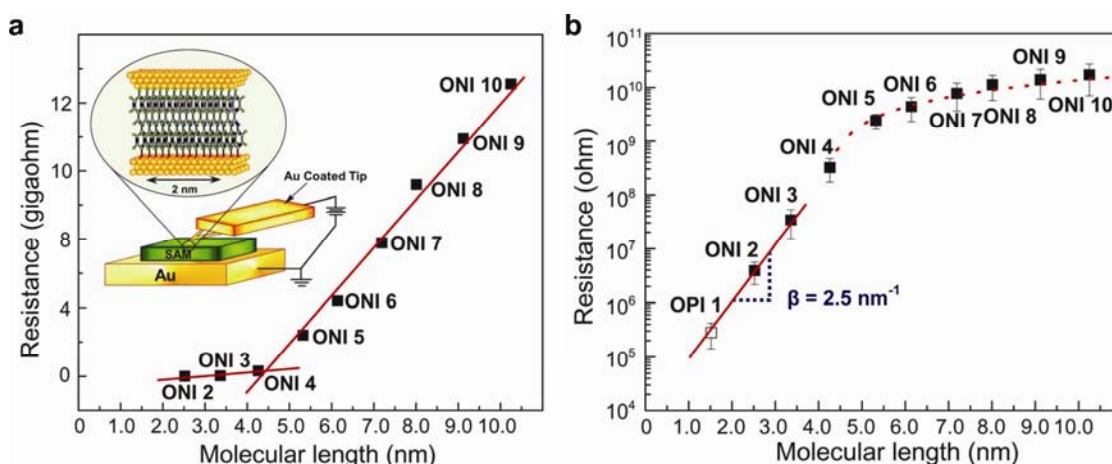


**Figure 5.8** Measurements of molecular wire resistance by conducting probe atomic force microscopy (CP-AFM). **(a)** A linear plot of  $R$  versus  $L$  for the Au/wire/Au junctions. Each data point is the average differential resistance obtained from 20  $I$ - $V$  traces in the range  $-0.1$  to  $+0.1$  V. Straight lines are linear fits to the data. Inset: An Au-coated tip was brought into contact with an ONI monolayer on Au.  $I$ - $V$  traces were obtained over  $\pm 1.5$  V at a load of 2 nN on the tip contact. **(b)** Semilog plot of  $R$  versus  $L$  for the Au/wire/Au junctions. Each data point is the average differential resistance obtained from 20  $I$ - $V$  traces in the range  $-0.1$  to  $+0.1$  V. Error bars represent one standard deviation. The straight line is a linear fit to the data according to Eq. 2. The dashed line indicates a linear fit obtained in (a) for long ONI wires.

**Conjugation Broken ONI Wires (CB-ONIs).** For the purpose of examining the sensitivity of conduction to wire architecture, we prepared a set of engineered wires that incorporate a deliberate conjugation breaking (CB) link (an aliphatic cyclohexyl group) within the ONI backbone (CB-ONIs). The structure of CB-ONI wires and their low-voltage resistances are shown in Figure 5.9. The conduction in the long wires is much more sensitive to the presence of the cyclohexyl group than in the short molecules, as we previously demonstrated with an analogous OPI set (CB-OPIs).<sup>33</sup> For CB-ONI 3, the resistance is slightly increased compared to ONI 3, as expected, because the aliphatic cyclohexyl links raise the average tunneling barrier. In contrast, for the longer CB-ONI 6 and CB-ONI 7, the resistance change from the corresponding ONI 6 and ONI 7 wires is considerably greater, approximately 15 times greater. For hopping transport in the long

wires, a large change in resistance is expected upon interrupting the conjugation because injected carriers now feel the energetic details of atomic orbitals through molecular backbone instead of averaging them, and the mismatched HOMO energy of the cyclohexyl group represents a significant hopping barrier. Overall, the conjugation blocking experiments confirm that conduction depends upon the bond architecture and they also support the conclusion that tunneling occurs in the short wires and hopping transport prevails in the long wires.

**Temperature Dependent Resistance.** Although a change in transport mechanism is apparent in the  $R$  versus  $L$  plot, the temperature dependence is key to verifying different transport mechanisms. Figure 5.10 shows an Arrhenius plot of  $R$  versus the inverse of temperature ( $T$ ) for selected ONI wires. Clearly, the resistance for ONI 3 is independent of temperature from 246 to 333 K, as expected for tunneling. However, ONI 4 and longer wires (ONI 5, 7, and 10) display strongly thermally activated transport characteristic of hopping. The activation energies determined from the slopes of the data are nearly identical to each other at  $0.54$  to  $0.62 \pm 0.03$  eV ( $12.5$  to  $14.1 \pm 0.7$  kcal/mol), which implies that the same rate-determining step for hopping transport is active in all the wires regardless of the molecular lengths. Collectively, the data in Figures 5.8 – 5.10 provide unambiguous evidence for a change in transport mechanism from tunneling to hopping near 4 nm in ONI wire length. The temperature dependence and change in mechanism near 4 nm are similar to what we have observed previously with OPI wires.<sup>23</sup>

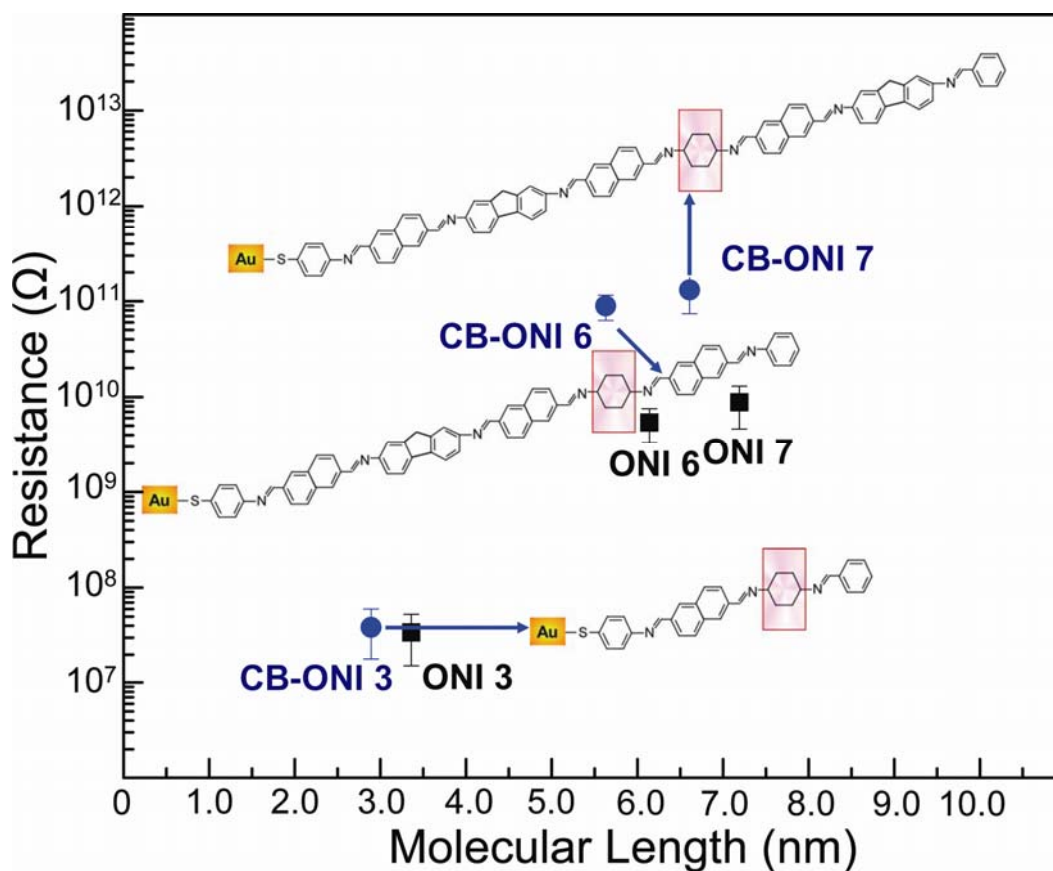


**Figure 5.9** A semilog plot of  $R$  versus  $L$  for Au/ONI/Au junctions and conjugation broken Au/CB-ONI/Au junctions. Each data point is the average differential resistance from 20  $I$ - $V$  traces in the interval  $-0.1$  V to  $0.1$  V. Error bars represent one standard deviation. The blue circles are the resistances of conjugation-broken ONI (CB-ONI) wires. Pink boxes indicate the position where conjugation is broken.

In an effort to understand the nature of the charge carriers and the hopping conduction process, we performed quantum chemical calculations on isolated, static, positively ionized ONI wires as a function of length (Figure 5.11). We found that positive charge is localized predominantly on the fluorene substituents in the backbone, which is consistent with the HOMO wavefunction shown in Figure 5.7. The molecule also remains relatively twisted in the ionized state (see Table 5.3 for torsional angles).

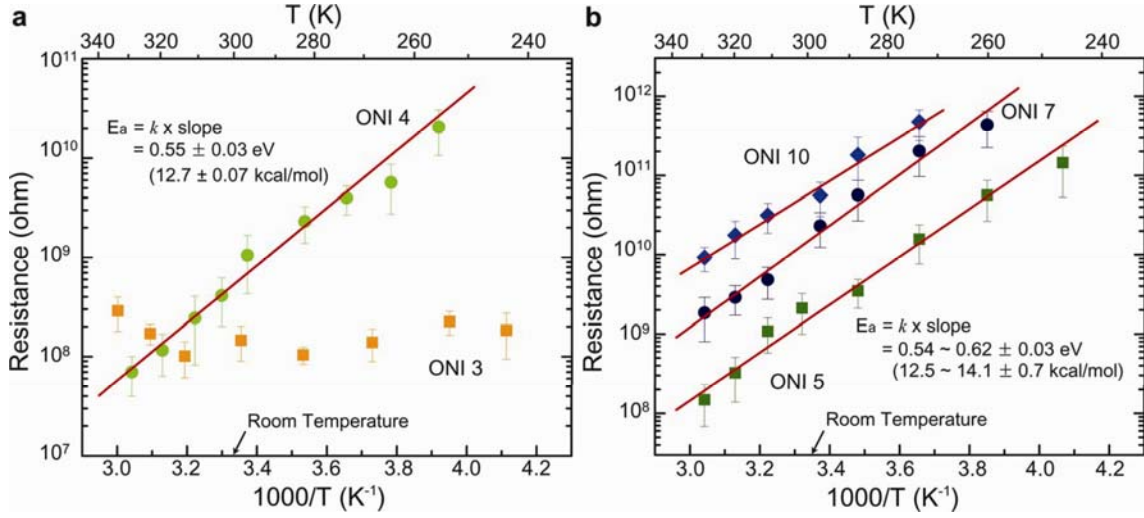


**Figure 5.10** Arrhenius plot for (a) ONI 3 and ONI 4 and (b) ONI 5, ONI 7, and ONI 10. Each data point is the average differential resistance obtained at six different locations of samples in the range  $-0.1$  to  $+0.1$  V. Error bars represent one standard deviation. Straight lines are linear fits to the data.

According to the Marcus theory of electron transfer, the charge hopping rate ( $k_{et}$ ) depends on the thermodynamic driving force ( $\Delta G^\circ$ ), which to a first approximation can be considered to correspond to the variations in hopping site energies, and the (polaronic) reorganization energy  $\lambda$ , as follows:

$$k_{et} \propto \exp\left(-\frac{(\lambda + \Delta G^\circ)^2}{4\lambda k_B T}\right) \quad (5.4)$$

where  $k_B$  is the Boltzmann constant and  $T$  is the temperature. We have computed the relaxation energies  $\lambda_1$  and  $\lambda_2$  associated with adiabatic ionization and neutralization of the ONI wires, Table 5.4. Their sum,  $\lambda_t$ , provides an estimate of the intramolecular reorganization energy.<sup>192</sup> In addition, in a polarizable medium like a molecular junction in which there are of order 100 molecules in parallel, there will be an environmental (electronic and nuclear) polarization that contributes to  $\lambda$  in Equation 5.4. In  $\pi$ -conjugated materials, this contribution is commonly estimated to have a magnitude similar to the intramolecular  $\lambda_t$ .<sup>192</sup>

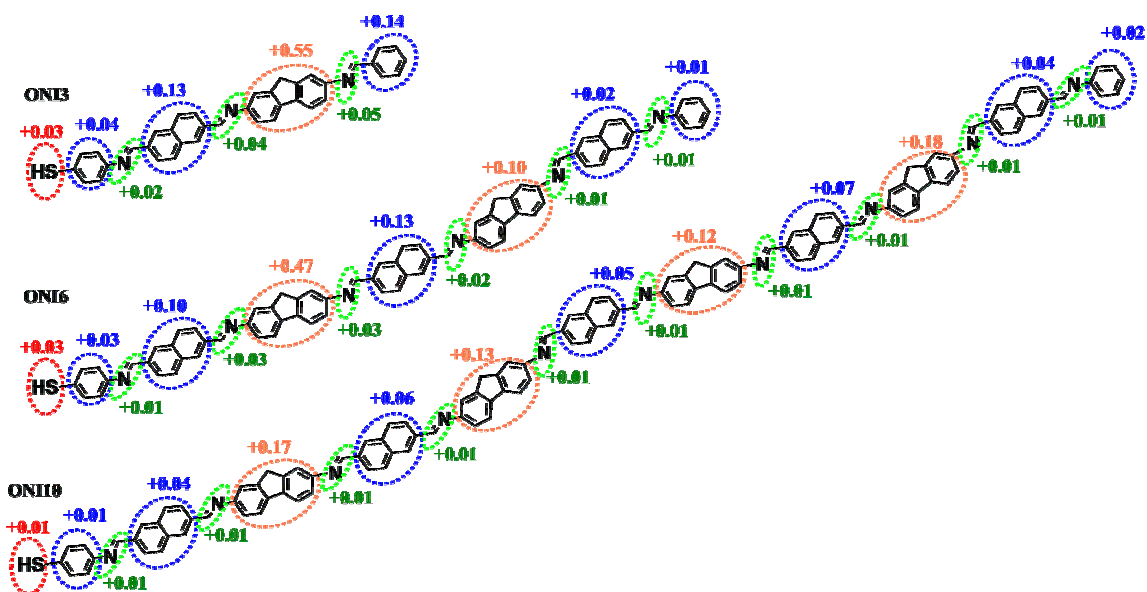


**Figure 5.11** Pictorial representation of excess positive charge distributions for selected ONI wires as calculated using the M062X/6-31G\*\* level of theory. Charge values correspond to the differences in Mulliken atomic charges of the radical-cation state with respect to the neutral ground state.

If we consider the hopping sites in long ONI wires to be short conjugated subunits, we can make a rough estimate of the total  $\lambda$ . Taking  $\lambda_1$  and  $\lambda_2$  from the ONI 3 wires (we estimate the hopping sites to be  $\sim 3$  units long because by UV-vis the decrease in the optical gap becomes more gradual beyond 3 units), we find  $\lambda_t$  to be 0.45 eV (see Table S4). Then if we double this value in order to account approximately for environmental contributions, we obtain  $\lambda_{total} \approx 0.90$  eV. According to Equation 3 we would predict that the total activation energy ( $E_a$ ) is  $(\lambda_{total} + \Delta G^\circ)^2/4\lambda_{total}$ .  $\Delta G^\circ$  can be estimated to be on the order of  $-25$  meV, taking into account the effects of the applied electric field (at 0.1 V) across the junction. We thus obtain  $E_a \approx 0.2$  eV, which is a factor of 2-3 lower than the measured activation energy.

It is generally known, however, that nuclear motions can be significantly hindered in the solid state relative to the liquid or gas phase, and this in turn can impact reorganization energies.<sup>36, 212</sup> For example, the torsional barrier for  $-CF_3$  rotation in 3-(trifluoromethyl)phenanthrene increases from 0.4 kcal/mol (17 meV) in the gas phase to 2.6 kcal/mol (112 meV) in the crystalline state, or a factor of 6.5. In this context, it is



reasonable to suppose that molecular relaxation energies of the ONI wire molecules in a SAM sandwiched between metal contacts may be substantially greater than we have calculated here for isolated molecules. Clearly, more work will need to be done to determine the true nature of the hopping process in ONI wires, and in particular the origin of the activation energy. However, these estimations indicate that the magnitude of the measured activation energy is not unreasonable and it is indeed in approximate agreement with expectations based on molecular reorganization upon charge transfer.

**Electric Field Dependent  $I$ - $V$  Characteristics.** We have also carefully examined the voltage and electric field dependence of the  $I$ - $V$  characteristics of ONI wires (Figure 5.12). The semilog plot of  $I$  versus  $V$  in Figure 5.12a demonstrates that for short ONI molecules (ONI 2 and 3), there are larger decreases in current with wire length, whereas these changes become much smaller for the long wires (ONI 4–10). A plot of  $\log I$  versus electric field ( $E$ ) (see inset) reveals that the traces for the long wires collapse nearly on top of one another. This result indicates that for the long wires transport is field driven, as expected for a hopping mechanism in which the electric field pushes the carriers. In short molecules, voltage is the key parameter for the tunneling process.

As we demonstrated for OPI wires,<sup>33</sup> short and long ONI wires also exhibit different transport regimes in log–log plots of the  $I$ - $V$  characteristics, Figure 5.12b. The data for ONI 3 reveal a transition at 0.33 V from linear (regime I) to non-linear  $I$ - $V$  behavior (regime II). In approximate terms, this transition arises from changes in the tunneling barrier shape from trapezoidal to triangular.<sup>81, 82</sup> At low bias, the simple linear tunneling behavior is described by Equation 5.5,

$$I \propto V \exp\left(-\frac{2d\sqrt{2m_e\phi}}{\hbar}\right) \quad (5.5)$$

where  $d$  is the barrier width (wire length),  $m_e$  is the electron effective mass, and  $\phi$  is the effective barrier height. Above the transition voltage  $V_{trans} = 0.33$  V (regime II), the  $I$ - $V$  behavior adapts to the Fowler-Nordheim (field emission) relation:

$$\ln\left(\frac{I}{V^2}\right) \propto \frac{-4d\sqrt{2m_e\phi^3}}{3\hbar q} \left(\frac{1}{V}\right) \quad (5.6)$$

where  $q$  is the elementary charge.

The change in mechanism to field emission for ONI 3 is clearly evident in the corresponding Fowler-Nordheim plot in Figure 5.12c. For low voltages (regime I), the current scales logarithmically with  $1/V$  as predicted from Equation 4, indicative of direct tunneling. Above  $V_{trans}$  (regime II), the current scales linearly with  $1/V$  with a negative slope characteristic of field emission (Equation 5.6). The transition point,  $V_{trans}$  (0.33 V) provides an estimate of the effective tunneling barrier height at  $V = 0$ . A compilation of  $V_{trans}$  values for different wires is included in Table 2. The  $V_{trans}$  values are smaller than those of the corresponding short OPI molecules (0.75 V in case of OPI 3)<sup>23</sup> and they also decrease with length, consistent with the trend in oxidation potentials and  $E_F-E_{HOMO}$  offsets (see Table 5.1).

The longer ONI 8 wires exhibit three distinct transport regimes in Figures 5.12b and d. The principal mechanisms governing these regimes were already proposed with long OPI wires.<sup>23</sup> Regime I' and III' correspond to ohmic (field-driven) conduction and field emission, respectively, while regime II' may correspond to space charge limited conduction (SCLC). In regime I', the current scales linearly with voltage, characteristic of ohmic hopping conduction and consistent with the length and temperature dependent transport (Figures 6 and 8). The correspondence of regime III' with field emission is evident in the Fowler-Nordheim plot in Figure 10d, where it is clear that at voltages above 0.6 V the plot has the expected negative slope. From the slope in regime III', we calculated the emission barrier height ( $\phi_{FE}$ )<sup>213</sup> to be in the range of 0.1–0.3 eV assuming carrier effective mass ratios in the range 0.1 to 1.0, which are typical for molecular junctions.<sup>17</sup>

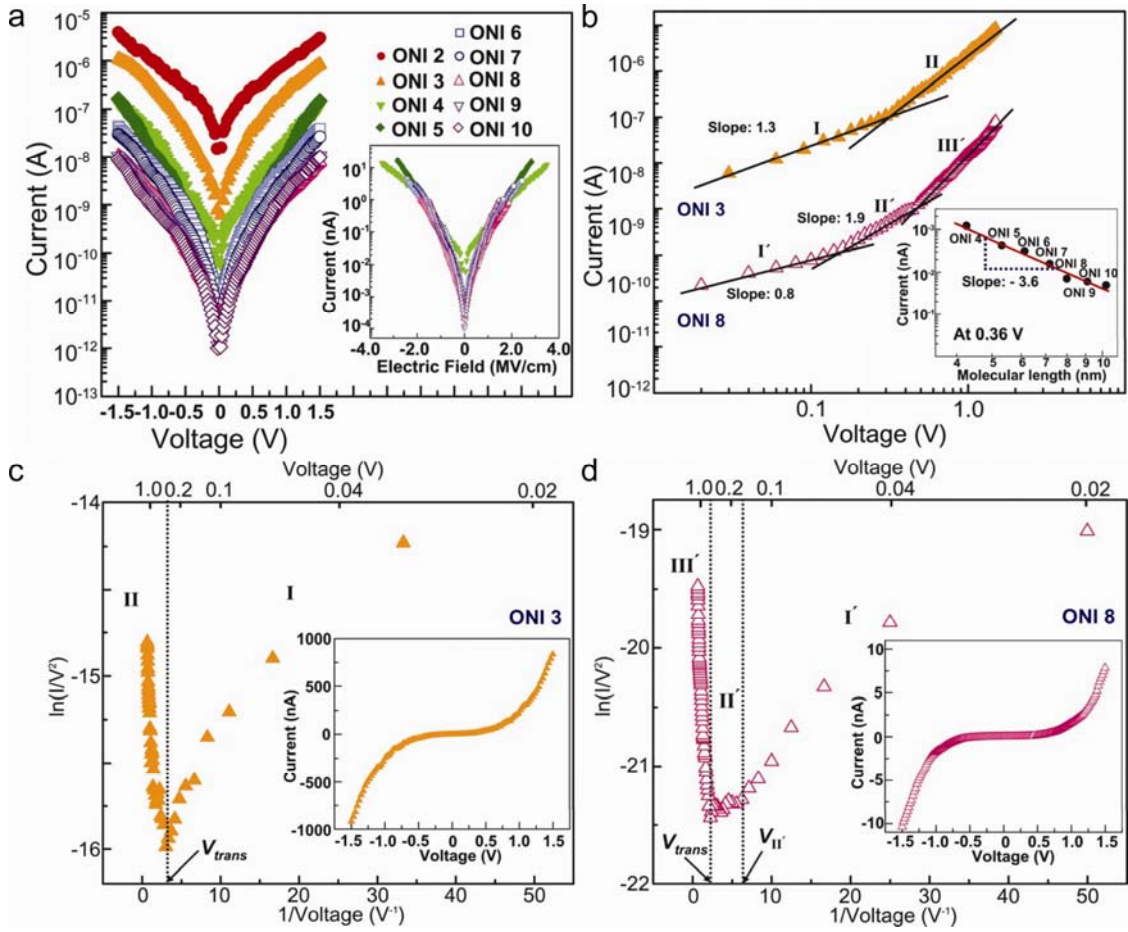


**Figure 5.12** (a) Semilog plot of the average current for 20  $I$ - $V$  traces for Au/ONI/Au junctions. The inset is a semilog plot of  $I$  versus electric field ( $E$ ) for long ONI wires. (b) Log-log plot of the average of 20  $I$ - $V$  traces for the Au/ONI 3/Au and Au/ONI 8/Au junctions. Fits are shown in the different transport regimes. Inset: A log-log plot of  $I$  versus  $L$  obtained at 0.36 V for all long ONI wires, displaying the linear fit with a slope of -3.6 (0.36 V is the bias at which all long ONI wires are within regime II'). (c) Fowler-Nordheim plot for the ONI 3 data in (b). Two distinct regimes (I and II) are clearly observable with an inflection point at  $V_{trans}$ , indicating the switch from tunneling to field emission. The inset displays the sigmoidal  $I$ - $V$  curve on a linear scale. (d) Fowler-Nordheim plot for the ONI 8 data in (b). Three distinct regimes (I', II', and III') are evident. The inset shows the sigmoidal  $I$ - $V$  curve.

This barrier is very much in line with measurements for the HOMO-to-Fermi level offset for long wires.<sup>214</sup> Recall that  $E_F - E_{HOMO}$  was determined to be 0.3-0.5 eV by UPS for long wires, but the expectation is that the real barrier for a junction will be lower. The

estimated emission barrier heights for the other long ONI wires are also listed in Table 5.2.

**Table 5.2** Analyses of  $I$ - $V$  characteristics for ONI wires.

Monolayer	n in I, I'	n in II'	$V_{trans}$ (V)	$V_{II'}$ (V)	$\phi_{FE}$ (eV)
	$I \propto V^n$	$I \propto V^n$	$[E_{trans}$ (MV/cm)]	$[E_{II'}$ (MV/cm)]	
ONI 2	1.0	-	0.63 [2.5]	-	0.3– 0.5
ONI 3	1.3	-	0.33 [1.0]	-	0.3– 0.5
CB-ONI 3	1.0	-	0.54 [1.9]	-	-
ONI 4	0.9	2.7	0.90 [2.1]	0.28 [0.65]	0.2– 0.4
ONI 5	1.1	2.8	0.64 [1.2]	0.22 [0.42]	0.2– 0.4
ONI 6	1.2	2.3	0.54 [0.89]	0.14 [0.23]	0.2– 0.4
CB-ONI 6	1.1	2.2	0.54 [0.96]	0.14 [0.25]	-
ONI 7	1.0	2.3	0.48 [0.67]	0.14 [0.19]	0.1– 0.3
CB-ONI 7	1.1	1.9	0.44 [0.67]	0.12 [0.18]	-
ONI 8	0.8	1.9	0.44 [0.55]	0.12 [0.15]	0.1– 0.3
ONI 9	1.0	2.0	0.42 [0.46]	0.10 [0.11]	0.1– 0.3
ONI 10	1.0	2.0	0.42 [0.41]	0.10 [0.10]	0.1– 0.3

We propose that SCLC is responsible for regime II', based on the slope of 1.9 in the  $\log I$  versus  $\log V$  plot (Figure 8b) and the slope of -3.6 in the  $\log I$  versus  $\log L$  plot at 0.36 V (inset in Figure 10b). Under bias, the carrier concentrations in the wires can be increased beyond their values in equilibrium. In SCLC transport, current scales with voltage and length as  $I \propto V^2/L^3$ , close to what we have observed in regime II' (Table 2 and inset in Figure 10b). More detailed work will have to be done, however, to confirm the interpretation that SCLC transport is operative in Regime II'.

**Table 5.3** Torsion angles for the neutral (radical-cation) states of the ONI wires as determined at the M062X/6-31G\*\* level of theory. See Figure 5.13.

	$\varphi_1$	$\varphi_2$	$\varphi_3$	$\varphi_4$	$\varphi_5$	$\varphi_6$	$\varphi_7$	$\varphi_8$	$\varphi_9$	$\varphi_{10}$
ONI2	38 (23)	41 (30)								
ONI3	39 (33)	39 (37)	40 (44)							
ONI4	38 (34)	39 (37)	39 (39)	41 (38)						
ONI5	39 (35)	40 (39)	39 (36)	39 (33)	40 (41)					
ONI6	38 (34)	39 (38)	39 (35)	39 (33)	39 (40)	41 (40)				
ONI7	39 (36)	40 (39)	39 (35)	39 (36)	39 (36)	40 (36)	40 (41)			
ONI8	38 (36)	40 (39)	39 (36)	40 (37)	39 (36)	40 (36)	39 (39)	41 (39)		
ONI9	39 (36)	40 (39)	39 (37)	40 (37)	39 (38)	40 (39)	39 (36)	39 (36)	40 (41)	
ONI10	39 (37)	40 (39)	38 (36)	40 (36)	40 (37)	39 (37)	39 (37)	39 (36)	39 (39)	41 (40)

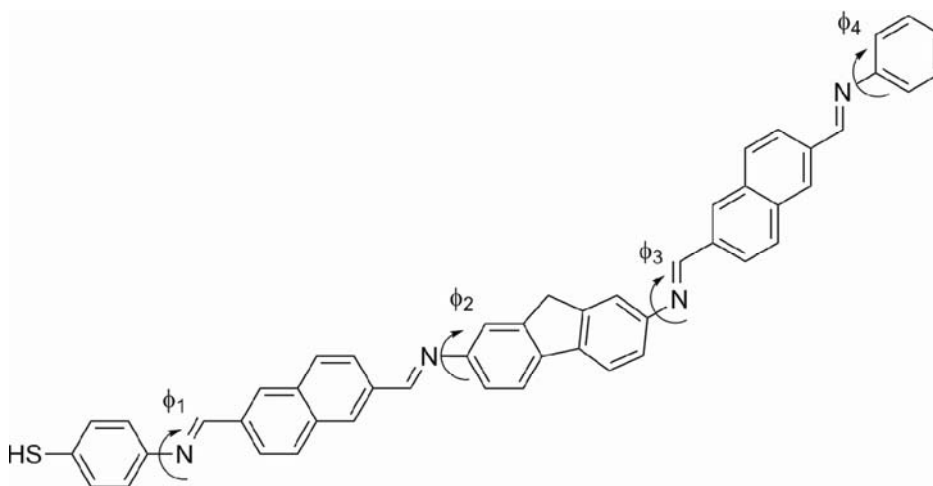


**Figure 5.13** Example torsion angles measured for the ONI wires. ONI4 is shown for reference.

**Table 5.4** Torsion angles for the neutral (radical-cation) states of the OPI oligomer series as determined at the M062X/6-31G\*\* level of theory.

	$\phi_1$	$\phi_2$	$\phi_3$	$\phi_4$	$\phi_5$	$\phi_6$	$\phi_7$	$\phi_8$	$\phi_9$	$\phi_{10}$
OPI1	39 (91)									
OPI2	38 (26)	41 (27)								
OPI3	39 (23)	39 (26)	40 (42)							
OPI4	38 (25)	38 (29)	39 (35)	41 (34)						
OPI5	38 (30)	39 (35)	39 (27)	39 (33)	40 (42)					
OPI6	38 (28)	37 (31)	39 (29)	39 (29)	39 (33)	41 (31)				
OPI7	38 (36)	38 (41)	39 (28)	39 (31)	39 (30)	38 (26)	40 (42)			
OPI8	38 (35)	39 (40)	39 (27)	39 (30)	39 (31)	39 (27)	39 (41)	41 (39)		

OPI9	38 (35)	39 (36)	39 (33)	39 (35)	39 (32)	39 (33)	39 (33)	39 (31)	40 (41)	
OPI10	38 (30)	39 (33)	39 (32)	39 (32)	39 (32)	39 (32)	39 (32)	40 (31)	40 (35)	41 (34)

**Table 5.5** Torsion angles for the neutral (radical-cation) states of the OPI and ONI oligomer series as determined at the B3LYP/6-31G\*\* level of theory.

	$\varphi_1$	$\varphi_2$	$\varphi_3$	$\varphi_4$	$\varphi_5$	$\varphi_6$	$\varphi_7$	$\varphi_8$	$\varphi_9$	$\varphi_{10}$
OPI1	36 (42)									
OPI2	34 (24)	38 (23)								
OPI3	34 (22)	34 (25)	37 (39)							
OPI4	34 (24)	35 (28)	35 (31)	38 (28)						
OPI5	34 (27)	35 (31)	35 (28)	34 (26)	37 (39)					
OPI6	34(2 8)	35 (31)	35 (29)	35 (29)	35 (33)	38 (31)				
OPI7	34 (29)	35 (32)	35 (31)	35 (31)	35 (31)	34 (28)	37 (38)			
OPI8	34 (29)	35 (32)	35 (31)	35 (32)	35 (31)	35 (30)	35 (34)	38 (33)		
OPI9	34 (30)	35 (33)	35 (32)	35 (32)	35 (32)	35 (32)	35 (31)	35 (30)	37 (38)	
OPI10	34 (30)	35 (33)	35 (32)	35 (32)	35 (32)	35 (32)	35 (32)	35 (31)	35 (35)	38 (34)
ONI2	35	38								

---

	(24)	(25)								
ONI3	34	35	36							
	(26)	(31)	(41)							
ONI4	34	36	35	38						
	(28)	(32)	(34)	(32)						
ONI5	34	36	35	35	36					
	(30)	(34)	(32)	(32)	(39)					
ONI6	34	36	35	36	35	38				
	(30)	(34)	(32)	(33)	(35)	(34)				
ONI7	34	36	35	36	35	36	36			
	(31)	(35)	(33)	(34)	(33)	(33)	(39)			
ONI8	34	36	35	36	35	36	35	38		
	(31)	(35)	(34)	(34)	(33)	(34)	(36)	(35)		
ONI9	35	36	35	36	35	36	35	35	36	
	(32)	(35)	(34)	(34)	(34)	(35)	(33)	(34)	(38)	
ONI10	34	36	35	36	35	36	35	36(3	35	38
	(32)	(35)	(33)	(34)	(34)	(35)	(34)	4)	(36)	(36)



**Table 5.6** M062X/6-31G\*\* data for the ONI wires. All energies in eV.

	M062X/6-31G**							
	AIP <sup>†</sup>	$\lambda_1$	$\lambda_2$	$\lambda_t$	HOMO	LUMO	E <sub>g</sub>	E <sup>OP</sup>
ONI2	7.23	0.23	0.21	0.44	-6.86	-1.33	5.53	3.74
ONI3	6.78	0.24	0.21	0.45	-6.54	-1.36	5.17	3.50
ONI4	6.77	0.24	0.20	0.44	-6.56	-1.43	5.13	3.43
ONI5	6.74	0.19	0.11	0.30	-6.49	-1.44	5.05	3.38
ONI6	6.74	0.18	0.10	0.28	-6.50	-1.46	5.04	3.36
ONI7	6.70	0.07	0.07	0.14	-6.47	-1.47	5.01	3.34
ONI8	6.70	0.07	0.07	0.14	-6.49	-1.48	5.01	3.33
ONI9	6.67	0.05	0.05	0.10	-6.47	-1.48	4.99	3.32
ONI10	6.67	0.05	0.05	0.10	-6.47	-1.48	4.99	3.31

† Adiabatic Ionization Potential.

**Table 5.7** B3LYP/6-31G\*\* data for the ONI wires. All energies in eV.

	B3LYP/6-31G**							
	AIP <sup>†</sup>	$\lambda_1$	$\lambda_2$	$\lambda_t$	HOMO	LUMO	E <sub>g</sub>	E <sup>OP</sup>
ONI2	6.62	0.12	0.11	0.23	3.04	-5.57	-2.19	3.38
ONI3	6.13	0.12	0.11	0.21	2.72	-5.27	-2.20	3.07
ONI4	6.08	0.09	0.08	0.17	2.64	-5.30	-2.28	3.02
ONI5	5.87	0.06	0.06	0.12	2.57	-5.22	-2.28	2.94
ONI6	5.86	0.06	0.06	0.12	2.55	-5.24	-2.30	2.94
ONI7	5.73	0.05	0.04	0.09	-5.21	-2.31	2.93	2.52
ONI8	5.73	0.04	0.04	0.08	5.22	-2.32	2.90	2.51
ONI9	5.65	0.04	0.04	0.08	-5.20	-2.32	2.88	2.49
ONI10	5.65	0.03	0.03	0.06	-5.21	-2.33	2.88	2.49

† Adiabatic Ionization Potential.

**Table 5.8** M062X/6-31G\*\* data for the OPI wires. All energies in eV.

	M062X/6-31G**							
	AIP <sup>†</sup>	$\lambda_1$	$\lambda_2$	$\lambda_t$	HOMO	LUMO	$E_g$	$E^{OP}$
OPI1	7.33	0.72	0.30	1.02	-6.88	-0.70	6.18	3.98
OPI2	7.30	0.26	0.23	0.49	-6.90	-1.32	5.59	3.70
OPI3	7.08	0.30	0.23	0.52	-6.81	-1.37	5.44	3.54
OPI4	7.08	0.28	0.21	0.50	-6.83	-1.50	5.33	3.46
OPI5	7.02	0.24	0.16	0.41	-6.78	-1.51	5.27	3.40
OPI6	7.03	0.23	0.15	0.38	-6.80	-1.56	5.23	3.37
OPI7	7.00	0.21	0.11	0.32	-6.77	-1.57	5.20	3.34
OPI8	7.01	0.20	0.10	0.30	-6.78	-1.60	5.19	3.33
OPI9	6.99	0.09	0.08	0.17	-6.76	-1.60	5.17	3.32
OPI10					-6.77	-1.61	5.16	3.31

† Adiabatic Ionization Potential.

**Table 5.9** B3LYP/6-31G\*\* data for the OPI wires. All energies in eV.

	B3LYP/6-31G**							
	AIP <sup>†</sup>	$\lambda_1$	$\lambda_2$	$\lambda_t$	HOMO	LUMO	$E_g$	$E^{OP}$
OPI1	6.95	0.33	0.20	0.53	3.49	-5.58	-1.64	3.94
OPI2	6.72	0.14	0.13	0.27	3.02	-5.61	-2.22	3.44
OPI3	6.40	0.15	0.13	0.28	2.83	-5.49	-2.26	3.22
OPI4	6.34	0.11	0.10	0.21	2.72	-5.52	-2.40	3.10
OPI5	6.18	0.10	0.09	0.19	2.64	-5.45	-2.41	3.02
OPI6	6.16	0.08	0.07	0.15	2.59	-5.48	-2.47	2.98
OPI7	6.05	0.07	0.07	0.14	2.55	-5.44	-2.47	2.94
OPI8	6.04	0.06	0.06	0.12	2.53	-5.45	-2.50	2.95
OPI9	5.97	0.05	0.05	0.11	2.51	-5.43	-2.50	2.93
OPI10	5.96	0.05	0.05	0.10	2.50	-5.45	-2.52	2.93

† Adiabatic Ionization Potential.

**Table 5.10** Estimated molecular height (d) above the gold surface (nm) as determined at the M062X/-31G\*\* level of theory.

d		d	
OPI1	1.4		
OPI2	2.1	ONI2	2.3
OPI3	2.7	ONI3	3.3
OPI4	3.4	ONI4	4.1
OPI5	4.0	ONI5	5.2
OPI6	4.6	ONI6	5.9
OPI7	5.3	ONI7	6.7
OPI8	5.9	ONI8	7.4
OPI9	6.5	ONI9	8.3
OPI10	7.2	ONI10	8.6

<sup>a</sup>Molecular heights were determined from the M062X/6-31G\*\* optimized ground-state structures as the distance between the sulfur atom and the terminal hydrogen on the end phenyl unit. 2.36Å was used as the estimate of the distance between the sulfur atom and the Au electrode plane.

**Table 5.11** Estimated molecular height (d) above the gold surface (nm) as determined at the B3LYP/-31G\*\* level of theory.

d		d	
OPI1	1.4		
OPI2	2.1	ONI2	2.3
OPI3	2.7	ONI3	3.3
OPI4	3.4	ONI4	4.2
OPI5	4.0	ONI5	5.2
OPI6	4.7	ONI6	5.9
OPI7	5.3	ONI7	6.8
OPI8	5.9	ONI8	7.4
OPI9	6.6	ONI9	8.3
OPI10	7.2	ONI10	8.7

<sup>a</sup>Molecular heights were determined from the B3LYP/6-31G\*\* optimized ground-state structures as the distance between the sulfur atom and the terminal hydrogen on the end phenyl unit. 2.36Å was used as the estimate of the distance between the sulfur atom and the Au electrode plane.

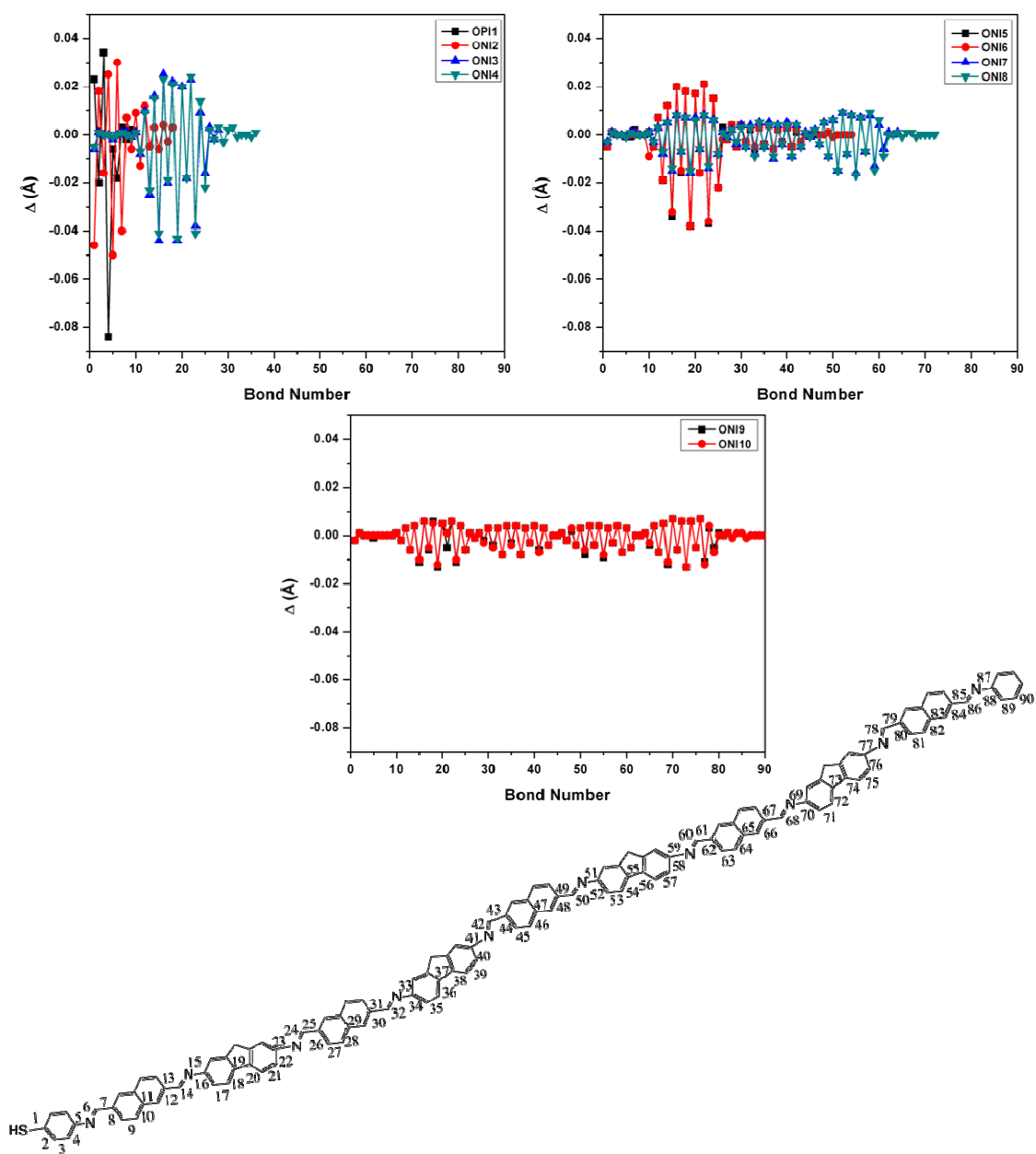


**Figure 5.14** Change in bond length on ionization in the ONI series as determined at the M062X/6-31G\*\* level of theory.

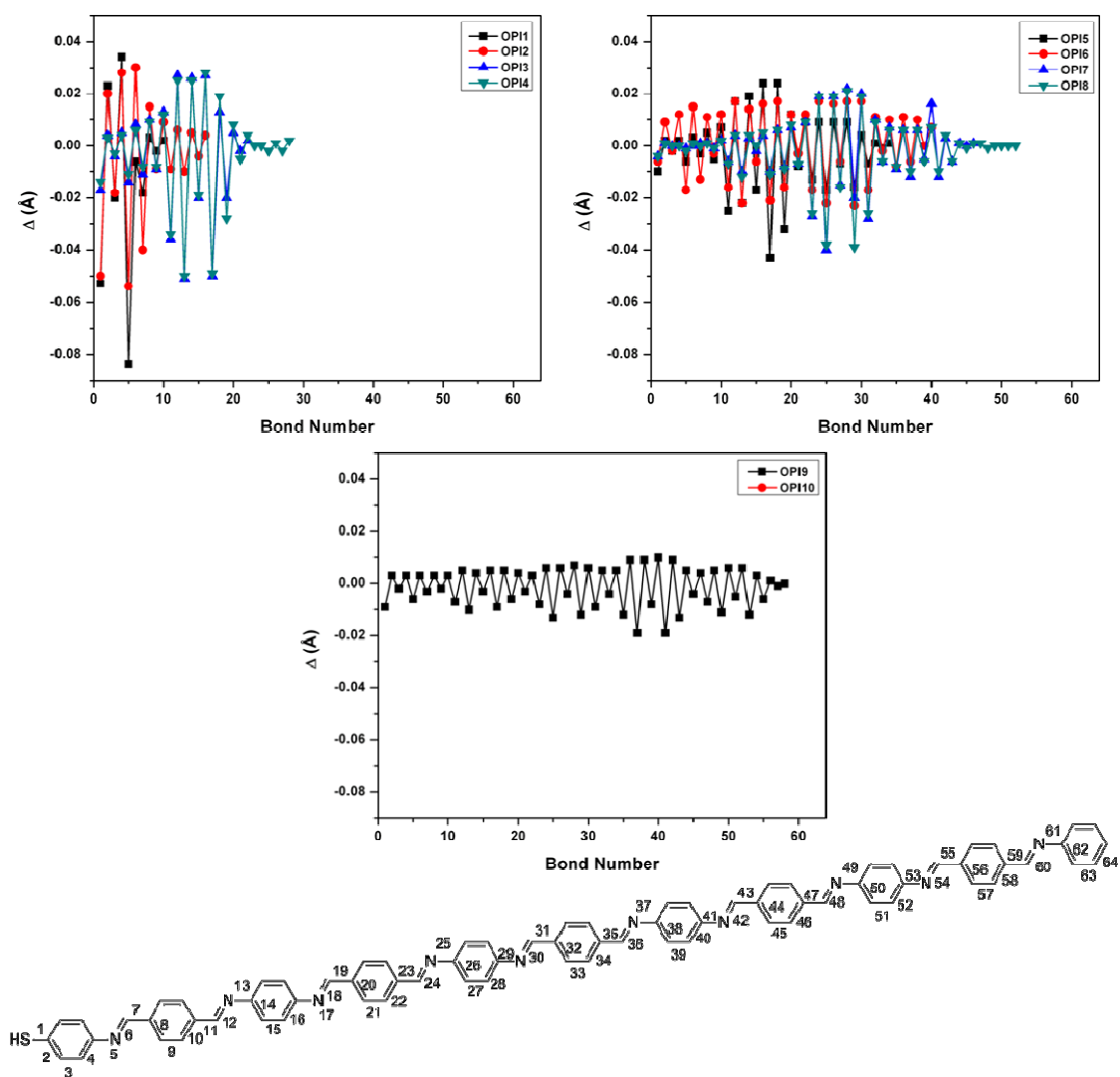


**Figure 5.15** Change in bond length on ionization in the OPI series as determined at the M062X/6-31G\*\* level of theory.

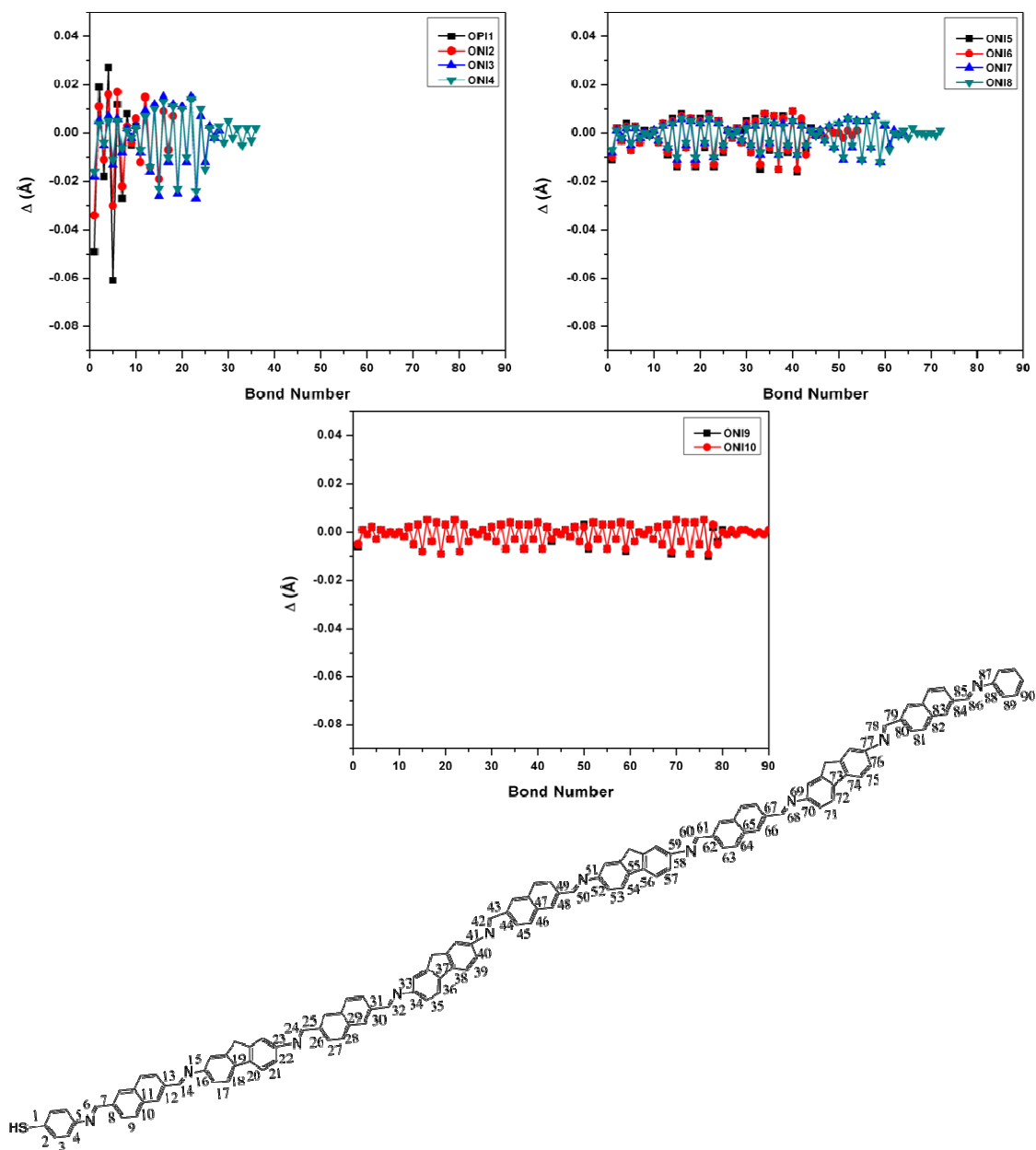


**Figure 5.16** Change in bond length on ionization in the ONI series as determined at the B3LYP/6-31G\*\* level of theory.

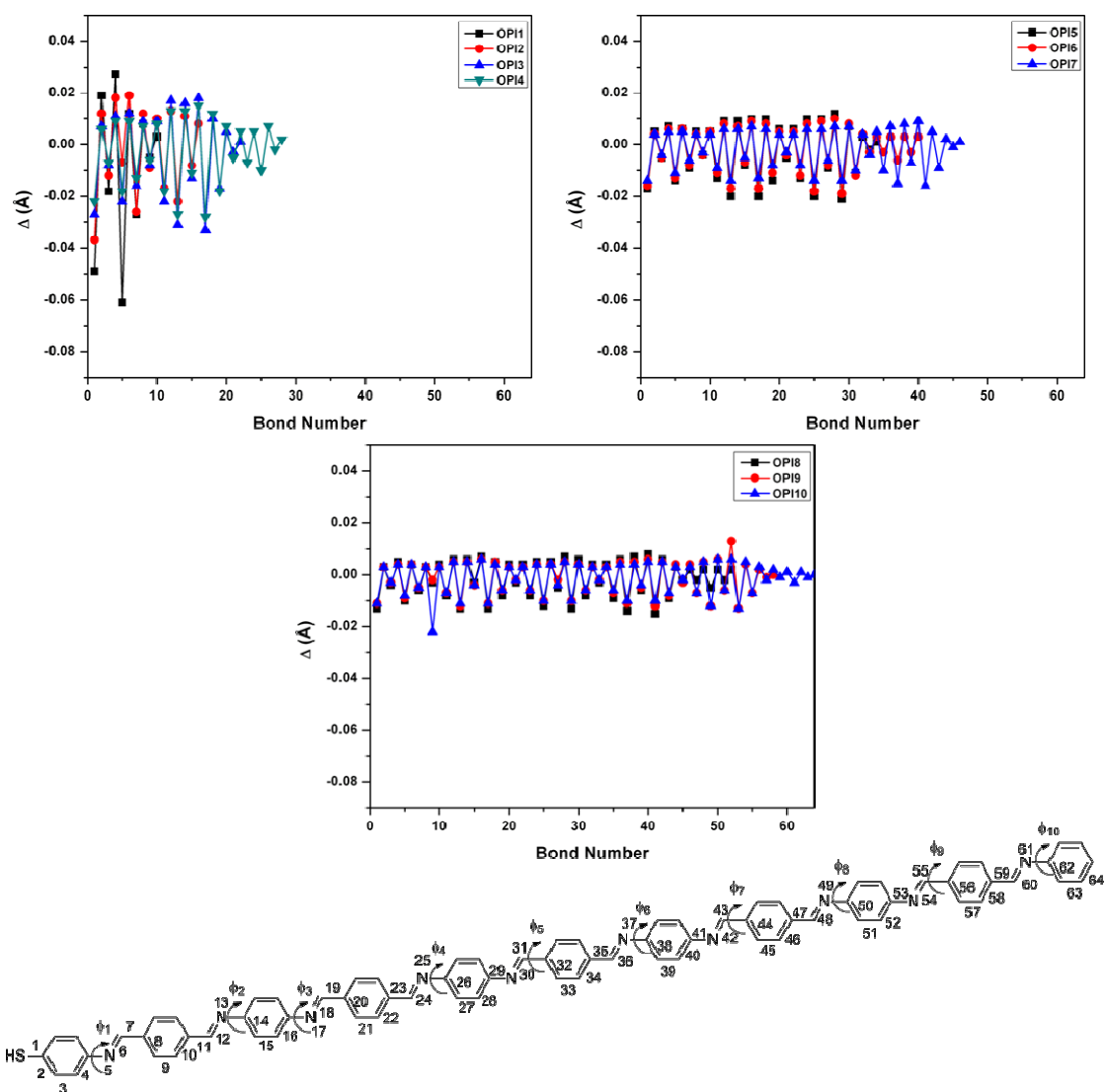


**Figure 5.17** Change in bond length on ionization in the OPI series as determined at the B3LYP/6-31G\*\* level of theory.



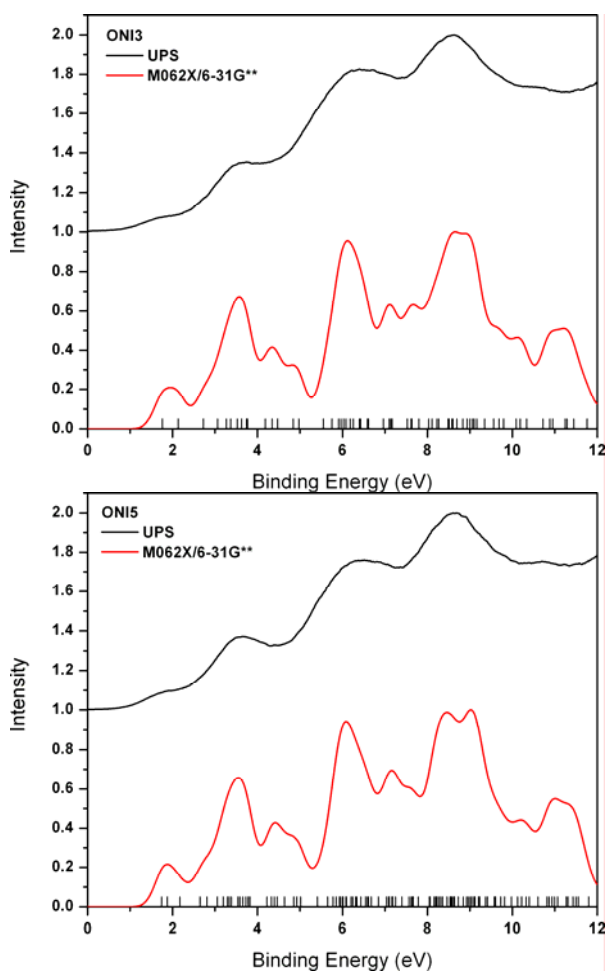


**Figure 5.18** ONI3 (left) and ONI5 (right) normalized UPS spectra and one-electron density of states as determined at the M062X/6-31G\*\* level of theory. The density of states were shifted to align with the UPS spectra: ONI3=4.78 eV; ONI5 = 4.75 eV.

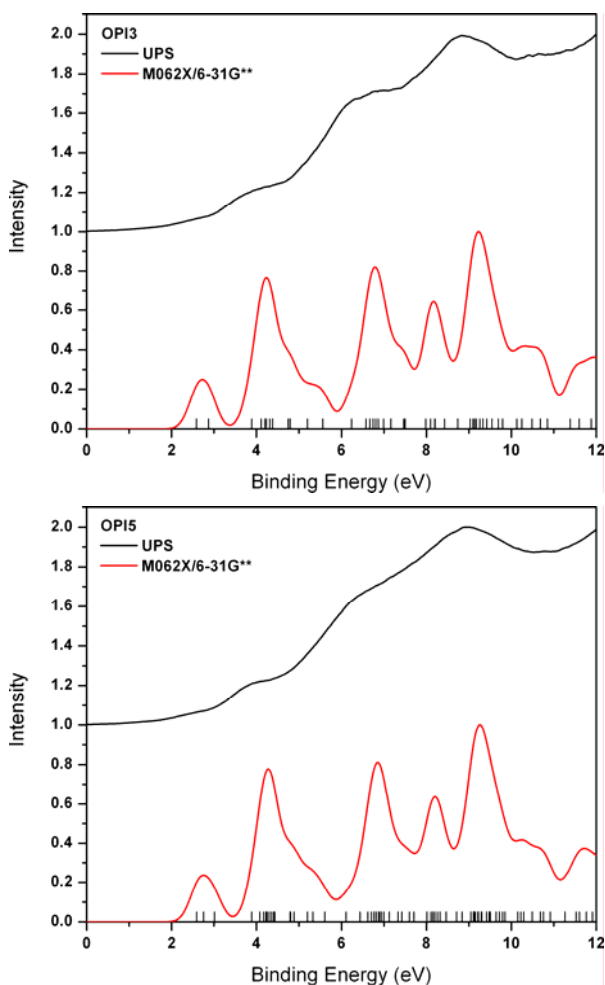


**Figure 5.19** OPI3 (left) and OPI5 (right) normalized UPS spectra and one-electron density of states as determined at the M062X/6-31G\*\* level of theory. The density of states were shifted to align with the UPS spectra: OPI3=4.22 eV; OPI5 = 4.19 eV.

## 5.5 Conclusion

We have measured DC electrical conduction in a set of conjugated oligoimine wires having systematically controlled lengths varying between 2.5 and 10.3 nm. These ONI wires exhibit electrical characteristics that are similar to previously reported OPI wires. In particular, there is a clear transition from tunneling to hopping transport near 4 nm in wire length, as evidenced by the length, temperature, and electric field dependence of the  $I$ - $V$  characteristics. The wire resistance has an activation energy of 0.54 - 0.62 eV, which

is two to three times higher than quantum chemical estimations of the reorganization energy associated with charge transfer among conjugated sub-units in single, isolated chains. Because the conductance measurements involve ~100 wire molecules, and not single wires, intermolecular interactions may play a role in conduction. Overall, these experiments confirm that the oligoimine synthesis chemistry can be used to build wires that are long enough to probe the hopping regime and they open up significant opportunities to explore the connection between molecular structure and hopping transport in long wire architectures. Current efforts are aimed at understanding the roles of inter- and intramolecular steric interactions, electronic structures, and redox properties on hopping conduction.

## 6 Long Alternating Donor-Acceptor Molecular Wires

### 6.1 *Abstract*

We have measured the current-voltage characteristics of conjugated oligotetrathiafulvalenepyromelliticdiimideimine (OTPI) wires ranging in length from 2.5 to 20.2 nm, contacted by Au electrodes. OTPI wires were designed to have alternating donors (tetrathiafulvalene, TTF) and acceptors (pyromelliticdiimide, PMDI) where the two building blocks are linked via an aryl imine group. The long OTPI wires exhibit a narrow band gap ( $< 1.5$  eV) and multiple redox states, which can facilitate the carrier injection for hopping transport. We observe the theoretically predicted change in direct current (DC) transport from tunneling to hopping as a function of systematically controlled wire length, as well as enhanced single-chain conductivity for the hopping regime. Hopping conduction is confined by length, temperature, and field dependent measurements. These nanoscale transport measurements shed light on the role of molecular length and bond architecture on molecular conductivity and open opportunities for greater understanding of electrical transport in conjugated polymer films.

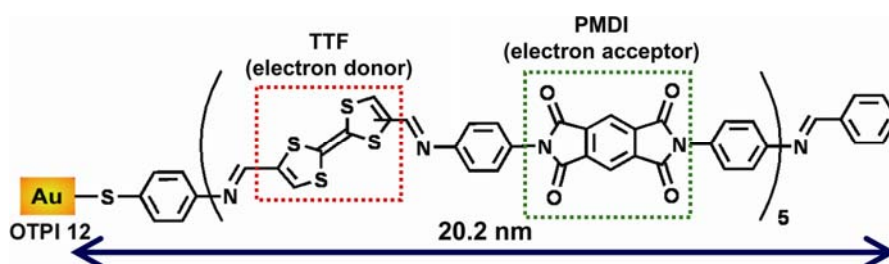
### 6.2 *Introduction*

The importance of exploring the relationship between molecular structure and hopping transport lies in future opportunities to exploit molecules in nanoelectronics and in aiding efforts to optimize conjugated polymer materials for applications in hybrid, flexible, or printed electronics. Our recent successes<sup>33, 215</sup> in building long molecular wires and measuring their direct current (DC) conduction properties suggest that a wide variety of experiments can be undertaken to probe the influence of molecular structure on hopping transport. There is now the very real and exciting possibility that we can understand electrical transport in molecular systems with unprecedented detail. One might describe this new research field as the physical organic chemistry of hopping conduction, in which classical methods of systematic structure variation are linked to measurable changes in rates of hopping transport.

Here we report a set of alternating donor-acceptor architectures within a molecular backbone. This approach may control carrier density for hopping transport. Previously built wires exhibited relatively low conductivity ( $\sim 1.0 \times 10^{-4}$  S/cm) partially due to the low carrier density.<sup>33, 215</sup> Utilizing donor-acceptor architectures<sup>216</sup> within the molecular backbone may increase the carrier concentration present in the wires. Donor-acceptor systems cause partial intramolecular charge transfer that enables manipulation of the electronic alignment (HOMO/LUMO levels), leading to low band gap systems ( $< 2.0$  eV).<sup>10, 216-220</sup> Narrow bandgap conjugated polymers often provide a unique set of redox and optoelectronic properties,<sup>217</sup> including broad and long wavelength light absorption,<sup>10</sup> solid-state transport of both holes and electrons,<sup>220</sup> and access to multiple charge states in a small potential window. A variety of researchers have sought to reduce the band gap by using a donor-acceptor approach. This method have proven to be an effective strategy for tailoring the properties of oligomers and polymers for applications in photovoltaics,<sup>221-223</sup> electrochromics,<sup>219, 224</sup> light emitting devices,<sup>225</sup> and field effect transistors.<sup>226, 227</sup> In addition, donor-acceptor structures are well known in chemistry to have rich electronic behavior. For example  $\pi$ -stacking crystals of the electron donor TTF and the electron acceptor TCNQ are metallic at room temperature due to partial electron transfer from TTF molecules to TCNQ which results in a partially filled LUMO band that facilitates high conductivity.<sup>228</sup> Likewise, the conduction properties of molecular wires built from alternation donor and acceptor sub-units offer potential opportunities to realize highly-conductive molecular wires.

Specifically, we have used alternating tetrathiafulvalene (TTF) and pyromellitic diimide (PMDI) blocks to build wires up to 20 nm in length, significantly longer than in our initial reports<sup>33, 215</sup>, (Oligotetrathiafulvalenepyromelliticdiimideimine (OTPI) wires, Scheme 6.1). TTF is chosen as a donor building block because of its interesting and versatile electrochemical properties.<sup>229</sup> The oxidation of the TTF ring system to the cation radical and dication species occurs sequentially and reversibly within a very accessible potential window.<sup>230</sup> In addition, the TTF cation radical is thermodynamically very stable because 1,3-dithiolium cation meets  $6\pi$ -electron heteroaromaticity, which contributes strong donor behavior of TTF in many charge transfer complexes. PMDI represents the smallest homolog of aromatic diimides which have been of much interest as the active

layer in organic field effect transistor because of its n-type semiconducting behavior.<sup>231</sup> PMDI also have a sufficient electron affinity<sup>232</sup> and can interact with electron rich  $\pi$ -systems such as TTF derivatives by inter/intra-molecular charge transfer in solution and the solid state regardless of the small  $\pi$ -core surface.<sup>233</sup> In particular, both building blocks exhibit well their optoelectronic properties with the absence of side functional groups, which makes less bulky in building molecular wires, facilitating to form a closely packed monolayer.



**Scheme 6.1** Molecular Structure of OTPI 12, the longest OTPI wire.

We have grown OTPI wires from one gold substrate using aryl imine addition chemistry, ranging in length from 2.5 to 20.2 nm. The addition chemistry works cleanly in every repeated step. Low optical band gaps (smaller than 1.5 eV) are achieved in long OTPI wires as expected for alternating donor-acceptor systems. As wire length increases, much rich redox properties are observed with a smaller potential gap ( $\sim 1.0$  V) between the first oxidation and reduction peak, which is consistent with the red-shift of the maximum UV-vis absorption for OTPI wires. Nanoscopic measurements using CP-AFM reveal that there is a change in transport mechanism from tunneling to hopping based on OTPI wires near 5 nm as evidenced by striking changes in the length, temperature, and electric field dependence of the current-voltage ( $I$ - $V$ ) characteristics. In longer OTPI wires, we are able to estimate  $0.02$  S/cm<sup>2</sup> of wire conductivity, nearly two orders of magnitude higher than our previous wires.<sup>33, 215</sup>

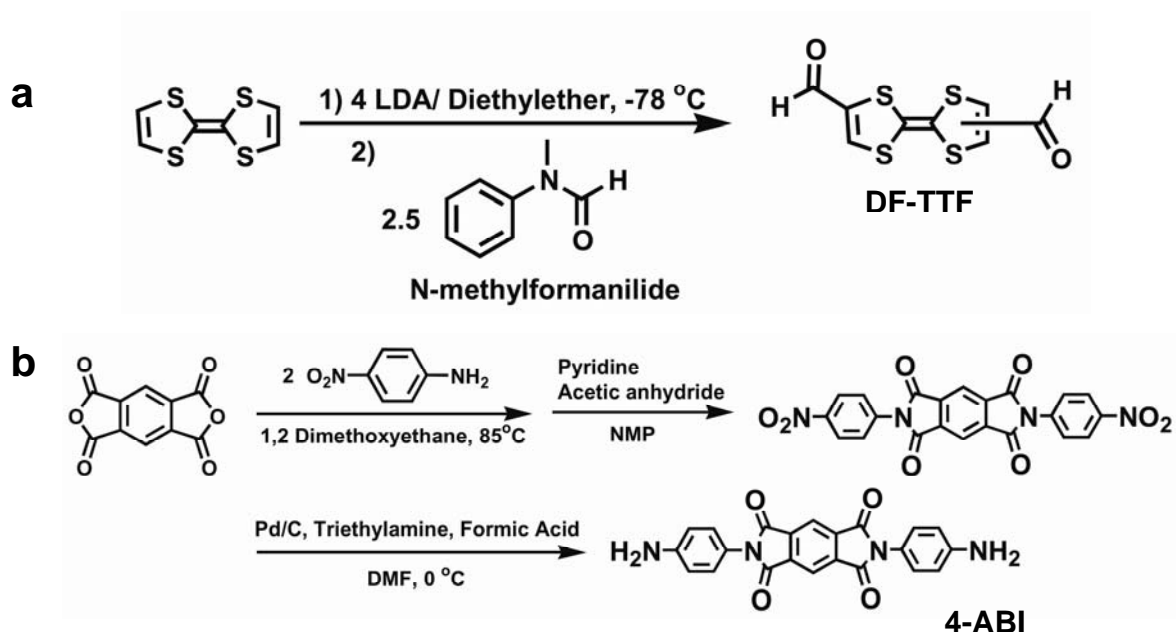
### 6.3 Experimental

**Materials** Gold nuggets (99.999% pure) were purchased from Mowrey, Inc. (St. Paul, MN). Evaporation boats and chromium evaporation rods were purchased from R. D. Matthis (Long Beach, CA). Silicon (100) wafers were purchased from WaferNet (San Jose, CA). Contact mode AFM tips (DNP or NP silicon nitride probes) were purchased

from Veeco Instruments (Camarillo, CA). Absolute ethanol was purchased from Fisher Scientific.

**Synthesis of Molecular Building Blocks** 4,4'(5')-diformyltetrathiafulvalene (DF-TTF) and N,N'-di-(4-anilino)-1,2,4,5-benzenebis(dicarboximide) (4-ABI) were synthesized as in the literatures (Synthetic schemes of DF-TTF and 4-ABI are shown in Scheme 6.2).<sup>234, 235</sup> However, we have taken a different work-up procedure for DF-TTF synthesis to acquire higher yield. The reaction mixture synthesized from 2 g of TTF was added to 200 mL H<sub>2</sub>O which was then extracted with 200 mL of CH<sub>2</sub>Cl<sub>2</sub> in a separatory funnel. The organic layer was isolated and the solvent was removed under pressure till the solution becomes almost saturated. The solvent was then dried and the crude product was purified by column chromatography (silica gel, dimethylformamide). The solvent was removed under pressure and then rinsed with copious amount of methanol. The product was dried at room temperature, yielding 1.6 g (68%). Compound is a dark red solid as a mixture of (*E*) and (*Z*) isomers. Chromatographic separation of both isomers has not been achieved.

**Growth and Characterization of Molecular Wires** The Au substrates were 1000 Å thick thin films on silicon (with a 50 Å Cr adhesion layer) prepared in a Balzers thermal evaporator at a rate of 1.0 Å/s at a base pressure of  $\leq 2 \times 10^{-6}$  Torr. The metal surfaces were immersed in 10 ml of 1 mM solutions of 4-aminothiophenol (ATP) in argon purged absolute ethanol. Self assembled monolayer (SAM) of ATP was grown for 18-24 h. After removing the sample from the solutions and immersing with absolute ethanol for a half hour to get rid of physisorbed molecules, we immersed the sample in 10 mL of 10mM of DF-TTF solution in the chromatographic grade of dimethyl sulfoxide (DMSO) with 5  $\mu$ L of HCl (37%) as an acid catalyst for 24 hours to ensure the complete formation of imine bonds. The sample was then immersed in pure DMSO for 1 hour, and the same procedure was taken in 10 mM of 4-ADI solution in DMSO. Molecular lengths of wires were controlled with the number of the alternating additions of DF-TTF and 4-ABI on Au substrates. Last, odd and even OTPI wires were end-capped respectively with benzaldehyde and aniline. All OTPI wires were rinsed with absolute ethanol and dried under a stream of N<sub>2</sub> before all measurements.



**Scheme 6.2** Synthetic routes for (a) DF-TTF and (b) 4-ABI.

OTPI wires were characterized by ellipsometry, X-ray photoelectron spectroscopy (XPS), reflection-absorption Fourier transform infrared spectroscopy (RAIRS), and cyclic voltammetry. Ellipsometry measurements were carried out on a VASE spectroscopic ellipsometer (J. A. Woolam Co., Inc.). Measurements of the polarization angles ( $\Psi$  and  $\Delta$ ) were taken as a function of wavelength ( $\lambda$ ) between 600 and 1000 nm at an incident angle of 65°. The indices of refraction ( $n(\lambda)$ ) and extinction coefficients ( $k(\lambda)$ ) of the Au-coated substrates were determined by measurement of the polarization angles prior to monolayer deposition and wire growth. The instrument software converted these values to  $n(\lambda)$  and  $k(\lambda)$  of Au films and saved them as a material file. After monolayer formation and wire growth on gold substrates, the polarization angles were measured again and the film thicknesses were determined by a built-in algorithm. The  $n(\lambda)$  and  $k(\lambda)$  of the SAMs were assumed to be 1.45 and 0, respectively, over the wavelength range.

XPS spectra were taken on a Perkin-Elmer Phi 5400 spectrometer with a Mg K $\alpha$  X-ray source (1253.6 eV) using a hemispherical analyzer in an ultrahigh vacuum ( $< 10^{-9}$  Torr) system. The X-ray anode was operated at 200 W, and the analyzer was set at a pass energy of 89.45 eV for survey scans and 17.9 eV for high-resolution scans. The binding



energy scales were referenced to the Au<sub>4f7/2</sub> peak (84.0 eV). The monolayer thickness was calculated using the relative intensities of the Au<sub>4f</sub> and C<sub>1s</sub> peak and by using hexadecanethiol SAM on Au as a reference ( $d = 1.86$  nm). Assuming the same attenuation length of gold ( $\lambda_{Au} = 3.36$  nm) and carbon ( $\lambda_C = 2.27$  nm) photoelectrons for monolayers, the calculation based on Equation 6.1 yielded the thickness.

$$\frac{\frac{I_C}{I_{Au}}(sample)}{\frac{I_C}{I_{Au}}(reference)} = \frac{\left\{1 - \exp\left(-\frac{d_{sample}}{\lambda_C}\right)\right\} \exp\left(-\frac{d_{reference}}{\lambda_{Au}}\right)}{\exp\left(-\frac{d_{sample}}{\lambda_{Au}}\right) \left\{1 - \exp\left(-\frac{d_{reference}}{\lambda_C}\right)\right\}} \quad (6.1)$$

where  $I_C$  = the intensity of C<sub>1s</sub> peaks,  $I_{Au}$  = the intensity of Au<sub>4f</sub> peaks, and  $d$  is the thickness. The estimated length and film thickness measured by ellipsometry and XPS for all OTPI wires are shown in Figure 6.4.

RAIRS was taken with a Nicolet Series II Magna-IR System 750 FTIR with a Harrick Seagull accessory for grazing angle specular reflectance measurements. The infrared beam was incident at an 84° angle with respect to the surface normal. A total of 2000 scans were collected at 1.0 cm<sup>-1</sup> resolution. RAIRS was used for monitoring step-wise imination, and was shown in Figure 6.1b and 6.2b. Cyclic voltammetry (CV) experiments were undertaken to determine the redox states of OTPI wires and to measure surface coverage. In these experiments, a three-neck electrochemical cell was used. A clean O-ring (1.0 cm diameter) in a cylindrical cavity surrounding a hole in the bottom of the cell was placed between the cell and a monolayer-coated Au substrate, which acted as the working electrode. The cell was filled with 0.2 M tetrabutylammonium hexafluorophosphate (Bu<sub>4</sub>NPF<sub>6</sub>) in purified acetonitrile which was deoxygenated by three cycles of freeze-pump-thaw treatments. A Pt wire was used as the counter electrode and the cell was referenced to a Ag wire. Prior to examining the monolayer oxidation potentials, the system was calibrated to the ferrocene oxidation potential. For each monolayer, the scan was recorded at a sweep rate of 100 mV/s and the CV curves were reproducible and stable to electrochemical cycling within the range of -2.0 – +1.5 V vs. Ag wire. In addition, the surface coverage ( $\Gamma$ ) was determined according to the following Equation 6.2:

$$\Gamma = \frac{Q}{nFA} \quad (6.2)$$

where  $Q$  is the charge injected into the SAM,  $n$  is the number of electrons involved in the electron-transfer process,  $F$  is the Faraday constant, and  $A$  is the surface area of the monolayer examined, that is, the area inside of the O-ring.  $Q$  was obtained by integrating the area under the forward cyclic voltammogram using the first oxidation wave for each wire. Cyclic voltammograms of selected OTPI wires are displayed in Figure 6.5. Oxidation potentials and the estimated surface coverages for all OTPI wires are compiled in Table 6.1.

**Determination of Molecular Energy Levels.** The electronic structures of OTPI wires were determined by UV-visible spectroscopy experiments. UV/visible absorption spectra were taken of the molecular films on semi-transparent thin gold films using Beckman Coulter DU720 UV/visible spectrometer. 20 nm thick gold films were thermally deposited on a plastic UV cell which has the solvent resistance against DMSO. Molecular films were formed on the gold film in the same way described previously. Figure 6.6 shows the UV/visible absorption spectra for selected OTPI, and their optical gaps obtained from the absorption edge are given in Table 6.1.

**CP-AFM Junction formation and measurement.** Molecular junctions were formed by bringing a gold-coated tip into contact with a monolayer, as illustrated in the inset of Figure 6.7a. These experiments were performed with a multimode AFM from Veeco Instruments in a glove box ( $O_2 < 8$  ppm). 1 nN of a load force was used to make a soft contact. Gold-coated tips were prepared as reported previously. We have examined  $I$ - $V$  characteristics of OTPI wires up to  $\pm 0.2$  V for OTPI 1,  $\pm 0.5$  V for OTPI 2,  $\pm 1.0$  V for OPI 3–5, and  $\pm 1.5$  V for OTPI 6–12. The resistance was determined from the linear current-voltage relationship within the range of  $\pm 0.05$  V. Four gold-coated AFM tips having a radius of  $\sim 50$  nm were used for the measurements, each of which gave the same resistance value for tunneling through an octanethiol SAM (an effective calibration standard). The four tips were used separately to examine three sets of wires: OTPI 1–3 (tip 1), OTPI 3–7 (tip 2), OTPI 7–10 (tip 3), and OTPI 10–12 (tip 4). Note that OTPI 3, 7 and 10 were each measured with two different tips to confirm that the same resistances

were obtained. The number of molecules in each junction was estimated from the size of the tip radius and the wire surface coverage to be  $\sim 100$ .

Variable temperature measurements of the OTPI wire resistances were performed with an environmentally controlled Molecular Imaging PicoScan/PicoSPM. We have checked that the tunneling current of the octanethiol SAM remains constant within an error range<sup>236</sup> from  $-30\text{ }^{\circ}\text{C}$  (243 K) of a setpoint temperature to room temperature in  $< 5\%$  RH of chamber humidity. Two different sample stages, a normal heating stage and a peltier stage were used to vary temperature above and below room temperature, respectively. Silver paste was painted at the edge of each sample to make thermal contact between the sample and stage. The measured temperatures on samples were consistent with the setpoint temperatures. The resistances shown in Figure 6.8 were determined from linear current-voltage relationships within the range of  $\pm 1\text{ mV}$  for OTPI 1 and 2, and  $\pm 0.05\text{ V}$  for OTPI 3, 6, 9, and 12, and they are the average values of resistances obtained at six different locations on the samples. The current-voltage curves of OTPI 1, 2, 3, 6, and 9 at different temperatures are shown in Figure 6.9. The current-voltage curves of OTPI 12 are displayed in Figure 6.11. Two gold-coated AFM tips having a radius of  $\sim 50\text{ nm}$  were used for the measurements, each of which gave the same resistance value for tunneling through an octanethiol SAM and OTPI 2. The two tips were used separately to examine the resistances of OTPI 1, 2, 3, 6, 9, and 12 in two temperature ranges:  $245\text{--}293\text{ K}$  (tip 1), and  $303\text{--}333\text{ K}$  (tip 2). Note that all measurements were performed while keeping the humidity of chamber below  $5\%$  RH.

## 6.4 Results and Discussion

**Growth and Characterizations of Molecular Wires** OTPI wires were prepared from a gold substrate using the aryl imine chemistry with alternate addition of 4,4'-(5')-diformyltetrathiafulvalene (DF-TTF) and N,N'-di-(4-anilino)-1,2,4,5-benzenebis (dicarboximide) (4-ABI). Figure 6.1a shows the molecular structure of OTPI wire precursors (OTPIp) up to 5<sup>th</sup> layers, and their synthetic routes. The rest of molecular structures for longer wires and their procedures are shown in Figure 6.2a. Each OTPIp wire terminated with  $-\text{NH}_2$  or  $-\text{CHO}$  groups was end-capped with benzaldehyde or

aniline, respectively. The end-capping provided a consistent terminal group throughout the OTPI series that facilitated reproducible electrical characterization.

The growth of wires was monitored using reflection-absorption Fourier transform infrared spectroscopy (RAIRS). The RAIRS data, shown in Figure 6.1b reveal the alternate appearance and disappearance of carbonyl stretches ( $1680\text{ cm}^{-1}$ ) in aldehyde terminal group and symmetric amine stretches ( $3370\text{ cm}^{-1}$ ) in OTPIp molecules up to 5<sup>th</sup> layers (Figure 6.1b) and 12<sup>th</sup> layers (Figure 6.2b), which verified the imination mechanism and indicated near quantitative reaction of all exposed reactive endgroups. The intensity of imine stretching ( $1610\text{ cm}^{-1}$ ) and the benzene ring vibrational mode ( $\sim 1500\text{ cm}^{-1}$ ) increased with the number of repeat units, as expected. The intensity of carbonyl stretches in imide group ( $1730\text{ cm}^{-1}$ ) increased with the number of PMDI units incorporated in OTPI wires. Complete end-capping was confirmed by the disappearance of the terminal group vibrational modes as shown in Figure 6.2b.

In addition, OTPI monolayers were extensively characterized by ellipsometry, X-ray photoelectron spectroscopy (XPS), cyclic voltammetry (CV), and UV-vis spectroscopy. Key results are shown in Figure 6.3– Figure 6.5, and compiled in Table 6.1. Figure 6.3a shows the estimated molecular length and the measured thickness from ellipsometry and XPS for all OTPI wires. While monolayer thicknesses from ellipsometry have a very nice correlation with the estimated length, the thicknesses measured by XPS are deviated from the corresponding estimated length, regardless of the increasing trace with wire lengths. The thickness measured by XPS can be underestimated because we only take the relative intensity of C 1s to Au 4f in the calculation of molecular thickness. It is important to note that the photoelectron intensity emitted from hetero atoms (S 2p, N 1s, O 1s) also increase with the number of repeated units as shown in Figure 6.3b. All binding energy scales were referenced to those of the metal substrate (Au  $4f_{7/2}$  at 84.0 eV). We fitted each spectrum using a combination of Gaussian and Lorentzian line shapes. In particular, the S 2p spectra for shorter OTPI wires (up to 5<sup>th</sup> layer) were decomposed with a pair of peaks at about 164 and 161 eV, which represent sulfurs in TTF and the bound thiol with gold, respectively. However, S 2p spectra at  $\sim 161\text{ eV}$  displays less distinct for longer wires because of the intensity attenuation from the bounded thiol. Overall we suggest that OTPI wires have grown in

keeping with their upright (essentially untilted) orientation as wire length increases up to 20 nm.

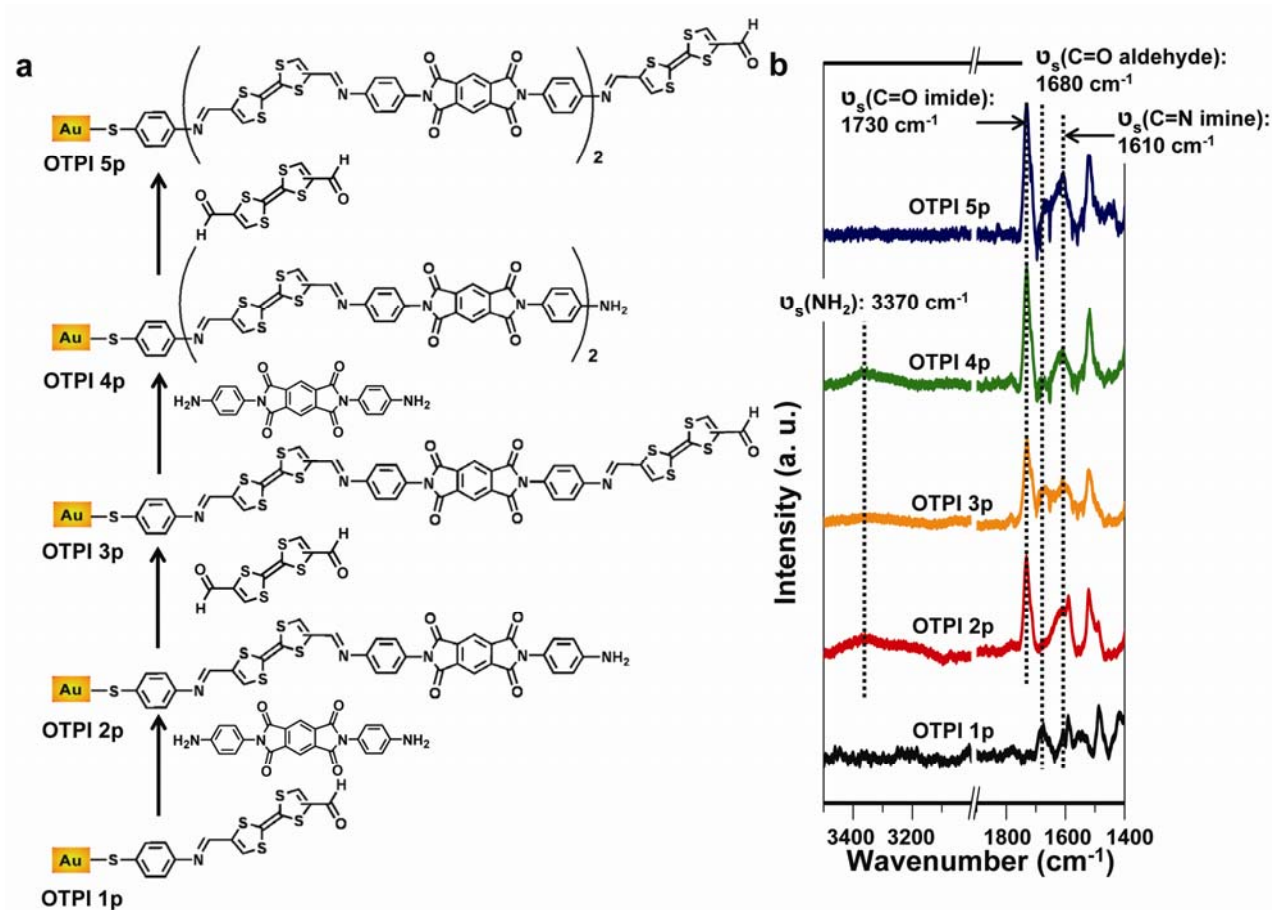


**Figure 6.1** (a) Molecular structure and synthetic route to OTPI *p* on gold substrates up to 5<sup>th</sup> layers. (b) RAIRS spectra of OTPI-*p* monolayers up to 5<sup>th</sup> layers.

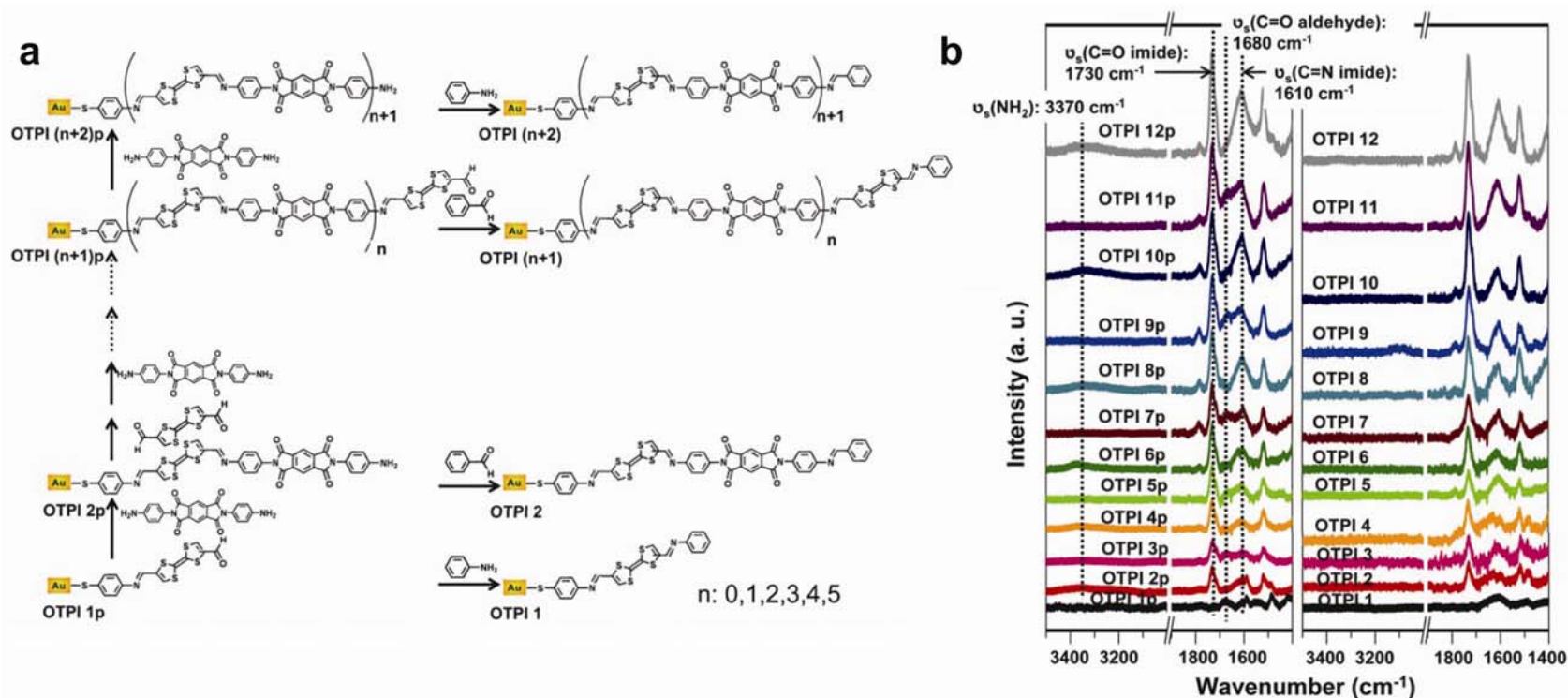


**Figure 6.2** (a) Molecular structure and synthetic route to OTPI-p and OTPI monolayers on gold substrates. (b) RAIRS spectra of OTPI-p (left) and OTPI monolayers (right). Vertical dashed lines indicate positions of symmetric amine stretches ( $\text{NH}_2$ , 3370  $\text{cm}^{-1}$ ), carbonyl stretches ( $\text{C}=\text{O}$ , 1680  $\text{cm}^{-1}$  in aldehyde,  $\text{C}=\text{O}$ , 1730  $\text{cm}^{-1}$  in imide), and imine stretches ( $\text{C}=\text{N}$ , 1610  $\text{cm}^{-1}$ ). Peaks for  $\text{NH}_2$  and  $\text{C}=\text{O}$  disappear after OTPI-p wires were end-capped with aniline and benzaldehyde for odd and even layers, respectively.

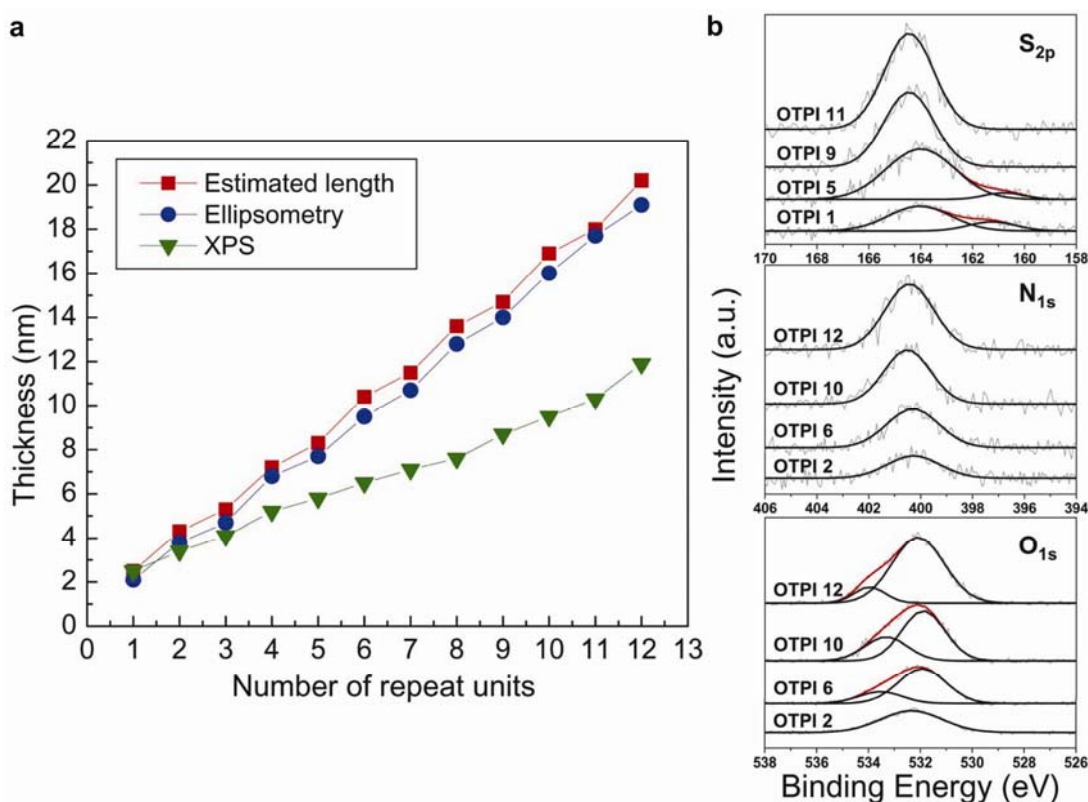


**Figure 6.3 (a)** The measured thicknesses and estimated lengths for OTPI wires as a function of the number of repeat. Blue circles and green inverse triangles indicate the measured thickness respectively by ellipsometry and XPS. The estimated lengths are represented in red squares and obtained with the Cambridge Scientific Chem3D software. Molecular length is the terminal H to S distance plus the Au-S bond length. It was assumed that Au-S bond length is 2.36 Å. **(b)** High resolution XPS spectra in the S 2p region (top), the N 1s region (middle), and the O 1s region (bottom) for the selected OTPI wires at different lengths. In each scan, light gray lines represent experimental data, and black and red lines show individual contributions and overall fit, respectively.

Cyclic voltammograms (CV) of selected OTPI wires are displayed in Figure 6.4. The potentials of the first oxidation/reduction states and the estimated surface coverage for each OTPI wire are tabulated in Table 6.1. For OTPI 1, no reduction was detected within the solvent electrochemical window. For longer OTPI wires which incorporates with electron acceptor units (PMDI blocks), all oxidation and reduction peaks were reversible within the range of -2.0–0.8 V versus ferrocenium/ferrocene ( $\text{Fc}^+/\text{Fc}$ ). As we

emphasized in the introduction, TTF is a reversible, stable two-electron donor (see the inset scheme in Figure 6.4a). Two reversible oxidation peaks were thus observed with OTPI 1 as shown in Figure 6.4a. In addition, they shift to lower potentials by  $\sim 0.4$  V compared to the DF-TTF (the red line in Figure 6.4a), which is largely expected based on the increased conjugation length. This also confirms that the imine addition chemistry on a gold substrate works well with TTF building blocks because the strong withdrawing effect of non-reacted aldehyde terminal groups prevents the oxidation potential from shifting to lower potential. Once PMDI moieties incorporate in the molecular backbone (after OTPI 2), the reduction features begin to appear within a stable potential window as displayed in Figure 6.4b. Importantly, the potential gap between the first oxidation and reduction, an electrochemical bandgap ( $\Delta E_{\text{HOMO-LUMO}}$ ) is significantly reduced from 1.6 V to 1.0 V as wire lengths increase (Figure 6.4b and Table 6.1), which accounts for the increased conjugation of system.

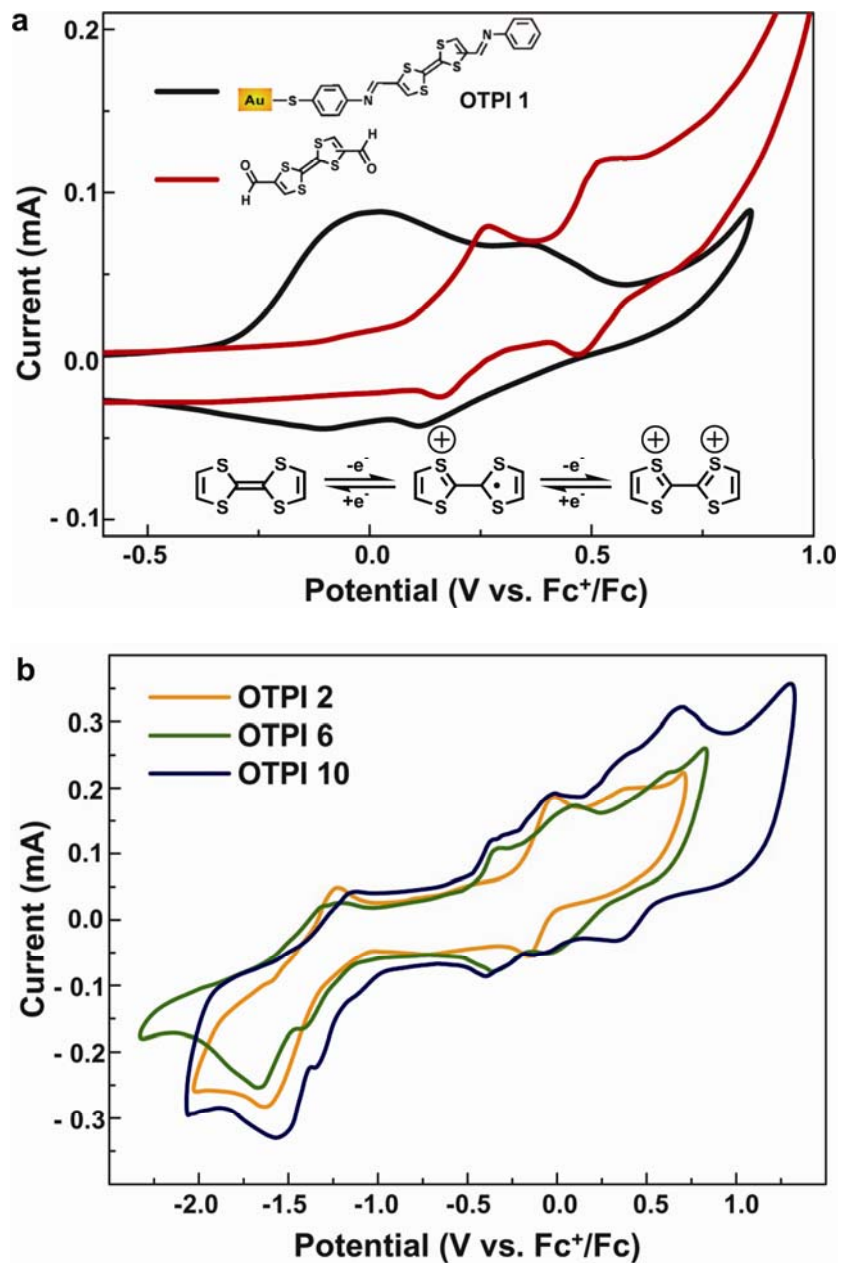
Furthermore, the CV sweeps of long OTPI wires show much richer redox properties than shorter wires. As shown in Figure 6.4b, multiple charge states (four oxidations and two reductions) are accessible for OTPI 10 in less than 3 V of the potential window, whereas two oxidations and one reduction are observed for OTPI 2 within the same potential window. Nevertheless, the surface coverage obtained from the first oxidation peak is nearly identical over the entire set of wires ( $2.1 \times 10^{-10}$  to  $5.6 \times 10^{-10}$  mol/cm<sup>2</sup>). These surface coverage data indicate that the number of molecular wires contacted by the electrodes in junction experiments varies by a factor of 2 or so, and thus differences in the magnitude of measured current cannot be explained by surface coverage arguments in the analysis of CP-AFM data. Collectively, the surface characterization data indicate that high-quality monolayers of OTPI wires were prepared.

Figure 6.5 shows the UV-vis absorption spectra for selected OTPI wires. As established with a variety of donor-acceptor polymers and charge transfer complexes, the absorptions for OTPI wires are observed in a broad range of wavelength, which reveals the narrow optical band gap up to 1.3 eV. Potential mixing of the HOMO and LUMO levels of the donors and acceptors respectively lead to “low bandgap” wires. Optical band gaps ( $E_g$ ) for each OTPI wire deduced from the onset of the lowest absorption band are listed



in Table 6.1. They are in fairly good agreement with the redox potential differences ( $\Delta E_{\text{HOMO-LUMO}}$ ) from CV sweeps (see Table 6.1). The disparity between the electrochemical and optical band gap (smaller  $\Delta E_{\text{HOMO-LUMO}}$  than  $E_g$ ) is often reported in many donor-acceptor dyads based on TTF and aromatic diimide.<sup>237-239</sup> None of these literatures clearly explain this point. We propose that it can be attributed by different localization of orbital density in HOMO and LUMO for OTPI wires. In fact, Gao, X. *et al.*<sup>240</sup> shows DFT calculation for HOMO and LUMO of dibenzoTTF bisimides; the largest coefficients in the HOMO are mainly located on the central TTF core, whereas, the coefficients in the LUMO are mostly localized on two imide rings. Indeed, the close proximity between HOMO and LUMO orbital density is important to determine the band gap.<sup>239</sup> What we found for  $E_g$  of OTPI wires perhaps corresponds to the optical transition from HOMO-1 or 2 to LUMO, where their orbital densities are similarly localized.<sup>238</sup> Note that  $\Delta E_{\text{HOMO-LUMO}}$  rather depends on the interaction between electrolytes and accessible redox states than the positions between HOMO and LUMO orbital density.

In particular, the maximum absorption peaks shift to the longer wavelength as wire lengths increase (2.3 to 1.9 eV, see the dotted arrow in Figure 6.5). This bathochromic shift was not observed with our previous wires based on phenylene imines<sup>33</sup> and naphthalene/fluorene imines,<sup>215</sup> which electronic delocalization extends only over three repeating units because of their twisted conformations. OTPI wires perhaps have more planar conformation than our previous wires because the five-membered ring in TTF have less steric interaction with imine bonds than phenylene ring does. As we will discuss below, more planar geometry of OTPI wires correlates with lower activation energy of hopping conduction.



**Figure 6.4** Cyclic voltammograms of selected OTPI wires. The reference and counter electrodes were Ag wire and Pt gauze, respectively. The scan rate was 100 mV/s.

**Table 6.1** Redox properties and energy level alignments of OTPI wires. Redox potential differences were determined from the potential gap of the first oxidation/reduction peak (peak to peak) for OTPI wires, referenced to ferrocenium/ferrocene ( $\text{Fc}^+/\text{Fc}$ ). The optical

Monolayer	First Oxidation Potentials, $E_{1\text{Ox}}^{1/2}$ (V)	First Reduction Potentials, $E_{1\text{Red}}^{1/2}$ (V)	Surface Coverage ( $\times 10^{-10}$ mol/cm <sup>2</sup> )	$\Delta E_{\text{HOMO-LUMO}}$ (V)	$E_g$ (eV)
OTPI 1	-0.07	-	5.1	-	1.70
OTPI 2	-0.09	-1.69	5.6	1.60	1.59
OTPI 3	-0.13	-1.65	4.9	1.52	1.53
OTPI 4	-0.15	-1.55	3.8	1.40	1.36
OTPI 5	-0.21	-1.55	4.2	1.34	1.36
OTPI 6	-0.28	-1.45	3.4	1.17	1.35
OTPI 7	-0.30	-1.45	3.1	1.15	1.35
OTPI 8	-0.30	-1.41	3.2	1.11	1.35
OTPI 9	-0.32	-1.39	2.9	1.07	1.32
OTPI 10	-0.31	-1.36	2.6	1.05	1.30
OTPI 11	-0.34	-1.32	2.8	0.98	-
OTPI 12	-0.35	-1.32	2.1	0.97	-

gap was obtained from the edge of UV-vis absorption.

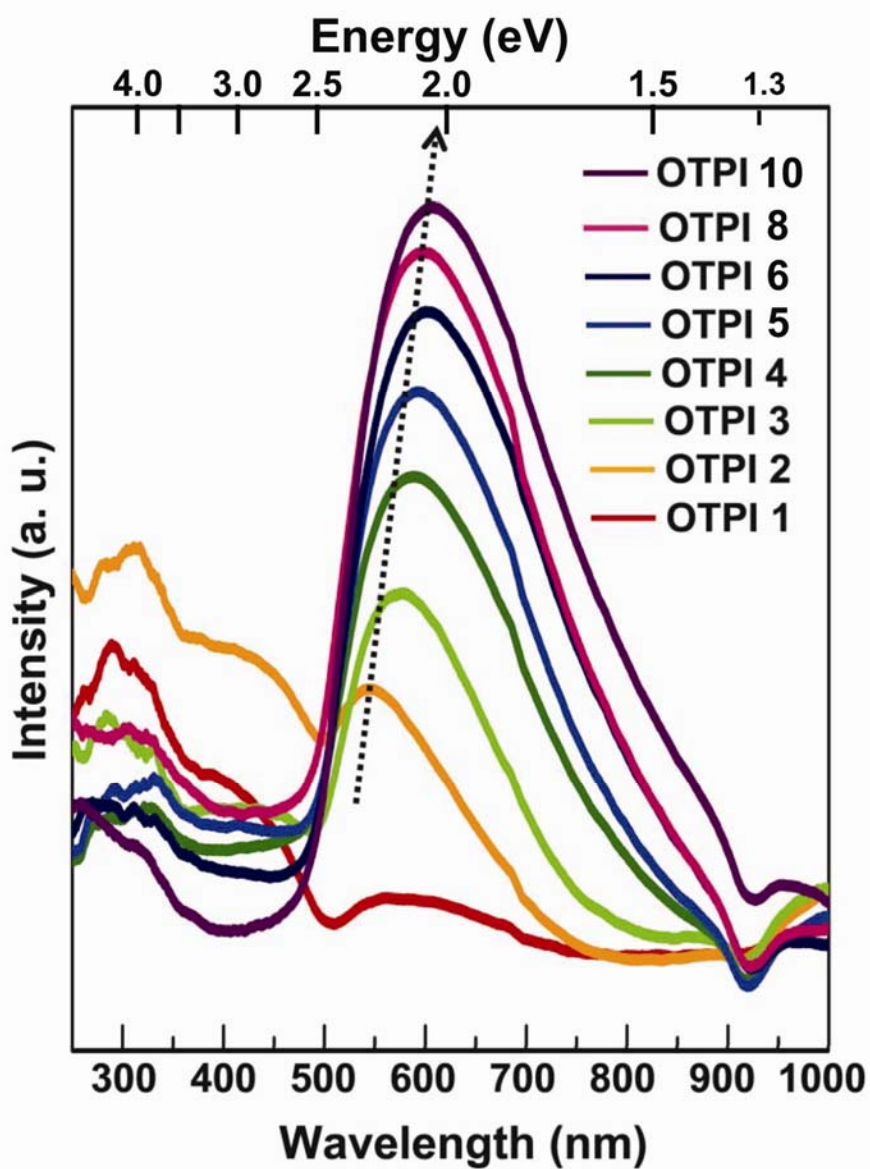


**Figure 6.5** UV-vis absorption spectra of selected OTPI wires. The dotted arrow indicates the increase of maximum absorption wavelength with wire lengths. UV-vis spectra of OTPI 11 and 12 are not available because a layer of gold coated on plastic cuvette became unstable for such a long period of wire growth (> 260 hrs) in DMSO solution.

### Electrical Characterization of OTPI wires (Low Bias Resistances)

**Length Dependent Resistances** We investigated the transport characteristics of OTPI wires using CP-AFM (inset Figure 6.6a), which has been used to measure conduction in a variety of molecular systems.<sup>26, 81, 82, 118</sup> The resistance was determined using gold-coated AFM tips in contact with the OTPI wires grown on gold substrate. The applied load force was less than 1 nN to make a soft contact. A current-voltage ( $I$ - $V$ ) sweep generally yields a sigmoidally shaped curve as will be shown later, but over a very small voltage range ( $\pm 0.05$  V) the response is linear. The resistances shown in Figure 6.6 are low voltage resistances determined over this small voltage range, and averaged for 20  $I$ - $V$  traces. Figure 6.6a shows the semi-log plot of resistances ( $R$ ) versus molecular length ( $L$ ) for entire OTPI wires. A clear transition in length dependence of resistance is observed near 5 nm, which suggest a change of transport mechanism as we have seen in our previous systems.<sup>33, 215</sup> While resistances for short wires (OTPI 1–3) exponentially increase with lengths, resistances in long wires (OTPI 3–12) are much less sensitive to the wire lengths. For short wires, the exponential increase of resistances is well characterized by non-resonant tunneling process, described by

$$R = R_0 \exp(\beta L) \quad (6.3)$$

where  $R$  is the junction resistance,  $R_0$  is an effective contact resistance,  $L$  is molecular length, and  $\beta$  is the tunneling attenuation factor that depends on the nature of bonding in the molecular backbone. The  $\beta$  value obtained from a linear fit of data is found to be  $2.5 \text{ nm}^{-1}$ , within a range of  $\beta$  observed in typical conjugated systems.<sup>17, 22, 188</sup>

For long wires, the resistances linearly depend on the molecular length as shown in a linear plot of  $R$  versus  $L$  (Figure 6.6b), which suggests that hopping transport prevails in wires. Importantly, the wire conductivity estimated from slope in a linear fit of Figure 6.6b is  $2.4 \times 10^{-2} \text{ S/cm}$ , more than two orders of magnitude higher than our previous oligoimine wires ( $\sim 1.0$ - $1.8 \times 10^{-4} \text{ S/cm}$ ).<sup>33, 215</sup> Indeed, this alternating donor-acceptor approach reveals the enhanced conductivity perhaps because of larger amount of carriers and/or the increased carrier mobility. Significant lowering of the optical band gap and ease access of multiple redox states, as evidenced by UV-vis spectra and CV sweeps

respectively, allows either holes or electrons to be readily injected into OTPI wires through a smaller energy barrier. As the increase of conjugation length is proven to be continuous over 10 repeat units for OTPI wires, spanning around 17 nm (see Figure 6.5), the conformation of OTPI wires can be more planar than previous ones, which may lead to the enhanced carrier mobility. This speculation is also consistent with a significant decrease of hopping energy for OTPI wires, as we will discuss in the following section.

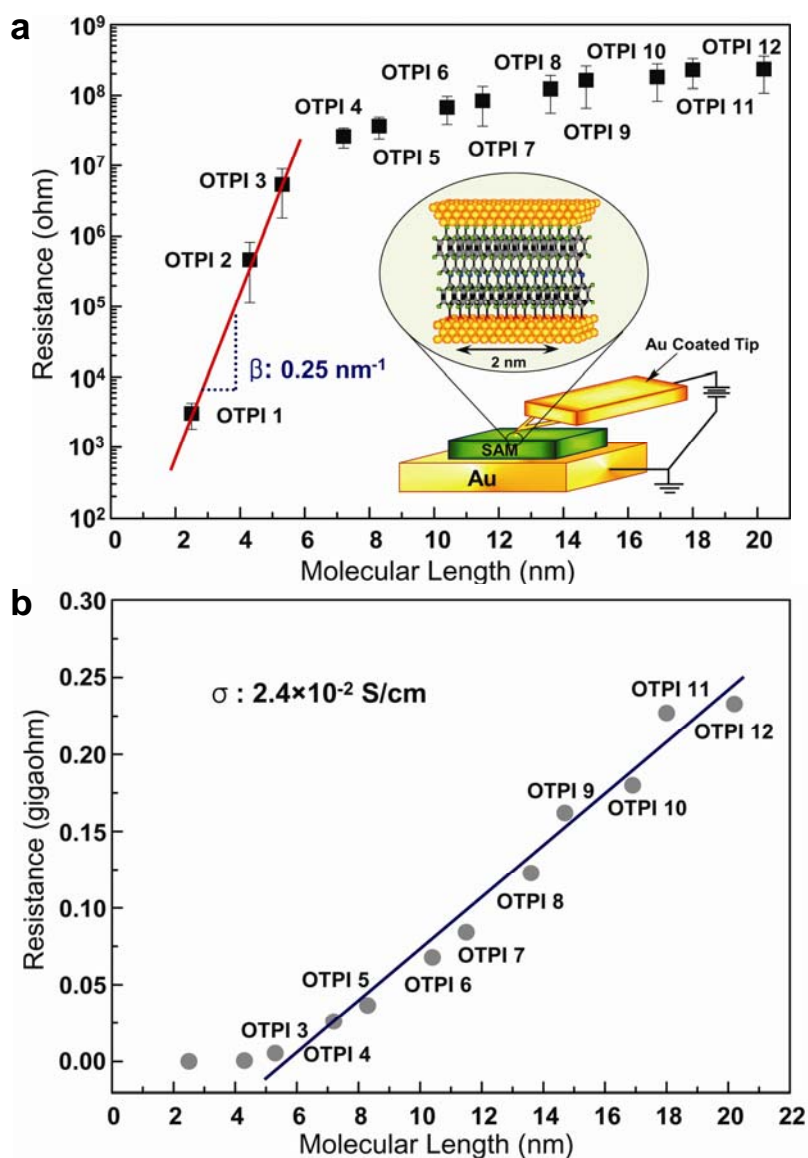


**Figure 6.6** Measurements of molecular wire resistance with conducting probe atomic force microscopy (CP-AFM). **(a)** Semilog plot of  $R$  versus  $L$  for the gold/wire/gold junctions. Each data point is the average differential resistance obtained from 20  $I$ - $V$  traces in the range  $-0.05$  to  $+0.05$  V. Error bars represent one standard deviation. A straight line is a linear fit to the data according to Eq. 6.3. Inset: A gold coated tip was brought into contact with an OTPI monolayer on a gold substrate. **(b)** A linear plot of  $R$  versus  $L$  for the gold/wire/gold junctions. A straight line is a linear fit to the data.

**Temperature Dependent Resistances** Although a change in transport mechanism is apparent in the  $R$  versus  $L$  plot, the temperature dependence is key to verify different transport mechanisms. Figure 6.7 shows an Arrhenius plot of  $R$  versus the inverse of temperature ( $T$ ) for selected OTPI wires. Their  $I$ - $V$  curves are given in Figure 6.8. Clearly, the resistance for OTPI 1 is independent of temperature from 246 to 333 K, as expected for tunneling. For OTPI 2, the resistances are seemingly not independent of temperature over entire  $T$  range. The resistances from 313 to 333 K exhibit the activated behavior with the activation energy of 0.45 eV, and have flatter relationship at lower temperature ( $< 298$  K). This transition can be either simply an experimental error or characterized by a change in charge transport from tunneling at low  $T$  to hopping at high  $T$ . Selzer *et. al.*<sup>30, 36</sup> observed this characteristic transition at very low  $T$  ( $\sim 100$  K) in molecular junctions incorporating with individual molecules of 1-nitro-2,5-di(phenylethynyl-4'-mercapto) benzene (NDB). They claimed, however, that a transition to hopping is suppressed once a few thousands of molecules incorporate in a junction.<sup>36</sup> Hopping processes can be driven by phenyl ring fluctuations of NDB, but the torsional modes of phenyl rings have the restricted amplitudes in a close packed matrix. For OTPI 2, however, there are good reasons to take the transition to hopping into account at  $\sim 313$  K. First, we have a higher transition temperature, which may have enough thermal energy to induce molecular motions for hopping events. Also, OTPI 2 does not have a side functional group like a nitro group in NDB, which allow ring fluctuations to occur above 313 K even in a close packed matrix because of its less steric nature than NDB. More data points at higher  $T$  ( $> 333$  K) might be necessary to conclude this argument, but

unfortunately a nanoscale contact formed by CP-AFM becomes unstable at higher than 333 K due to the problem of fast tip-drift by thermal energy. Nevertheless, resistances of OTPI 2 are independent of temperature, the characteristic of tunneling at around room  $T$  (298 K).

OTPI 3 and longer wires (OTPI 6, 9, and 12) displays strongly thermally activated transport, characteristic of hopping as shown in Figure 6.7. The activation energies ( $E_a$ ) determined from the slopes of the data are however smaller at 0.27 eV (6.3 kcal/mol) for relatively longer wires (OTPI 9 and 12) than at 0.41 eV (9.5 kcal/mol) for shorter wires (OTPI 3 and 6). The difference of the hopping energy by 140 meV in two length regimes perhaps correlates with changes in polaron (localized ionic radicals formed by carrier injection from contacts) conformation associated with contact effects. The equilibrated geometry (*i.e.* bond lengths and bond angles) of polarons could be significantly altered in two length regimes. It has been known that polarizable response of given dielectric media between two metals depends on the gap distance between metals.<sup>179</sup> For example, it is realistic that the average dielectric constant ( $\epsilon$ ) assumes to be 10 in the nanogap while the same media can have  $\sim 1$  of the averaged dielectric constant in gas phase.<sup>179</sup> In this regard, we suggest that electron clouds of polarons in close proximity of metal surface (OTPI 3 and 6) are more polarizable than those of polarons in longer length regime (OTPI 9 and 12). Therefore, polaronic conformation is far more distorted up on hopping events in shorter length regime (higher polarizability), which result in the increased reorganization energy. In other words, more energy of 140 meV is required to compensate additional molecular distortion up on charge hopping in shorter length regime (highly polarizable media). This difference of charge transport in two length regimes is also manifested in  $I$ - $V$  characteristics, which will be discussed in the next section.

Nevertheless, the obtained activation energy is significantly reduced by 70–160 meV in comparison with our previous wires ( $E_a = 0.54$ – $0.64$  eV).<sup>33, 215</sup> The lowering of hopping energy can be explained to be a consequence of more planar conformation for OTPI wires than for previous ones. UV-vis spectra of OTPI wires suggest that there are strong couplings of electronic wavefunction through atomic orbitals of wires over long



distance, spanning 17 nm, which also contributes higher conductivity of OPTI wires compared to the others.<sup>33, 215</sup>

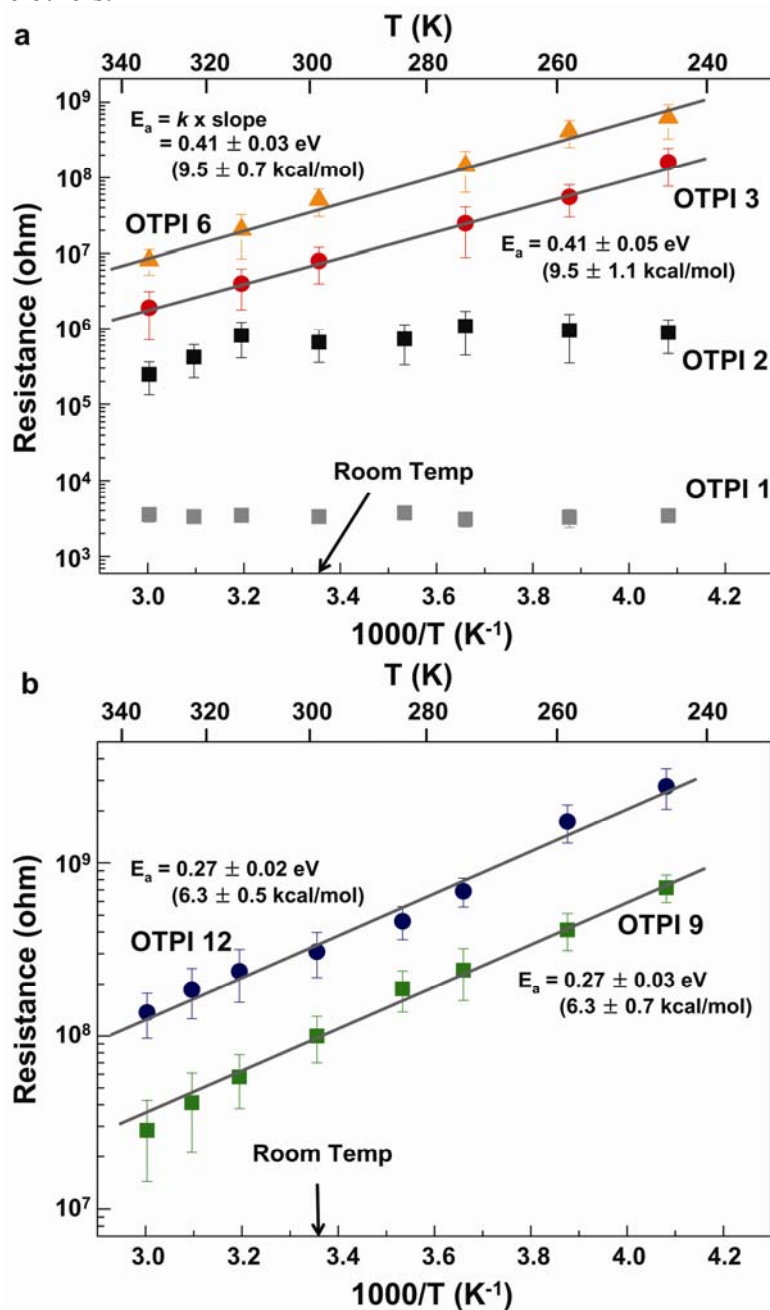


**Figure 6.7** Arrhenius plot for (a) OTPI 1, 2, 3 and 6 (b) OTPI 9 and 12. Each data point is the average differential resistance obtained at six different locations of samples in the range  $-1.0$  to  $+1.0$  mV for OTPI 1 and 2,  $-0.05$  to  $+0.05$  V for OTPI 3, 6, 9, and 12. Error bars represent one standard deviation. Straight lines are linear fits to the data.

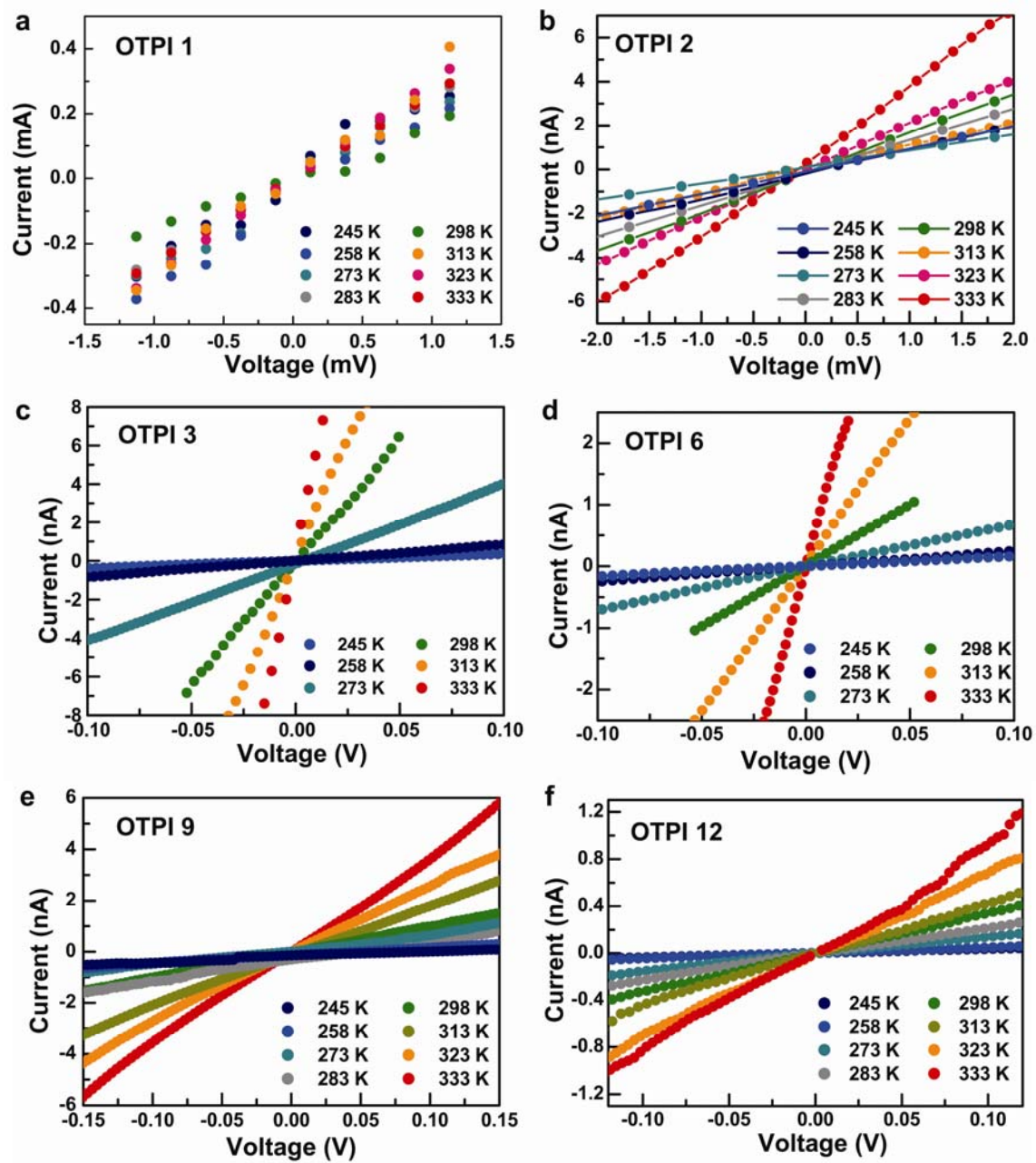


**Figure 6.8** I-V curves in a range of temperature from 245 to 333 K for (a) OPTI 1, (b) OPTI 2, (c) OPTI 3, (d) OPTI 6, (e) OPTI 9, (f) OPTI 12.

### Electrical Characterization of OTPI wires (High Bias Regimes)

**Electric Field Dependence of Charge Transport** To have a complete understanding of transport in a molecular wire it is also necessary to characterize the voltage and electric field dependence of the  $I$ - $V$  characteristics. Applying a bias across a junction may perturb the electronic structure of the wire as the electric fields may be very large, of order  $10^5 - 10^7$  V/cm; certainly there can be field driven changes in conduction mechanisms. In the case of OTPI wires the situation is admittedly somewhat complex, as will be seen, though the field, temperature, and length dependence are all self-consistent.

The semilog plot of  $I$  versus  $E$  for short OTPI wires in Figure 6.9a demonstrates that current decreases as wire length increases, in keeping with the resistance results shown in Figure 6.6. However, for the long wires (OTPI 3–12), a plot of  $\log I$  versus electric field ( $E$ ) reveals that the traces for the long wires collapse nearly on top of one another as shown in Figure 6.9b, c, and d. This indicates that for the long wires transport is *field driven*, as expected for a hopping mechanism in which the electric field pushes the carriers along the molecules. On the other hand, for the short wires, the  $I$ - $E$  curves do not collapse on top of one another because tunneling is a *voltage driven* process. In addition, fundamental differences in a plot of  $\log I$  versus  $E$  are exhibited between two length regimes over long wires (regime 1: OTPI 3–6 (5 to 10 nm) in Figure 6.9b, regime 2: OTPI 7–12 (10 to 20 nm) in Figure 6.9c). In the same magnitude of axes, regime 2 has a thinner shaped  $\log I$ - $E$  trace than regime 1, which indicates that currents in regime 2 is more sensitive to the electric field (Figure 6.9d). The sensitive  $I$ - $E$  characteristics for regime 2 are consistent with smaller hopping energy in Figure 6.7; carriers can be effectively field-driven in regime 2.

Insets in Figure 6.9 display  $I$ - $V$  curves for selected OTPI wires. All of them are sigmoidal shaped, but there is the difference in the symmetry, and also a quantitative difference in the transition from low to high voltages. For  $I$ - $V$  curves for short wires, while a symmetric curve is observed in OTPI 1 (that incorporated with TTF with the absence of PMDI), OTPI 2 (that incorporated with both TTF and PMDI) shows the asymmetric behavior in its  $I$ - $V$  curve with  $\sim 2$  of asymmetric ratio ( $AR$ ) at  $\pm 0.5$  V (Current flows more at the forward bias, and bias is applied on the tip). These

asymmetries in  $I$ - $V$  curve or rectifying behaviors (that current rectification can be caused by intramolecular energy offsets, not by asymmetries from either a work function or contact geometry standpoint) have been well known in donor-acceptor molecules as first suggested by Aviram and Ratner<sup>63</sup> and measured later by Metzger's group.<sup>180</sup> However, details in rectifying mechanism are still open to questions. Further increase of wire lengths yields less distinct asymmetry in  $I$ - $V$  curves (*i.e.*  $AR$  is  $\sim 1.5$  for OTPI 6 at  $\pm 0.5V$ ), and  $I$ - $V$  curves become totally symmetric for regime 2 of long wires (OTPI 7 to 12).

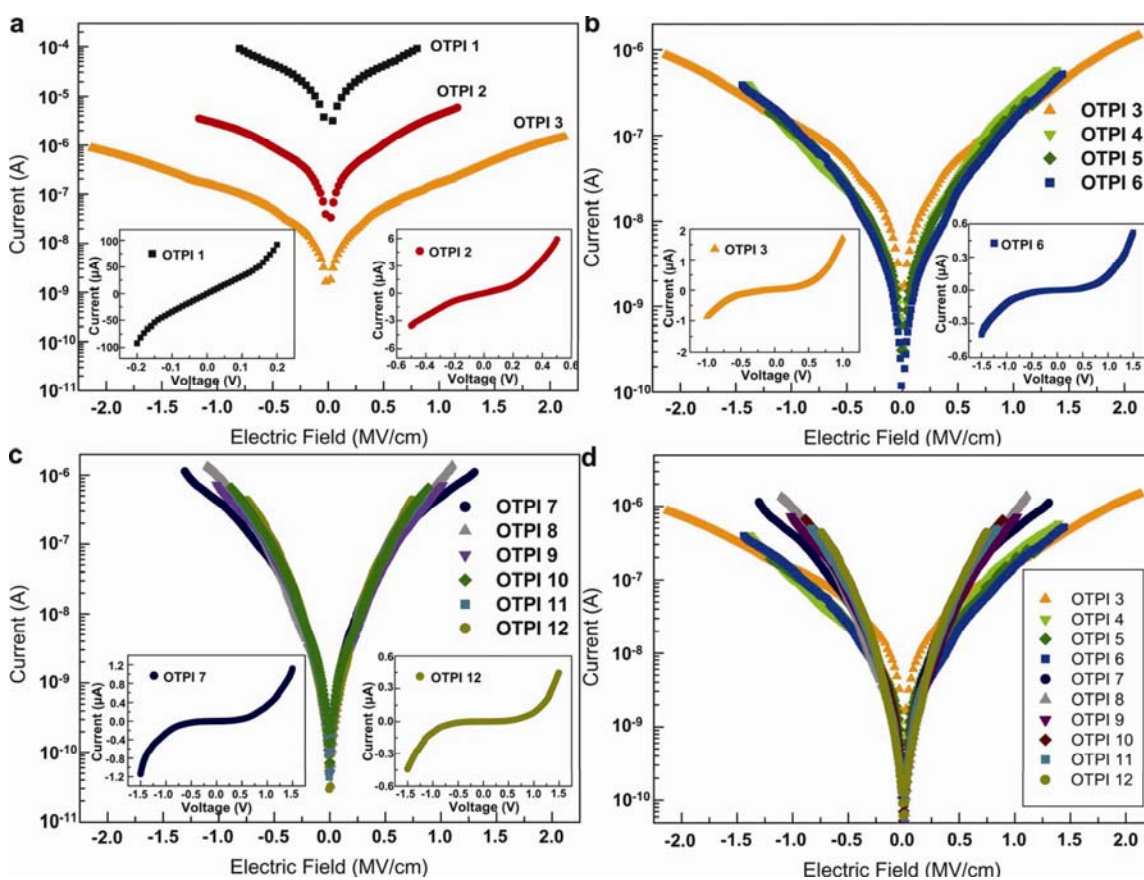


**Figure 6.9** Semilog plot of the average current of 20  $I$ - $E$  traces **(a)** for gold/short wires/gold junctions, **(b)** for gold/long wires (regime 1)/gold junctions, **(c)** for gold/long wires (regime 2)/gold junctions, **(d)** for gold/long wires (regime 1 and 2)/gold junctions. The  $I$ - $E$  trace for a gold/OTPI 3/gold junction is included in (a) in the comparison with relative current levels of other long wires. The insets are  $I$ - $V$  curves in a linear scale for the selected wires of each figure.

Figures 6.10a, b, and c show the  $I$ - $V$  curves of OTPI 2 and OTPI 12, representative of short and long OTPI wires plotted on different axes. Surprisingly, the Fowler-Nordheim plots for OTPI 2 and 12 in Figures 6.10a and b reveal that there is a striking change in conduction behavior with applied bias. This change in behavior is not readily apparent in either the log  $I$ - $V$  or the  $I$ - $V$  characteristics. Considering first OTPI 2 (Figure 6.10a), the current scales logarithmically with  $1/V$  for low voltages (regime I) as expected from Equation 6.4, indicative of direct tunneling. To a first approximation, the metal-wire-metal junction can be modeled as a simple trapezoidal tunneling barrier. In this case, the tunneling current at low bias is given by Equation 6.4.

$$I \propto V \exp\left(-\frac{2d\sqrt{2m_e\phi}}{\hbar}\right) \quad (6.4)$$

where  $d$  is the barrier width (wire length),  $m_e$  is the electron effective mass, and  $\phi$  is the effective barrier height. At higher bias the electric field changes the shape of the tunneling barrier from trapezoidal to triangular. In this case, the  $I$ - $V$  behavior can be described by the Fowler-Nordheim relationship:

$$\ln\left(\frac{I}{V^2}\right) \propto \frac{-4d\sqrt{2m_e\phi^3}}{3\hbar q} \left(\frac{1}{V}\right) \quad (6.5)$$

where  $q$  is the elementary charge. Above the transition voltage  $V_{trans}$  (regime II), the current scales linearly with  $1/V$  with a negative slope. This is clear evidence for the onset of field emission. For short wires such as OTPI 2, the change in mechanism from tunneling to field emission has already been recognized in a variety of molecular systems.

The Fowler-Nordheim plot for OTPI 12 in Figure 6.10b is similar but appears *three* transport regimes (I', II', and III'). In the low-bias regime I', the current scales logarithmically with  $1/V$ , also characteristic of ohmic hopping conduction and consistent with the length and temperature dependence data. The negative slope in the high voltage regime III' suggests that field emission can also occur in OTPI 12 (similar results were obtained for OTPI 3–12 with different steepness of slopes). From the slope in regime III', the emission barrier height ( $\phi_{FE}$ ) is estimated to be in the range of 40–130 meV assuming carrier effective mass ratios in the range 0.1 to 1.0,<sup>17</sup> which are typical for molecular

junctions (see Table 6.2). Further discussions of transport mechanism in regime II' and III' will be followed.

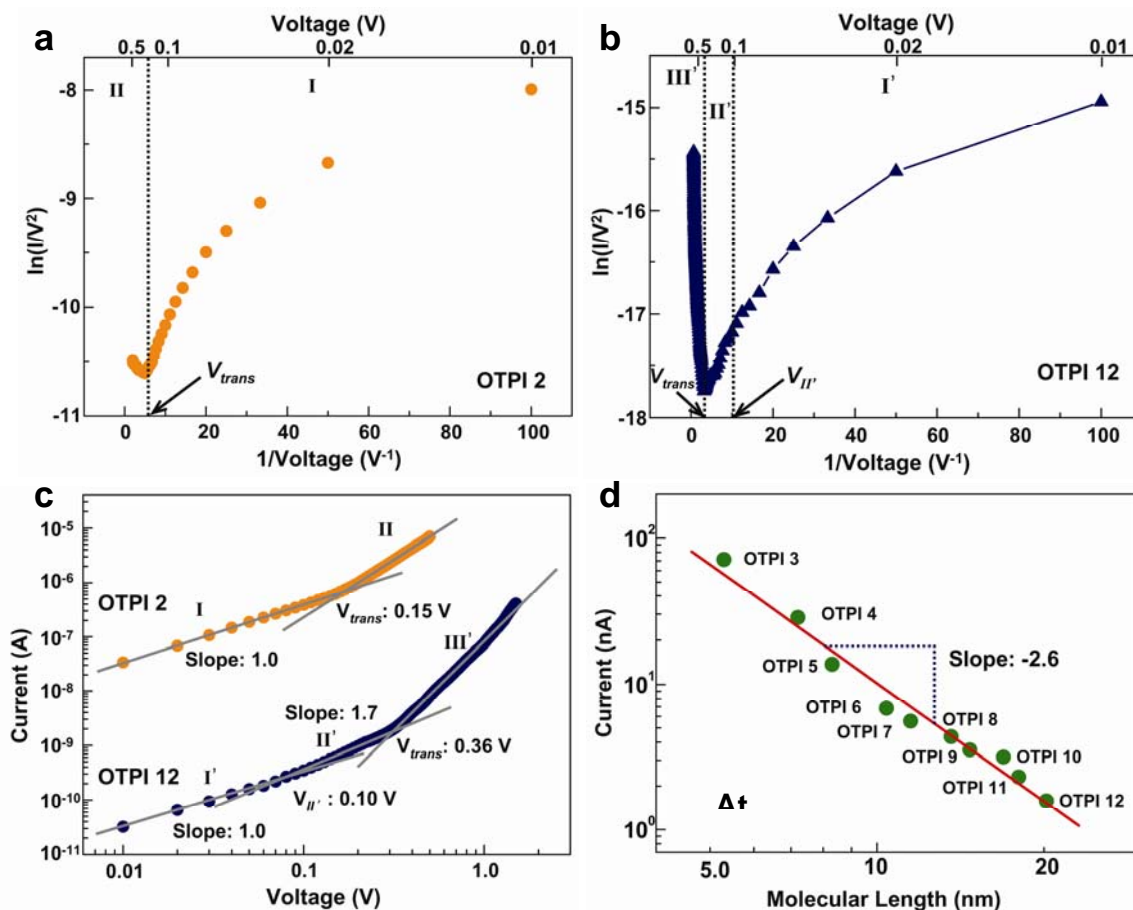


**Figure 6.10** Fowler-Nordheim plots of the average of 20  $I$ - $V$  traces **(a)** for the gold/OTPI 2/gold, and **(b)** for the gold/OTPI 12/gold. For (a), two distinct regimes (I and II) are clearly observable with an inflection point at  $V_{trans}$ , indicating the switch from tunneling to field emission. For (b), three regimes (I', II', and III') are evident. **(c)** Log-log plot for OTPI 2 and OTPI 12 in (a) and (b), respectively. Fits are shown in the different transport regimes. **(d)** A log-log plot of  $I$  versus  $L$  obtained at 0.24 V for all long OTPI wires, displaying the linear fit with a slope of -2.6 (0.24 V is the bias at which all long OTPI wires are within regime II').

**Table 6.2** Analyses of  $I$ - $V$  characteristics for OTPI wires.

Monolayer	n in $I$ , $I'$	n in $II'$	$V_{trans}$ (V)	$V_{II'}$ (V)	$\phi_{FE}$ (eV)
	$I \propto V^n$	$I \propto V^n$	$[E_{trans}$ (MV/cm)]	$[E_{II'}$ (MV/cm)]	
OTPI 1	1.0	-	0.15 [0.60]	-	0.14–0.20
OTPI 2	1.1	-	0.16 [0.43]	-	0.11–0.17
OTPI 3	1.0	1.8	0.49 [0.93]	0.13 [0.25]	0.08–0.13
OTPI 4	1.1	1.7	0.35 [0.49]	0.11 [0.15]	0.05–0.11
OTPI 5	1.0	1.6	0.34 [0.41]	0.11 [0.13]	0.04–0.10
OTPI 6	1.1	1.5	0.35 [0.34]	0.08 [0.08]	0.08–0.13
OTPI 7	1.1	1.8	0.28 [0.24]	0.07 [0.06]	0.03–0.08
OTPI 8	1.0	2.1	0.36 [0.26]	0.08 [0.06]	0.06–0.11
OTPI 9	1.1	1.7	0.37 [0.25]	0.09 [0.06]	0.05–0.11
OTPI 10	1.0	1.6	0.39 [0.23]	0.09 [0.05]	0.05–0.10
OTPI 11	0.9	1.6	0.37 [0.21]	0.08 [0.04]	0.04–0.09
OTPI 12	1.1	1.7	0.36 [0.18]	0.10 [0.05]	0.04–0.09

Interpretation of  $I$ - $V$  data for OTPI 2 and 12 can be further aided by yet one more type of analysis, in this case  $\log I - \log V$  plots shown in Figure 6.10c. These plots also clearly reveal the same two regimes of transport for OTPI 2 and the same three regimes for OTPI 12. Direct comparison can be made between the Fowler-Nordheim plots in Figure 6.10a, b and the log-log plots in Figure 6.10c. The two types of figures are entirely consistent showing clear transitions in  $I$ - $V$  behavior at the same voltages. However, it is worthwhile noting that analyzing the data in these different formats is crucial to elucidating mechanisms. For example, it would have been difficult to identify field

emission as a key mechanism from Figure 6.10c alone; the Fowler-Nordheim plots were essential to that.

While transports in short OTPI wires are apparent at both low and high bias, not all aspects of the bias dependence are clear for long OTPI wires. The linear dependence on  $V$  in the low voltage regime (I') is consistent with ohmic hopping. The principal issue in this regime is the steady state concentration of carriers. Are carriers present in the wires at equilibrium (no bias) when the junction is formed? Such carriers would likely arise by equilibration/charge transfer with the contacts,<sup>178</sup> but understanding the carrier generation/injection mechanism in molecular wires in the hopping regime is an important unresolved issue. As the applied bias increases and reaches  $V_{II'}$ , it is possible that the contacts inject additional charges into the wires such that the mechanism switches to the so-called space charge limited (SCLC) current regime (II'); in this regime the dependence of current on voltage would be expected to be super-linear<sup>97, 98, 213</sup> (slope is 1.7 in regime II' as shown in Figure 6.10c, and similar results are observed for other long OTPI wires, see Table 6.2). In addition, a log-log plot of  $I$  versus molecular length ( $L$ ) reveals a linear decay with -2.6 of slope (Figure 6.10d) as expected for SCLC. Field emission can be dominated mechanism in regime III' based on the negative linearity in Figure 6.10b the extracted emission barriers from it (see Table 6.2).

In order to clarify transport mechanisms in long wires, we have carried out the temperature dependent measurements for  $I$ - $V$  characteristics of OTPI 12 over all three regimes. Figure 6.11 show the  $I$ - $V$  curves of OTPI 12 plotted on different axes in a range of temperature from 245 to 333K. As seen in Figure 6.11a and b, temperature dependent  $I$ - $V$  characteristics are apparent over all three regimes. In particular, the activation energy for hopping decreases as a function of the electric field from 0.3 eV at 0.05 V to 0.2 eV at 0.46 V (see inset in Figure 6.11b), and hopping energy is further reduced to 87 meV (obtained in a rang of  $T$  from 245 K to 273 K) at 0.57 V (0.28 MV/cm). This trend is a natural outcome of field-induced barrier lowering as established in a variety of metal-semiconductor (insulator) interfaces<sup>213</sup> and in a nano-scale junction incorporated with individual molecules.<sup>30</sup> Temperature dependences in regime I' and II' of OTPI 12 are conceivable as we proposed their mechanisms to be ohmic hopping and SCLC,



respectively. However, the temperature dependence in regime III' is somewhat surprising that field emission is expected to be temperature independent. Assuming that field emission governs charge transport in regime III', there could be several explanations for this temperature dependent behavior. First, Fowler-Nordheim relationship in Equation 6.5 is inherently applicable at absolute zero temperature. In real world, the thermal energy can populate electrons near metal Fermi level in forms of Boltzmann distribution. The energy barrier for field emission therefore can be altered at different temperatures as recent publication showed in a molecular junction.<sup>241</sup> The higher temperature increases electron population near the Fermi level of a gold, which results in the lowering for emission heights (lower work function), and this is also consistent with the reduction of the turn-on voltages ( $V_{trans}$ ) for field emission as temperature increases (Figure 6.11c). This effect is known as thermo-field emission<sup>242, 243</sup> which is considered as an intermediate region between field emission and thermal emission, and often exhibited in conditions of high temperature and high electric field for carbon nanotube,<sup>244</sup> tungsten,<sup>245</sup> and ceramic/metal interfaces. Second, if field emission occurs from HOMO to LUMO of molecular wires (This case can be conceived of dielectric breakdown occurred at high field.<sup>213</sup>), the temperature dependence is probable because more carriers are already field-driven up to  $V_{trans}$  ( $E_{trans}$ ) at higher temperatures. We also considered alternative mechanisms for regime III' based on principal high field conduction processes in insulators:<sup>98, 173, 213</sup> (i) space charge limited current (SCLC) in the trap filling limit, (ii) Schottky emission, and (iii) Poole-Frenkel conduction. We did not obtain reasonable values for extracted physical parameters with these mechanisms.

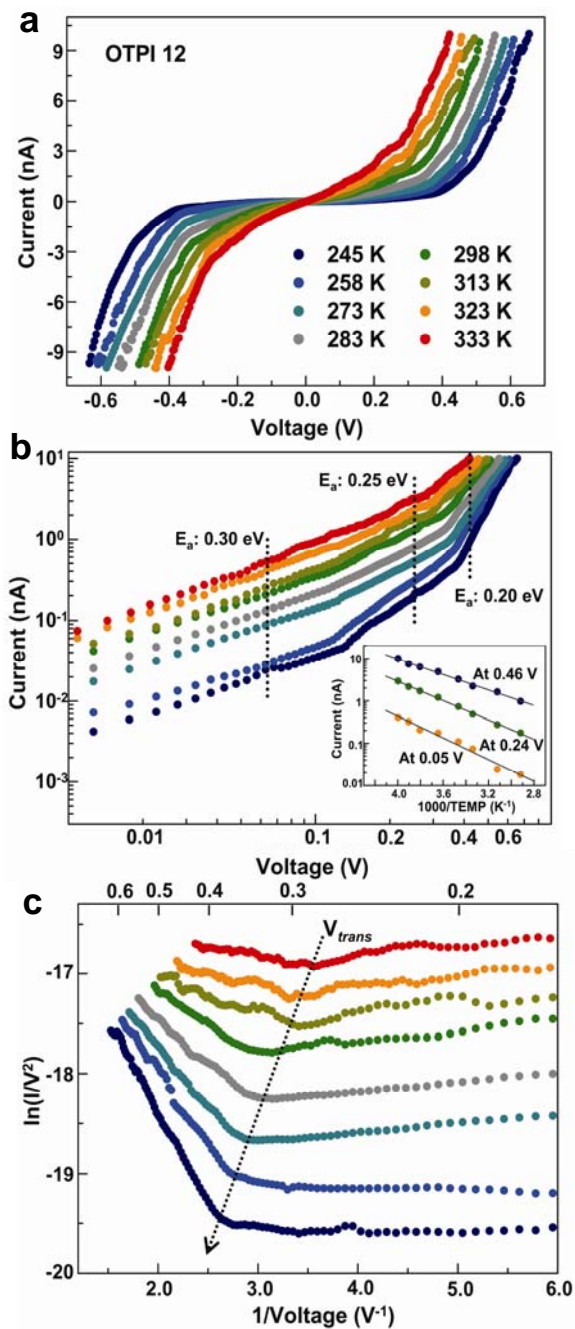


**Figure 6.11** Temperature dependent  $I$ - $V$  characteristics for OTPI 12 on (a) a linear axes, (b) a log-log axes, and (c) Fowler-Nordheim axes. Inset in (b) shows Arrhenius plots at three regimes (I', II', III'). Note that the magnitude of currents is limited up to 10 nA for our setup of variable temperature measurements.

## 6.5 Conclusion

To summarize, direct current (DC) electrical conduction has been measured in a set of conjugated alternating donor acceptor oligoimine wires having systematically controlled lengths between 2.5 and 20.2 nm. These wires constitute TTF as donor building blocks and PMDI as acceptor building blocks to build wires from one gold electrode using aryl imine addition chemistry, and are thereby named as OTPI wires. At low bias voltages, we have found not only that the predicted transition from tunneling to hopping transport is exhibited at a molecular length of 5 nm, as supported by striking and mutually consistent changes of the length, temperature, and electric field dependence of the transport characteristics, but also that the donor-acceptor strategy reveals the enhanced single-chain conductivity (two orders of magnitude higher than previous wires<sup>33, 215</sup>). In addition, the significantly increased range of molecular lengths allows us to measure hopping conduction in the regime (10–20 nm) that is less influenced from contacts. This regime can be truly the phase where bulk properties resembled with organic films in a variety of devices are exhibited with minimum morphological complexities. At high biases, the transition from tunneling to field emission is apparent in short OTPI wires, whereas three regimes can be distinct in long wires. Ohmic hopping and SCLC can be operative at low and medium bias, respectively. Charge transport at high bias can be temperature dependent field emission evidenced by electric field and temperature dependent  $I$ - $V$  characteristics. The reproducibility of the measurements and the flexibility of the imine wire synthesis chemistry together create significant opportunities to improve fundamental understanding of hopping transport in conjugated molecules.

## 7 Outlook: Probing the Physical Organic Chemistry of Hopping Conduction

Recent successes summarized in this thesis in building long molecular wires and measuring their DC conduction properties suggest that a wide variety of experiments can be undertaken to probe the influence of molecular structure on hopping transport. There is now the very real and exciting possibility that we can understand electrical transport in molecular systems with unprecedented detail. One might describe this new research field as the physical organic chemistry of hopping conduction, in which classical methods of systematic structure variation are linked to measurable changes in rates of hopping transport. As explained in the introduction, the importance of exploring the relationship between molecular structure and hopping transport lies in future opportunities to exploit molecules in nanoelectronics and in aiding efforts to optimize conjugated polymer materials for applications in hybrid, flexible, or printed electronics. In this final part of this thesis, we consider several new wire designs aimed at understanding the roles of (i) conjugation length, (ii) electronic structures, and (iii) redox properties on hopping conduction. Furthermore, we will investigate the possibility of alternative chemistries for building long conjugated molecular wires on a gold substrate.

### 7.1 Conjugated Oligoimine Wires

(i) *The role of conjugation length on molecular conduction.* The conjugation length of OPI wires extends only over three repeat units as assessed by UV-vis spectroscopy on wires assembled on semi-transparent gold electrodes. This short conjugation length results from steric hindrance along the oligoimine backbone, which causes the phenyl rings to adopt a dihedral angle of approximately  $30^\circ$  with respect to each other.<sup>33</sup> To increase conjugation length it is therefore necessary to enforce a more planar wire structure. We expect that enhancing the conjugation length will improve the wire conductivity and also modify the activation energy for hopping transport. We propose to probe the role of conjugation length by building wires with reduced steric hindrance, such as structure **1** in Figure 7.1. Replacing a phenylene with the smaller

thiophene ring, as in wire structure 1, will release the strain between adjacent rings allowing a more coplanar geometry and increasing the overall conjugation length. In fact, it has already been reported that incorporating thiophene rings significantly reduced the dihedral angle around the imine linkage in conjugated azomethine polymers.<sup>207, 246</sup> Several repeat units of the molecule 1 structure could be connected to create long wires.

Another strategy for manipulating the dihedral angle of the imine linkage is to use intramolecular hydrogen bonding between a hydroxyl group and the nitrogen in the imine bond as in wire structure 2. The energy gain from intramolecular hydrogen bonding, forming quasi six-membered rings, may be large enough to compensate the steric strain energy associated with a more coplanar configuration. It has already been demonstrated that intramolecular hydrogen bonding can enable increased  $\pi$ -conjugation in extended systems.<sup>247</sup>

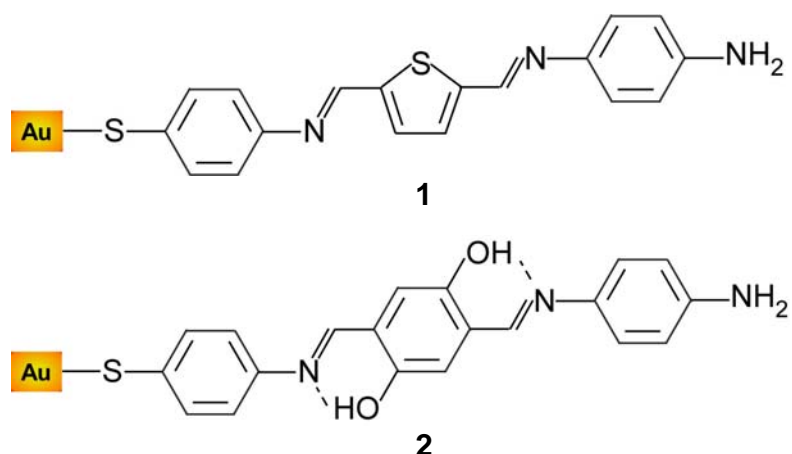


**Figure 7.1** Oligoimine systems: Wire 1 is designed to release steric strain in the wire. Wire 2 is designed to planarize the dihedral angle with hydrogen bonds.

(ii) *Tuning electronic structure.* To investigate the influence of electronic structure on hopping transport, one can imagine developing conjugated oligoimine systems substituted with electron donating or withdrawing substituents (wire **3** in Fig. 7.2) and thiophene-based molecular wires (wire **4** in Fig. 7.2). Fluorine substitution is chosen for structure 3 because it has a strong electronegative inductive effect on  $\pi$ -systems and is not sterically bulky.<sup>248-251</sup> It can be anticipated that fluorine substitution will stabilize the frontier molecular orbitals (i.e., create a negative shift in the HOMO and LUMO energies) with respect to the Fermi level of the metal contacts. This in turn may result in electron (as opposed to hole) injection into the wire orbitals, allowing examination of electron hopping. It has been recently reported that fluoroarene-thiophene oligomers exhibit n-type mobility in the field effect transistors,<sup>250</sup> and the LUMO of perfluorinated distyrylbenzenes (DSB) is lowered by 0.5 eV compared to DSB while the optical band gap nearly remains the same.<sup>251</sup>

Thiophene-based building blocks offer some exciting opportunities for the synthesis of molecular wires with tailored electronic properties. Thiophene structures are well known in chemistry to have rich electronic behavior. For example, poly 3-hexyl thiophene (P3HT) is widely used as an active layer in organic semiconductor because of its electron-rich nature and semicrystalline structure. Likewise, the conduction properties of molecular wires built from thiophene sub-units offer potential opportunities to realize highly-conductive molecular wires. We plan to build wires based thiophenes; example is shown in Figure 7.2 (wire **4**), that are inherently more conductive because carriers can be more easily injected into the wires due to the low oxidation potential of thiophene structures. In addition, the proposed structure involves a relatively long molecular building block to facilitate building the extremely long molecular wires (more than  $\sim 20$  nm) and planar conformation because of less steric interaction of thiophene subunits with imine bonds.

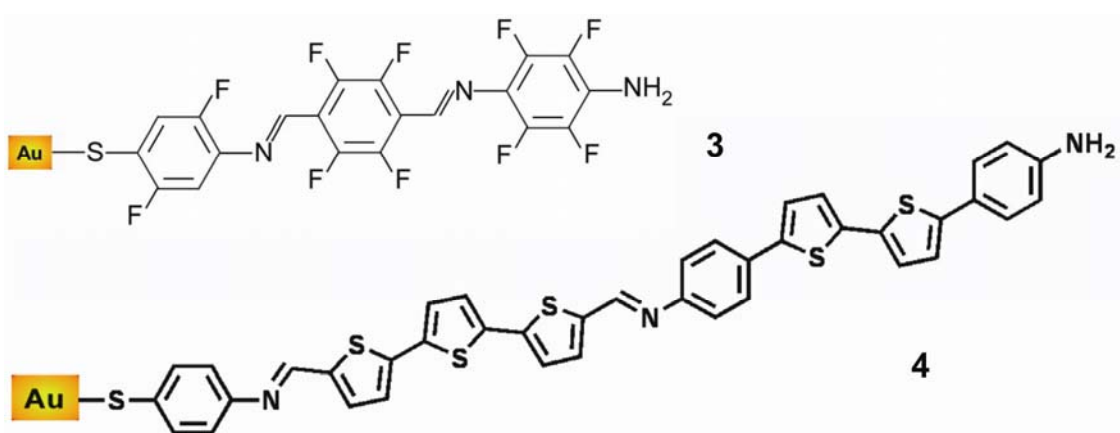


**Figure 7.2** In wire **3**, the fluorine substituents will lower the LUMO level perhaps allowing electron (as opposed to hole) conduction. Wire **4** is a thiophene-based architecture that may lead to a low oxidation potential with higher conductivity.

(iii) *Electrochemical gating of redox-active molecular wires: transport and spectro-electrochemistry.* The redox-active wires described in this thesis can serve as an excellent testbed for electrochemical gating experiments and spectroelectrochemistry. The CP-AFM conduction measurement can be performed under liquid electrolyte, which allows the oxidation state of the redox center to be electrochemically controlled, *i.e.*, gated.<sup>20, 32</sup> This kind of measurement will reveal that the conductance is a strong function of electrochemical potential. But more importantly, for any conjugated wire **1-4** above and molecular wires in this thesis, the ability to tune the charge density on the wires electrochemically may allow the charge mobility to be determined. That is, by measuring the wire conductivity as a function of charge density, one can estimate the mobility (from the slope of conductivity vs. charge). This is an ambitious experiment, which can be complicated by the fact that in CP-AFM the junction area is not precisely known. Also the role that the ions will have on the conduction is not clear. Nevertheless, the inherent redox activity of many of our proposed wire structures makes such electrochemical gating experiments potentially very interesting. We also propose to examine the UV-vis spectra of different molecular wires at different electrochemically induced redox states. Such spectra will inform us about the nature of the charges on the wires, *e.g.*, whether

polarons are formed and, in addition, how the polaron state varies with the length of the wire.

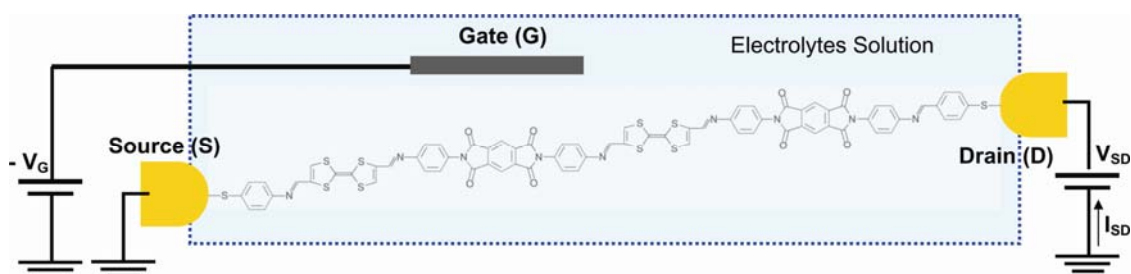


**Figure 7.3** Schematic of electrochemical gating of long conjugated donor-acceptor wires.  $V_{SD}$  and  $V_G$  represent the source-drain and gate voltage, respectively. We can control the charge density of molecular wires by adjusting the gate voltage ( $V_G$ ).

## 7.2 New Chemistry

(i) *Incorporating redox groups via metal coordination chemistry: examining charge correlation effects.* The flexibility of the oligoimine chemistry also allows incorporation of redox-active groups into molecular wires. For example, we envision building conjugated wires with a well-defined redox center in the middle of the wire, Figure 7.4 wire **5**. Such a redox center may serve to trap or localize a charge carrier. For some range of applied bias the charge will remain stuck and will thus block conduction down the wire. At some critical applied bias (or field) the charge will become detrapped and conduction will resume. Such behavior would result in an unusual I-V characteristic for the wire, e.g., a Coulomb staircase,<sup>61</sup> which has been observed previously in redox molecules connected to metal electrodes. There is the possibility if the wires are designed appropriately that this blockading effect could be observed at room temperature, and this might suggest an avenue for applications (in memory, for example).

The metal complex approach to building molecular wires (wire **6** in Fig. 7.4) offers opportunities to make wires with multiple well-defined redox states. Already it has been shown that long metal complex wires are highly conductive<sup>120</sup>, which is attributed to the presence of d-electrons that can be delocalized over the ligands. Such structures



offer opportunities to examine wire conduction as a function of metal type (d electron count), ligand design, and the position of redox sites. Because multiple charges can be accommodated by the redox sites, correlative effects (charge-charge repulsion) may lead to interesting I-V behavior. Many other wire architectures having a range of intentionally designed electrical transport behaviors, such as rectification, can be imagined. The ability to synthesize and measure conduction in molecular wires easily and reproducibly has opened up an exciting new research area for chemists and physicists

### Metal containing wires

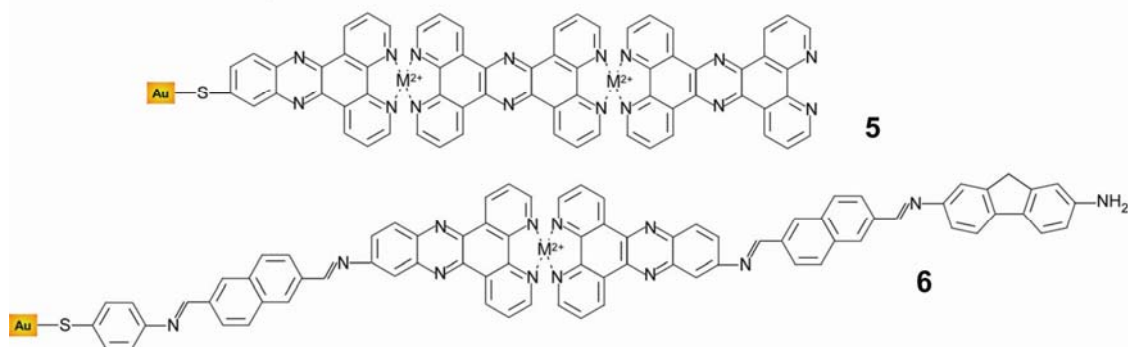


**Figure 7.4** Metal containing systems: Wire **5** can be prepared by metal coordination chemistry and may be highly conductive by virtue of the multiple metal centers. Wire **6** contains a single redox center that might lead to charge correlation effects (Coulomb blockades) and interesting I-V behavior.

(ii) **Knoevenagel Condensation: New chemistry for building isonitrile substituted conjugated oligovinylene wires.** Knoevenagel condensation is another alternative chemistry which can be applicable to build long conjugated molecular wires. The condensation reaction often runs at very mild conditions (at room temperature, under weak base condition), which allows to grow wires in a step-wise fashion without breaking a chemical bond on a metal electrode. It is noted that a chemical bond between gold and sulfur becomes unstable at the condition of high temperature (more than 60 °C), which often destroy the self-assembly of molecules. In fact, a variety of polyarylvinylenes based on Knoevenagel condensation has been successfully synthesized

at mild condition in the high yield.<sup>252-254</sup> Wire growth can begin with 4-thiobenzaldehyde monolayer on a gold substrate. The alternative additions of bifunctional aryl compounds: 1,4-aryldiisonitrile and 1,4-aryldialdehyde reveals an isonitrile substituted oligoarylvinylene structure (wire 7, Fig. 7.5). In particular, one can build wires based on molecular building blocks that are fully composed of thiophene subunits with this chemistry (In aryl imine addition chemistry, diaminothiophene is chemically unstable because of its ease in oxidation), one can examine the effect of conjugation links (vinylenes vs. imines) and isonitrile substituents on hopping transport.

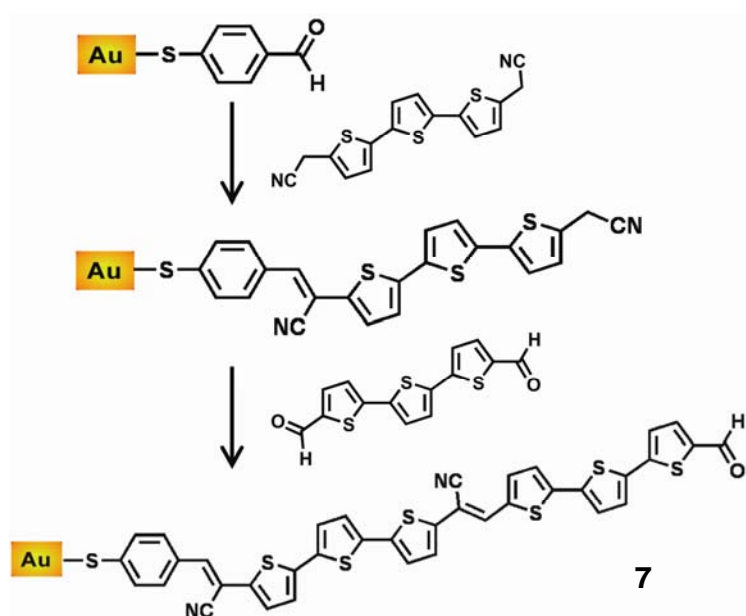


**Figure 7.5** Conjugated oligovinylene wires: Wire 7 can be prepared by step-wise Knoevenagel condensation.

### 7.3 References

## Bibliography

- (1) Nitzan, A.; Ratner, M. A., *Science* **2003**, *300*, 1384-1389.
- (2) Davis, W. B.; Svec, W. A.; Ratner, M. A.; Wasielewski, M. R., *Nature* **1998**, *396*, 60-63.
- (3) Schwab, P. F. H.; Levin, M. D.; Michl, J., *Chem. Rev.* **1999**, *99*, 1863-1934.
- (4) Joachim, C.; Gimzewski, J. K.; Aviram, A., *Nature* **2000**, *408*, 541-548.
- (5) Carroll, R. L.; Gorman, C. B., *Angew. Chem. Int. Ed.* **2002**, *41*, 4378-4400.
- (6) Heath, J. R.; Ratner, M. A., *Physics Today* **2003**, *May* 43-49.
- (7) Kwok, K. S.; Ellenbogen, J. C., *Materials Today* **2002**, *Feb.*, 28-37.
- (8) Chen, Y.; Jung, G.-Y.; Ohlberg, D. A. A.; Li, X.; Stewart, D. R.; Jeppesen, J. O.; Nielsen, K. A.; Stoddart, J. F.; Williams, R. S., *Nanotechnology* **2003**, *14*, 462-468.
- (9) Li, G.; Shrotriya, V.; Huang, J.; Yao, Y.; Moriarty, T.; Emery, K.; Yang, Y., *Nat. Mater.* **2005**, *4*, 864-868.
- (10) Peet, J.; Kim, J. Y.; Coates, N. E.; Ma, W. L.; Moses, D.; Heeger, A. J.; Bazan, G. C., *Nat. Mater.* **2007**, *6*, 497-500.
- (11) Sirringhaus, H.; Tessler, N.; Friend, R. H., *Science* **1998**, *280*, 1741-1744.
- (12) Shen, Z.; Burrows, P. E.; Bulovi, V.; Forrest, S. R.; Thompson, M. E., *Science* **1997**, *276*, 2009-2011.
- (13) Greenham, N. C.; Moratti, S. C.; Bradley, D. D. C.; Friend, R. H.; Holmes, A. B., *Nature* **1993**, *365*, 628-630.
- (14) Yan, H.; Chen, Z.; Zheng, Y.; Newman, C.; Quinn, J. R.; Dotz, F.; Kastler, M.; Facchetti, A., *Nature* **2009**, *457*, 679-686.
- (15) Cho, J. H.; Lee, J.; Xia, Y.; Kim, B.; He, Y.; Renn, M. J.; Lodge, T. P.; Daniel Frisbie, C., *Nat. Mater.* **2008**, *7*, 900-906.
- (16) Ruitenbeek, J.; Scheer, E.; Weber, H. B.; Wang, W.; Lee, T.; Reed, M. A., Introducing molecular electronics. In *Introducing molecular electronics*, Cuniberti, G.; Fagas, G.; Richter, K., Eds. Springer: Heidelberg, Germany, 2005; Vol. 680, p Part II Experiment.
- (17) Salomon, A.; Cahen, D.; Lindsay, S.; Tomfohr, J.; Engelkes, V. B.; Frisbie, C. D., *Adv. Mater.* **2003**, *15*, 1881-1890.
- (18) Mantooth, B. A.; Weiss, P. S., *Proc. IEEE* **2003**, *91*, 1785-1802.
- (19) Wang, W. Y.; Lee, T. H.; Reed, M. A., *Proc. IEEE* **2005**, *93*, 1815-1824.
- (20) Chen, F.; Hihath, J.; Huang, Z.; Li, X.; Tao, N. J., *Annu. Rev. Phys. Chem.* **2007**, *58*, 535-564.
- (21) Selzer, Y.; Allara, D. L., *Annu. Rev. Phys. Chem.* **2006**, *57*, 593-623.
- (22) McCreery, R. L., *Chem. Mater.* **2004**, *16*, 4477-4496.
- (23) Venkataraman, L.; Klare, J. E.; Nuckolls, C.; Hybertsen, M. S.; Steigerwald, M. L., *Nature* **2006**, *442*, 904-907.
- (24) Wold, D. J.; Haag, R.; Rampi, M. A.; Frisbie, C. D., *J. Phys. Chem. B* **2002**, *106*, 2813-2816.
- (25) Liu, H.; Wang, N.; Zhao, J.; Guo, Y.; Yin, X.; Boey, F. Y. C.; Zhang, H., *ChemPhysChem* **2008**, *9*, 1416-1424.

- (26) Kim, B.-S.; Beebe, J. M.; Jun, Y.; Zhu, X. Y.; Frisbie, C. D., *J. Am. Chem. Soc.* **2006**, *128*, 4970-4971.
- (27) Engelkes, V. B.; Beebe, J. M.; Frisbie, C. D., *J. Am. Chem. Soc.* **2004**, *126*, 14287-14296.
- (28) Lakshmi, S.; Dutta, S.; Pati, S. K., *J. Phys. Chem. C* **2008**, *112*, 14718-14730.
- (29) Wang, W.; Lee, T.; Reed, M. A., *Phys. Rev. B* **2003**, *68*, 035416.
- (30) Selzer, Y.; Cabassi, M. A.; Mayer, T. S.; Allara, D. L., *J. Am. Chem. Soc.* **2004**, *126*, 4052-4053.
- (31) Poot, M.; Osorio, E.; O'Neill, K.; Thijssen, J. M.; Vanmaekelbergh, D.; van Walree, C. A.; Jennekens, L. W.; van der Zant, H. S. J., *Nano Lett.* **2006**, *6*, 1031-1035.
- (32) Li; Hihath, J.; Chen, F.; Masuda, T.; Zang, L.; Tao, *J. Am. Chem. Soc.* **2007**, *129*, 11535-11542.
- (33) Choi, S. H.; Kim, B.-S.; Frisbie, C. D., *Science* **2008**, *320*, 1482-1486.
- (34) Mayor, M.; Weber, H. B.; Reichert, J.; Elbing, M.; Hanisch, C. v.; Beckmann, D.; Fischer, M., *Angew. Chem. Int. Ed.* **2003**, *42*, 5834-5838.
- (35) Haiss, W.; Zalinge, H. v.; Bethell, D.; Ulstrup, J.; Schiffrin, D. J.; Nichols, R. J., *Faraday Discuss.* **2006**, *131*, 253-264.
- (36) Selzer, Y.; Cai, L.; Cabassi, M. A.; Yao, Y.; Tour, J. M.; Mayer, T. S.; Allara, D. L., *Nano Lett.* **2005**, *5*, 61-65.
- (37) Selzer, Y.; Cabassi, M. A.; Mayer, T. S.; Allara, D. L., *Nanotechnology* **2004**, *15*, S483-S488.
- (38) Venkataraman, L.; Klare, J. E.; Tam, I. W.; Nuckolls, C.; Hybertsen, M. S.; Steigerwald, M. L., *Nano Lett.* **2006**, *6*, 458-462.
- (39) Venkataraman, L.; Park, Y. S.; Whalley, A. C.; Nuckolls, C.; Hybertsen, M. S.; Steigerwald, M. L., *Nano Lett.* **2007**, *7*, 502-506.
- (40) Chen, F.; Li, X.; Hihath, J.; Huang, Z.; Tao, N., *J. Am. Chem. Soc.* **2006**, *128*, 15874-15881.
- (41) Xu, B.; Tao, N. J., *Science* **2003**, *301*, 1221-1223.
- (42) Yasuda, S.; Yoshida, S.; Sasaki, J.; Okutsu, Y.; Nakamura, T.; Taninaka, A.; Takeuchi, O.; Shigekawa, H., *J. Am. Chem. Soc.* **2006**, *128*, 7746-7747.
- (43) Anslyn, E. V.; Dougherty, D. A., *Modern physical organic chemistry*. University Science Books: Sausalito, USA, 2006; p Chapter 10.
- (44) L.Closs, G.; Miller, J. R., *Science* **1988**, *240*, 440-447.
- (45) Jordan, K. D.; Paddon-row, M. N., *Chem. Rev.* **1992**, *92*, 395-410.
- (46) Marcus, R. A., *Angew. Chem. Int. Ed.* **1993**, *32*, 1111-1222.
- (47) Barbara, P. F.; Meyer, T. J.; Ratner, M. A., *J. Phys. Chem.* **1996**, *100*, 13148-13168.
- (48) Weiss, E. A.; Tauber, M. J.; Kelley, R. F.; Ahrens, M. J.; Ratner, M. A.; Wasielewski, M. R., *J. Am. Chem. Soc.* **2005**, *127*, 11842-11850.
- (49) Newton, M. D., *Chem. Rev.* **1991**, *91*, 767-792.
- (50) Lambert, C.; Noll, G.; Schelter, J., *Nat. Mater.* **2002**, *1*, 69-73.
- (51) Berlin, Y. A.; Hutchison, G. R.; Rempala, P.; Ratner, M. A.; Michl, J., *J. Phys. Chem. A* **2003**, *107*, 3970-3980.
- (52) Sachs, S. B.; Dudek, S. P.; Hsung, R. P.; Sita, L. R.; Smalley, J. F.; Newton, M. D.; Feldberg, S. W.; Chidsey, C. E. D., *J. Am. Chem. Soc.* **1997**, *119*, 10563-10564.

- (53) Curtiss, L. A.; Naleway, C. A.; Miller, J. R., *J. Phys. Chem.* **1995**, *99*, 1182-1193.
- (54) Paulson, B.; Pramod, K.; Eaton, P.; Closs, G.; Miller, J. R., *J. Phys. Chem.* **1993**, *97*, 13042-13045.
- (55) Berlin, Y. A.; Grozema, F. C.; Siebbeles, L. D. A.; Ratner, M. A., *J. Phys. Chem. C* **2008**, *112*, 10988-11000.
- (56) Nitzan, A., *J. Phys. Chem. A* **2001**, *105*, 2677-2679.
- (57) Adams, D. M.; Brus, L.; Chidsey, C. E. D.; Creager, S.; Creutz, C.; Kagan, C. R.; Kamat, P. V.; Miller, J. R.; Newton, M. D.; Zhu, X., *J. Phys. Chem. B* **2003**, *107*, 6668-6697.
- (58) Zhu, X.-Y., *J. Phys. Chem. B* **2004**, *108*, 8778-8793.
- (59) Zhu, X. Y., *Surf. Sci. Rep.* **2004**, *56*, 1-83.
- (60) Park, H.; Park, J.; Lim, A. K. L.; Anderson, E. H.; Alivisatos, A. P.; McEuen, P. L., *Nature* **2000**, *407*, 57-60.
- (61) Park, J.; Pasupathy, A. N.; Goldsmith, J. I.; Chang, C.; Yaish, Y.; Petta, J. R.; Rinkoski, M.; Sethna, J. P.; Abruña, H. D.; McEuen, P. L.; Ralph, D. C., *Nature* **2002**, *417*, 722-725.
- (62) Chae, D.-H.; Berry, J. F.; Jung, S.; Cotton, F. A.; Murillo, C. A.; Yao, Z., *Nano Lett.* **2006**, *6*, 165-168.
- (63) Avram, A.; Ratner, M., *Chem. Phys. Lett.* **1974**, *29*, 277-283.
- (64) Kuznetsov, A. M.; Ulstrup, J., *Electron Transfer in Chemistry and Biology: An Introduction to the Theory*. Wiley: Chichester, 1999.
- (65) Hush, H. S., *Ann. NY Acad. Sci.* **2003**, *1006*, 1-20.
- (66) Hihath, J.; Xu, B.; Zhang, P.; Tao, N., *Proc. Natl. Acad. Sci. USA* **2005**, *102*, 16979-16983.
- (67) Xiao, X.; Xu, B.; Tao, N., *Angew. Chem. Int. Ed. Engl.* **2004**, *43*, 6148-6158.
- (68) M. Kitamura; Imada, T.; Arakawa, Y., *Appl. Phys. Lett.* **2003**, *83*, 3410-3412.
- (69) Granstrom, E. L.; Frisbie, C. D., *J. Phys. Chem. B* **1999**, *103*, 8842-8849.
- (70) Ashcroft, N. W.; Mermin, N. D., *Solid State Physics*. Holt Rinehart & Winston: Austin, USA, 1976; p Chapter 1.
- (71) Wiesendanger, R., *Scanning Probe Microscopy*. Cambridge University Press: Cambridge, UK, 1994.
- (72) Simmons, J. G., *J. Appl. Phys.* **1963**, *34*, 1793-1803.
- (73) Landauer, R., *Phys. Lett. A* **1981**, *85*, 91-93.
- (74) Datta, S., *Nanotechnology* **2004**, *15*, S433-S451.
- (75) Nitzan, A., *Annu. Rev. Phys. Chem.* **2001**, *52*, 681-750.
- (76) Joachim, C.; Ratner, M. A., *Proc. Natl. Acad. Sci. USA* **2005**, *102*, 8801-8808.
- (77) Segal, D.; Nitzan, A.; Davis, W. B.; Wasielewski, M. R.; Ratner, M. A., *J. Phys. Chem. B* **2000**, *104*, 3817-3829.
- (78) Segal, D.; Nitzan, A.; Ratner, M.; Davis, W. B., *J. Phys. Chem. B* **2000**, *104*, 2790-2793.
- (79) Segal, D.; Nitzan, A., *Chem. Phys.* **2001**, *268*, 315-335.
- (80) Young, R.; Ward, J.; Scire, F., *Phys. Rev. Lett.* **1971**, *27*, 922-924.
- (81) Beebe, J. M.; Kim, B.-S.; Gadzuk, J. W.; Frisbie, C. D.; Kushmerick, J. G., *Phys. Rev. Lett.* **2006**, *97*, 026801.

- (82) Beebe, J. M.; Kim, B.-S.; Frisbie, C. D.; Kushmerick, J. G., *ACS Nano* **2008**, *2*, 827-832.
- (83) Mujica, V.; Kemp, M.; Ratner, M. A., *J. Chem. Phys.* **1994**, *101*, 6856-6864.
- (84) Mujica, V.; Kemp, M.; Ratner, M. A., *J. Chem. Phys.* **1994**, *101*, 6849-6855.
- (85) Beebe, J. M.; Engelkes, V. B.; Miller, L. L.; Frisbie, C. D., *J. Am. Chem. Soc.* **2002**, *124*, 11268-11269.
- (86) Baranovski, S.; Rubel, O., In *Charge Transport in Disordered Solids with Applications in Electronics*, Baranovski, S., Ed. John Wiley & Sons, Ltd.: New York, USA, 2006; p Chapter 2.
- (87) Miller, A.; Abrahams, E., *Phys. Rev.* **1960**, *120*, 745.
- (88) Cui, X. D.; Primak, A.; Zarate, X.; Tomfohr, J.; Sankey, O. F.; Moore, A. L.; Moore, T. A.; Gust, D.; Harris, G.; Lindsay, S. M., *Science* **2001**, *294*, 571-574.
- (89) Yaliraki, S. N.; Kemp, M.; Ratner, M. A., *J. Am. Chem. Soc.* **1999**, *121*, 3428-3434.
- (90) Yaliraki, S. N.; Ratner, M. A., *J. Chem. Phys.* **1998**, *109*, 5036-5043.
- (91) Datta, S., *Electronic transport in mesoscopic systems*. Cambridge University Press: New York, USA, 1995; Vol. 3.
- (92) Gadzuk, J. W.; Plummer, E. W., *Rev. Mod. Phys.* **1971**, *45*, 487-548.
- (93) Meisel, K. D.; Vocks, H.; Bobbert, P. A., *Phys. Rev. B* **2005**, *71*, 205206.
- (94) Segal, D.; Nitzan, A., *Chem. Phys.* **2002**, *281*, 235-256.
- (95) Zade, S. S.; Bendikov, M., *Chem. Eur. J.* **2008**, *14*, 6734-6741.
- (96) Efros, A. L.; Shklovskii, B. I., *J. Phys. C: Solid State Phys.* **1975**, *8*, L49-L51.
- (97) Rose, A., *Phys. Rev.* **1955**, *97*, 1538.
- (98) Lampert, M. A., *Phys. Rev.* **1956**, *103*, 1648.
- (99) Blum, A. S.; Kushmerick, J. G.; Long, D. P.; Patterson, C. H.; Yang, J. C.; Henderson, J. C.; Tour, J. M.; Shashidhar, R.; Ratna, B. R., *Nat. Mater.* **2005**, *4*, 167-172.
- (100) Kummel, A. C., *Science* **2003**, *302*, 1384.
- (101) Bumm, L. A.; Anorld, J. J.; Dunbar, T. D.; Allara, D. L.; Weiss, P. S., *J. Phys. Chem. B* **1999**, *103*, 8122.
- (102) Nakasa, A.; Akiba, U.; Fujihira, M., *Appl. Surf. Sci.* **2000**, *157*, 326-331.
- (103) Tao, N. J., *Phys. Rev. Lett.* **1996**, *76*, 4066.
- (104) Reed, M. A.; Zhou, C.; Muller, C. J.; Burgin, T. P.; Tour, J. M., *Science* **1997**, *278*, 252.
- (105) Reichert, J.; Ochs, R. D.; Beckmann, D.; Weber, H. B.; Mayor, M., *Phys. Rev. Lett.* **2002**, *88*, 176804.
- (106) Holmlin, R.; Haag, R.; Chabinye, M. L.; Ismagilov, R. F.; Cohen, A. E.; Terfort, A.; Rampi, M. A.; Whitesides, G. M., *J. Am. Chem. Soc.* **2001**, *123*, 5075.
- (107) Venkataraman, L.; Klare, J. E.; Nuckolls, C.; Hybertsen, M.; Steigerwald, M. L., *Nature* **2006**, *442*, 904.
- (108) Slowinski, K.; Fong, H. K. Y.; Majda, M., *J. Am. Chem. Soc.* **1999**, *121*, 7257.
- (109) Slowinski, K.; Majda, M., *J. Electroanal. Chem.* **2000**, *491*, 139.
- (110) Holmlin, R. E.; Haag, R.; Chabinye, M. L.; Ismagilov, R. F.; Cohen, A. E.; Terfort, A.; Rampi, M. A.; Whitesides, G. M., *J. Am. Chem. Soc.* **2001**, *123*, 5075-5085.
- (111) Kushmerick, J. G.; Holt, D. B.; Pollack, S. K.; Ratner, M. A.; Yang, J. C.; Schull, T. L.; Naciri, J.; Moore, M. H.; Shashidhar, R., *J. Am. Chem. Soc.* **2002**, *124*, 10654.

- (112) Chen, J.; Reed, M. A.; Rawlett, A. M.; Tour, J. M., *Science* **1999**, *286*, 1550.
- (113) Chen, J.; Calvet, L. C.; Reed, M. A.; Carr, D. W.; Grubisha, D. S.; Bennett, D. W., *Chem. Phys. Lett.* **1999**, *313*, 741.
- (114) T. W. Kelley; Granstrom, E.; Frisbie, C. D., *Adv. Mater.* **1999**, *11*, 261-264.
- (115) Wold, D. J.; Frisbie, C. D., *J. Am. Chem. Soc.* **2000**, *122*, 2970-2971.
- (116) Wold, D. J.; Frisbie, C. D., *J. Am. Chem. Soc.* **2001**, *123*, 5549-5556.
- (117) Leatherman, G.; Durantini, E. N.; Gust, D.; Moore, T. A.; Moore, A. L.; Stone, S.; Zhou, Z.; Rez, P.; Liu, Y. Z.; Lindsay, S. M., *J. Phys. Chem. B* **1999**, *103*, 4006-4010.
- (118) Engelkes, V. B.; Frisbie, C. D., *J. Phys. Chem. B* **2006**, *110*, 10011-10020.
- (119) Engelkes, V. B.; Beebe, J. M.; Frisbie, C. D., *J. Phys. Chem. B* **2005**, *109*, 16801-16810.
- (120) Tuccitto, N.; Ferri, V.; Cavazzini, M.; Quici, S.; Zhavnerko, G.; Licciardello, A.; Rampi, M. A., *Nat. Mater.* **2009**, *8*, 41-46.
- (121) Lafferentz, L.; Ample, F.; Yu, H.; Hecht, S.; Joachim, C.; Grill, L., *Science* **2009**, *323*, 1193-1197.
- (122) Langmuir, I.; Schaefer, V. J.; Wrinch, D. M., *Science* **1937**, *85*, 76.
- (123) Langmuir, I.; Schaefer, V. J., *J. Am. Chem. Soc.* **1936**, *58*, 284.
- (124) Blodgett, K. B., *J. Am. Chem. Soc.* **1935**, *57*, 1007.
- (125) Timp, G., *Nanotechnology*. Springer-Verlag: New York, 1999.
- (126) Tour, J. M.; Jones, L.; Pearson, D. L.; Lamba, J. J. S.; Burgin, T. P.; Whitesides, G. M.; Allara, D. L.; Parikh, A. N.; Atre, S., *J. Am. Chem. Soc.* **1995**, *117*, 9529-9534.
- (127) Bensebaa, F.; Vaicu, R.; Huron, L.; Ellis, T. H., *Langmuir* **1997**, *13*, 5335.
- (128) Yamada, R.; Uosaki, K., *Langmuir* **1997**, *13*, 5218.
- (129) Yamada, R.; Uosaki, K., *Langmuir* **1998**, *14*, 855.
- (130) Xu, S.; Cruchon-Dupeyrat, S. J. N.; Garno, J. C.; Liu, G. Y.; Jennings, G. K., *J. Chem. Phys.* **1998**, *108*, 5002.
- (131) Walczak, M. M.; Popenoe, D. D.; Deinhammer, R. S.; Lamp, B. D.; Chung, C.; Porter, M. D., *Langmuir* **1991**, *7*, 2687.
- (132) Delamarche, E.; Michel, B., *Thin Solid Films* **1996**, *273*, 54.
- (133) Poirier, G. E.; Tarlov, M. J., *Langmuir* **1994**, *10*, 2853.
- (134) Ulman, A.; Eilers, J. E.; Tillman, N., *Langmuir* **1989**, *5*, 1147.
- (135) Sabatani, E.; Cohn-Boulakia, J.; Bruening, M.; Rubinstein, I., *Langmuir* **1993**, *9*, 2914.
- (136) Ishida, T.; Mizutani, W.; Akiba, U.; Umemura, K.; Inoue, A.; Choi, N.; Rujihira, M.; Tokumoto, H. J., *J. Phys. Chem. B* **1999**, *103*, 1686.
- (137) Kim, Y.-T.; McCarley, R. L.; Bard, A. J., *J. Phys. Chem. B* **1992**, *96*, 7416.
- (138) Porter, M. D.; Bright, T. B.; Allara, D. L.; Chidsey, D. E. D., *J. Am. Chem. Soc.* **1987**, *109*, 3559.
- (139) Blackstock, J. J.; Li, Z. F., M. R.; Stewart, D. R., *Surface science* **2003**, *546*, 87.
- (140) Wagner, P.; Hegner, M.; Guntherodt, H.-J.; Semenza, G., *Langmuir* **1995**, *11*, 3867.
- (141) Rosink, J. J. W. M.; Blauw, M. A.; Geerligs, L. J.; van der Drift, E.; Rousseeuw, B. A. C.; Radelaar, S.; Sloof, W. G.; Fakkeldij, E. J. M., *Langmuir* **2000**, *16*, 4547-4553.
- (142) Tang, J.; Wang, Y.; Klare, J. E.; Tulevski, G. S.; Wind, S. J.; Nuckolls, C., *Angew. Chem. Int. Ed.* **2007**, *46*, 3892-3895.

- (143) Ulman, A., *An introduction to ultrathin organic films: from Langmuir-Blodgett to self-assembly*. Academic Press: San Diego, 1991.
- (144) Bain, C. D.; Troughton, E. B.; Tao, Y.-T.; Evall, J.; Whitesides, G. M.; Nuzzo, R. G., *J. Am. Chem. Soc.* **1989**, *111*, 321.
- (145) Beebe, J. M.; Engelkes, V. B.; Liu, J.; Gooding, J. J.; Eggers, P. K.; Jun, Y.; Zhu, X.; Paddon-Row, M. N.; Frisbie, C. D., *J. Phys. Chem. B* **2005**, *109*, 5207.
- (146) Terrill, R. H.; Tanzer, T. A.; Bohn, P. W., *Langmuir* **1998**, *14*, 845.
- (147) Allara, D. L.; Nuzzo, R. G., *Langmuir* **1985**, *1*, 52.
- (148) Allara, D. L.; Nuzzo, R. G., *Langmuir* **1985**, *1*, 45.
- (149) Arnold, R.; Terfort, A.; Woll, C., *Langmuir* **2001**, *17*, 4980.
- (150) Jun, Y.; Zhu, X.-Y., *J. Am. Chem. Soc.* **2004**, *126*, 13224.
- (151) Sikes, H. D.; Smalley, J. F.; Dudek, S. P.; Cook, A. R.; Newton, M. D.; Chidsey, C. E. D.; Feldberg, S. W., *Science* **2001**, *291*, 1519.
- (152) Nuzzo, R. G.; Fusco, F. A.; Allara, D. L., *J. Am. Chem. Soc.* **1987**, *109*, 2358.
- (153) Liu, D.; Szulczewski, G. J.; Kispert, L. D.; Primak, A.; Moore, T. A.; Moore, A. L.; Gust, D., *J. Phys. Chem. B* **2002**, *106*, 2933.
- (154) Fuxen, C.; Azzam, W.; Arnold, R.; Witte, G.; Terfort, A.; Woll, C., *Langmuir* **2001**, *17*, 3689.
- (155) Carroll, R. L.; Gorman, C. B., *Angew. Chem. Int. Ed.* **2002**, *41*, 4378-4400.
- (156) Kwok, K. S.; Ellenbogen, J. C., *MaterialsToday* **2002**, *February*, 28-37.
- (157) Segal, D.; Nitzan, A.; Davis, W. B.; Wasielewski, M. R.; Ratner, M. A., *Journal of Physical Chemistry B* **2000**, *104*, 3817-3829.
- (158) Davis, W. B.; Svec, W. A.; Ratner, M. A.; Wasielewski, M. R., *Nature* **1998**, *396*, 60-63.
- (159) Giese, B.; Amaudrut, J.; Kohler, A. K.; Spormann, M.; Wessely, S., *Nature* **2001**, *412*, 318-320.
- (160) Giese, B., *Accounts of Chemical Research* **2000**, *33*, 631-636.
- (161) Conwell, E. M., *Proceedings of the National Academy of Sciences of the United States of America* **2005**, *102*, 8795-8799.
- (162) Beratan, D. N.; Onuchic, J. N.; Winkler, J. R.; Gray, H. B., *Science* **1992**, *258*, 1740-1741.
- (163) Gray, H. B.; Winkler, J. R., *Proceedings of the National Academy of Sciences of the United States of America* **2005**, *102*, 3534-3539.
- (164) Hu, W. P.; Jiang, J.; Nakashima, H.; Luo, Y.; Kashimura, Y.; Chen, K. Q.; Shuai, Z.; Furukawa, K.; Lu, W.; Liu, Y. Q.; Zhu, D. B.; Torimitsu, K., *Physical Review Letters* **2006**, *96*, 027801.
- (165) Kubatkin, S.; Danilov, A.; Hjort, M.; Cornil, J.; Bredas, J. L.; Stuhr-Hansen, N.; Hedegard, P.; Bjornholm, T., *Nature* **2003**, *425*, 698-701.
- (166) Selzer, Y.; Cabassi, M. A.; Mayer, T. S.; Allara, D. L., *Journal of the American Chemical Society* **2004**, *126*, 4052-4053.
- (167) Selzer, Y.; Cai, L. T.; Cabassi, M. A.; Yao, Y. X.; Tour, J. M.; Mayer, T. S.; Allara, D. L., *Nano Letters* **2005**, *5*, 61-65.
- (168) Laibinis, P. E.; Bain, C. D.; Whitesides, G. M., *Journal of Physical Chemistry* **1991**, *95*, 7017-7021.



- (169) Fuxen, C.; Azzam, W.; Arnold, R.; Witte, G.; Terfort, A.; Woll, C., *Langmuir* **2001**, *17*, 3689-3695.
- (170) Bain, C. D.; Whitesides, G. M., *Journal of Physical Chemistry* **1989**, *93*, 1670-1673.
- (171) Corrigan, D. S.; Gao, P.; Leung, L. W. H.; Weaver, M. J., *Langmuir* **1986**, *2*, 744-752.
- (172) Sze, S. M., *Physics of Semiconductor Devices*. John Wiley & Sons: New York, 1981; p 402-407.
- (173) O'Dwyer, *The theory of electrical conduction and breakdown in solid dielectrics*. Clarendon press: Oxford, 1973.
- (174) Lampert, M. A., *Physical Review* **1956**, *103*, 1648-1656.
- (175) Lampert, M. A.; Mark, P., *Current Injection in Solids*. Academic Press: New York, 1970.
- (176) Nelson, D. L.; Cox, M. M., *Lehninger Principles of Biochemistry*. W. H. Freeman: **2005**.
- (177) Schwarz, G.; Mendel, R. R.; Ribbe, M. W., *Nature* **2009**, *460*, 839-847.
- (178) Kubatkin, S.; Danilov, A.; Hjort, M.; Cornil, J.; Bredas, J.-L.; Stuhr-Hansen, N.; Hedegard, P.; Bjornholm, T., *Nature* **2003**, *425*, 698-701.
- (179) Moth-Poulsen, K.; Bjornholm, T., *Nat. Nanotech.* **2009**, *4*, 551-556.
- (180) Metzger, R. M., *Chem. Rev.* **2003**, *103*, 3803-3834.
- (181) Chen, J.; Reed, M. A.; Rawlett, A. M.; Tour, J. M., *Science* **1999**, *286*, 1550-1552.
- (182) McQuade, D. T.; Pullen, A. E.; Swager, T. M., *Chem. Rev.* **2000**, *100*, 2537-2574.
- (183) McCreery, R. L.; Bergren, A. J., *Adv. Mater.* **2009**, *21*, 1-20.
- (184) Kronemeijer, A. J.; Akkerman, H. B.; Kudernac, T.; Wees, B. J. v.; Feringa, B. L.; Blom, P. W. M.; deBoer, B., *Adv. Mater.* **2008**, *20*, 1467-1473.
- (185) Akkerman, H. B.; Naber, R. C. G.; Jongbloed, B.; vanHalt, P. A.; Blom, P. W. M.; deLeeuw, D. M.; deBoer, B., *Proc. Natl. Acad. Sci. U. S. A.* **2007**, *104*, 11161-11166.
- (186) Cai, L.; Cabassi, M. A.; Yoon, H.; Cabarcos, O. M.; McGuinness, C. L.; Flatt, A. K.; Allara, D. L.; Tour, J. M.; Mayer, T. S., *Nano Lett.* **2005**, *5*, 2635-2372.
- (187) Akkerman, H. B.; Blom, P. W. M.; deLeeuw, D. M.; deBoer, B., *Nature* **2006**, *441*, 69-72.
- (188) McCreery, R. L.; Bergren, A. J., *Adv. mater.* **2009**, *21*, 1.
- (189) Haick, H.; Cahen, D., *Prog. Surf. Sci.* **2008**, *83*, 217-261.
- (190) Thieblemont, F.; Seitz, O.; Vilan, A.; Cohen, H.; Salomon, E.; Kahn, A.; Cahen, D., *Adv. Mater.* **2008**, *20*, 3931-3936.
- (191) Salomon, A.; Boecking, T.; Chan, C. K.; Amy, F.; Girshevitz, O.; Cahen, D.; Kahn, A., *Phys. Rev. Lett.* **2005**, *95*, 266807/266801-266807/266804.
- (192) Coropceanu, V.; Cornil, J.; Filho, D. A. S.; Oliver, Y.; Silbey, R.; Bredas, J.-L., *Chem. Rev.* **2007**, *107*, 926-952.
- (193) Bixon, M.; Jortner, J., *J. Chem. Phys.* **1997**, *107*, 5154-5170.
- (194) Hagiya, K.; Mitsui, S.; Taguchi, H., *Synthesis* **2003**, *6*, 823.
- (195) Bain, C. D.; Troughton, E. B.; Tao, Y.-T.; Evll, J.; Whitesides, G. M.; Nuzzo, R. G., *J. Am. Chem. Soc.* **1989**, *111*, 321-335.

- (196) Laibinis, P. E.; Bain, C. D.; Whitesides, G. M., *J. Phys. Chem.* **2002**, *95*, 7017-7021.
- (197) Bain, C. D.; Whitesides, G. M., *J. Phys. Chem.* **2002**, *93*, 1670-1673.
- (198) Becke, A. D., *J. Chem. Phys.* **1993**, *98*, 5648-5652.
- (199) Becke, A. D., *Phys. Rev. A: At. Mol. Opt. Phys.* **1988**, *38*, 3098-3100.
- (200) Lee, C.; Yang, W.; Parr, R. G., *Phys. Rev. B: Condens. Matter* **1987**, 785-789.
- (201) Zhao, Y.; Truhlar, D. G., *Theor. Chem. Acc.* **2008**, *120*, 215-241.
- (202) Risko, C.; Zangmeister, C. D.; Yao, Y.; Marks, T. J.; Tour, J. M.; Ratner, M. A.; van Zee, R. D., *J. Phys. Chem. C* **2008**, *112*, 13215-13225.
- (203) Zhan, X.; Risko, C.; Amy, F.; Chan, C.; Zhao, W.; Barlow, S.; Kahn, A.; Bredas, J.-L.; Marder, S. R., *J. Am. Chem. Soc.* **2005**, *127*, 9021-9029.
- (204) Chan, C. K.; Kim, E.-G.; Bredas, J.-L.; Kahn, A., *Adv. Funct. Mater.* **2006**, *16*, 831-837.
- (205) Frisch, M. J. *et al.* *Gaussian09*, Revision A.02; Gaussian, Inc.: Wallingford, CT, 2009.
- (206) Thompson, M. A. *ArgusLab 4.0.1*, Planaria Software LLC: Seattle, WA.
- (207) Liu, C.-L.; Chen, W.-C., *Macromol. Chem. Phys.* **2005**, *206*, 2212-2222.
- (208) Andres, S.; Guarin, P.; Dufresne, S.; Tsang, D.; Sylla, A.; Skene, W. G., *J. Mater. Chem.* **2007**, *17*, 2801-2811.
- (209) Schulze, J.; Gerson, F.; Murrell, J. N.; Heilbronner, E., *Helv. Chim. Acta* **1961**, *44*, 428-441.
- (210) Kaasbjerg, K.; Flensberg, K., *Nano Lett.* **2008**, *8*, 3809-3814.
- (211) Bredas, J.-L.; Street, G. B.; Themans, B.; Andre, J. M., *J. Chem. Phys.* **1985**, *83*, 1323-1329.
- (212) Wang, X.; Mallory, F. B.; Mallory, C. W.; Beckmann, P. A.; Rheingold, A. L.; Francl, M. M., *J. Phys. Chem. A* **2006**, *110*, 3954-3960.
- (213) Sze, S. M., *Physics of semiconductor devices*. 2nd ed.; John Wiley & Sons, Inc: New York, USA, 1981; p Chapter 7.
- (214) Rideout, V. L., *Thin Solid Films* **1978**, *48*, 261-291.
- (215) Choi, S. H.; Risko, C.; Delgado, M. C. R.; Kim, B.; Bredas, J.-L.; Frisbie, C. D., *J. Am. Chem. Soc.* **2010**, *132*, 4358-4368.
- (216) Roncali, J., *Chem. Rev.* **1997**, *97*, 173-206.
- (217) Segura, J. L.; Gomez, R.; Blanco, R.; Reinold, E.; Bauerle, P., *Chemistry of Materials* **2006**, *18*, 2834-2847.
- (218) Gunbas, G.; Durmus, A.; Toppare, L., *Chem. Mater.* **2008**, *20*, 7510-7513.
- (219) Beaujuge, P. M.; Ellinger, S.; Reynolds, J. R., *Nat. Mater.* **2008**, *7*, 795.
- (220) Steckler, T. T.; Zhang, X.; Hwang, J.; Honeyager, R.; Ohira, S.; Zhang, X.-H.; Grant, A.; Ellinger, S.; Odom, S. A.; Sweat, D.; Tanner, D. B.; Rinzler, A. G.; Barlow, S.; Bredas, J.-L.; Kippelen, B.; Marder, S. R.; Reynolds, J. R., *J. Amer. Chem. Soc.* **2009**, *131*, 2824-2826.
- (221) Martijn, M. W.; Mathieu, T.; Jan, G.; Ren, A. J. J., *Adv. Mater.* **2008**, *20*, 2556-2560.
- (222) Blouin, N.; Leclerc, M., *Acc. Chem. Res.* **2008**, *41*, 1110-1119.
- (223) Yongfang, L.; Yingping, Z., *Adv. Mat.* **2008**, *20*, 2952-2958.

- (224) Thompson, B. C.; Kim, Y.-G.; McCarley, T. D.; Reynolds, J. R., *J. Amer. Chem. Soc.* **2006**, *128*, 12714-12725.
- (225) Kulkarni, A. P.; Zhu, Y.; Babel, A.; Wu, P.-T.; Jenekhe, S. A., *Chem. Mater.* **2008**, *20*, 4212-4223.
- (226) Usta, H.; Facchetti, A.; Marks, T. J., *J. Amer. Chem. Soc.* **2008**, *130*, 8580-8581.
- (227) Liu, J.; Zhang, R.; Sauve, G. v.; Kowalewski, T.; McCullough, R. D., *J. Am. Chem. Soc.* **2008**, *130*, 13167-13176.
- (228) Alves, H.; Molinari, A. S.; Xie, H.; Morpurgo, A. F., *Nat Mater* **2008**, *7*, 574-580.
- (229) Segura, J. L.; Martin, N., *Angew. Chem. Int. Ed.* **2001**, *40*, 1372.
- (230) Bryce, M. R., *J. Mater. Chem.* **2000**, *10*, 589.
- (231) Katz, H. E.; Lovinger, A. J.; Johnson, J.; Kloc, C.; Siegrist, T.; Li, W.; Lin, Y. Y.; Dodabalapur, A., *Nature* **2000**, *404*, 478-481.
- (232) Wang, L.; Goodloe, G. W.; Stallman, G.; Cammarata, V., *Chem. Mater.* **1996**, *8*, 1175.
- (233) Hansen, J. G.; Bang, K. S.; Thorup, N.; Becher, J., *Eur. J. Org. Chem.* **2000**, 2135.
- (234) Andreu, R.; Garin, J.; Orduna, J., *Tetrahedron Lett.* **1994**, *35*, 9243.
- (235) Neuber, C.; Bate, M.; Giesa, R.; Schmidt, H.-W., *J. Mater. Chem.* **2006**, *16*, 3466.
- (236) Kwatra, B.; Ramakrishna, V.; Suri, S. K., *Thermochimica Acta* **1981**, *48*, 231-235.
- (237) Jaggi, M.; Blum, C.; Dupont, N.; Grilj, J.; Liu, S.-X.; Hauser, J. r.; Hauser, A.; Decurtins, S., *Org. Lett.* **2009**, *11*, 3096-3099.
- (238) Jaggi, M.; Blum, C.; Marti, B. S.; Liu, S.-X.; Leutwyler, S.; Decurtins, S., *Org. Lett.* **2010**, *12*, 1344-1347.
- (239) Perepichka, D. F.; Bryce, M. R.; Pearson, C.; Petty, M. C.; McInnes, E. J. L.; Zhao, J. P., *Angew. Chem. Int. Ed.* **2003**, *42*, 4636-4639.
- (240) Gao, X.; Wang, Y.; Yang, X.; Liu, Y.; Qiu, W.; Wu, W.; Zhang, H.; Qi, T.; Liu, Y.; Lu, K.; Du, C.; Shuai, Z.; Yu, G.; Zhu, D., *Adv. Mater.* **2007**, *19*, 3037-3042.
- (241) Pakoulev, A. V.; Burtman, V., *J. Phys. Chem. C* **2009**, *113*, 21413-21421.
- (242) Klein, R.; Leder, L. B., *Phys. Rev.* **1961**, *124*, 1046.
- (243) Murphy, E. L.; Good, R. H., *Phys. Rev.* **1956**, *102*, 1464.
- (244) Chen, S.-Y.; Lue, J.-T., *Phys. Lett. A* **2003**, *309*, 114.
- (245) Dyke, Y. K.; Barbour, J. P.; Martin, E. E.; Trolan, J. K., *Phys. Rev.* **1955**, *99*, 1192.
- (246) Tsai, F.-C.; Chang, C.-C.; Liu, C.-L.; Chen, W.-C.; Jenekhe, S. A., *Macromolecules* **2005**, *38*, 1958-1966.
- (247) Berkesi, O.; Kortvelyesi, T.; Hetenyi, C.; Nemeth, T.; Palinko, I., *Phys. Chem. Chem. Phys.* **2003**, *5*, 2009-2014.
- (248) Krebs, F. C.; Jorgensen, M., *Macromolecules* **2002**, *35*, 7200-7206.
- (249) Anthony, J. E., *Chem. Rev.* **2006**, *106*, 5028-5048.
- (250) Yoon, M.-H.; Facchetti, A.; Stern, C. E.; Marks, T. J., *J. Am. Chem. Soc.* **2006**, *128*, 5792-5801.
- (251) Renak, M. L.; Bartholomew, G. P.; Wang, S.; Ricatto, P. J.; Lachicotte, R. J.; Bazan, G. C., *J. Am. Chem. Soc.* **1999**, *121*, 7787-7799.
- (252) Seshadri, V.; Sotzing, G. A., *Chem. Mater.* **2004**, *16*, 5644-5649.

(253) Hoang Anh, H.; Hugues, B.; El Hadj, E.; Pierre, F. e.; Jean, R., *Advanced Materials* **1996**, *8*, 990-994.

(254) Heiner, D.; Erli, S., *J. Phys. Org. Chem.* **2000**, *13*, 587-590.

# Appendices

## 1. Curriculum Vitae

### Seong Ho Choi

**October 31, 1975** Born in Incheon, Republic of Korea

#### Education

**Ph.D. Candidate in Materials Chemistry**, October 2009

**University of Minnesota**, Minneapolis, MN

Thesis: Electrical Characterization of Long Conjugated Molecular Wires

Advisor: Professor C. Daniel Frisbie

**M.S. Organic/Polymer Chemistry**, February 2001

**Korea University**, Seoul, Republic of Korea

Thesis: Synthesis and Characterization of Hyperbranched Liquid Crystalline Polyester and Light-emitting Molecules based on Oxadiazoles

Advisor: Professor Jung-Il Jin

**B.S. Chemistry**, February 1999

**Korea University**, Seoul, Republic of Korea

## 2. List of Publications

- “Enhanced Hopping Conductivity in Low Bandgap Donor-Acceptor Molecular Wires up to 20 nm in Length” Choi, S. H. and Frisbie, C. D.  
In preparation for **J. Am. Chem. Soc.**
- “Length-Dependent Transport in Molecular Junctions based on SAMs of Aromatic Monothiols and Aromatic Dithiols: Effect of Contact Type and Metal Work Function.”  
Kim, B.-S.; Choi, S. H.; Kang, M. S.; Zhu, X.-Y.; Frisbie, C. D.  
Submitted to **J. Am. Chem. Soc.**
- “Transition from Tunneling to Hopping Transport in Long Conjugated Oligo-imine Wires Connected to Metals” Choi, S. H.; Risko, C.; Delgado, M. C. R.; Kim, B.-S.; Bredas, J.-L.; Frisbie, C. D. **J. Am. Chem. Soc.** **2010**, 132, 4358.
- “Electrical Resistance of Long Conjugated Molecular Wires.” Choi, S. H.; Kim, B.-S.; Frisbie, C. D. **Science** **2008**, 320, 1482.
- “Hopping Transport in Conjugated Molecular Wires Connected to Metal Contacts” Choi, S. H. and Frisbie, C. D., in Charge and Exciton Transport in Molecular Wires, ed. Siebbeles, L. D. A. and Grozema, F. C., **Wiley-VCH**, **2010** (Invited, in press)

### 3. Copyright Permission Letters

**THE AMERICAN ASSOCIATION FOR THE ADVANCEMENT OF SCIENCE LICENSE  
TERMS AND CONDITIONS**

Oct 05, 2009

---

This is a License Agreement between Seong Ho Choi ("You") and The American Association for the Advancement of Science ("The American Association for the Advancement of Science") provided by Copyright Clearance Center ("CCC"). The license consists of your order details, the terms and conditions provided by The American Association for the Advancement of Science, and the payment terms and conditions.

**All payments must be made in full to CCC. For payment instructions, please see information listed at the bottom of this form.**

License Number	2282760460121
License date	Oct 05, 2009
Licensed content publisher	The American Association for the Advancement of Science
Licensed content publication	Science
Licensed content title	Conductance of a Single Conjugated Polymer as a Continuous Function of Its Length
Licensed content author	Leif Lafferentz, Francisco Ample, Hao Yu, Stefan Hecht, Christian Joachim, Leonhard Grill
Licensed content date	Feb 27, 2009
Type of Use	Thesis
Requestor type	Other Individual
Format	Print and electronic
Portion	Figure
Number of figures/tables	1
Order reference number	
Title of your thesis / dissertation	Electrical Characterization of Long Conjugated Molecular Wires
Expected completion date	Oct 2009
Estimated size(pages)	150
Total	0.00 USD

**Terms and Conditions**

**American Association for the Advancement of Science TERMS AND CONDITIONS**

Regarding your request, we are pleased to grant you non-exclusive, non-transferable permission, to republish the AAAS material identified above in your work identified above, subject to the terms and conditions herein. We must be contacted for permission for any uses other than those specifically identified in your request above.

The following credit line must be printed along with the AAAS material: "From [Full Reference Citation]. Reprinted with permission from AAAS."

All required credit lines and notices must be visible any time a user accesses any part of the AAAS material and must appear on any printed copies and authorized user might make.

**THE AMERICAN ASSOCIATION FOR THE ADVANCEMENT OF SCIENCE LICENSE  
TERMS AND CONDITIONS**

Oct 05, 2009

---

---

This is a License Agreement between Seong Ho Choi ("You") and The American Association for the Advancement of Science ("The American Association for the Advancement of Science") provided by Copyright Clearance Center ("CCC"). The license consists of your order details, the terms and conditions provided by The American Association for the Advancement of Science, and the payment terms and conditions.

**All payments must be made in full to CCC. For payment instructions, please see information listed at the bottom of this form.**

License Number	2282760196759
License date	Oct 05, 2009
Licensed content publisher	The American Association for the Advancement of Science
Licensed content publication	Science
Licensed content title	Conductance of a Molecular Junction
Licensed content author	M. A. Reed, C. Zhou, C. J. Muller, T. P. Burgin, J. M. Tour
Licensed content date	Oct 10, 1997
Type of Use	Thesis
Requestor type	Other Individual
Format	Print and electronic
Portion	Figure
Number of figures/tables	1
Order reference number	
Title of your thesis / dissertation	Electrical Characterization of Long Conjugated Molecular Wires
Expected completion date	Oct 2009
Estimated size(pages)	150
Total	0.00 USD
Terms and Conditions	

American Association for the Advancement of Science TERMS AND CONDITIONS



**THE AMERICAN ASSOCIATION FOR THE ADVANCEMENT OF SCIENCE LICENSE  
TERMS AND CONDITIONS**

Oct 05, 2009

---

This is a License Agreement between Seong Ho Choi ("You") and The American Association for the Advancement of Science ("The American Association for the Advancement of Science") provided by Copyright Clearance Center ("CCC"). The license consists of your order details, the terms and conditions provided by The American Association for the Advancement of Science, and the payment terms and conditions.

**All payments must be made in full to CCC. For payment instructions, please see information listed at the bottom of this form.**

License Number	2282740713181
License date	Oct 05, 2009
Licensed content publisher	The American Association for the Advancement of Science
Licensed content publication	Science
Licensed content title	Electrical Resistance of Long Conjugated Molecular Wires
Licensed content author	Seong Ho Choi, BongSoo Kim, C. Daniel Frisbie
Licensed content date	Jun 13, 2008
Type of Use	Thesis
Requestor type	Original Author
Format	Print and electronic
Portion	Full Text
Order reference number	
Title of your thesis / dissertation	Electrical Characterization of Long Conjugated Molecular Wires
Expected completion date	Oct 2009
Estimated size(pages)	150
Total	0.00 USD
Terms and Conditions	

**THE AMERICAN ASSOCIATION FOR THE ADVANCEMENT OF SCIENCE LICENSE  
TERMS AND CONDITIONS**

Oct 05, 2009

---

---

This is a License Agreement between Seong Ho Choi ("You") and The American Association for the Advancement of Science ("The American Association for the Advancement of Science") provided by Copyright Clearance Center ("CCC"). The license consists of your order details, the terms and conditions provided by The American Association for the Advancement of Science, and the payment terms and conditions.

**All payments must be made in full to CCC. For payment instructions, please see information listed at the bottom of this form.**

License Number	2282760343979
License date	Oct 05, 2009
Licensed content publisher	The American Association for the Advancement of Science
Licensed content publication	Science
Licensed content title	Large On-Off Ratios and Negative Differential Resistance in a Molecular Electronic Device
Licensed content author	J. Chen, M. A. Reed, A. M. Rawlett, J. M. Tour
Licensed content date	Nov 19, 1999
Type of Use	Thesis
Requestor type	Other Individual
Format	Print and electronic
Portion	Figure
Number of figures/tables	1
Order reference number	
Title of your thesis / dissertation	Electrical Characterization of Long Conjugated Molecular Wires
Expected completion date	Oct 2009
Estimated size(pages)	150
Total	0.00 USD
Terms and Conditions	

**NATURE PUBLISHING GROUP LICENSE  
TERMS AND CONDITIONS**

Oct 05, 2009

---

---

This is a License Agreement between Seong Ho Choi ("You") and Nature Publishing Group ("Nature Publishing Group") provided by Copyright Clearance Center ("CCC"). The license consists of your order details, the terms and conditions provided by Nature Publishing Group, and the payment terms and conditions.

**All payments must be made in full to CCC. For payment instructions, please see information listed at the bottom of this form.**

License Number	2282760697778
License date	Oct 05, 2009
Licensed content publisher	Nature Publishing Group
Licensed content publication	Nature Materials
Licensed content title	
Licensed content author	Nunzio Tuccitto, Violetta Ferri, Marco Cavazzini, Silvio Quici, Genady Zhavnerko et al.
Volume number	8
Issue number	1
Pages	pp41-46
Year of publication	2008
Portion used	Figures / tables
Requestor type	Student
Type of Use	Thesis / Dissertation
High-res requested	No
Billing Type	Invoice
Company	Seong Ho Choi
Billing Address	1178 Gibbs Ave #S1  Saint Paul, MN 55108 United States
Customer reference info	
Total	0.00 USD
Terms and Conditions	

**AMERICAN CHEMICAL SOCIETY LICENSE  
TERMS AND CONDITIONS**

Oct 05, 2009

---

This is a License Agreement between Seong Ho Choi ("You") and American Chemical Society ("American Chemical Society") provided by Copyright Clearance Center ("CCC"). The license consists of your order details, the terms and conditions provided by American Chemical Society, and the payment terms and conditions.

**All payments must be made in full to CCC. For payment instructions, please see information listed at the bottom of this form.**

License Number	2282750675706
License Date	Oct 05, 2009
Licensed content publisher	American Chemical Society
Licensed content publication	Journal of the American Chemical Society
Licensed content title	Electron Transport through Thin Organic Films in Metal-Insulator-Metal Junctions Based on Self-Assembled Monolayers
Licensed content author	R. Erik Holmlin et al.
Licensed content date	May 1, 2001
Volume number	123
Issue number	21
Type of Use	Thesis/Dissertation
Requestor type	Not specified
Format	Print and Electronic
Portion	Table/Figure/Chart
Number of Table/Figure/Charts	1
Author of this ACS article	No
Order reference number	
Title of the thesis / dissertation	Electrical Characterization of Long Conjugated Molecular Wires
Expected completion date	Oct 2009
Estimated size(pages)	150
Billing Type	Invoice
Billing Address	1178 Gibbs Ave #S1
	Saint Paul, MN 55108
	United States
Customer reference info	
Total	0.00 USD
Terms and Conditions	

**AMERICAN CHEMICAL SOCIETY LICENSE  
TERMS AND CONDITIONS**

Oct 05, 2009

---

This is a License Agreement between Seong Ho Choi ("You") and American Chemical Society ("American Chemical Society") provided by Copyright Clearance Center ("CCC"). The license consists of your order details, the terms and conditions provided by American Chemical Society, and the payment terms and conditions.

**All payments must be made in full to CCC. For payment instructions, please see information listed at the bottom of this form.**

License Number	2282750328860
License Date	Oct 05, 2009
Licensed content publisher	American Chemical Society
Licensed content publication	Nano Letters
Licensed content title	Effect of Local Environment on Molecular Conduction: Isolated Molecule versus Self-Assembled Monolayer
Licensed content author	Yoram Selzer et al.
Licensed content date	Jan 1, 2005
Volume number	5
Issue number	1
Type of Use	Thesis/Dissertation
Requestor type	Not specified
Format	Print and Electronic
Portion	Table/Figure/Chart
Number of Table/Figure/Charts	1
Author of this ACS article	No
Order reference number	
Title of the thesis / dissertation	Electrical Characterization of Long Conjugated Molecular Wires
Expected completion date	Oct 2009
Estimated size(pages)	150
Billing Type	Invoice
Billing Address	1178 Gibbs Ave #S1
	Saint Paul, MN 55108
	United States
Customer reference info	
Total	0.00 USD
Terms and Conditions	

**Thesis/Dissertation**

**AMERICAN CHEMICAL SOCIETY LICENSE  
TERMS AND CONDITIONS**

Oct 05, 2009

---

This is a License Agreement between Seong Ho Choi ("You") and American Chemical Society ("American Chemical Society") provided by Copyright Clearance Center ("CCC"). The license consists of your order details, the terms and conditions provided by American Chemical Society, and the payment terms and conditions.

**All payments must be made in full to CCC. For payment instructions, please see information listed at the bottom of this form.**

License Number	2282750022264
License Date	Oct 05, 2009
Licensed content publisher	American Chemical Society
Licensed content publication	Journal of the American Chemical Society
Licensed content title	FTIR Spectroscopy of Buried Interfaces in Molecular Junctions
Licensed content author	Yongseok Jun et al.
Licensed content date	Oct 1, 2004
Volume number	126
Issue number	41
Type of Use	Thesis/Dissertation
Requestor type	Not specified
Format	Print and Electronic
Portion	Table/Figure/Chart
Number of Table/Figure/Charts	1
Author of this ACS article	No
Order reference number	
Title of the thesis / dissertation	Electrical Characterization of Long Conjugated Molecular Wires
Expected completion date	Oct 2009
Estimated size(pages)	150
Billing Type	Invoice
Billing Address	1178 Gibbs Ave #S1
	Saint Paul, MN 55108
	United States
Customer reference info	
Total	0.00 USD
Terms and Conditions	

**Thesis/Dissertation**

**AMERICAN CHEMICAL SOCIETY LICENSE  
TERMS AND CONDITIONS**

Oct 05, 2009

---

---

This is a License Agreement between Seong Ho Choi ("You") and American Chemical Society ("American Chemical Society") provided by Copyright Clearance Center ("CCC"). The license consists of your order details, the terms and conditions provided by American Chemical Society, and the payment terms and conditions.

**All payments must be made in full to CCC. For payment instructions, please see information listed at the bottom of this form.**

License Number	2282750524361
License Date	Oct 05, 2009
Licensed content publisher	American Chemical Society
Licensed content publication	Journal of the American Chemical Society
Licensed content title	Effect of Bond-Length Alternation in Molecular Wires
Licensed content author	James G. Kushmerick et al.
Licensed content date	Sep 1, 2002
Volume number	124
Issue number	36
Type of Use	Thesis/Dissertation
Requestor type	Not specified
Format	Print and Electronic
Portion	Table/Figure/Chart
Number of Table/Figure/Charts	1
Author of this ACS article	No
Order reference number	
Title of the thesis / dissertation	Electrical Characterization of Long Conjugated Molecular Wires
Expected completion date	Oct 2009
Estimated size(pages)	150
Billing Type	Invoice
Billing Address	1178 Gibbs Ave #S1  Saint Paul, MN 55108 United States
Customer reference info	
Total	0.00 USD
Terms and Conditions	

**Thesis/Dissertation**

**AMERICAN CHEMICAL SOCIETY LICENSE  
TERMS AND CONDITIONS**

Oct 05, 2009

---

---

This is a License Agreement between Seong Ho Choi ("You") and American Chemical Society ("American Chemical Society") provided by Copyright Clearance Center ("CCC"). The license consists of your order details, the terms and conditions provided by American Chemical Society, and the payment terms and conditions.

**All payments must be made in full to CCC. For payment instructions, please see information listed at the bottom of this form.**

License Number	2282750841723
License Date	Oct 05, 2009
Licensed content publisher	American Chemical Society
Licensed content publication	Journal of the American Chemical Society
Licensed content title	Mercury–Mercury Tunneling Junctions. 1. Electron Tunneling Across Symmetric and Asymmetric Alkanethiolate Bilayers
Licensed content author	Krzysztof Slowinski et al.
Licensed content date	Aug 1, 1999
Volume number	121
Issue number	31
Type of Use	Thesis/Dissertation
Requestor type	Not specified
Format	Print and Electronic
Portion	Table/Figure/Chart
Number of Table/Figure/Charts	1
Author of this ACS article	No
Order reference number	
Title of the thesis / dissertation	Electrical Characterization of Long Conjugated Molecular Wires
Expected completion date	Oct 2009
Estimated size(pages)	150
Billing Type	Invoice
Billing Address	1178 Gibbs Ave #S1
	Saint Paul, MN 55108
	United States
Customer reference info	
Total	0.00 USD
Terms and Conditions	

**Thesis/Dissertation**



**AMERICAN CHEMICAL SOCIETY LICENSE  
TERMS AND CONDITIONS**

Oct 05, 2009

---

This is a License Agreement between Seong Ho Choi ("You") and American Chemical Society ("American Chemical Society") provided by Copyright Clearance Center ("CCC"). The license consists of your order details, the terms and conditions provided by American Chemical Society, and the payment terms and conditions.

**All payments must be made in full to CCC. For payment instructions, please see information listed at the bottom of this form.**

License Number	2282741297950
License Date	Oct 05, 2009
Licensed content publisher	American Chemical Society
Licensed content publication	Journal of the American Chemical Society
Licensed content title	Thermally Activated Electron Transport in Single Redox Molecules
Licensed content author	Li et al.
Licensed content date	Sep 1, 2007
Volume number	129
Issue number	37
Type of Use	Thesis/Dissertation
Requestor type	Not specified
Format	Print and Electronic
Portion	Table/Figure/Chart
Number of Table/Figure/Charts	1
Author of this ACS article	No
Order reference number	
Title of the thesis / dissertation	Electrical Characterization of Long Conjugated Molecular Wires
Expected completion date	Oct 2009
Estimated size(pages)	150
Billing Type	Invoice
Billing Address	1178 Gibbs Ave #S1
	Saint Paul, MN 55108
	United States
Customer reference info	
Total	0.00 USD
Terms and Conditions	

**Thesis/Dissertation**